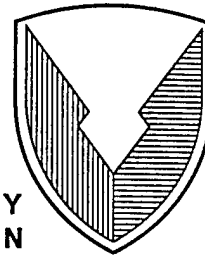


USAATCOM TR 95-D-5

U.S. ARMY  
AVIATION  
AND TROOP COMMAND



## **PREDICTION AND CONTROL OF HEAT TREAT DISTORTION OF HELICOPTER GEARS**

Arthur D. Little, Inc.  
Acorn Park  
Cambridge, Massachusetts 02140-2390

August 1995

Final Report

EWIC QUALITY INSPECTED 8

**APPROVED FOR PUBLIC RELEASE; DISTRIBUTION IS UNLIMITED.**

Prepared for:

**AVIATION APPLIED TECHNOLOGY DIRECTORATE  
U.S. ARMY AVIATION AND TROOP COMMAND  
FORT EUSTIS, VA 23604-5577**

19960924 010

Aviation Applied Technology Directorate  
Position Statement

This report presents the results of an effort to develop a computer model to predict the distortion arising in helicopter gears as a result of carburization, harden/quench, and temper heat treatment processes. Modelling and experiments were carried out on simplified flat disk and rim/web gear blank geometries. The results of this effort provide basic insight into the mechanisms affecting distortion in helicopter gears during heat treatment. This effort will be useful in the development of more refined distortion prediction models which can be used in the design of gears, quench presses, and heat treatment processes.

Philip LaFerriere of the Power Systems Division served as project engineer for this effort.

Trade names cited in this report do not constitute an official endorsement or approval of the use of such commercial hardware and software.

# REPORT DOCUMENTATION PAGE

Form Approved  
OMB No. 0704-0188

Public reporting burden for this collection of information is estimated to average 1 hour per response, including the time for reviewing instructions, searching existing data sources, gathering and maintaining the data needed, and completing and reviewing the collection of information. Send comments regarding this burden estimate or any other aspect of this collection of information, including suggestions for reducing this burden, to Washington Headquarters Services, Directorate for Information Operations and Reports, 1215 Jefferson Davis Highway, Suite 1204, Arlington, VA 22202-4302, and to the Office of Management and Budget, Paperwork Reduction Project (0704-0188), Washington, DC 20503.

1. AGENCY USE ONLY (Leave blank)		2. REPORT DATE August 1995	3. REPORT TYPE AND DATES COVERED Final; June 1992 - May 1995
4. TITLE AND SUBTITLE Prediction and Control of Heat Treat Distortion of Helicopter Gears			5. FUNDING NUMBERS  DAAJ02-92-C-0030
6. AUTHOR(S)  R. Stringfellow			8. PERFORMING ORGANIZATION REPORT NUMBER
7. PERFORMING ORGANIZATION NAME(S) AND ADDRESS(ES) Arthur D. Little, Inc. Acorn Park Cambridge, MA 02140			10. SPONSORING/MONITORING AGENCY REPORT NUMBER  USAATCOM TR 95-D-5
9. SPONSORING/MONITORING AGENCY NAME(S) AND ADDRESS(ES) Aviation Applied Technology Directorate U.S. Army Aviation and Troop Command Fort Eustis, Virginia 23604-5577			11. SUPPLEMENTARY NOTES
12a. DISTRIBUTION/AVAILABILITY STATEMENT  Approved for public release; distribution is unlimited.			12b. DISTRIBUTION CODE
13. ABSTRACT (Maximum 200 words) A helicopter gear heat treatment distortion modelling approach was developed using a commercially available finite element program. The model predicts distortion and residual stresses resulting from carburization, harden/quench and temper processes performed on gears fabricated from 9310 steel. Accurate prediction of heat treatment distortion could aid in the design of gears, heat treatment processes and quench dies to reduce distortion. This would result in a significant reduction in scrap and rework for new gear designs.  The model development included the development of constitutive equations, gathering of materials property data and determination of heat transfer coefficients.  The model was demonstrated on a simple flat disk geometry and a rim/web accessory gear blank. Model results are compared to experimental heat treatments of these configurations.			
14. SUBJECT TERMS Helicopters, drive systems, gears, heat treatment, distortion, modelling			15. NUMBER OF PAGES 192
			16. PRICE CODE
17. SECURITY CLASSIFICATION OF REPORT Unclassified	18. SECURITY CLASSIFICATION OF THIS PAGE Unclassified	19. SECURITY CLASSIFICATION OF ABSTRACT Unclassified	20. LIMITATION OF ABSTRACT Unlimited

# DISCLAIMER NOTICE



**THIS DOCUMENT IS BEST  
QUALITY AVAILABLE. THE  
COPY FURNISHED TO DTIC  
CONTAINED A SIGNIFICANT  
NUMBER OF PAGES WHICH DO  
NOT REPRODUCE LEGIBLY.**

## TABLE OF CONTENTS

LIST OF FIGURES .....	iii
LIST OF TABLES .....	ix
BACKGROUND .....	1
Objectives .....	2
Approach .....	2
MODEL DEVELOPMENT .....	3
Carbon diffusion model .....	3
Thermomechanical model .....	5
UMAT subroutine .....	7
Heat transfer equations .....	12
DETERMINATION OF MATERIAL PROPERTIES .....	19
Carbon diffusivity .....	20
Surface carbon reaction rate .....	20
Phase transformation properties .....	23
Specific heat and heat of transformation .....	30
Thermal conductivity .....	30
Stress-strain behavior .....	30
Elastic constants .....	36
Incorporating material properties into the model .....	36
DETERMINATION OF SURFACE HEAT TRANSFER COEFFICIENTS .....	42
Experiments .....	42
Numerical approach .....	44
EVALUATION OF THE MODEL THROUGH APPLICATION TO A CARBURIZED FLAT DISK .....	52
Experimental procedure .....	52
Experimental results .....	55
Finite element model .....	60

## TABLE OF CONTENTS (cont.)

APPLICATION OF THE MODEL TO A PRESS-QUENCHED GEAR	
BLANK .....	78
Experimental procedure .....	78
Experimental results .....	87
Model Description .....	99
Modeling Results .....	103
Summary .....	122
CONCLUSIONS .....	125
RECOMMENDATIONS .....	127
ACKNOWLEDGMENTS .....	129
REFERENCES .....	130
Appendix A. ....	131
Appendix B. ....	135
Appendix C. ....	159
Appendix D. ....	168
Appendix E. ....	175

## LIST OF FIGURES

<u>Figure</u>	<u>Page</u>
1 Carbon distribution near outer edge of disk during carburization . . . . .	4
2 Schematic of finite element analysis process, showing inputs, outputs and procedural interactions. . . . .	6
3 Schematic of infinite cylinder quench simulation. . . . .	14
4 Variation of temperature within cylinder at five times during the quench. .	15
5 Variation of circumferential stress within cylinder at five times during the quench. . . . .	16
6 Variation of martensite volume fraction within cylinder at five times during the quench. . . . .	17
7 Radial displacement history of outer surface of the cylinder during the simulated quench transient. . . . .	18
8 Variation of Rockwell C hardness between the surface and the core for each of three carburization levels. . . . .	21
9 Variation of diffusivity parameter, $D_c$ , with carburization temperature and carbon content, as defined by equation (28). . . . .	22
10 CCT diagram for SAE 9310, austenitized 20 minutes at 830 C. . . . .	24
11 Change in length of dilatometer specimen with temperature for uncarburized 9310 steel austenitized and cooled at 80 C/sec. . . . .	25
12 Calculated variation of martensite volume fraction $f$ and martensite evolution rate $df/dT$ for the base 9310 alloy. . . . .	26
13 CCT diagram for 9310 at two different carbon contents. Left: blank carburized base alloy at 0.1 C ( $C_c = 0.001$ ). Right: base alloy through carburized to 0.34%C . . . . .	27
14 CCT diagram for 9310 at two different carbon contents. Left: base alloy through carburized to 0.58 C ( $C_c = 0.0058$ ). Right: base alloy through carburized to 0.83% C. . . . .	28

15	Variation of $M_s$ and $M_d$ with carbon content. . . . .	29
16	Variation of specific heat, including heat of transformation, with temperature. . . . .	31
17	Calculated variation of the coefficient of thermal expansion with temperature based upon thermal diffusivity data given in Solter [9]. . . . .	32
18	Measured variation of 0.2% offset yield strength with temperature and carbon content. . . . .	34
19	Measured variation of stress at 2% strain with temperature and carbon content. . . . .	35
20	Variation of Young's Modulus of austenite and martensite phases given by equation (32). . . . .	37
21	Calculated variation of martensite volume fraction $f$ and martensite evolution rate $df/dT$ shown with functional fits based upon a two-sided normal distribution. . . . .	39
22	Comparison of model fit to measured variation in 0.2% offset yield strength with temperature and carbon content. . . . .	41
23	Specimens used in surface heat transfer measurement experiments. Left: half inch diameter specimen. Right: 6 inch diameter specimen. . . . .	43
24	Fixture used to measure the surface heat transfer between 9310 steel and oil flowing parallel to the specimen surface. . . . .	45
25	Fixture used to measure the surface heat transfer between 9310 steel and flowing oil impinging the specimen surface. . . . .	46
26	Test fixture used to conduct the metal-to-metal contact test. . . . .	47
27	Cooling curves for each of the surface heat transfer measurement tests. . . . .	48
28	Calculated variation of surface heat transfer with temperature for each of the measured conditions. . . . .	50
29	Schematic of disk specimen used for experiments and modeling study. . . . .	53
30	Measured distortion prior to carburization, following carburization, and following quench for one of the three carburized disk specimens (D1). . . . .	56



31	Measured distortion prior to carburization, following carburization, and following quench for one of the two uncarburized disk specimens (D5). . .	57
32	Averaged edge distortion following carburization, quench, deep-freeze and temper operations for each of the eight disks processed in the parameter study. . . . .	59
33	Finite element mesh used to model the heat treatment of the rim/web gear blank . . . . .	61
34	Model fit to experiments performed on 9310 steel specimen to quantify difference between surface heat . . . . .	62
35	Comparison of model prediction of carbon profile at top surface of disk versus directly and indirectly measured values. . . . .	63
36	Temperature history of the surrounding media imposed as thermal boundary conditions for each of eight steps used to simulate the carburization, quench, deep-freeze and temper operations. . . . .	65
37	A comparison of undeformed and deformed meshes showing the growth of the disk and a contour diagram showing the nearly uniform temperature distribution following heat-up to the carburization temperature. . . . .	66
38	Contours of temperature, bainite volume fraction, and equivalent plastic strain superposed on the deformed mesh for a time just after the temperature has decreased below that for start of the bainite transformation for the uncarburized material, causing the disk to bend upward. . . . .	67
39	Contours of temperature, bainite volume fraction, and equivalent plastic strain superposed on the deformed mesh for a later time at which the bainite transformation of the uncarburized region is nearing completion, and the disk is bending further upward . . . . .	68
40	Contours of temperature, bainite volume fraction, and equivalent plastic strain superposed on the deformed mesh for a time at which the carburized layer has begun to transform, straightening the disk out. . . . .	69
41	Contours of temperature, bainite volume fraction, and equivalent plastic strain superposed on the deformed mesh after the disk has cooled down, showing the resulting deformation, the untransformed layer, and the residual plastic strain. . . . .	70

42	A comparison of deformed and deformed meshes showing the growth and residual bending due to carburization, and a contour diagram showing the nearly uniform temperature distribution following heat-up due to the austenitization temperature. . . . .	71
43	Contours of temperature, martensite volume fraction, and equivalent plastic strain superposed on the deformed mesh for a time just after the temperature has decreased below that for start of the martensite transformation for the uncarburized material, causing the disk to again bend upward. . . . .	72
44	Contours of temperature, martensite volume fraction, and equivalent plastic strain superposed on the deformed mesh after the disk has cooled down, showing the resulting deformation, the untransformed upper layer, and the residual plastic strain. . . . .	73
45	Comparison of model predictions for of edge distortion with averaged measured values following carburization, quench, deep-freeze and temper operations for each of the eight disks processed in the parameter study. . . .	74
46	A schematic of the rim/web gear blank with carburized regions indicated. . . . .	79
47	The tooling configuration for the press quench operation. . . . .	81
48	The lower die. . . . .	82
49	Thermocouple placement for measurement of surface temperature histories. . . . .	84
50	The instrumented gear. . . . .	85
51	Dimensional measurement locations. . . . .	86
52	Averaged measured temperature histories. The number of valid data sets for each thermocouple are indicated in parentheses. . . . .	88
53	Comparison of averaged measured temperature histories between top and the bottom of the web. . . . .	89
54	Measured temperature history at thermocouple TC2 for each of the six tests. . . . .	90
55	Average measured distortion following carburization. . . . .	92

56	Average measured distortion following deep-freeze/temper. ....	94
57	Variation of measured distortion around the circumference following deep-freeze for gear blank RW2 .....	95
58	Indentation pattern along support shoulder of lower part of shaft following quench .....	96
59	Measured variation of hardness underneath surface of rim following quench and temper. ....	98
60	Finite element mesh for the rim/web gear blank. ....	100
61	Flow chart illustrating procedure used to model gear blank heat treatment. ....	101
62	Calculated contours of carbon content showing steep carbon gradient near surface of each carburized region. ....	104
63	Comparison between calculated carbon content and values inferred from hardness measurements. ....	105
64	Comparison between model predictions of distortion following carburization and measured values. ....	106
65	Contours of temperature and martensite volume fraction during quench $t = 7.2$ seconds. ....	108
66	Contours of temperature and martensite volume fraction during quench. $t = 15.6$ seconds .....	110
67	Contours of temperature and martensite volume fraction during quench. $t = 17.1$ seconds. ....	111
68	Contours of temperature and martensite volume fraction during quench. $t = 19.2$ seconds. ....	112
69	Contours of temperature and martensite volume fraction during quench. $t = 20.9$ seconds. ....	113
70	Contours of temperature and martensite volume fraction during quench. $t = 23.7$ seconds. ....	114

71	Contours of temperature and martensite volume fraction during quench. t = 28.2 seconds. ....	115
72	Contours of temperature and martensite volume fraction during quench. t = 38.0 seconds. ....	116
73	Comparison between model predictions of distortion following carburization and measured values. ....	118
74	Contours of calculated residual circumferential stress (left) and radial stress (right), in MP <sub>a</sub> , following quench. ....	120
75	Profiles of calculated circumferential stress near the edge of the rim following deep-freeze and temperature ....	121
76	Profiles of calculated radial stress along the top of the web following deep-freeze. ....	123

## LIST OF TABLES

<u>Table</u>	<u>Page</u>
1. Material properties required for the model . . . . .	19
2. Tensile specimen carburization levels . . . . .	33
3. Tensile data at the tempering temperature . . . . .	36
4. Coefficients used in model to fit transformation parameters using functional form given in equations 31-33 . . . . .	38
5. Coefficients used in model to fit tensile data using functional form given in equation 34 . . . . .	40
6. The physical properties used in the calculation of surface heat transfer coefficients . . . . .	49
7. Parameter combinations for the statistically-designed experimental study . . . . .	55
8. Measurements of distortion after carburization and quench for each of the three carburized disks . . . . .	58
9. Measurements of distortion for each of the eight experiments of the parameter study . . . . .	58
10. Comparison between model and experimental predictions for distortion following carburization, quench, deep-freeze and temper of the carburized disk specimen . . . . .	75
11. A comparison between model and experimentally determined significance of processing parameters on distortion after quench and deep- freeze . . . . .	76
12. Average distortion following carburization . . . . .	91
13. Average distortion following deep-freeze . . . . .	93
14. Data from residual stress measurements . . . . .	99

15.	Comparison of model calculated distortion following carburization with averaged measured values . . . . .	107
16.	Comparison of model calculated distortion following deep-freeze with averaged measured values . . . . .	117
17.	Comparison of key model predictions with measurements . . . . .	122

## BACKGROUND

Military helicopters play an increasingly important role in battlefield mobility. For example, the UH-60 BLACK HAWK, manufactured by Sikorsky Aircraft, performs a variety of missions, including assaults, resupply, medical evacuation, command and control, and tactical positioning of reserves. Among the critical components influencing the performance and reliability of helicopters are the gears in the drive trains. Sikorsky and other helicopter manufacturers currently rely on experience when making improvements to present gear production processes or when developing production processes for advanced larger and lighter weight gears. Process designers would greatly benefit from a tool that could assist them in the prediction and control of the least understood portion of the gear manufacturing process, heat treatment.

Heat treatment is performed to achieve the necessary surface hardness and through-toughness of precision helicopter gears. The heat treating process is comprised of four stages: carburization, austenitization and quench, deep-freeze, and tempering. At each of these stages, part distortion and residual stress are introduced. Rejection or rework of gears due to excessive heat treat distortion adds significantly to the cost of gear production. Industry estimates are that 15% of all production gears are scrapped as a result of distortion and that this figure can reach 50% for some of the newer, lighter gear designs. As helicopters are required to be more and more lightweight, thinner gears will likely be even more susceptible to heat treat distortion.

Industry practice relies on process designer experience to estimate how or where in the heat treating process the distortion and stress are introduced. However, there are practical limits to this approach. Because empirical methods often require several iterations to achieve process improvements, the approach is time consuming, expensive, and less effective as part complexity increases. Furthermore, as new materials are introduced, the lack of practical experience makes these methods that much more difficult.

Improvement in prediction and control of the heat treat process requires the development and introduction of simulation tools. Development of such tools are made feasible by recent advances computer processing speed, finite element analysis methodologies, and materials property characterization, which make it possible to predict behavior for parts with complicated geometries and nonlinear boundary conditions and material properties.

Finite element analysis is a powerful computer-based method that has been commonly used for many years to solve complex problems in engineering. It is only the last several years— as computers have become much faster and cheaper—that this method has been used to simulate materials processes. The use of finite element methods to simulate heat treat processes presents itself as one of the many challenging subjects in the area of materials processing research.

The complex interaction of the many fields that come to bear in heat treatment—metallurgy, nonlinear solid mechanics, solid and fluid heat transfer, coupled with the need for materials

property data that is not commonly available, make the simulation of heat treat processes a challenging task. However, the benefits provided by a successful modeling program — a cost-effective tool that can reduce or eliminate much of the trial-and-error currently used to design gears and gear processes and to troubleshoot problematic processes — make this challenge one that many in the heat treatment community believe is necessary to confront.

The development of a computer simulation methodology for prediction of heat treat distortion described in this report is one of many efforts currently underway. These include, to name a few: a multi-year program directed by the National Center for Manufacturing Sciences aimed at developing methodologies for distortion prediction and control in automotive gears, the HEARTS program developed in Japan, and TRAST, a program that is currently being developed in Europe. None of these programs, however, has been applied or tailored to the unique problems and needs of the helicopter gear industry.

## OBJECTIVES

The ultimate objective of this research and development effort is to develop a simulation tool which will assist process engineers in the design of heat treat processes. The tool will enable the user to predict the distortion and residual stresses which are likely to occur during heat treating in terms of part geometry and processing conditions. In addition, the tool will allow the user to predict such things as carbon profiles, furnace soak times, residual stress patterns, and phase content.

The immediate objectives of this first phase of investigation include the development of the computational methodology for the heat treat simulation model; the determination, through measurement and literature review, of the material properties required for the model; and an initial evaluation of the model by comparison of model predictions with experimental results for heat treatments of parts with simplified geometries. This first phase has also served to identify those areas of the problem that need more attention and to define the logical next steps for improvement of the model.

## APPROACH

In order to achieve the immediate objectives presented above, the program was divided into five activities:

1. development of the simulation model
2. evaluation of required material properties
3. measurement of surface heat transfer coefficients
4. evaluation of the model through application to a carburized flat disk
5. application of the model to a press-quenched gear blank.

In each of the last two activities, controlled heat treatments were carried out to provide a basis for evaluation of the model's simulation capabilities.



## MODEL DEVELOPMENT

The model developed for simulation of the carburization, quench, deep-freeze and temper processes is structured around the commercially-available finite element analysis package ABAQUS [1].

The model consists of two distinct components: one for simulation of carbon diffusion, and another for thermo-mechanical analysis of each of the heat treat stages. The carbon profile calculated using the carbon diffusion model is stored in a file and read into the thermo-mechanical model as an input.

### CARBON DIFFUSION MODEL

The carbon diffusion model was implemented in the ABAQUS program using its \*HEAT TRANSFER procedure, taking advantage of the mathematical analogy between the equations governing diffusion and heat conduction. The governing equation for diffusion in a solid is given as:

$$\partial C_c / \partial t = D_c \nabla^2 C_c , \quad (1)$$

where  $C_c$  is the weight percent of carbon and  $D_c$  is the diffusivity of carbon in iron. This equation is therefore analogous to the heat conduction equation

$$\partial T / \partial t = D_h \nabla^2 T , \quad (2)$$

with carbon diffusivity  $D_c$  analogous to heat diffusivity  $D_h = k / \rho c_p$ , where  $k$  is conductivity,  $\rho$  is density and  $c_p$  is specific heat. The diffusivity coefficient  $D_c$  is a function of both temperature and carbon content.

The boundary condition for this equation is:

$$q_C = \beta \rho (C_{atm} - C_{c,0}) , \quad (3)$$

where  $q_C$  is the surface carbon flux rate,  $\beta$  is an effective reaction rate constant,  $\rho$  is density,  $C_{atm}$  is the atmosphere carbon potential and  $C_{c,0}$  is the baseline carbon content.

The temperature is fixed for the carburization simulation. ABAQUS allows for the diffusivity coefficient  $D_c$  to vary as a function of  $C_c$  through use of the temperature-dependence of the conductivity parameter.

To provide some verification for the model, we simulated the carburization of the outer edge of a six inch diameter by one inch thick disk. The baseline helicopter gear material, SAE-9310 steel, with a baseline carbon content of 0.1 percent, was subjected to carburization at 1800 F (982 C) for 24 hours with an imposed atmospheric carbon potential of 0.9 percent. Figure 1 shows the variation of carbon content near the outer edge of the disk at 6 hour

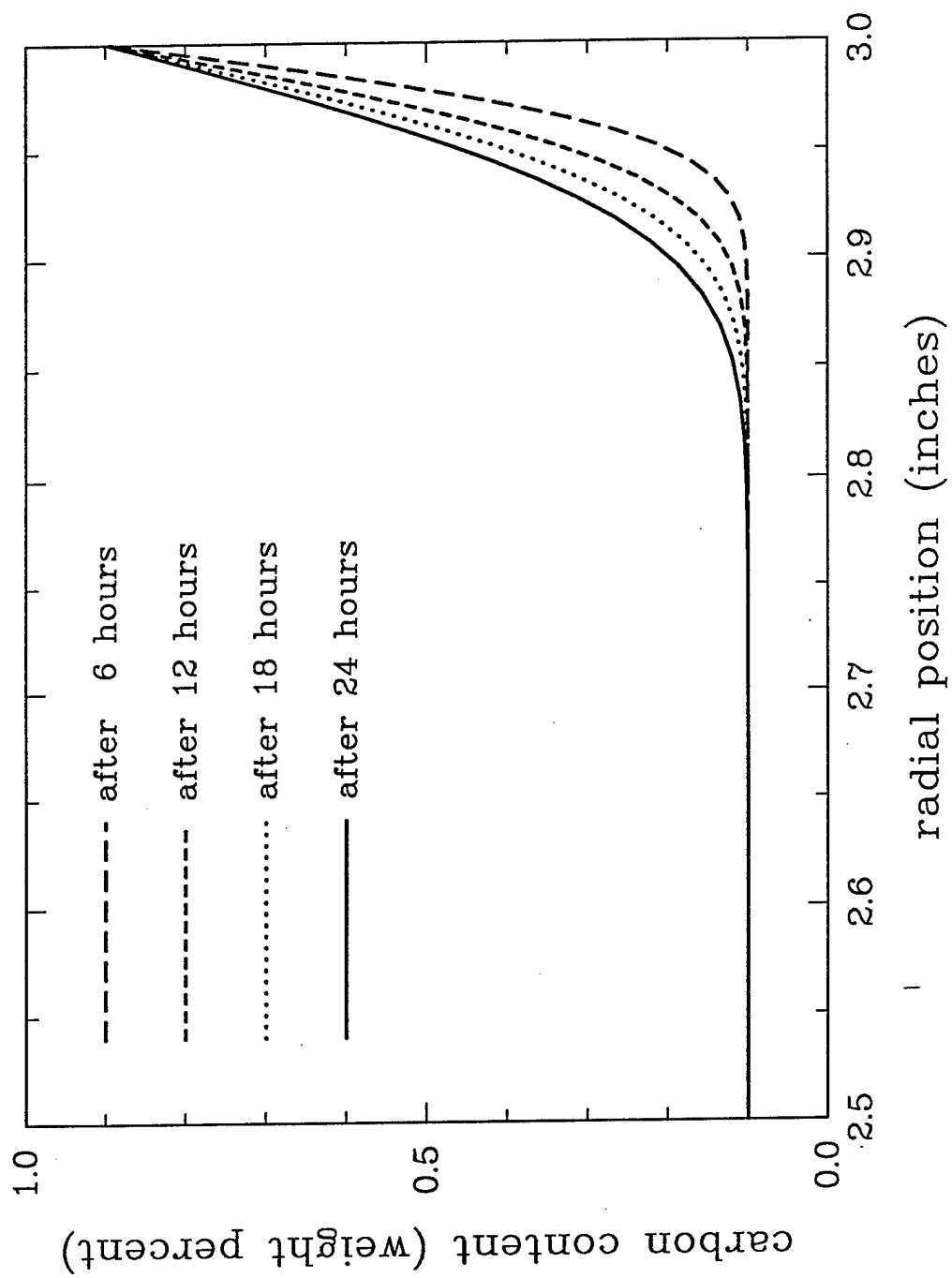


Figure 1. Carbon distribution near outer edge of disk during carburization.

intervals during the carburization. The calculated final value of total case depth — defined to be the radial inward distance from the outer edge of the disk to a point at which the carbon content increases from its core value to 0.4 percent — is about 0.13 inches, which is in good agreement with data taken from Stickels [2].

### THERMOMECHANICAL MODEL

Heat treatment processes, and, in particular, the quench process, are characterized by rapid temperature change and large temperature gradients. The heat treat simulation model must account for transient heat transfer, both within the solid (conduction), and between the solid and its surroundings, whether it be air, a quenchant, or a constraining die. The change in temperature accompanying heat transfer produces thermal expansion and contraction, and can also lead to changes in the structure of the material, namely phase transformations. The model must therefore be able to account for evolution of phase volume fractions, transformation volume and shape change, and the latent heat of transformation. Finally, in order to describe the mechanics of heat treat processes, the model must be able to describe the elastic-plastic deformation of this evolving two-phase material.

The ABAQUS program provides two different approaches for conducting thermomechanical calculations: coupled and uncoupled. Using the uncoupled method, a heat transfer analysis is first carried out and the calculated temperatures are stored in a file. A stress analysis is then performed using the stored temperature profiles as inputs. Using the coupled procedure, these calculations are made in an incremental fashion, i.e., the heat transfer calculation for a given time increment is first made, and then the stress calculation for that same time increment is made. If necessary, the heat transfer calculation is repeated based upon the stress calculation, and so on. The coupled method appears to have one disadvantage — it generally requires more CPU time. However, there are two distinct advantages to the coupled method: it does not require the storage of large quantities of temperature data; and it allows for coupling between the solution of the stress/equilibrium equations with those governing heat transfer. This latter feature is potentially very important in models for heat treatment because of the phase transformations that occur during quench. The transformation is a strong function of temperature (and can also depend upon the state of stress). In turn, the stress state is a strong function of the properties of the transformation products. At the same, time, the transformation absorbs heat and therefore affects heat transfer.

For our model, we have chosen the coupled approach, due to the potentially significant coupling between the mechanics of the transformation and heat transfer, and because it is a little more user-friendly in that it requires only a single analysis,

The thermomechanical model is described schematically in a flow diagram in Figure 2. Each heat treatment process is simulated by means of an iterative time-stepping procedure wherein the time associated with each process step is broken into a number of smaller pieces. Thermal properties (conductivity, density and heat capacity) and thermal conditions at the beginning of the time step (i.e., the temperature of the part and its surroundings) are fed into the heat transfer solver for a given time increment,  $t_i$ . Surface heat flux is calculated via the FILM subroutine, which allows the user to define surface heat transfer characteristics as a

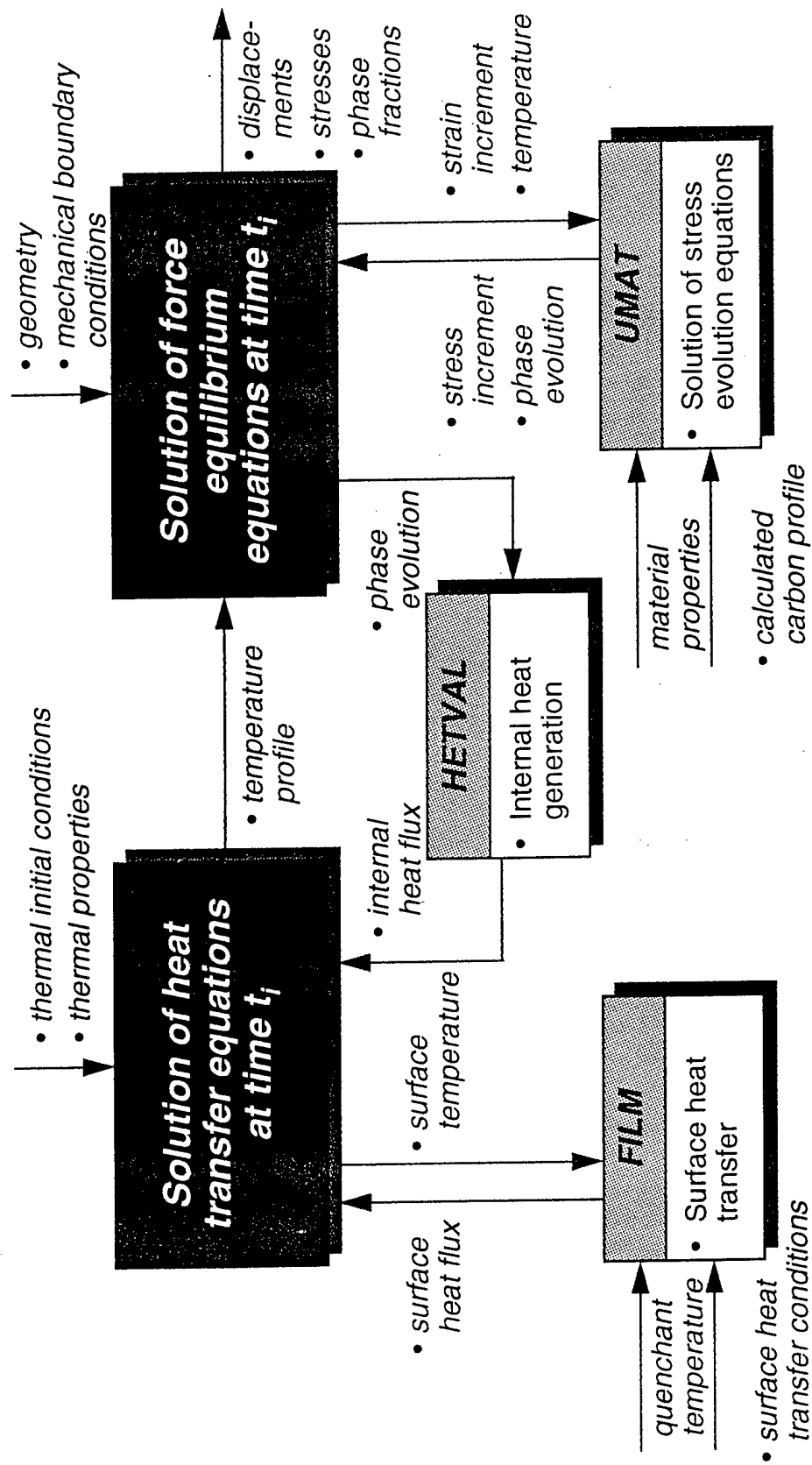


Figure 2. Schematic of finite element analysis process, showing inputs, outputs and procedural interactions.

function of temperature, time, position, etc. The heat transfer calculation is solved to determine a temperature profile for time  $t_i$ , which is then fed into the force equilibrium solver along with the mechanical boundary conditions. An initial estimate of the strain increment at each material point is passed, along with the calculated temperature, into a subroutine called UMAT. In this subroutine, described in more detail below, the stress evolution equations are solved as functions of the temperature, strain increment, and the properties of the material (including the carbon content) at this location. The UMAT subroutine passes back the calculated stresses for that increment along with other data, including the phase evolution for the increment. Based upon this information, the force equilibrium equations for time  $t_i$  are solved iteratively. As required, phase evolution data is fed into a third subroutine, HETVAL, where internal heat generation is calculated and fed back into the heat transfer solver, where a new calculation of the temperature profile for time  $t_i$  is made. This iterative process continues until the equilibrium and heat transfer equations have both been satisfied to within some small tolerance. The output of the model at each time step  $t_i$  includes temperature, displacements, stresses, and phase fractions at each calculation point.

### UMAT SUBROUTINE

The mathematical model describing material behavior during quench, which is incorporated in the ABAQUS program via the UMAT subroutine, is described below. This model, without any additional complexity, also describes behavior during deep-freeze. A few modifications in material properties and program flow are used to model the carburization and temper steps, as noted.

As discussed above, the primary purpose of the UMAT subroutine is to integrate the stress state from time  $t$  to time  $t+\Delta t$  based upon estimates of the increment in strain and temperature over the increment provided by ABAQUS. The updated information is passed back into the main part of ABAQUS and used to solve the global equations of equilibrium. Other variables which describe the state of the material, such as the hardness and volume fraction of individual phases, are also updated within the UMAT. Finally, the heat generated by changes in stress and material state are calculated and used in solving the governing heat transfer equations.

To simplify the discussion that follows, we introduce notation such that, for example:

$$\sigma_{ij}^0 \equiv \sigma_{ij}(t) ;$$

$$\sigma_{ij} \equiv \sigma_{ij}(t+\Delta t)$$

are used to denote the stress tensor at time  $t$  (the beginning of the increment) and at time  $t+\Delta t$  (the end of the increment). Standard indicial notation is used.

The following variables are passed into the UMAT:

$$\sigma_{ij}^0 \equiv \text{beginning-of-increment stress tensor} ;$$

$\epsilon_{ij}^0 \equiv$  beginning-of-increment strain tensor ;  
 $\Delta\epsilon_{ij} \equiv$  strain increment tensor ;  
 $T^0 \equiv$  beginning-of-increment temperature ;  
 $\Delta T \equiv$  temperature increment;  
 $v^0(n) \equiv$  beginning-of-increment vector of state variables ;  
 $\Delta t \equiv$  time increment.

The primary objective of the UMAT is to calculate the stress tensor at the end of the increment:

$$\sigma_{ij} = \sigma_{ij}^0 + \Delta\sigma_{ij}. \quad (4)$$

The stress increment,  $\Delta\sigma_{ij}$ , is estimated to be equal to the stress rate,  $\dot{\sigma}_{ij}$ , multiplied by the time increment,  $\Delta t$ :

$$\Delta\sigma_{ij} = \dot{\sigma}_{ij}\Delta t. \quad (5)$$

The stress rate is in turn assumed to be related to the strain rate through a stress evolution equation:

$$\dot{\sigma}_{ij} = L_{ijkl}^e [\dot{\epsilon}_{kl}^e], \quad (6)$$

where  $L_{ijkl}^e$  is the 4th order elasticity tensor and  $\epsilon_{ij}^e$  is the elastic part of the strain rate tensor.

For SAE-9310 steel undergoing quench, the strain rate tensor has four parts:

$$\dot{\epsilon}_{ij} = \dot{\epsilon}_{ij}^e + \dot{\epsilon}_{ij}^T + \dot{\epsilon}_{ij}^p + \dot{\epsilon}_{ij}^{tr}, \quad (7)$$

where

- $\dot{\epsilon}_{ij}^T \equiv$  thermal strain rate ,
- $\dot{\epsilon}_{ij}^p \equiv$  plastic slip strain rate ,
- $\dot{\epsilon}_{ij}^{tr} \equiv$  transformation strain rate .

The total strain rate is provided as an input to the UMAT; the elastic part of the strain rate must be calculated in order to determine the stress rate. The contributions to the strain rate due to thermal expansion, plastic slip and transformation must therefore be calculated.

Since it has no shear component, calculation of the thermal contribution to the strain rate is straightforward:

$$\dot{\epsilon}_{kk}^T = \alpha \dot{T}, \quad (8)$$

where  $\dot{T}$  is the rate of temperature change (known),  $\dot{\epsilon}_{kk}^T$  represents the hydrostatic component of  $\dot{\epsilon}_{ij}^T$  and  $\alpha$  is the coefficient of thermal expansion.

Calculation of the plastic slip and transformation components of the strain rate tensor is more complex. To calculate the transformation strain, we must introduce an evolution law for the martensite phase. We assume the following evolution equation for martensite volume fraction,  $f$ :

$$\dot{f} = P(\Theta) \dot{\Theta}, \quad (9)$$

where  $P(\Theta)$  is a transformation distribution function, which prescribes the rate of formation of martensite for a given value of the driving force,  $\Theta$ , where:

$$\Theta = k_T(T_m - T) + k_e \sigma_e^0 + k_m \sigma_m^0, \quad (10)$$

and  $k_T$ ,  $k_e$  and  $k_m$  are constants that must be determined by experimentation.

The first term on the right hand side of equation (10) represents the predominant thermal part of the driving force; the second two terms are additional components of driving force due to stress and reflect the stress-dependence of the transformation kinetics.  $T_m$  is the mean temperature for transformation, which is a strong function of the carbon content.  $\sigma_e$  is the equivalent or von Mises stress, which provides a measure of the size of the deviatoric component of the stress tensor.  $\sigma_m$  is the mean stress, which provides a measure of the size of the hydrostatic component of the stress tensor.

Once the rate of formation of martensite has been calculated, we can calculate the associated transformation strain rate. The transformation strain rate has a deviatoric (shear) component, which is biased in the direction of deviatoric plastic strain, and a hydrostatic or volume change component. The transformation strain rate is further proportional to the rate of increase in martensite volume fraction, so that:

$$\dot{\epsilon}_{ij}^{tr} = \dot{f}(k_s N_{ij} + \Delta_v \delta_{ij}), \quad (11)$$

where  $k_s$  and  $\Delta_v$  are constants representing the shape strain and volume change accompanying the transformation,  $\delta_{ij}$  is the second order identity tensor, and  $N_{ij}$  is a unit tensor coaxial with the direction of deviatoric plastic strain. Following several authors, we use the method of radial return [3] to determine the direction of shear deformation. Using this method, we assume that the direction of deviatoric plastic strain rate,  $N_{ij}$ , is in the same direction as that given by an elastic predictor of the stress state,

$$\sigma_{ij}^{*'} = \sigma_{ij}^{0'} + 3\mu \Delta t (\dot{\epsilon}_{ij}^{e'}), \quad (12)$$

where  $\mu = \mu(T)$  is the elastic shear modulus.

In this equation, the prime (') is used to denote the deviatoric component of the given tensor,

which is defined such that, for example,

$$\sigma_{ij}' = \sigma_{ij} - 1/3\sigma_{kk} . \quad (13)$$

The tensor  $N_{ij}$  is thus defined as:

$$N_{ij} = \sigma_{ij}^{**} / |\sigma_{ij}^{**}| , \quad (14)$$

where  $|\sigma_{ij}^{**}|$  is the magnitude of  $\sigma_{ij}^{**}$ .

Using an isotropic hardening model, the plastic slip strain rate,  $\dot{\epsilon}_{ij}^p$ , is calculated indirectly by requiring that, when plastic flow is occurring, the equivalent stress,

$$\sigma_e \equiv \sqrt{3/2\sigma_{ij}'\sigma_{ij}'} ,$$

must satisfy the yield criterion of the evolving two-phase steel,  $Y$ , so that

$$\sigma_e = Y , \quad (15)$$

In addition, using the radial return method, the stress evolution equation for isotropic hardening must be satisfied:

$$\sigma_e = \sigma_e^* - 3\mu\Delta t(\dot{\epsilon}_e^p + \dot{\epsilon}_e^{tr}) , \quad (16)$$

with

$$\sigma_e^* N_{ij} \equiv \sigma_{ij}^* ;$$

$$\dot{\epsilon}_e^p N_{ij} \equiv \dot{\epsilon}_{ij}^p ;$$

$$\dot{\epsilon}_e^{tr} N_{ij} \equiv \dot{\epsilon}_{ij}^{tr} .$$

The yield function  $Y$  describes the internal resistance of the material to plastic slip deformation. We have chosen to use a rule of mixtures law to determine  $Y$ , which requires that

$$Y = fY_{mart} + (1-f)Y_{aust} . \quad (17)$$

We further assume that plastic slip is rate-independent over the range of strain rates encountered during quenching, so that

$$Y_{aust} \equiv s_{aust}(T, C_c) ;$$

$$Y_{mart} \equiv s_{mart}(T, C_c) .$$

where  $s_{aust}(T, C_c)$  and  $s_{mart}(T, C_c)$  are the hardnesses of the two phases. The hardnesses of each phase evolve with plastic deformation:



$$s_{\text{aust}} = s_{\text{aust}}^0 + h_{\text{aust}} \dot{\epsilon}_e^p \Delta t ; \quad (18)$$

$$s_{\text{mart}} = s_{\text{mart}}^0 + h_{\text{mart}} \dot{\epsilon}_e^p \Delta t , \quad (19)$$

where  $h_{\text{aust}} = \hat{h}_{\text{aust}}(s_{\text{aust}}, T, C_c)$  and  $h_{\text{mart}} = \hat{h}_{\text{mart}}(s_{\text{mart}}, T, C_c)$  are the hardening rates of the two phases and

$$\dot{\epsilon}_e^p \equiv \sqrt{2/3 \dot{\epsilon}_{ij} \dot{\epsilon}_{ij}} ,$$

is the equivalent plastic strain rate. Since the martensite phase is much harder than the austenite phase, plastic flow will occur in the austenite phase first. We therefore assume that, when the stress is less than  $Y_{\text{mart}}$ , the equivalent plastic strain rate in the austenite phase is equal to  $1/(1-f)$  times the composite equivalent plastic strain rate and the equivalent plastic strain rate in the martensite phase is zero. When the stress is greater than  $Y_{\text{mart}}$ , we assume that the strain rate in each phase is equal to the composite strain rate.

Subtracting (16) from (17), we thus arrive at an explicit equation which, after some manipulation, has one unknown — the equivalent plastic strain rate,  $\dot{\epsilon}_e^p$ .

Once  $\sigma_e$  has been determined, the end-of-increment stress tensor is given as:

$$\sigma_{ij} = \sigma_e N_{ij} + 1/3 \sigma_m , \quad (20)$$

where

$$\sigma_m = \sigma_m^0 + 3\kappa \Delta t (\dot{\epsilon}_{kk} - \dot{\epsilon}_{kk}^{\text{tr}} - \dot{\epsilon}_{kk}^T) , \quad (21)$$

and where  $\kappa = \kappa(T)$  is the bulk modulus.

The state variables,  $f = f^0 + f \Delta t$ , etc, are updated and placed into the end-of-increment state variable vector,  $v(n)$ .

Before returning control to the main part of ABAQUS, the material Jacobians,

$$J^e = d\sigma_{ij}/d\epsilon_{ij} ; \quad (22)$$

$$J^T = d\sigma_{ij}/dT \quad (23)$$

are calculated. The calculations of the Jacobians are too detailed to describe here; they simply involve mathematical manipulation of the equations used to determine the end-of-increment stress tensor.

Material behavior during carburization is modelled in the same manner as described above for quench. In this case the transformation temperatures and the transformation volume change become those associated with the slower cooling rates found in carburizing. The transformation product is assumed to be bainite instead of austenite. It should be noted that no diffusional transformations are assumed to take place.

Material behavior during the temper operation is modelled in a quite simple fashion. Tempering is performed in order to increase the surface toughness of the material, which is low due to the high carbon content. During temper, carbon atoms diffuse through the material and form carbides, thus reducing the effective carbon content. The amount of diffusion that takes place during the temper operation is a function of the tempering temperature, the tempering time, and the carbon content. As one might expect, high temperatures and high carbon levels promote diffusion and hardness change. At higher temperatures, the decrease in carbon content lowers hardness, but this effect is very small for the low tempering temperatures ( $T=150$  C) that are used for helicopter gears. There is, however, a small negative volume change associated with the loss of carbon from solution. A small modification to the UMAT is made to account for this volume change during the simulation of the temper operation; the volume change is accommodated as an effective change in the thermal expansion coefficient near the tempering temperature.

### HEAT TRANSFER EQUATIONS

As noted above, the primary coupling between the stress/equilibrium and heat transfer models is through the heat of transformation, which can be expressed as:

$$h^{tr} = k_{heat} \dot{f} \quad (24)$$

Heat of transformation data is used in the heat transfer calculation routines of ABAQUS in the solution of the heat conduction equation:

$$\partial T / \partial t = k / (\rho c_p) \nabla^2 T + h^{tr} \quad (25)$$

The value of  $\dot{f}$  at the end of the increment is passed into the subroutine, HETVAL, providing heat generation information to the heat transfer calculations for that increment.

The boundary condition for equation (25) depends upon the type of heat transfer. For convection, the surface heat flux  $q_c$  is assumed to be a linear function of the difference between the part surface temperature,  $T_s$  and the bath temperature  $T_b$ , through a film coefficient  $H$ :

$$q_c = H(T_s - T_b) \quad (26)$$

This relationship is incorporated into the heat transfer routine via the FILM subroutine. The film coefficient,  $H$ , is known to be a strong function of temperature; a significant effort has been devoted to measuring  $H$  under different conditions, as will be discussed in a later section of this report.

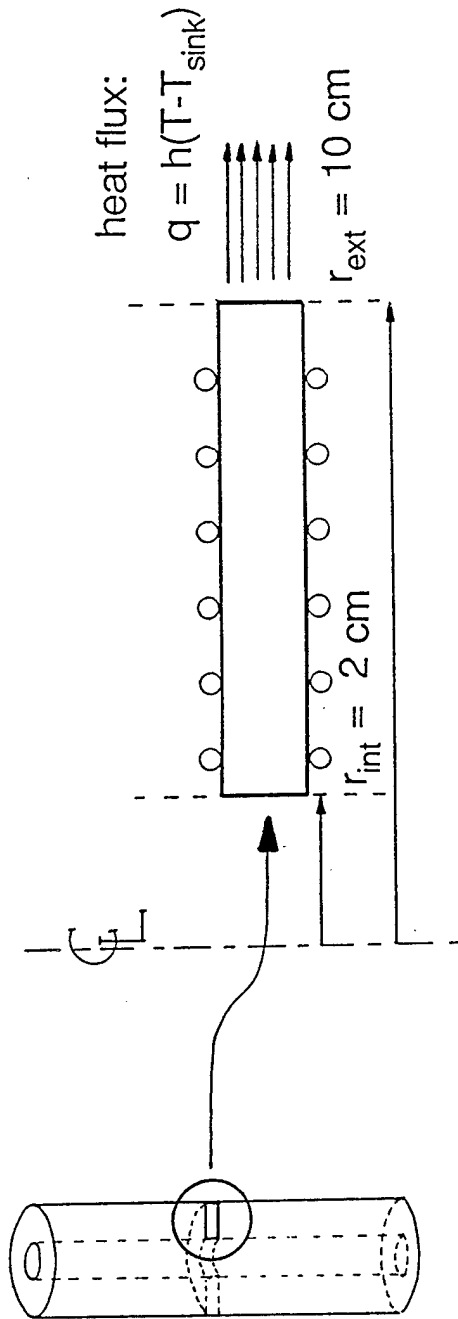
Although measurements of heat transfer between the part and air were made for this investigation, the mechanism of heat transfer was not considered to be critical to the model. As such, heat transfer data for both radiation and convection were lumped into an effective film coefficient.

If radiative heat transfer with air were deemed to be important, it could be included in the model using the DFLUX subroutine, which provides a more general definition of the surface heat flux. The equation governing surface heat loss due to radiation is:

$$q_r = \sigma_{sb} A (T_s^4 - T_a^4), \quad (27)$$

where  $T_a$  is air temperature,  $\sigma_{sb}$  is the Stefan-Boltzman constant and  $A$  is a constant which accounts for the surface emissivity and the geometry of the surrounding environment.

To illustrate the performance of the model, Figures 3 through 7 summarize model predictions of behavior for a infinitely long, hollow, right-circular cylinder subjected to an oil quench with heat transfer on its outer surface only. Figure 3 shows a schematic of this simple one-dimensional problem. The cylinder is assumed to be initially at the austenitization temperature, 830 C. The oil bath is at 20 C. The cylinder has not been carburized. Figure 4 shows the variation of temperature of the cylinder at five different times during the quench. As one might expect, the temperature drops more rapidly at the outer surface of the disk, creating a temperature gradient. The gradient becomes less severe with time until finally, after about 30 to 50 minutes, the temperature is uniform. This gradient in temperature produces a circumferential stress, as shown in Figure 5. At early times, a state of compressive stress with a steep gradient near the wall exists due to thermal contraction. After 300 seconds, however, the temperature of the wall has dropped well below the martensite start temperature, causing martensite to form (Figure 6). The accompanying transformation of martensite and its associated volume change causes the circumferential stress to reverse sign. After most of the martensite has formed and as the temperature continues to drop, a more complex stress state develops due to the combined effect of transformation volume change and thermal contraction. Finally, after the temperature has equalized, the stresses become smaller, but a residual stress state remains. Figure 7 shows the displacement history of the outer surface of the wall, illustrating the initial thermal contraction followed by transformation expansion followed by a secondary thermal contraction.



$$T_{\text{init}} = 830 \text{ C}$$

$$T_{\text{sink}} = 20 \text{ C}$$

$$M_s = 440 \text{ C}$$

$$M_f = 230 \text{ C}$$

Figure 3. Schematic of infinite cylinder quench simulation.

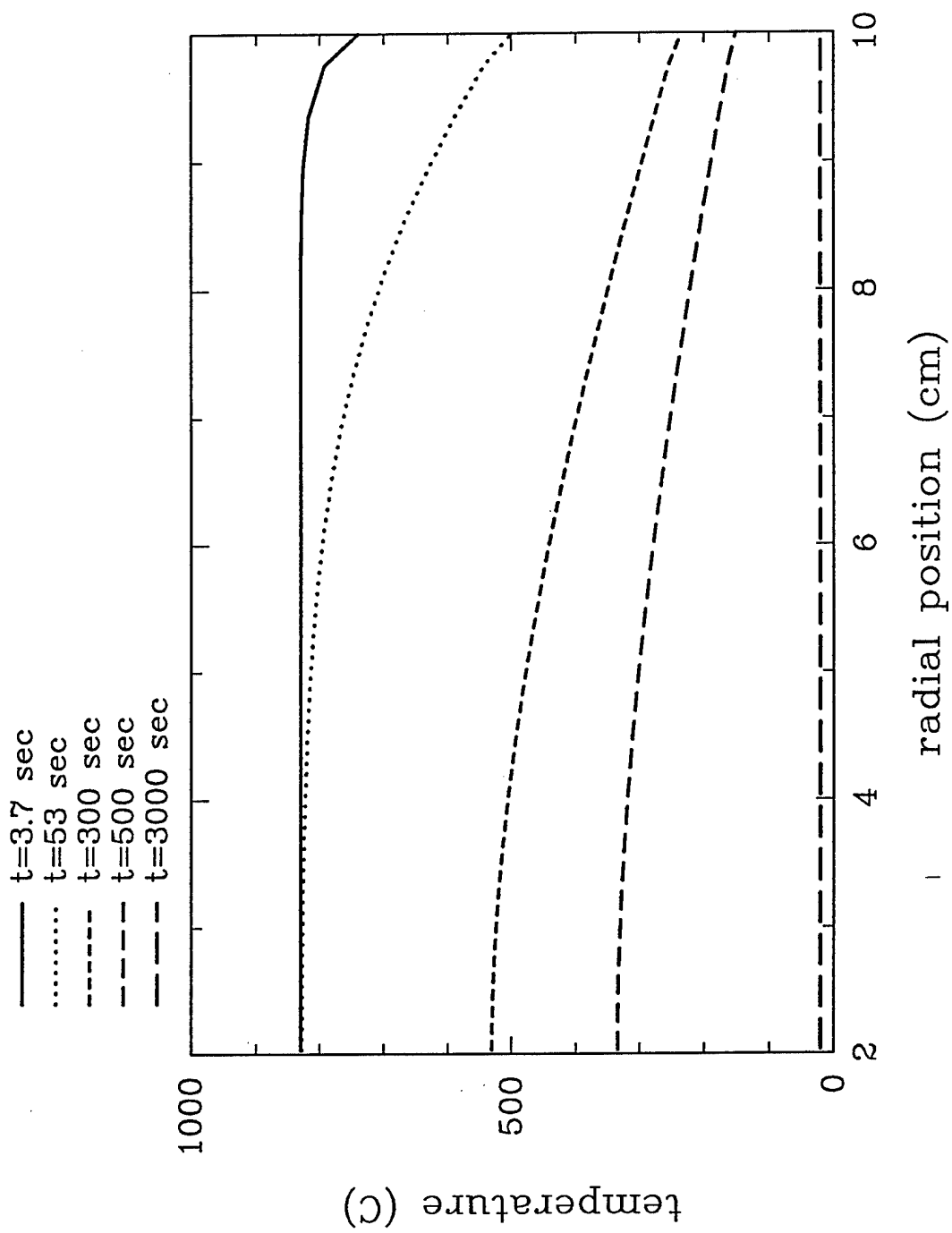


Figure 4. Variation of temperature within cylinder at five times during the quench.

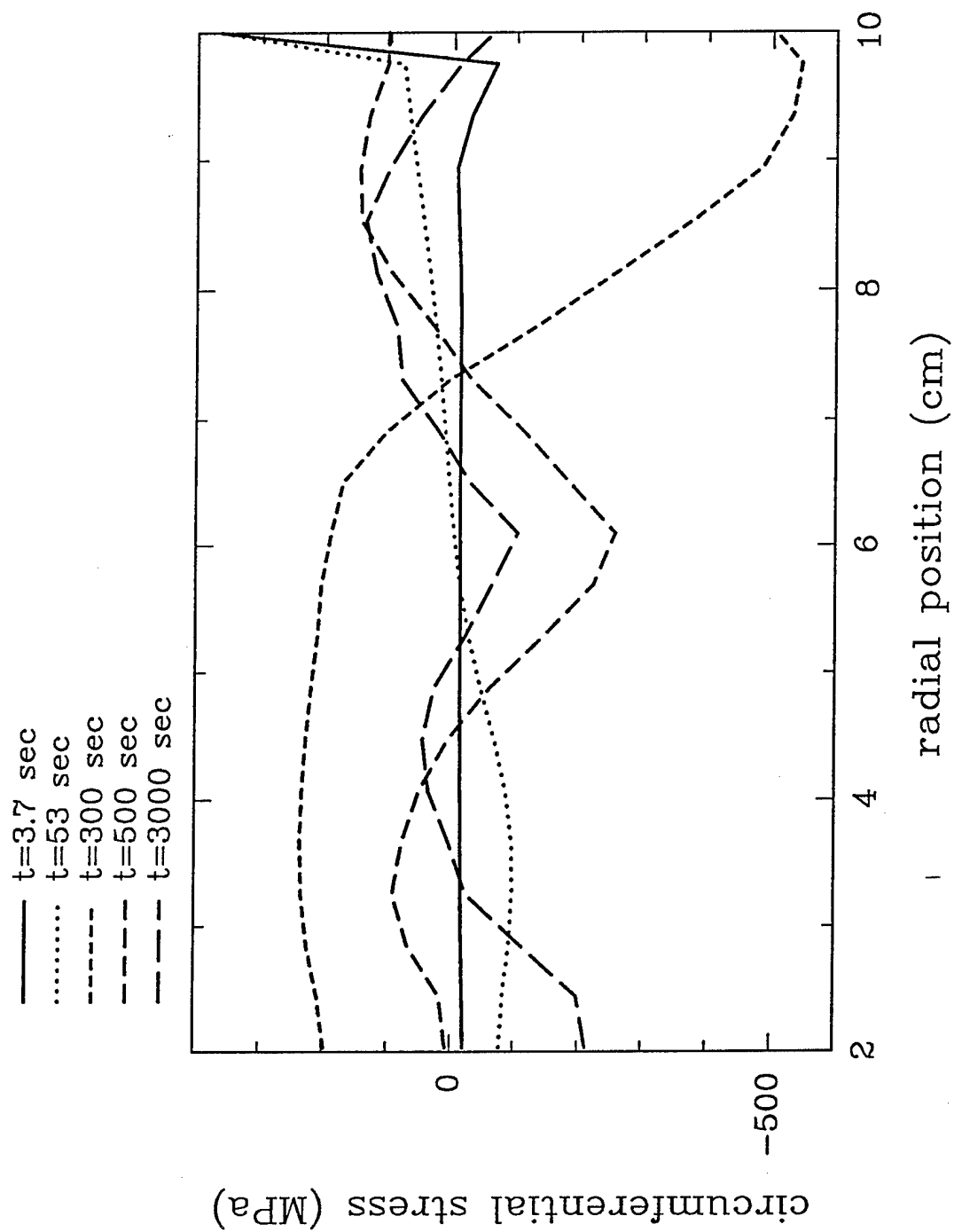


Figure 5. Variation of circumferential stress within cylinder at five times during the quench.

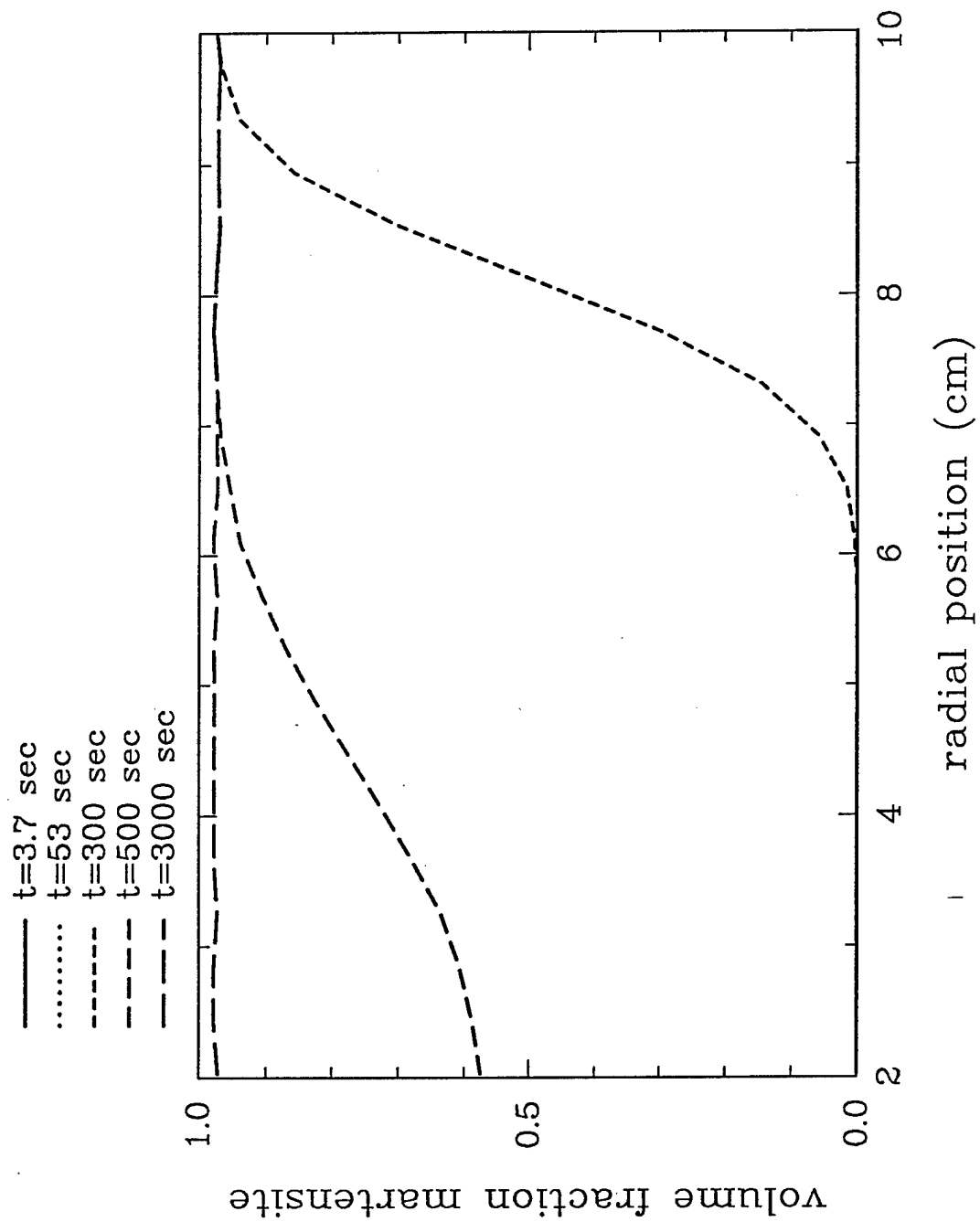


Figure 6. Variation of martensite volume fraction within cylinder at five times during the quench.

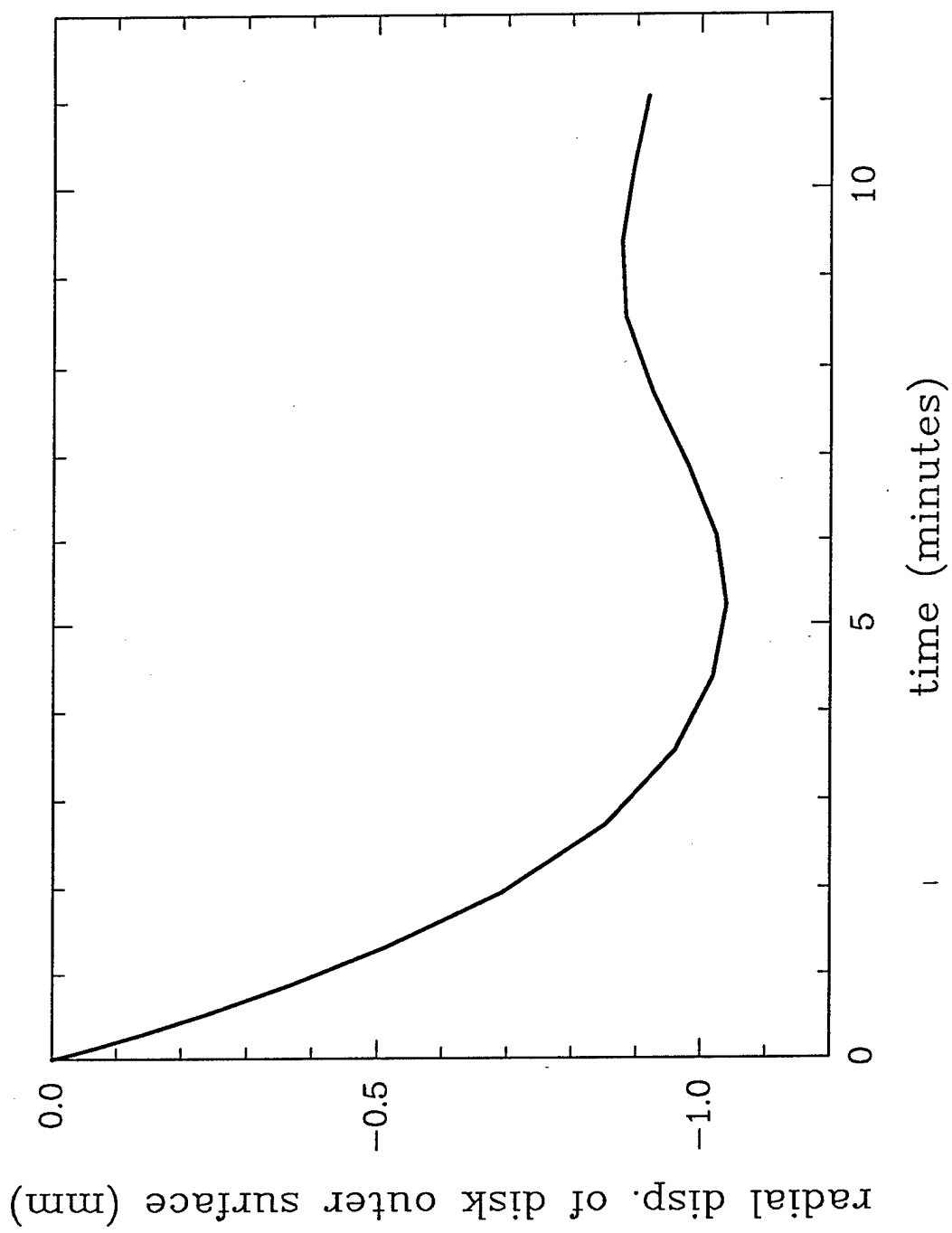


Figure 7. Radial displacement history of outer surface of the cylinder during the simulated quench transient.



## DETERMINATION OF MATERIAL PROPERTIES

The second task of the program focussed on the determination, through either measurement or literature review, the material properties necessary to describe the behavior of 9310 steel during carburization, austenitization and quench, deep-freeze, and tempering. The required material properties are summarized in Table 1. These properties are not generally available for 9310 steel. Where properties for 9310 were unavailable, properties for similar alloys were used. The properties that were thought to be most critical — stress-strain and phase transformation behavior — were measured.

TABLE 1. MATERIAL PROPERTIES REQUIRED FOR THE MODEL

Material Property	Determination Method	Conditions
diffusion coefficient	technical literature and calculation	temperature, carbon content
elastic-plastic stress-strain behavior	uniaxial tension tests and technical literature	- carbon levels - carburization temperature - quench range temperatures - tempering temperature
phase transformation temperatures	dilatometry/CCT diagram development	carbon levels
latent heat of transformation	technical literature and laboratory tests	carbon levels
specific heat	technical literature and calculation	temperature range
thermal and phase-induced volume change	dilatometer measurement	- carbon levels - cooling rates

Continuous Cooling Transformation (CCT) diagram development and dilatometry measurements were performed at Climax Research Services in Farmington Hills, MI. Stress-strain properties, as functions of temperature and carbon content, were measured at Manlabs in Cambridge, MA.

Dilatometry and stress-strain measurements were made at four carbon levels: 0.1 weight percent — the baseline level for 9310 steel, and elevated levels of 0.34, 0.58 and 0.83 weight percent which are needed to simulate the carbon levels at various depths in the carburized case. All specimens were normalized at the heat treatment facilities of Klock in Manchester, CT. The three sets of elevated carbon specimens were then through-carburized at Klock. Based upon calculations made at Arthur D. Little using the carbon diffusion model, a 30-hour carburization cycle was used. Since through-carburization is not often performed, there were concerns as to whether the specified carburization time would be sufficient. Therefore, after

carburization, the specimens were sent to Dirats Laboratories in Westfield, MA in order to verify the quality of the carburization. The average carbon content of each of the specimens and the variation of hardness throughout the cross-section of each specimen (carbon level can be inferred from hardness) were measured at Dirats. The results of their analyses are summarized in Figure 8 and indicate that the through-carburization procedure was successful. The reports provided by Dirats are attached as Appendix A.

The remainder of the properties specified in Table 1 were obtained through review of technical literature. The discussion that follows summarizes the results of our findings for each set of properties listed in the table and describes in detail how these results were obtained.

## CARBON DIFFUSION PROPERTIES

### Diffusivity

An initial estimate of the diffusivity of carbon into steel was determined through technical literature review. The diffusivity coefficient  $D_c$  in equation (1) is a function of both temperature and carbon content. The following empirical relationship proposed by Tibbetts [4] summarizes existing experimental data for diffusion of carbon in iron:

$$D_c = 0.47 \exp [-1.6C_c - (37000-6600C_c)/(RT)] , \quad (28)$$

where  $D_c$  is in  $\text{cm}^2/\text{s}$  and  $R$  is the Universal Gas Constant. This equation indicates that  $D$  is a strong function of both  $T$  and  $C_c$ , as shown in Figure 9. This relationship was used to determine  $D_c$  for initial simulations. However, as experimental data became available later in the program, data for  $D_c$  were modified to provide accurate fits to measured carbon profiles. In particular, the strong increase in  $D_c$  with  $C_c$  did not correlate well with the shape of the carbon profiles. Instead, constant values of  $D_c$  seemed to provide the best fits. In particular, a value of  $D_c = 2.8 \times 10^{-7} \text{ cm}^2/\text{sec}$  yielded the best agreement with data from the flat disk experiments, while a value of  $D_c = 3.8 \times 10^{-7} \text{ cm}^2/\text{sec}$  provided the best fit to the rim/web gear blank data.

### Surface carbon reaction rate

The surface carbon reaction rate constant  $\beta$  in equation (3) is a function of the degree of atmosphere circulation in the carburization furnace. Studies performed by Stickels [2] indicate that

$$\beta = 0.00002 \text{ s}^{-1}$$

yields results that are in good agreement with experiments, but that this constant may increase or decrease by a factor of two depending upon the particular furnace.

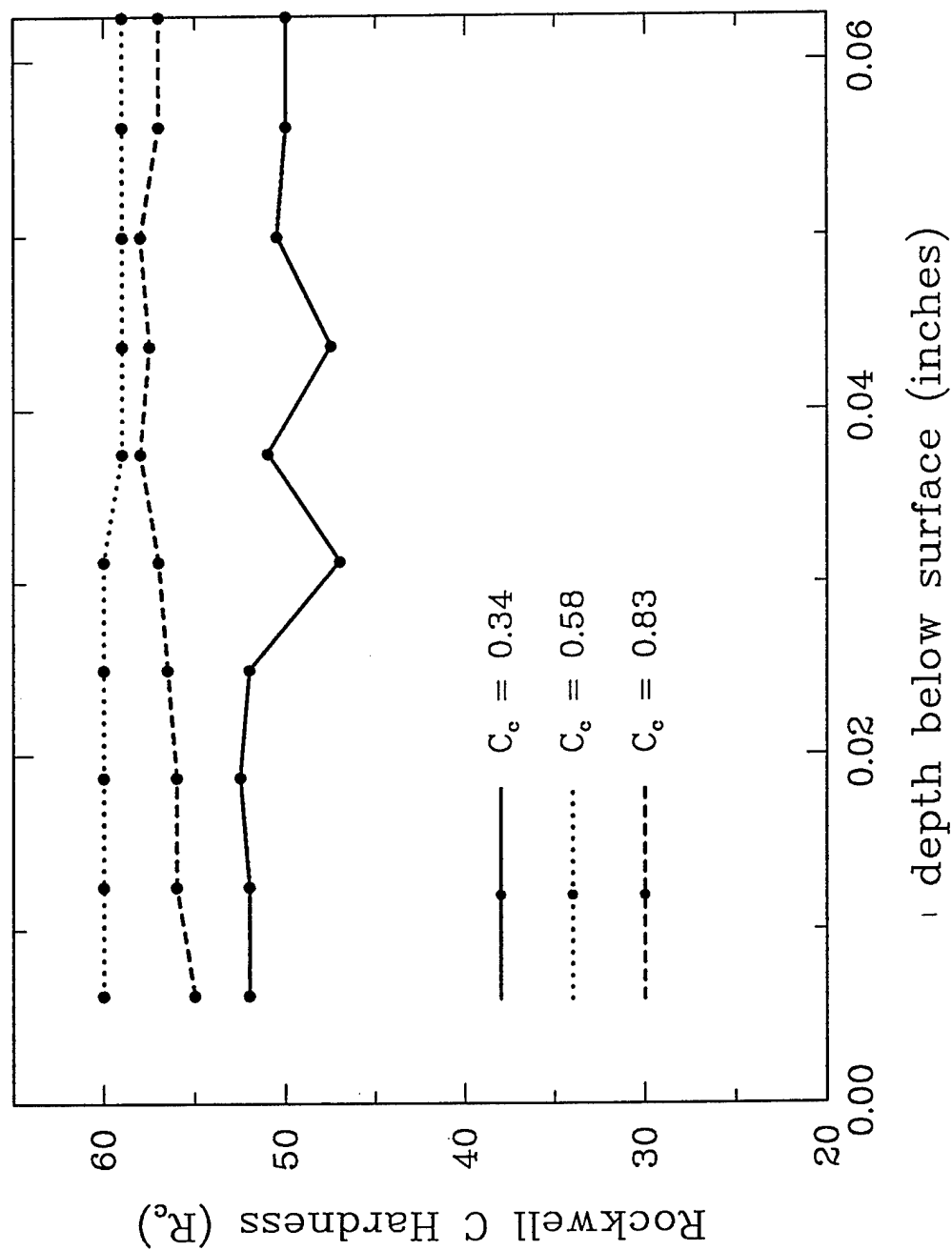


Figure 8. Variation of Rockwell C hardness between the surface and the core for each of three carburization levels. Measured carbon contents are indicated.

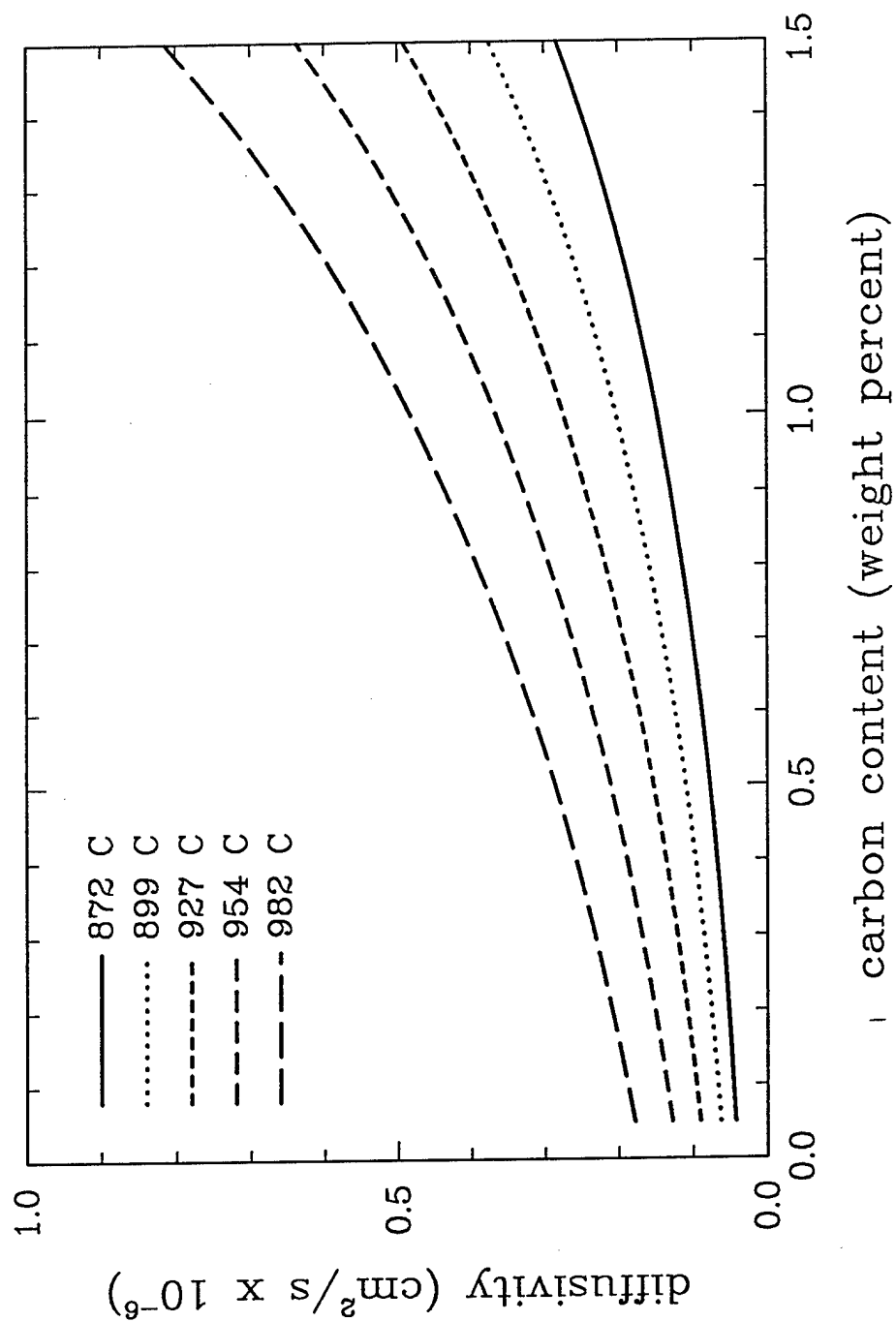


Figure 9. Variation of diffusivity parameter,  $D_e$ , with carburization temperature and carbon content, as defined by equation (28).

## PHASE TRANSFORMATION PROPERTIES

Continuous cooling transformation data were generated by means of dilatometry and metallographical observation by Climax. These curves show the evolution of the phase structure of the steel as a function of time and temperature when a 0.5 inch long by 0.1 inch diameter cylindrical specimen is cooled from its austenitization temperature to room temperature at various constant rates of temperature change.

Climax first developed a complete set of ten CCT curves for 9310 steel cooled at rates ranging from 0.05 C/sec to 80 C/sec. Phase transformation data are determined through dilatometry — the change in length of the specimen is recorded as a function of temperature and then related to the corresponding change in volume — and through metallographical evaluation of the specimen following the test. The coefficient of thermal expansion for each phase is also determined in this test.

Figure 10 shows the CCT curve for 9310 steel developed by Climax. Figure 11 shows the raw dilatometry data for the fastest cooling rate curve ( $dT/dt=80$  C/s). Upon cooling from the austenite start temperature, the specimen undergoes thermal contraction. When martensite begins to form, the transformation volume change causes the specimen to increase in length. Finally, when the transformation is over, the specimen continues to contract, at a rate that is characteristic of martensite. The martensite start ( $M_s$ ) and the martensite finish ( $M_f$ ) temperatures indicated in Figure 10 are determined directly as the inflection points in the dilatometer curve of Figure 11.

A simple FORTRAN program was written to further process the dilatometry data in order to determine the coefficients of thermal expansion of each phase, the total volume change associated with the transformation, and the rate of evolution of the martensite phase with temperature. The results of this processing are summarized in Figure 12.

Since helicopter gears are quenched rapidly, only martensitic transformations are generally encountered. In order to reduce the costs associated with CCT diagram development, Climax performed a smaller number of dilatometry experiments (4 curves instead of 10) for the remainder of the specimens, using only the faster cooling rates — 10 C/sec to 80 C/sec. They repeated the test for the 9310 material and performed partial tests for each of the elevated carbon levels. The results of these tests are summarized in Figure 13 and 14.

The variation of  $M_s$  and  $M_f$  with carbon content is summarized in Figure 15. It is well known that an increase in carbon content causes the  $M_s$  and  $M_f$  temperatures to decrease. The data presented in Figure 15 is in excellent agreement with similar data presented, for example, in [5]. Note that the  $M_f$  temperature for the two highest carbon levels are below room temperature. As will be discussed later, this presents a problem with regard to the determination of transformation and stress-strain behavior for these carbon levels at the low temperatures associated with deep-freeze process step.

Complete reports provided by Climax are attached as Appendix B.

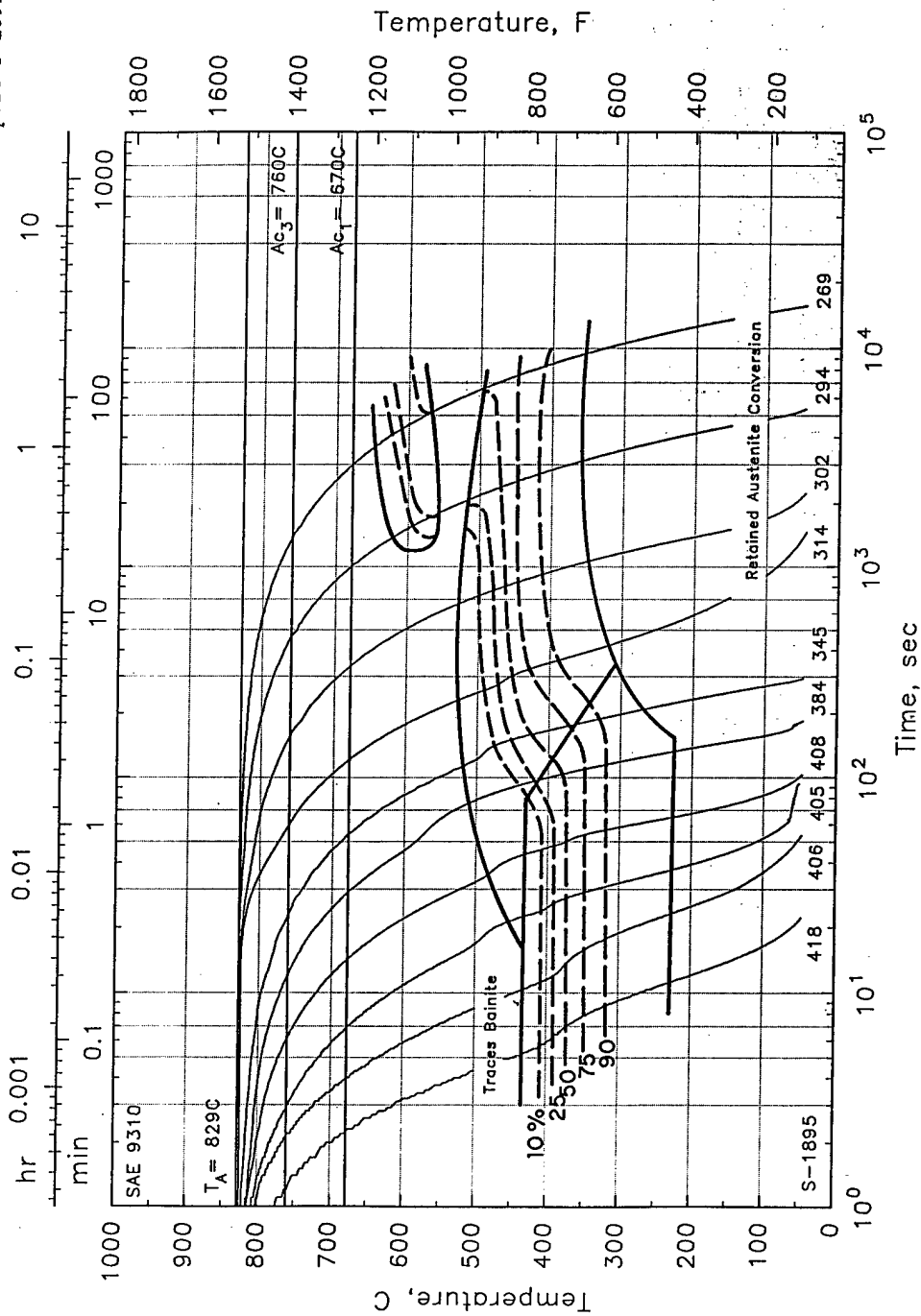


Figure 10. CCT diagram for SAE 9310, austenitized 20 minutes at 830 C.

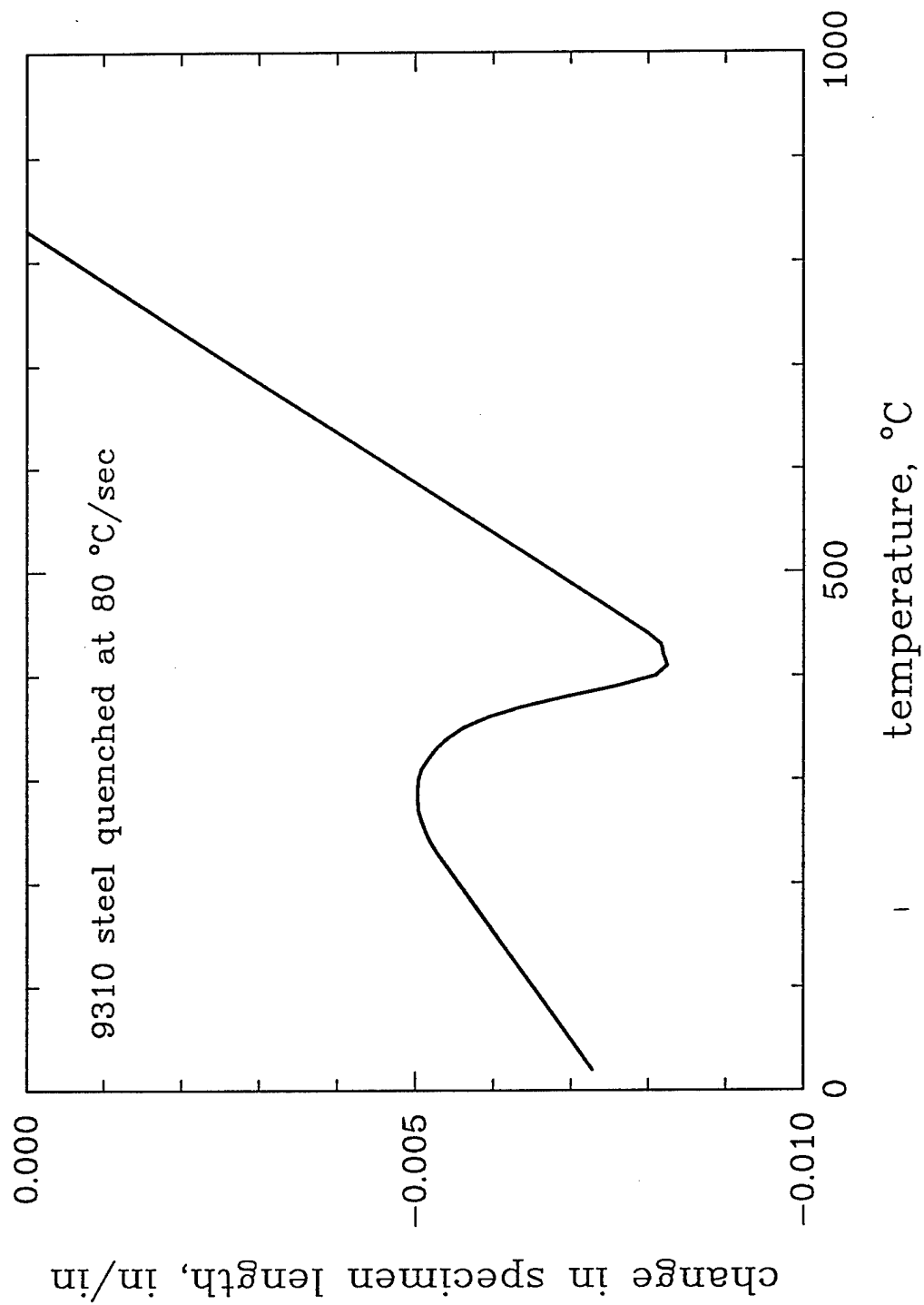


Figure 11. Change in length of dilatometer specimen with temperature for uncarburized 9310 steel austenitized and cooled at 80 C/sec

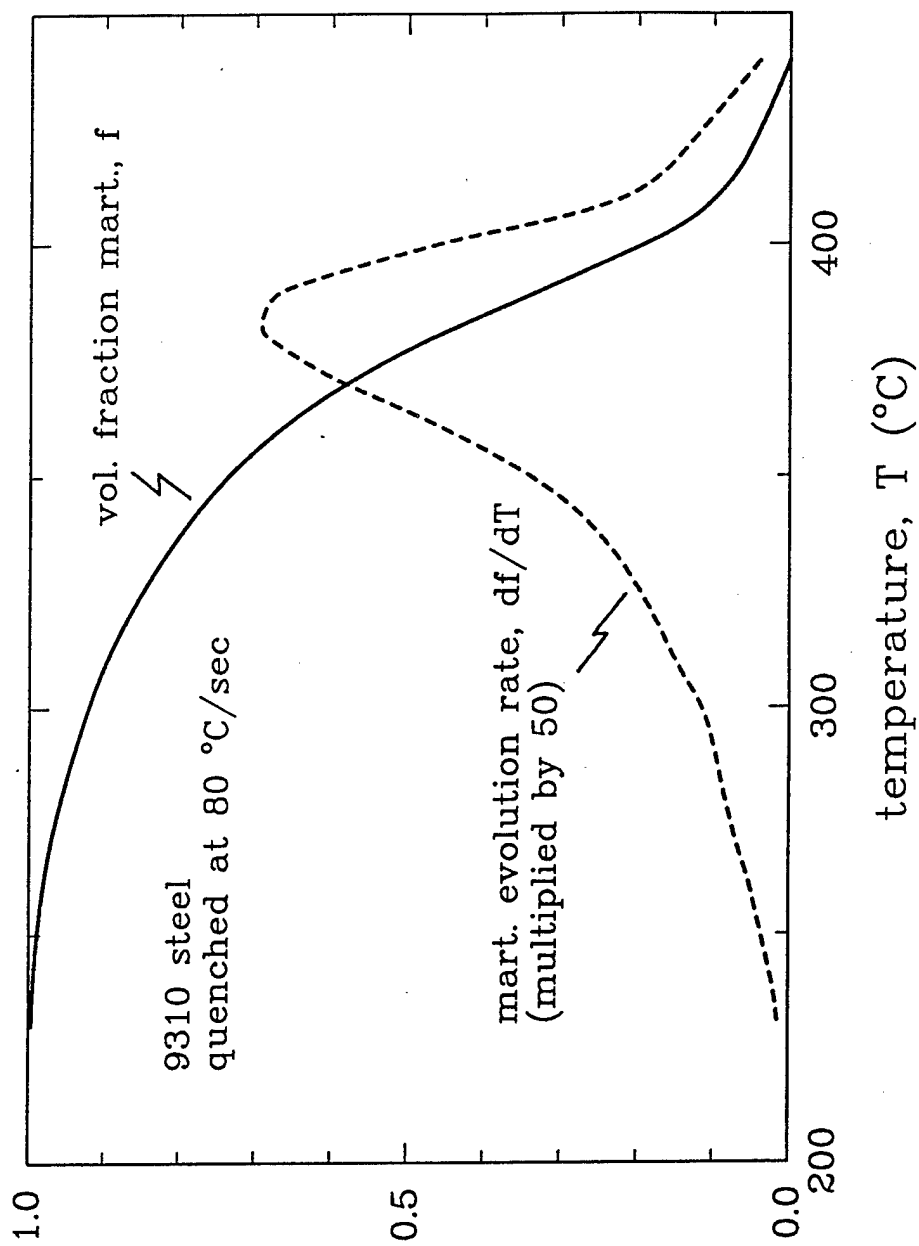


Figure 12. Calculated variation of martensite volume fraction  $f$  and martensite evolution rate  $df/dT$  for the base 9310 alloy.



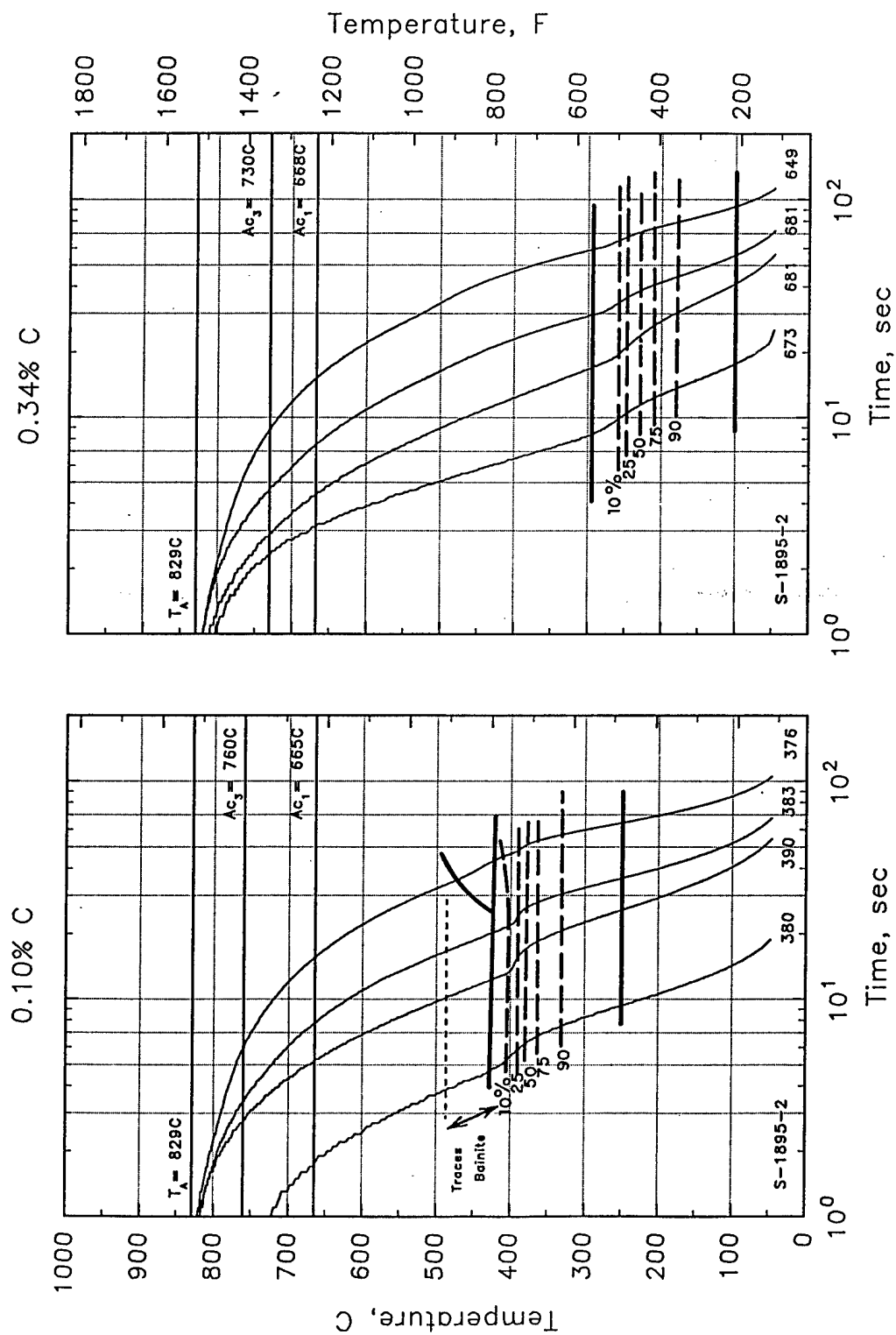


Figure 13. CCT diagram for 9310 at two different carbon contents. Left: blank carburized base alloy at 0.1 C ( $C_c=0.001$ ). Right: base alloy through-carburized to 0.34% C.

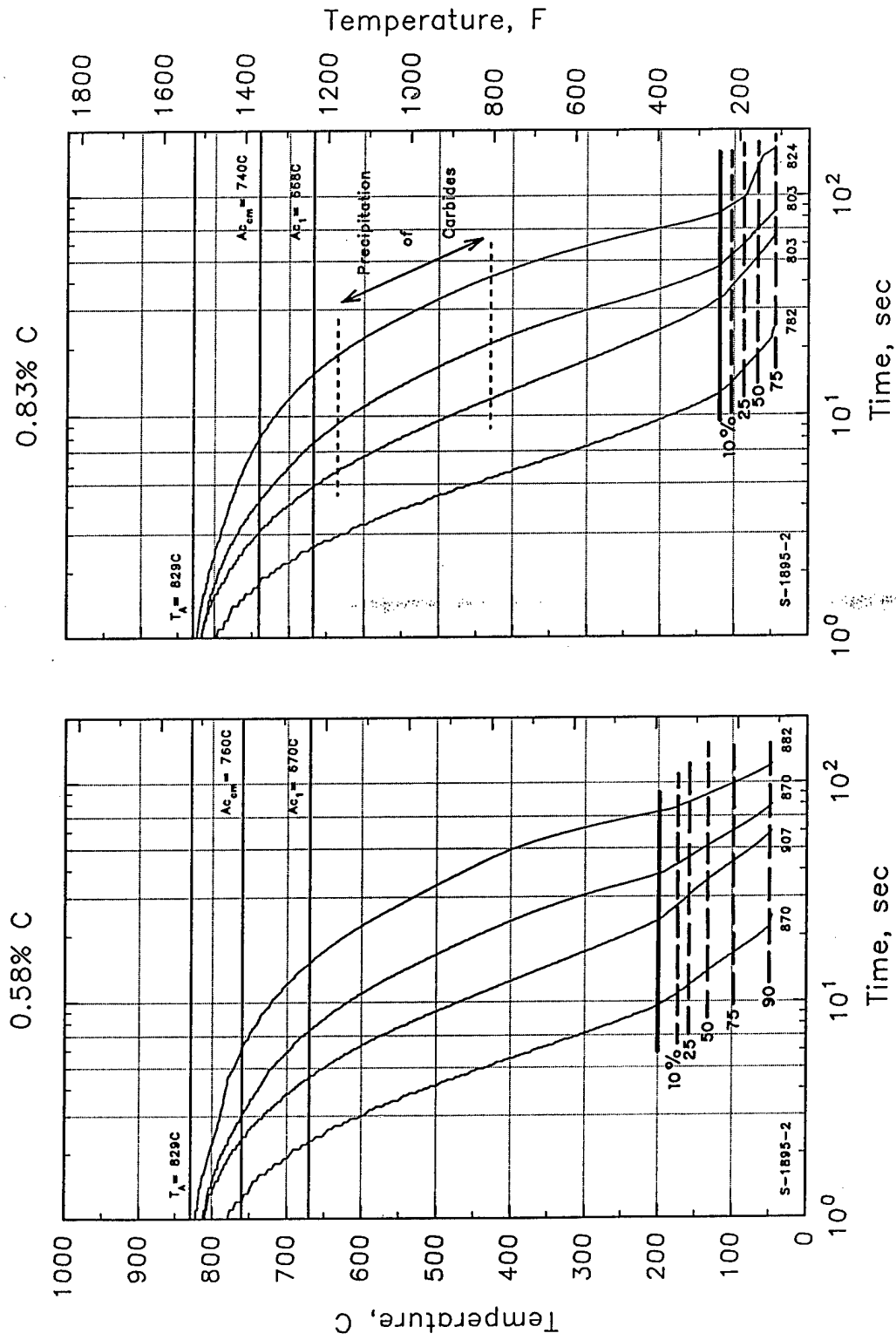


Figure 14. CCT diagram for 9310 at two different carbon contents. Left: base alloy through-carburized to 0.58 C ( $C_c=0.0058$ ). Right: base alloy through-carburized to 0.83% C.

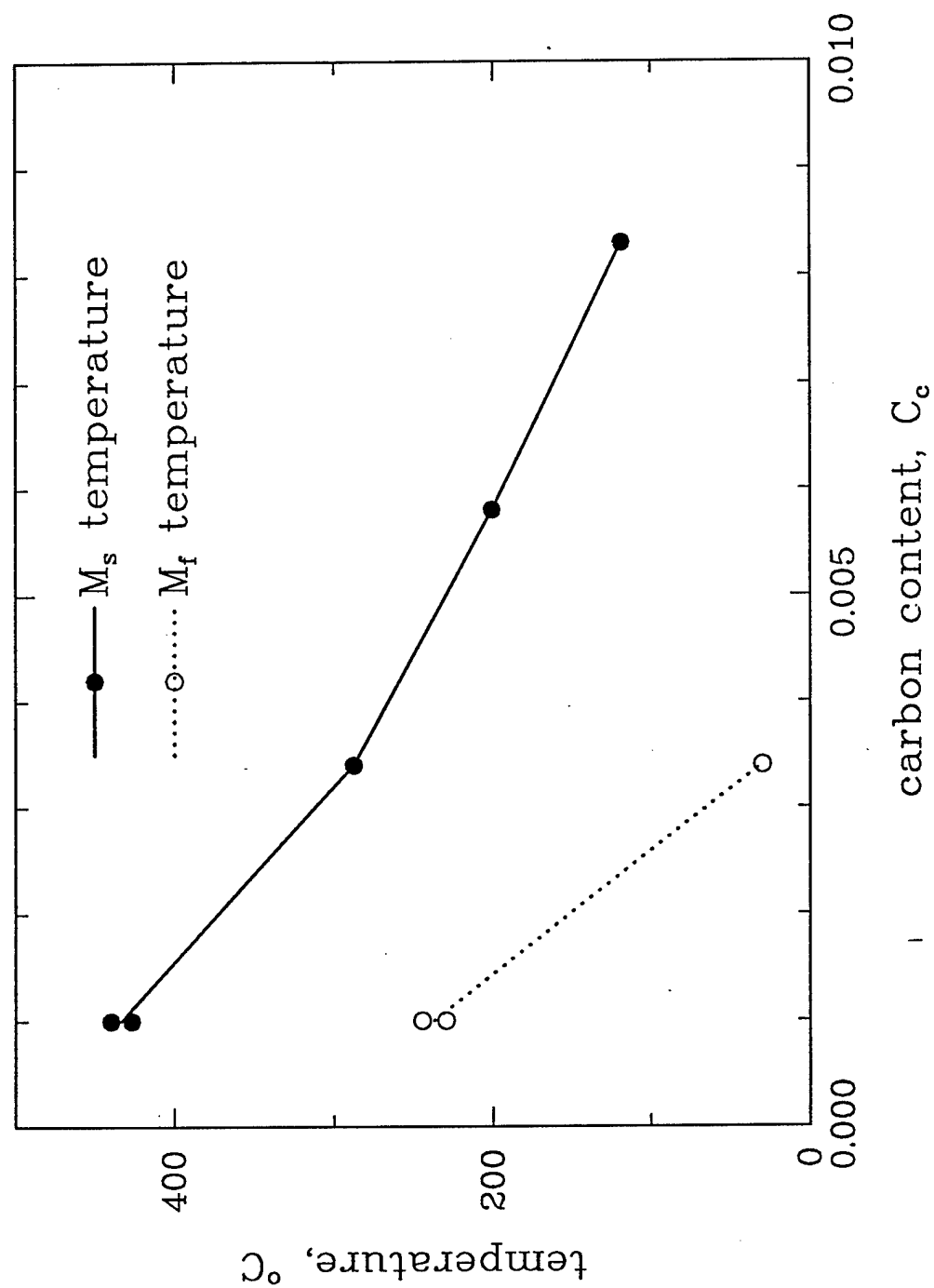


Figure 15. Variation of  $M_s$  and  $M_d$  with carbon content.

## SPECIFIC HEAT AND HEAT OF TRANSFORMATION

The variation of specific heat with temperature, including the heat required to produce the transformation, was determined through literature review and calculations based upon martensite evolution data determined in the CCT tests.

The variation of specific heat with temperature was evaluated from several literature sources [e.g., 6, 7]. Although none of these data were measured for 9310 steel, there appears to be little variation of specific heat with alloy content. Based upon these data, the specific heat was determined to vary from 600 J/kg C at 0 C to 660 J/kg C at 1000 C.

The latent heat of transformation for the transformation from austenite to martensite was determined to be about 60,000 J/kg, based upon data given in [8]. Using this value, and the data for rate of transformation versus temperature shown in Figure 12, we were able to determine the specific heat of transformation. The total specific heat, which is equal to the specific heat plus the heat of transformation, is plotted in Figure 16.

## THERMAL CONDUCTIVITY

The variation of the coefficient of thermal conductivity,  $k$  in equation 25, with temperature was determined through literature review. Again, data for 9310 steel could not be found in the literature. Data for a steel with an very similar alloy content — 31-NiCrMoV-12-3 was instead used. The variation of thermal conductivity with temperature for this steel was calculated based upon thermal diffusivity data for 32-NiCrMoV-12-3 given in [9] and are plotted in Figure 17.

The coefficient of thermal conductivity will likely vary with carbon concentration due to the change in martensite start and finish temperatures. Carbon content dependency can be approximated by varying the inflection points in the curve of Figure 17 to correspond to the calculated  $M_s$  and  $M_f$  temperatures. Since, however, increased carbon levels are found in such a restricted region near the surface of the gear, the variation of thermal conductivity with carbon content should not affect model predictions, and therefore was not accounted for in the model.

## STRESS-STRAIN BEHAVIOR

Uniaxial stress-strain curves provide the data needed to formulate the constitutive relations discussed earlier. These curves must be determined for the temperatures corresponding to the various heat-treating steps, including: carburization, austenitizing, quenching and tempering. Data must also be obtained for a range of carburization levels that represents the gradient from the surface to the core of the gear.

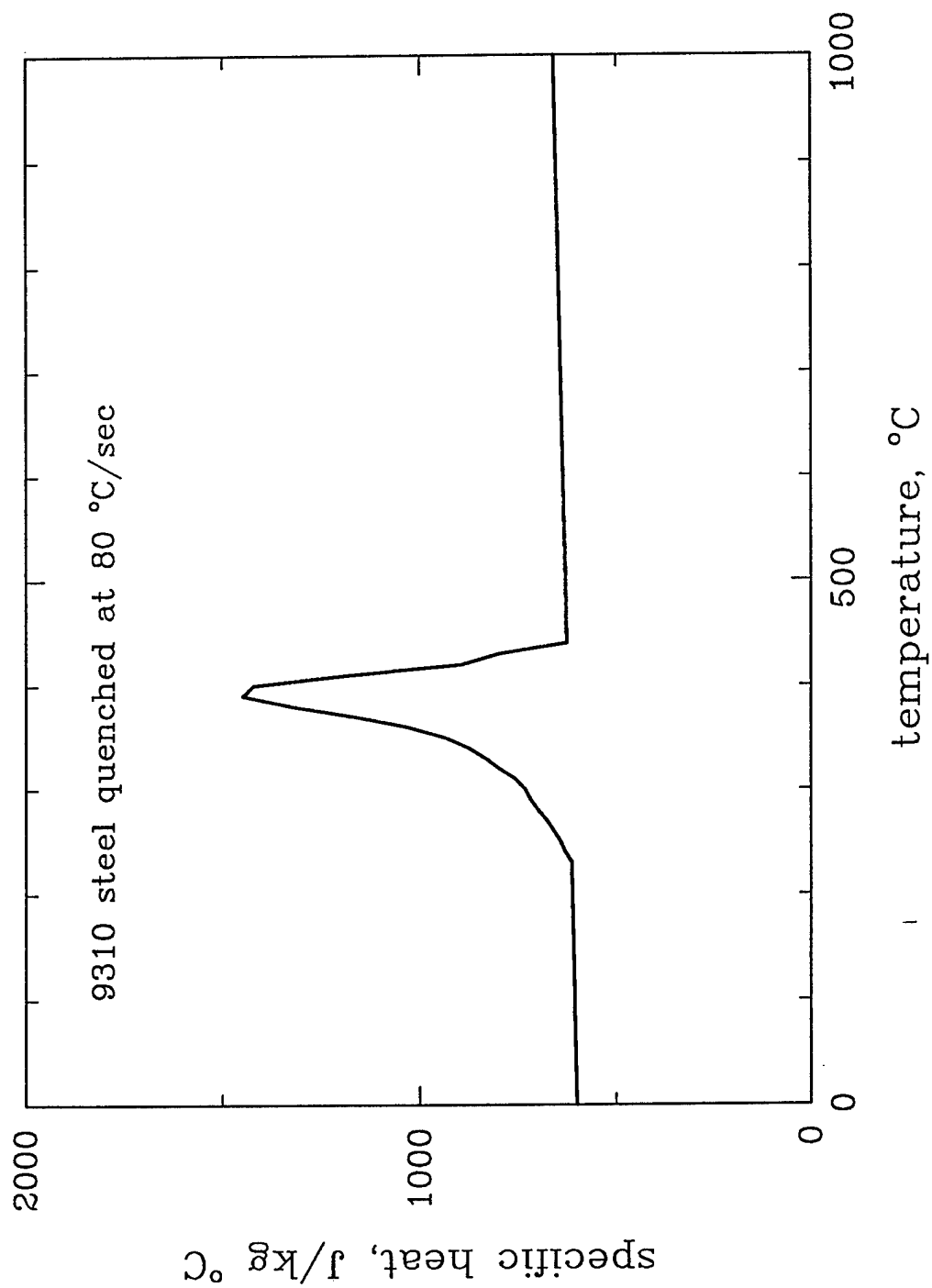


Figure 16. Variation of specific heat, including heat of transformation, with temperature.

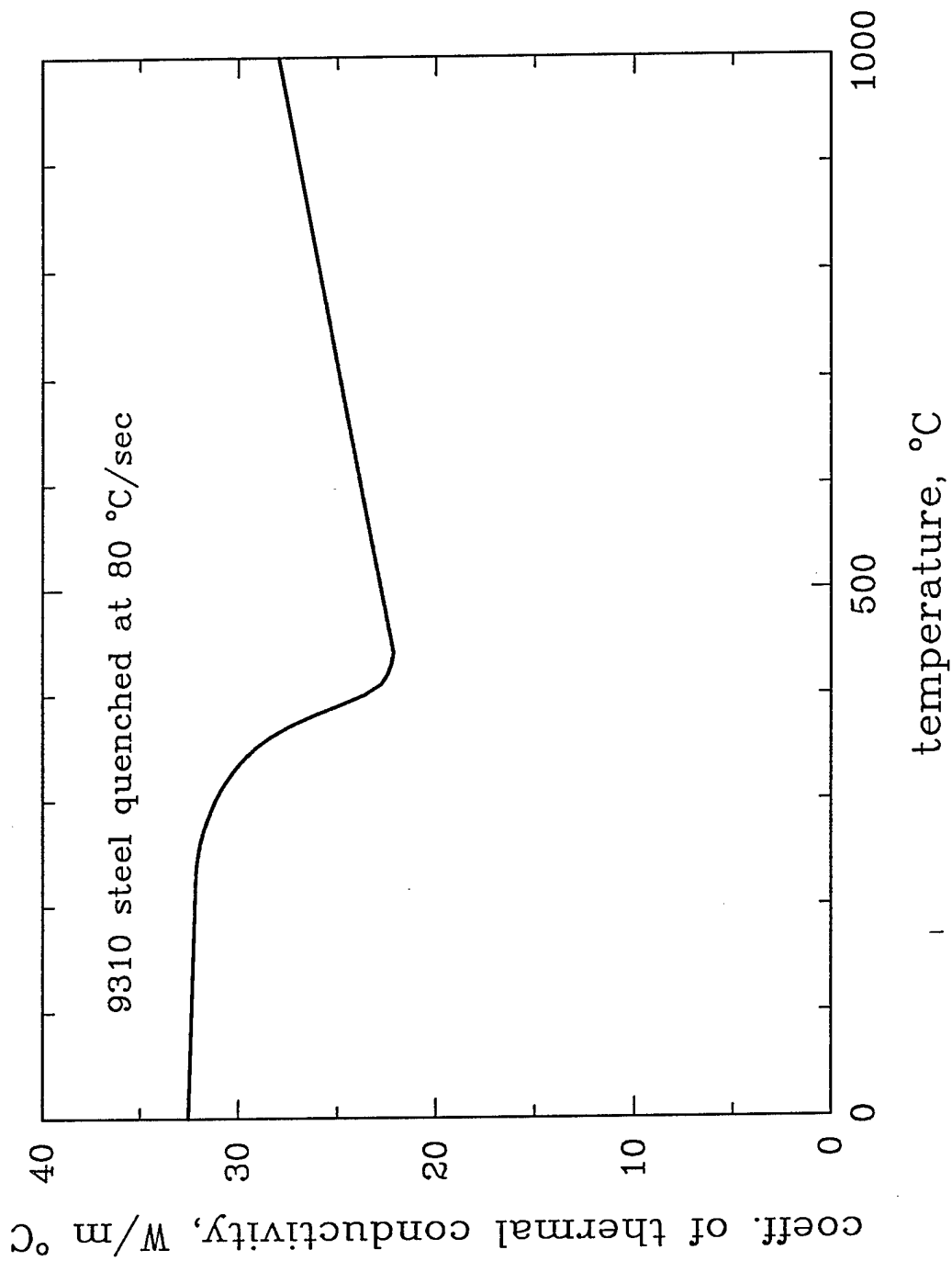


Figure 17. Calculated variation of the coefficient of thermal expansion with temperature based upon thermal diffusivity data given in Solter [9].

## Experiments

Uniaxial tensile tests were conducted with cylindrical specimens, threaded at the ends with a 0.125 inch (3.2 mm) diameter, 2 inch (50.8 mm) long gage section. Four lots of specimens were tested, three of these having been through-carburized to the levels shown in Table 2; this table also lists the martensite start and finish temperatures for later reference.

TABLE 2. TENSILE SPECIMEN CARBURIZATION LEVELS

Lot	Carbon Level (wt %)	$M_s$ (C)	$M_f$ (C)
U	0.10 (uncarburized)	430	230
X	0.35	280	20
Y	0.60	200	<20
Z	0.85	130	<20

Test temperatures were chosen to provide approximately one test each at the carburization, austenitizing and tempering temperatures, the latter being applied after the specimen had been quenched to room temperature. Approximately three test temperatures were selected to correspond to each of the three quenching temperature ranges: austenitizing-to-martensite start; martensite start-to-martensite finish, and; martensite finish-to-room temperature. However, fewer test temperatures could be chosen for the latter range at the higher carburization levels because the martensite finish temperature is below room temperature.

A thermocouple, used for monitoring and controlling temperature, was spot welded to the surface of each specimen at the midpoint of the gage section. An induction coil was used to heat the specimens and quenching was achieved with an air blast directed at the gage section from two points. Specimens were first heated to 830 C (except for the 980 C tests) for 20 minutes, were quenched to the test temperature of interest and then tested. This procedure provided the cooling rates needed to achieve the desired phase transformations, but it proved difficult to achieve steady temperatures below about 100 C after quenching. All tests were conducted in stroke control and an extensometer was used to record the displacement needed to calculate strain. The strain rate for these tests was on the order of  $1 \times 10^{-3} \text{ sec}^{-1}$ .

## Results

The results of the stress-strain curve tests are presented here as plots of the 0.2% offset yield strength and the stress at a plastic strain of 2% both as a function of temperature; Figures 18 and 19. These are the data used to form piecewise linear curves for the model constitutive equations.

Figures 18 and 19 show that the curves coincide at temperatures above approximately 450 C; this is the temperature range in which the microstructure is austenitic for each of the carburization levels. Both the yield strength and stress at 2% plastic strain increase rapidly with decreasing temperature as the temperature drops below the martensite start temperature for the particular carbon level. We also note that the strengths achieve greater values at the

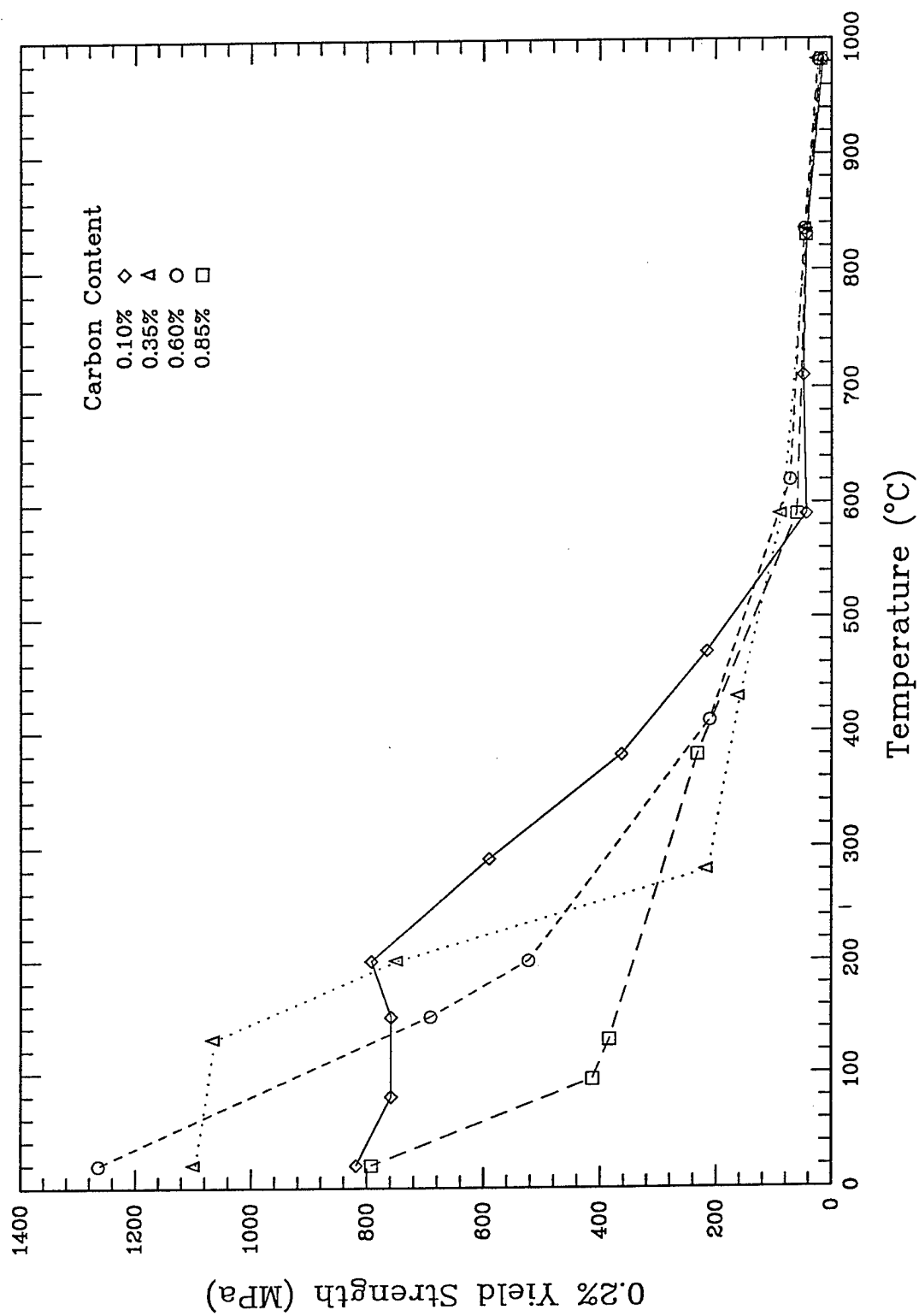


Figure 18. Measured variation of 0.2% offset yield strength with temperature and carbon content.



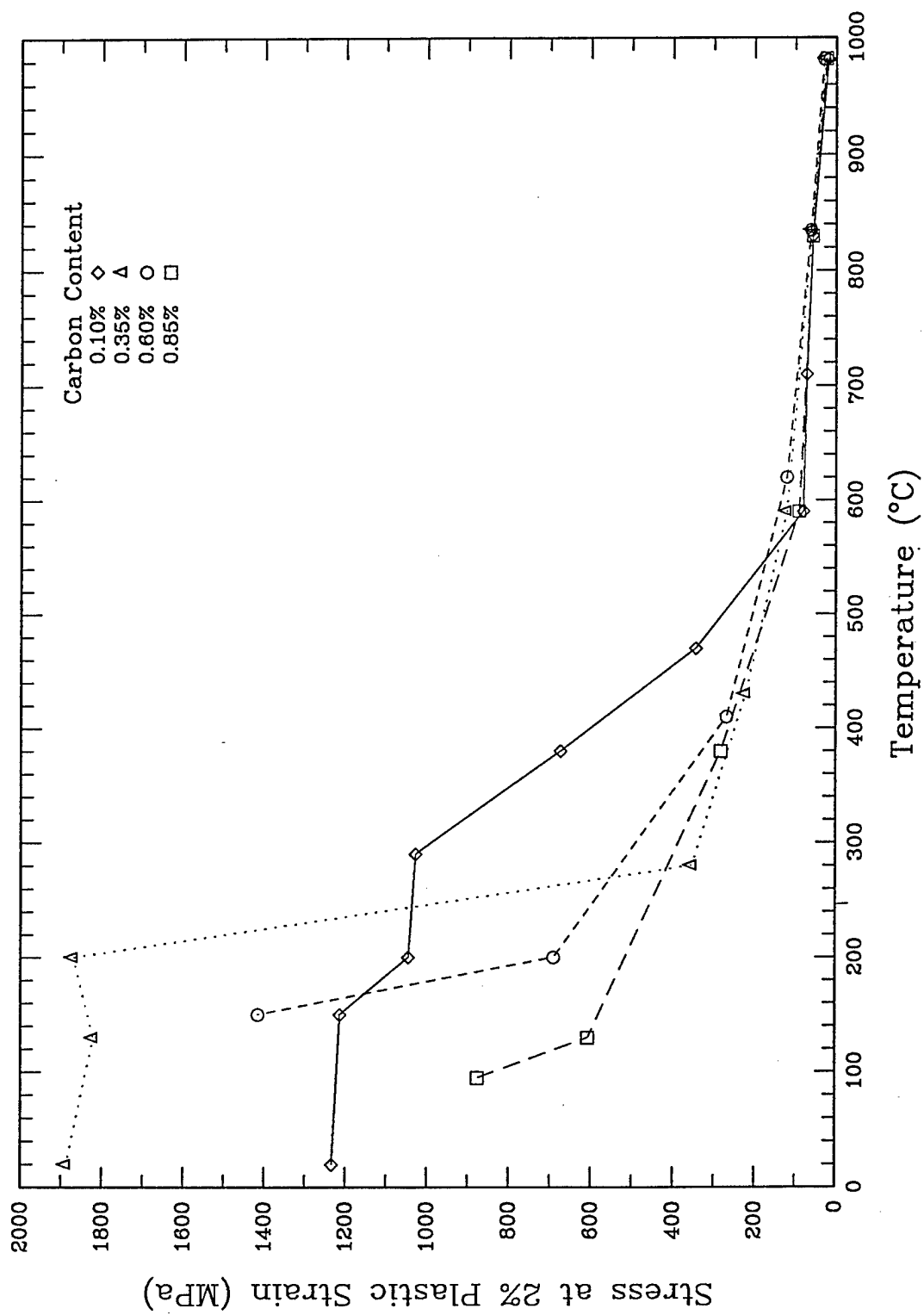


Figure 19. Measured variation of stress at 2% strain with temperature and carbon content.

lower temperatures for the higher carbon levels. Such a phenomenon is not observed for the highest carbon level because the martensite start temperature is relatively close to room temperature. A few of the 2% strain values at the low temperatures are missing because premature fracture occurred.

Table 3 lists the strength values for the tests conducted at 150 C after the specimens were quenched to room temperature; this condition represents the tempering temperature.

TABLE 3. TENSILE DATA AT THE TEMPERING TEMPERATURE

Lot	Carbon Level (wt%)	0.2% Yield Strength (MPa)	Strength at $\epsilon_p=2\%$ (MPa)
U	0.10	759	1214
X	0.35	1197	1720
Y	0.60	1753	*
Z	0.85	*	*

\* Premature fracture

### ELASTIC CONSTANTS

Data from tensile tests do not provide an accurate measure of elastic constants. Properties for the elastic modulus of the austenite and martensite phases were instead taken from the literature. Data presented in [10] was curve-fit using the following form:

$$E = E_0 - c_E T^n, \quad (29)$$

where  $E_0$  is the value of Young's modulus at 0 C. Figure 20 shows the variation of  $E$  for the austenite and martensite phases used in the model. These data were determined using the following parameter values:  $E_0$  (martensite) = 215,000 MPa;  $E_0$  (austenite) = 200,000. MPa;  $c_E = -2.187$  (both phases);  $n=1.6$  (both phases).

### INCORPORATING MATERIAL PROPERTIES INTO THE MODEL

The extensive set of material properties for 9310 during carburization, austenitization and quench, deep-freeze and temper described above must be incorporated into the finite element model.

In most cases the data can be incorporated directly into the model as constants. In other cases, where critical data are functions of model variables, particularly temperature and carbon content, data were incorporated by defining functional fits to measured values, using interpolation and extrapolation where required.

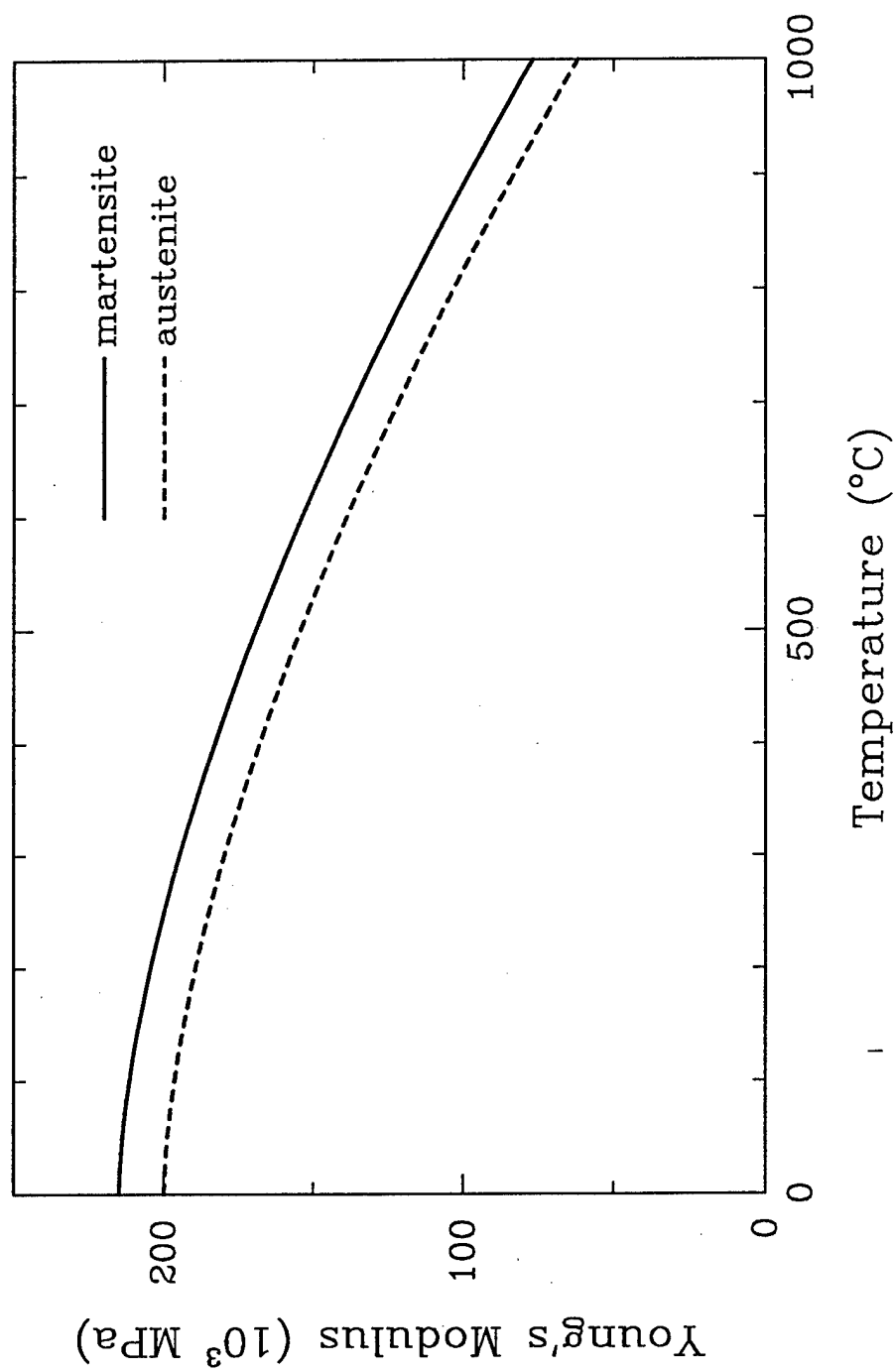


Figure 20. Variation of Young's Modulus of austenite and martensite phases given by equation (32).

### Phase transformation data

A two-sided normal distribution function was used to fit the martensitic transformation data (Figure 12) using the transformation rate function  $P(\Theta)$  given in equation 10:

$$\begin{aligned} P(\Theta) &= k_{tr}/(\sqrt{2\pi})\sigma_1 \cdot \exp[-1/2(\Theta-\Theta_m)^2] & \text{for } \Theta < \Theta_m ; \\ &= k_{tr}/(\sqrt{2\pi})\sigma_2 \cdot \exp[-1/2(\Theta-\Theta_m)^2] & \text{for } \Theta > \Theta_m , \end{aligned} \quad (30)$$

where  $\Theta_m$  is the mean temperature for transformation,  $\sigma_1$  and  $\sigma_2$  are standard deviations about either side of this mean, and  $k_{tr}$  is a constant. The fit to experimental data provided by equation (30) is also shown in Figure 21. While this fit is not ideal, the authors believe that it is better than that provided by the commonly used function  $P(\Theta) = -k_{tr}\exp[-k_{tr}\Theta]$ , which does not capture the shape of the curve for  $df/dT$ , especially near  $M_s$ .

As indicated in Figure 15, the  $M_s$  and  $M_f$  temperatures are strong functions of carbon content. Within the structure of equation (10), this is expressed through the carbon content dependency of the parameters. In the UMAT this dependency is assumed to be linear, i.e.:

$$\Theta = \Theta_0 + k_{\Theta}(C_c - C_{c,0}); \quad (31)$$

$$\sigma_1 = \sigma_{10} + k_1(C_c - C_{c,0}); \quad (32)$$

$$\sigma_2 = \sigma_{20} + k_2(C_c - C_{c,0}). \quad (33)$$

The temperature dependence of  $\sigma_1$  and  $\sigma_2$  is required because the temperature difference between  $M_s$  and  $M_f$  becomes larger as  $C_c$  increases. Values for  $\Theta_0$ ,  $k_{\Theta}$ ,  $\sigma_1^0$ ,  $k_1$ ,  $\sigma_{20}$ , and  $k_2$  used in the UMAT are given in Table 4.

TABLE 4. COEFFICIENTS USED TO FIT TRANSFORMATION PARAMETERS USING FUNCTIONAL FORM GIVEN IN EQUATIONS 31-33

$\Theta_0$ (°C)	$k_{\Theta}$	$\sigma_{10}$ (°C)	$k_1$ (°C)	$\sigma_{20}$ (°C)	$k_2$ (°C)
380.	-54000.	37.0	125.0	22.5	125.0

### Stress-strain data

The stress-strain properties of each phase are strong functions of both temperature and carbon content. Measured tensile data provide an estimate of the temperature-dependence of the yield stress of each phase as a function of temperature for each of four carbon levels. These data were used to define a functional dependence for flow stress,  $Y$ , in terms of temperature  $T$  and carbon content  $C_c$ .

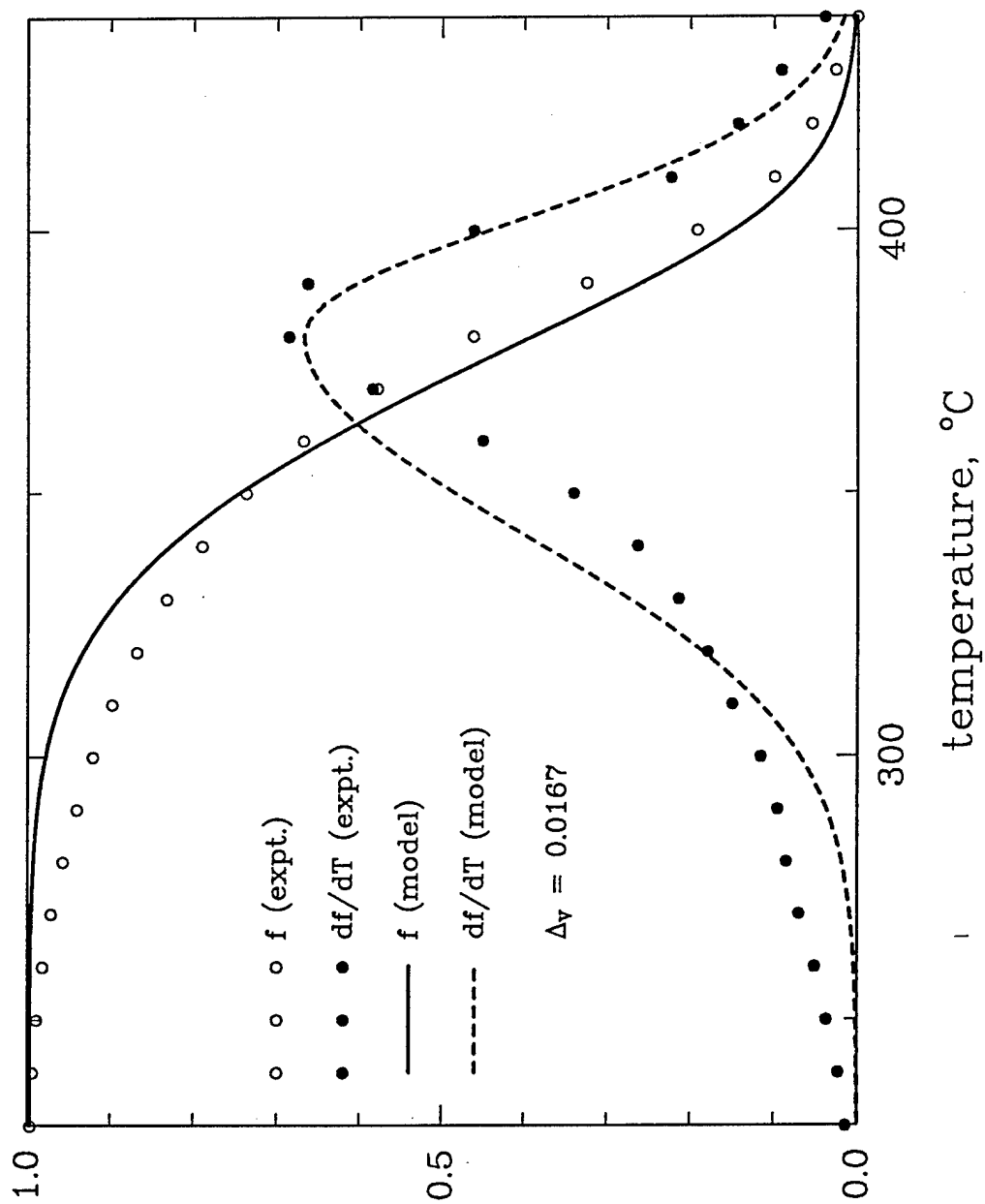


Figure 21. Calculated variation of martensite volume fraction  $f$  and martensite evolution rate  $df/dT$  shown with functional fits based upon a two-sided normal distribution.

Based upon examination of tensile data, a bilinear stress-strain behavior was assumed for each phase. Data from the tensile tests were used to determine a functional form for both the yield stress,  $Y_{01}$ , and the flow stress at 2 percent strain,  $Y_{02}$ , for each of the phases. These data curves were assumed to be linear with respect to both temperature and carbon content, with the general form:

$$Y = Y_0 + c_1 C_c - c_2 T, \quad (34)$$

where  $Y_0$  represents the flow stress at 0 C and the baseline carbon content, 0.1 percent. In order to provide a good fit to the experimental data for austenite, the temperature-dependence of the flow stress curves was assumed to be bi-linear, with  $c_2$  smaller for temperatures greater than 600 C. Data for 9310 incorporated into the UMAT are summarized in Table 5. Note that  $c_1$  for the austenite phase is zero.

TABLE 5. COEFFICIENTS USED IN MODEL TO FIT TENSILE DATA USING FUNCTIONAL FORM GIVEN IN EQUATION 34.

phase	$Y_{01}$ (MPa)	$c_{11}$ (MPa)	$c_{21}$ (MPa/°C)	$Y_{02}$ (MPa)	$c_{12}$ (MPa)	$c_{22}$ (MPa/°C)
martensite	705.5	112000.	0.24	880.0	280000.	0.24
austenite (below 600 C)	492.0	0.	0.72	772.0	0.	1.17
austenite (above 600 C)	116.1	0.	0.09	130.0	0.	0.10

As noted in equation (17), values for flow stress at temperatures between  $M_s$  and  $M_f$  were determined using a rule of mixtures. The experimental data are plotted together with the functional fit to the data for the four measured carbon levels. A comparison of the experimental data at temperatures where mixed phase fractions exist (which were not used to determine the curve-fitting parameters) with the curve-fit data provides some verification of the goodness-of-fit for these data. A comparison of experimental data with the curve-fits, shown in Figure 22, demonstrates that these curve-fits are quite reasonable, especially in light of the difficulty in obtaining experimental data when mixed phase fractions are present.

It should be noted that tensile data were not obtained for low temperatures following carburization. Instead, data for martensite at low temperatures was used. While this incompleteness in data should be corrected in future work, it is most likely not a source of significant error in the calculations presented in this report, because at the lower temperatures where the transformation product is present, it is unlikely that significant plastic flow is occurring in this phase.

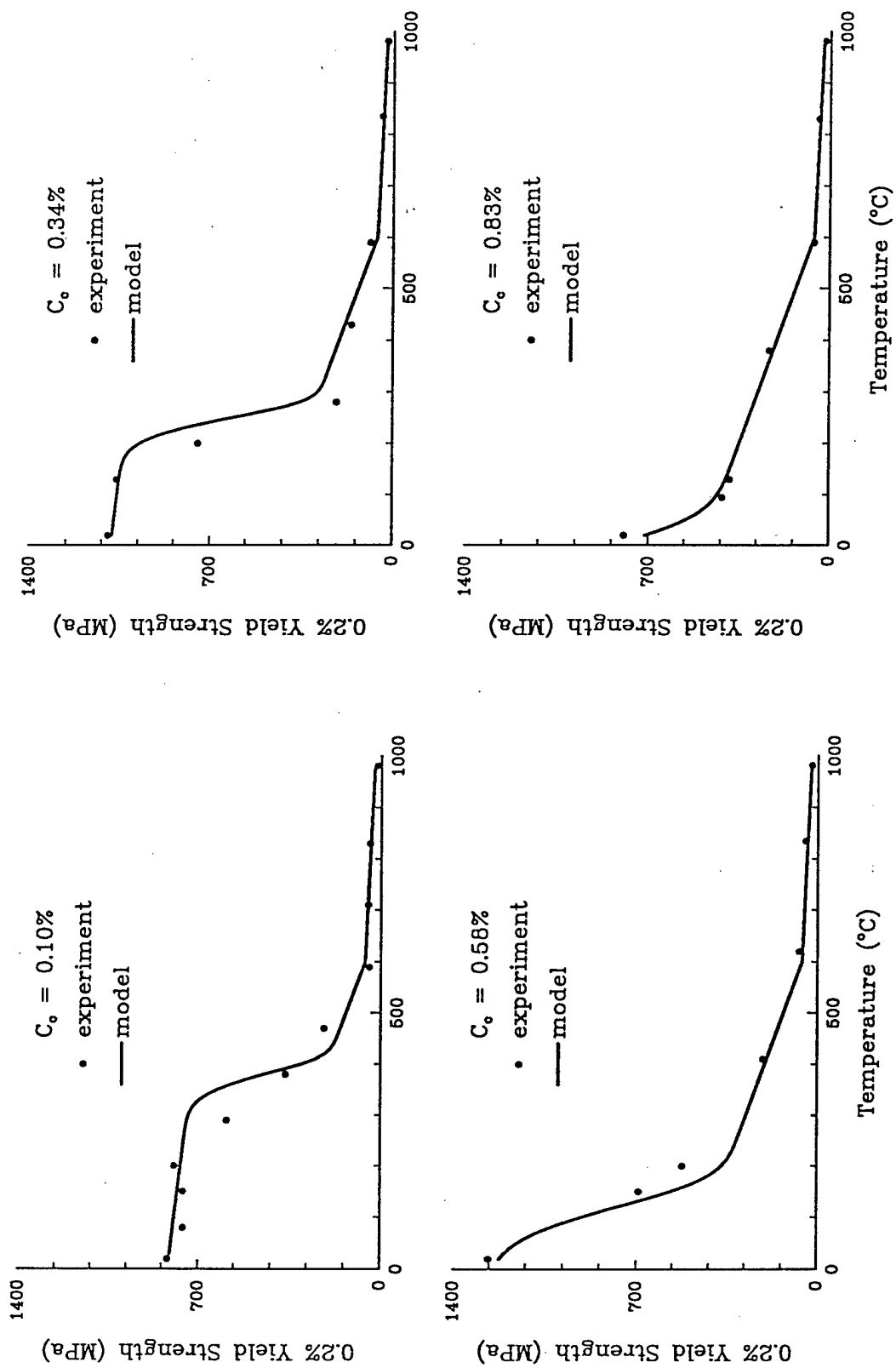


Figure 22. Comparison of model fit to measured variation in 0.2% offset yield strength with temperature and carbon content.

## DETERMINATION OF SURFACE HEAT TRANSFER COEFFICIENTS

The objective of this task was to measure the coefficients of surface heat transfer between the part and its surrounding environment as a function of surface temperature, for air, steel, quiescent oil and flowing oil.

Heat transfer coefficients are needed to conduct the thermal part of the thermo-mechanical heat treat simulation analysis. In practice, the boundary conditions for a quenched gear include quiescent air — when the gear is transferred from the oven to the press, flowing oil, and metal-to-metal (gear-to-die) contact.

The approach taken to determine heat transfer coefficients is very similar to that used by Price and Fletcher [6]. Internal temperature is measured near the surface of a part subjected to the quenching conditions of interest and an numerical analysis, based upon 1-D finite difference techniques, is used to deduce the surface heat transfer coefficient.

The experimental methodology used to determine heat transfer coefficients evolved throughout this program as experience was gained. The data eventually applied used in the model for the rim/web gear blank was derived from a thick, disc specimen fabricated from commercially pure nickel. This material enabled us to maintain a smooth, scale-free surface on the specimen similar to the surface that exists in a copper-plated steel part without having to copper plate and use inert oven atmospheres. Heat transfer coefficients are not material dependent [6].

Heat transfer coefficients used in the simulation of the flat disk experiment were derived from a set of experiments that were performed using the same experimental set-up that was used for the distortion experiments. These data are shown, together with the fit to the data used in the model, in Figure 34. Data are also reported here showing the effect of fast flowing oil on the heat transfer coefficients, even though analysis eventually showed that quiescent oil conditions are most representative of the quench press environment. These data were obtained from 9310 steel specimens that sometimes scaled. Therefore, the absolute magnitude of the heat transfers coefficient are not considered representative of copper plated parts austenitized in inert atmospheres. Nevertheless, the data are useful for revealing the dramatic effects of flowing vs. quiescent oil.

## EXPERIMENTS

Two types of specimens were used in this investigation, as shown in Figure 23. Both are 0.6 inches thick, with a 0.065 inch hole drilled in the center to within 0.040 inches of one surface; a thermocouple was spot welded to the bottom of this hole. The small cylindrical specimen, which was 0.5 inches in diameter and made of 9310 steel, included a flange for purposes of attachment to the quench fixtures. This smaller-diameter specimen was used primarily to determine the effects of flowing oil on the surface heat transfer coefficient,  $H$ . Larger disc specimens, 6 inches in diameter and made from 9310 steel were used for quiescent oil, stirred oil, and metal-to-metal contact conditions. As noted above, a pure nickel specimen of the same geometry was also used to determine  $H$ , but only for quiescent conditions.



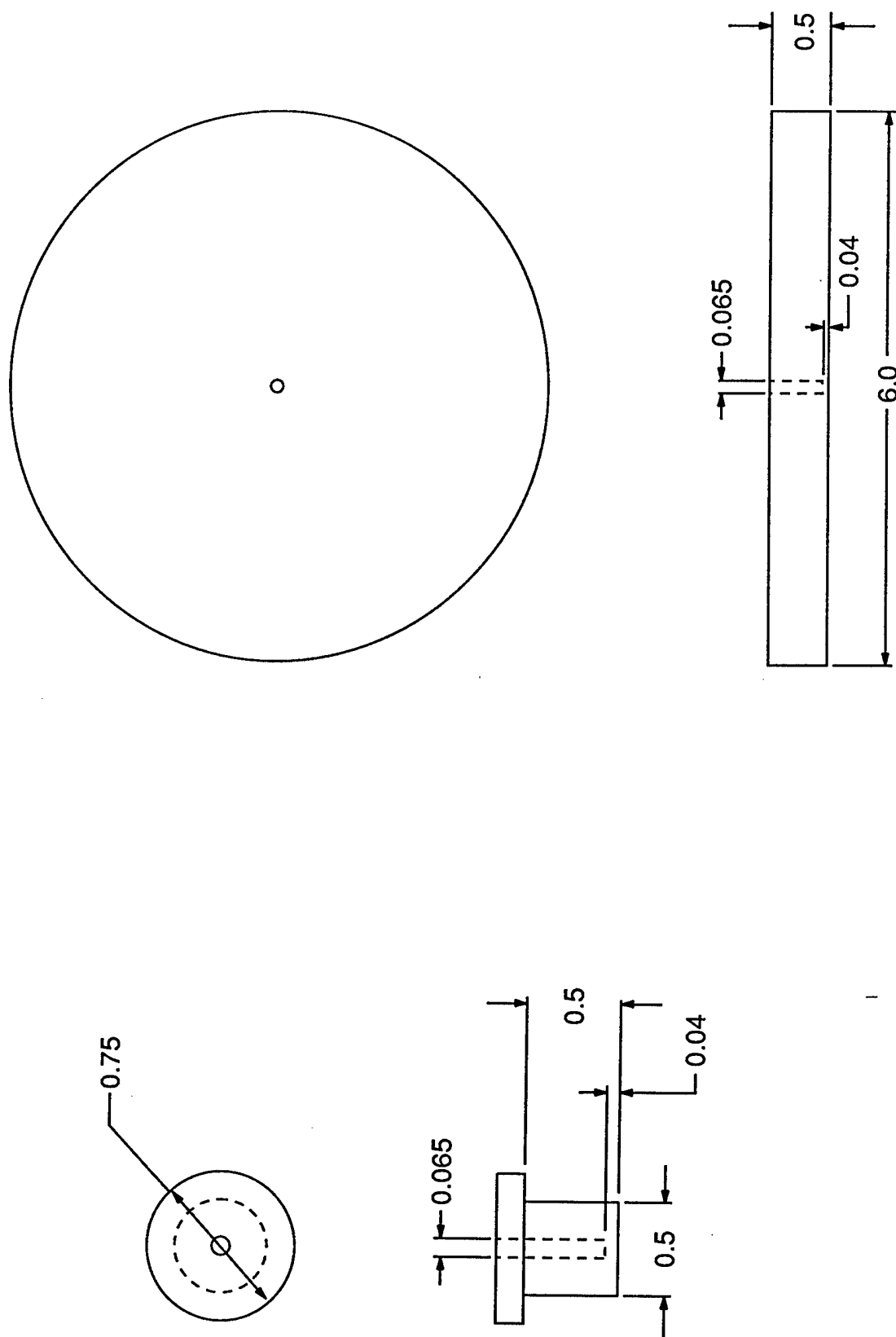


Figure 23. Specimens used in surface heat transfer measurement experiments. Left: half inch diameter specimen. Right: 6 inch diameter specimen.

Type K thermocouples, with 0.015 inch wire diameter, were used to measure internal metal temperature. The bare wires were insulated from each other with a ceramic cement before spot welding the junction bead to the bottom of the hole. The thermocouple leads were then attached to the specimen with a stress relief strap.

The general test procedure in all cases involved the heating of the specimen to 830-850 C and then holding for approximately 20 minutes. The quench oil, 'SUPERQUENCH', was heated to 60 C in all cases except one in which the oil was maintained at room temperature.

#### Quiescent air/oil tests

In these tests, the small, cylindrical specimen was removed from the oven and either allowed to sit in still, room temperature air or was submersed in oil at room temperature or 60 C.

#### Flowing oil

Two types of flowing oil tests were conducted: one in which the oil flow was parallel to the flat surface of the cylindrical specimen and one in which the oil impinged normal to this flat surface. The velocity of the oil in both cases was approximately 8 m/sec. Sketches of the fixtures used for these tests are shown in Figures 24 and 25.

#### Metal-to-Metal Contact

The test fixture used to conduct the metal-to-metal contact test is shown in Figure 26. One side of the disc contacts the end of a 0.75 inch diameter rod that is cooled by flowing water which, for this test, was maintained at 60 C. A load of 300 kg was applied to the opposite surface of the disc to create an average contact pressure of 12 MPa.

The cooling curves for each of these tests is shown in Figure 27. The curves in this figure were translated with respect to time so that they all intersected at a temperature of about 800 C. In this way, the relative cooling rates can be compared between the various boundary conditions. The figure shows that there is little apparent difference in cooling rates between quiescent and flowing conditions for this rapid quench oil. However, as shown below, there is a significant difference with respect to heat transfer coefficient.

### NUMERICAL APPROACH

A computer program was written to calculate the surface heat transfer coefficient,  $H$ , from the temperature-time data described above. The algorithm for this program, which is described in the paper by Price and Fletcher [6], utilizes an iterative approach. The first approximation of  $H$  at a particular time (and surface temperature) is obtained by assuming that heat transfer occurs under isothermal conditions. The value of  $H$  so obtained is then used to calculate the near-surface temperature distribution by means of forward, finite differences. Use is then made of the difference between the calculated and measured temperatures at the location of the thermocouple to derive the next approximation to  $H$  for that time (and surface temperature). The process is continued until the difference between successively calculated  $H$

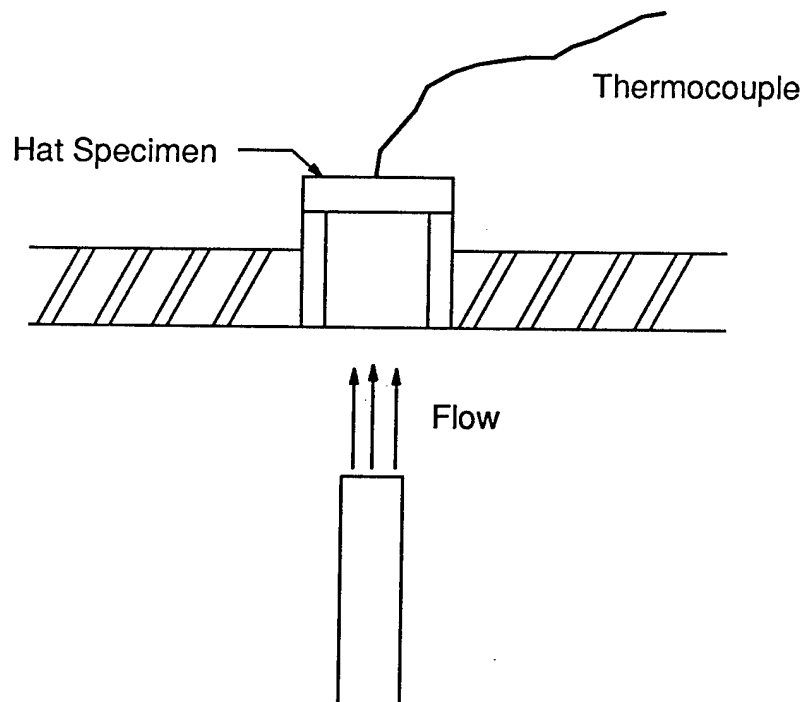


Figure 24. Fixture used to measure the surface heat transfer between 9310 steel and flowing oil impinging the specimen surface.

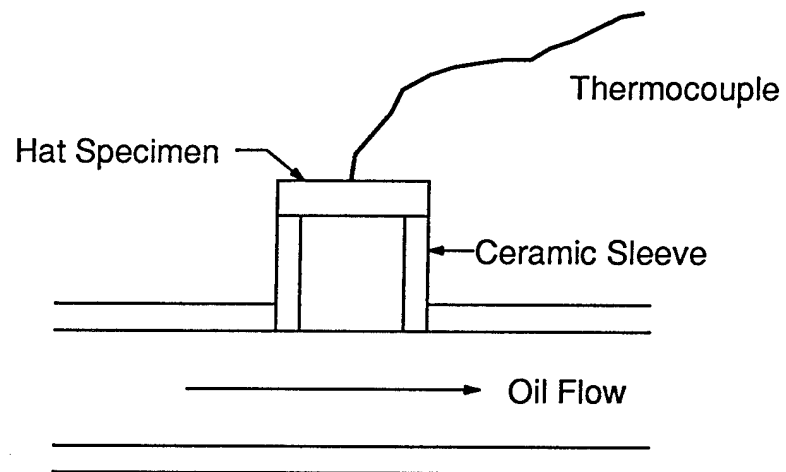


Figure 25. Fixture used to measure the surface heat transfer between 9310 steel and oil flowing parallel to the specimen surface.

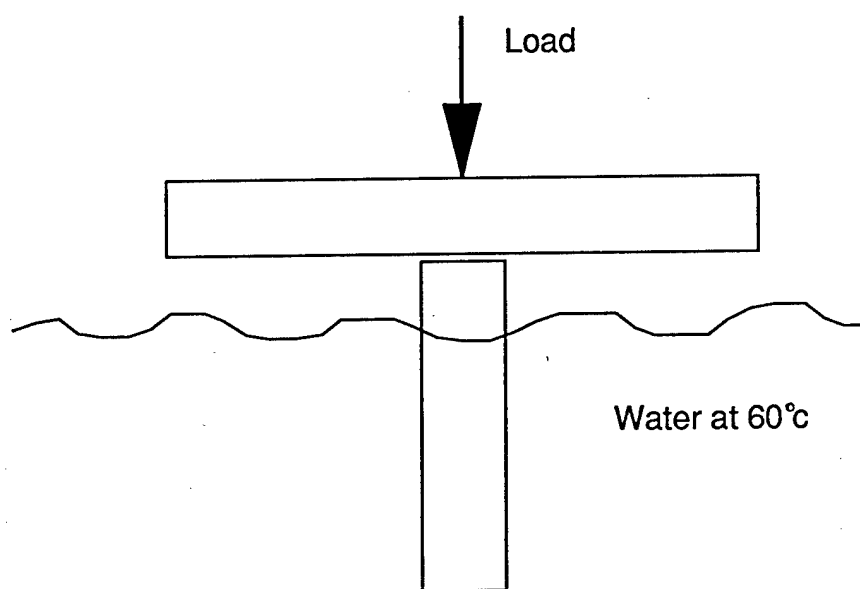


Figure 26. Test fixture used to conduct the metal-to-metal contact test.

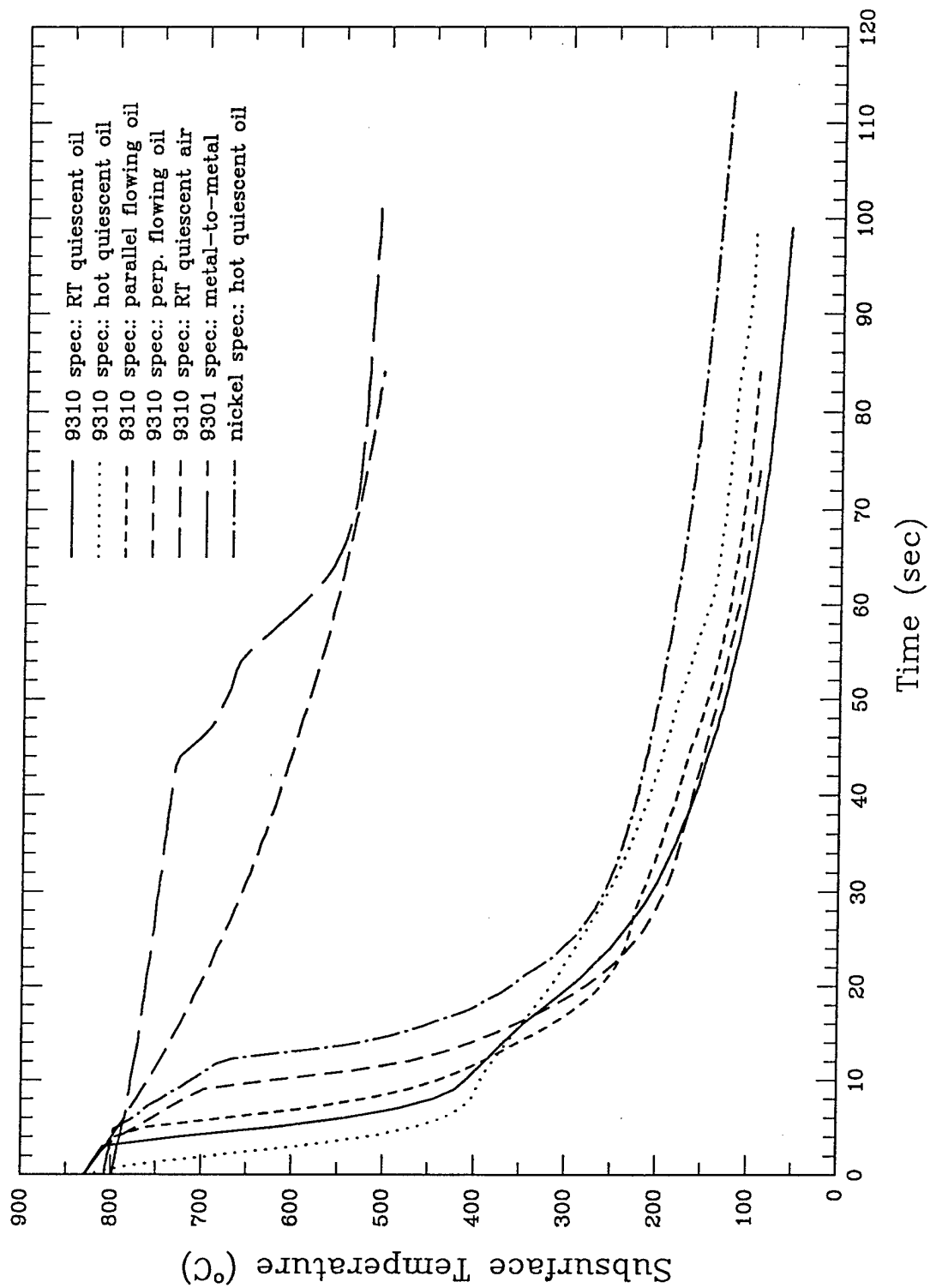


Figure 27. Cooling curves for each of the surface heat transfer measurement tests.

values is sufficiently small. The entire process is then repeated for the next time (and surface temperature) step.

The computer program requires a knowledge of the thermal conductivity, heat capacity and thermal diffusivity. Although these physical properties vary with temperature for the specimen materials, we used the constant values shown in Table 6. This approach was taken to simplify the analysis, and because these constants do not vary greatly over the critical temperature range. Analysis performed subsequent to the determination of heat transfer coefficients shows that incorporation of the variation in properties with temperature changes the peak value  $H$  by only about six percent, which is not large when measured against the variability of the experiments.

TABLE 6. THE PHYSICAL PROPERTIES USED IN THE CALCULATION OF SURFACE HEAT TRANSFER COEFFICIENTS

Property	9310 steel specimen	nickel specimen
Thermal Conductivity (W/m K)	25.	77.
Specific Heat J/kg K	600.	456.
Density (kg)	8000.	8890.

### Results

Figure 28 shows the calculated curves of surface heat transfer coefficient as a function of surface temperature that were determined, using the 9310 steel specimen, for each the boundary conditions tested. Also included in this figure is the calculated curve determined for quiescent conditions determined using the Nickel specimen.

The curves for both quiescent and flowing oil quench tests, that were performed using the 9310 steel specimen, show the common characteristic that  $H$  reaches a maximum of  $5000 \text{ W/m}^2 \text{ K}$  at approximately  $450\text{-}480 \text{ C}$ . In addition, the calculated  $H$  values above this temperature appear to be about the same for all of the oil conditions. (We believe that the differences observed are due primarily to time required to transfer the specimens into the flowing oil fixture. It was not possible to control this time accurately.) On the other hand, significant differences in  $H$  are observed below  $400 \text{ C}$ , and this is most likely because the flowing oil is more effective at carrying heat away from the surface in the quiescent heat transfer temperature regime. Of the four quenching conditions, the perpendicular flowing oil yields the highest values of  $H$  at these lower temperatures. We note that the quench in the hot quiescent oil yields a lower heat transfer coefficient than the quench in the room temperature oil at the lower temperatures.

Calculated values of  $H$  for quiescent air and metal-to-metal contact are considerably lower than for oil. The value of  $H$  for quiescent air is approximately  $200 \text{ W/m}^2 \text{ K}$ , while for the metal-to-metal contact,  $H$  reaches a peak value of  $550 \text{ W/m}^2 \text{ K}$ , but decreases at temperatures

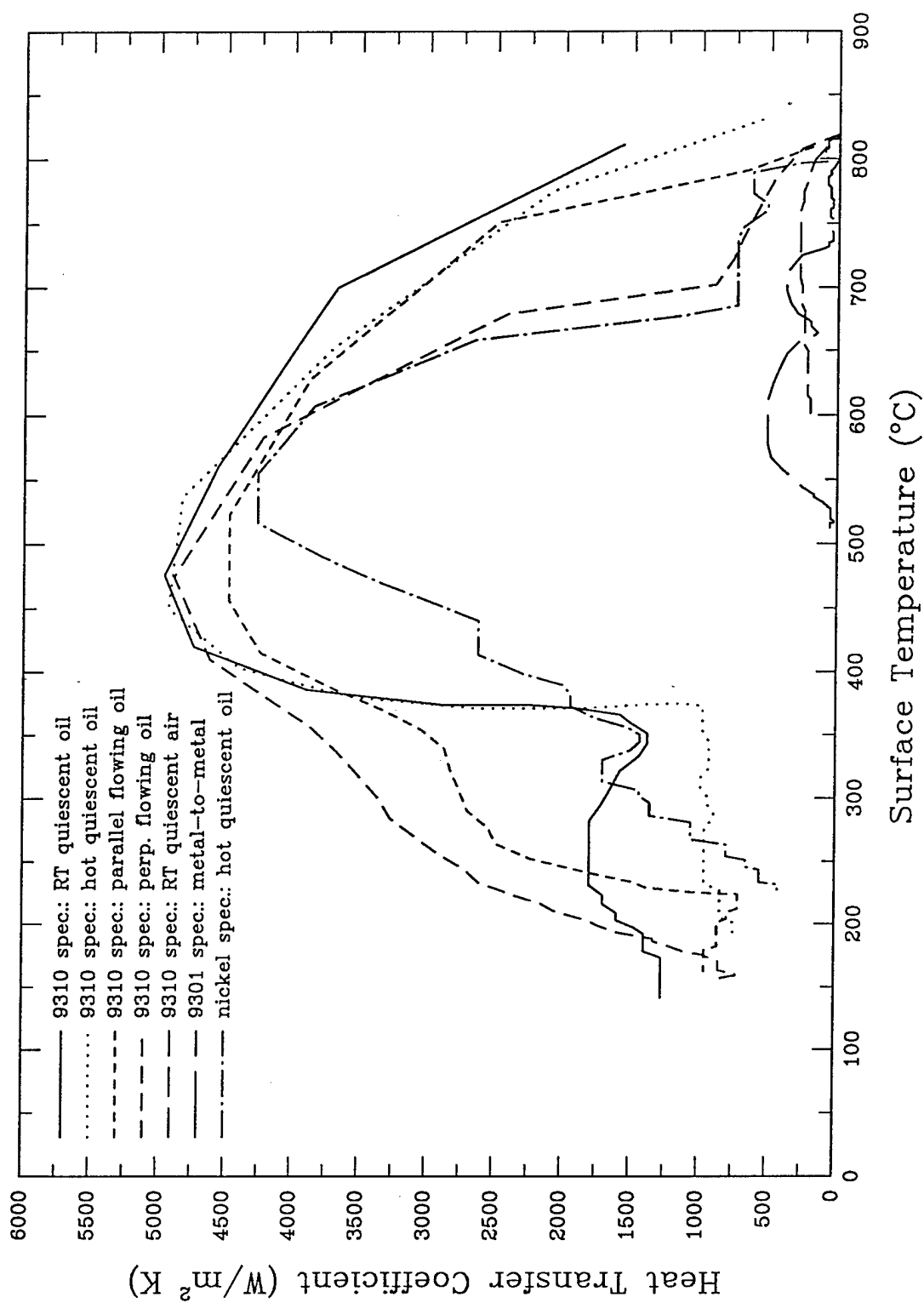


Figure 28. Calculated variation of surface heat transfer with temperature for each of the measured conditions.



less than about 530 C to values less than that for quiescent air. (Values for metal-to-metal contact at temperatures lower than 530 C were not determined, because the data acquisition system stopped recording data when the temperature reached this value.)

Calculated values of  $H$  for the nickel specimen in quiescent oil are somewhat less than those for the 9310 specimen.  $H$  reaches a peak of about  $4200 \text{ W/m}^2\text{K}$  at 550 C. The temperature region of high  $H$  appears to be smaller, as well.

## EVALUATION OF THE MODEL THROUGH APPLICATION TO A CARBURIZED FLAT DISK

Initial validation of the finite element model was accomplished through its application to the free-quench of a flat disk. Two sets of controlled experiments were run to provide a basis for assessment of the model's predictive capabilities.

In the first experiment, a total of five disks were heat treated. Three of these were carburized on one surface of the disk in order to promote distortion. The remaining two disks were subjected to the carburization thermal cycle, but were completely masked so that no carbon diffused into them. Each of the disks was then austenitized and free-quenched in stirred oil. Measurements of distortion were made at several points on the disk after each step. In the second set of experiments, the sensitivity of model predictions to variations in process variables was evaluated using in a statistically-designed matrix of eight heat treatments. These disks were processed through the temper operation. The finite element model was used to predict distortion for each of the experiments performed on the carburized disks. Because the three carburized disks heat treated in the first experiment are nominally the same as one of the cases studied in the eight-disk parameter study, model results are presented here only for the latter set of experiments.

### EXPERIMENTAL PROCEDURE

A schematic of the disk is shown in Figure 29. It is 6 inches (152 mm) in diameter and 0.15 inches (3.81 mm) thick. The disks were machined to a tolerance of  $\pm 0.001$  inches from a six-inch diameter by 10 inch long solid cylinder of 9310 steel. The thickness of the disk was chosen to reduce dimensional stability and promote distortion. The 0.15 inch disk thickness is also equal to the thickness of the web in the gear blanks investigated and reported later in this report. A 0.25 inch (6.3 mm) hole was drilled into the middle of the disk for fixturing during quench.

A baseline set of dimensional measurements was made for each of the disks using a dial gauge indicator; relatively large distortions,  $>0.010$  inches, were anticipated. A fixture was made for the indicator to ensure that the disk was held in a stable position during measurement. Measurements were made at four radial positions: 0.25 in (6.3 mm), 1.125 in (28.6 mm), 2.0 in (51 mm), and 2.875 in (73 mm). Measurements were taken at three circumferential positions:  $0^\circ$ ,  $120^\circ$ , and  $240^\circ$ . A total of twelve measurements were made on each of the disks at each stage of the process.

The disks that were to be carburized were then masked using copper electroplate of approximately 0.001 inches in thickness.

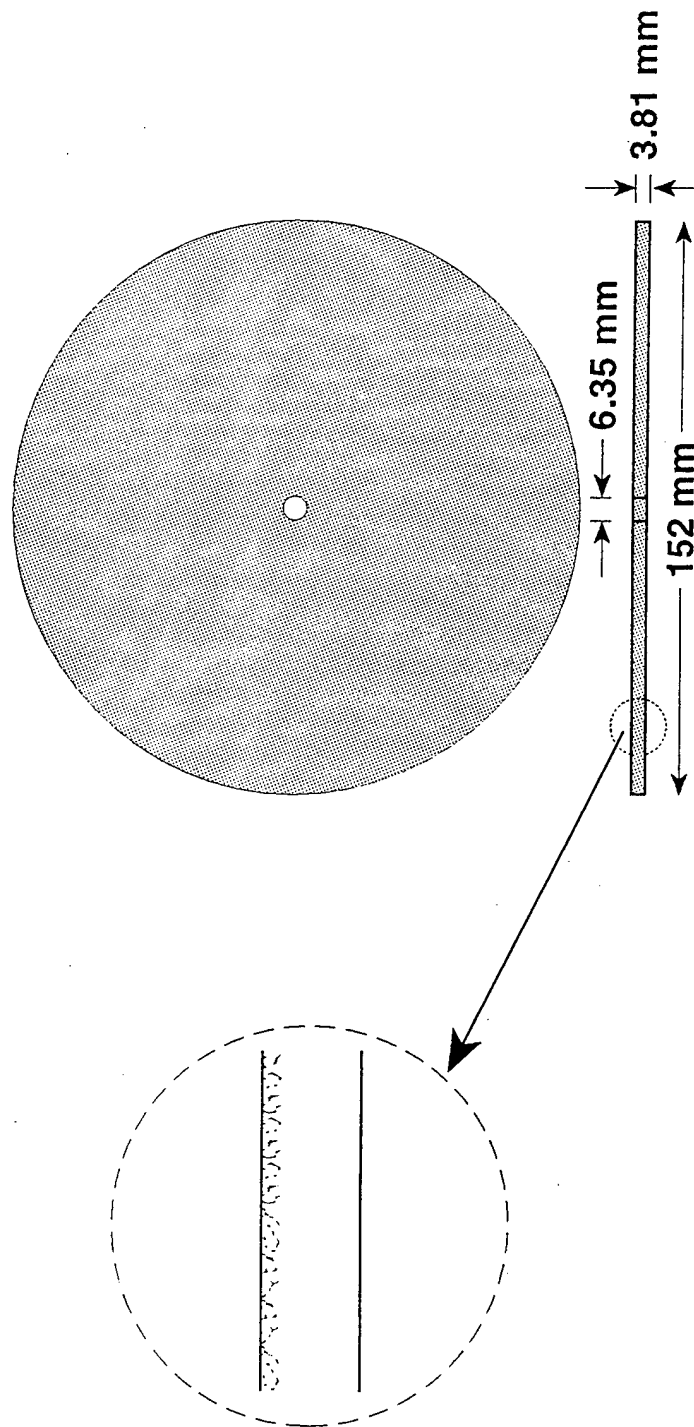


Figure 29. Schematic of disk specimen used for experiments and modeling study.

In order to assess the effect of the copper plating on dimensional measurements, the disks were then re-measured. Results from this procedure indicated that copper plating changed the disk flatness by no more than a 0.0002 inches. Subsequent measurements were made on as-plated specimens.

The disks were then sent to Klock. Each of the disks was heated in a carbon rich atmosphere to 927 C and held at this temperature for a period of three hours. The carbon potential,  $C_p$ , was set at 0.10.

Dimensional measurements were again performed on the carburized disks. The copper plating was then stripped off, and new plating was applied to the disks in preparation for austenitization and quench.

The disks were austenitized and quenched (one-at-a-time) in an Arthur D. Little laboratory. The disks were austenitized in a furnace at 830 C for a period of twenty minutes. Unfortunately, the furnace was not equipped with an inert atmosphere. As a result, there was occasional scaling of the copper plate during the quench process. This likely resulted in some circumferential variability in distortion, but had only a minor effect on average distortion.

Each disk was removed from the furnace using a thin rod that fit through the central hole. It was then quickly transferred to a fixture above the quench tank and lowered into the quenchant. Each disk was held so that it entered the quenchant edge-first.

Upon removal of the first few of the disks from the quenchant, some peeling of the copper plating was noticeable. This was clearly the result of the lack of an inert atmosphere in the furnace used for the experiments. It does not appear that such peeling had a significant adverse effect on the results. The introduction of a sacrificial piece of carbon into the furnace alleviated this problem to a certain extent.

Another set of dimensional measurements was made following quench for the five disks used in the first set of experiments.

The eight disks used in the parameter study were subsequently put through the deep-freeze and temper operations. The disks were deep-frozen to a temperature of -72 C and held for a period of 2 hours in order to promote further transformation of retained austenite. Finally, the disks were tempered in an oven at a temperature of 150 C for 2 hours. Additional dimensional measurements were made after each of these final processing steps.

A total of four process variables were selected for the experimental study:

1. Carburization temperature (927 C/954 C).
2. Austenitization temperature (830 C/900 C).
3. Quenchant temperature (24 C/78 C).
4. Presence or absence of quenchant agitation.

A fifth variable, distortion due to prior processes, was selected for study using the model only.

Using a statistical design of experiments approach, eight sets of experimental process variable combinations were determined; an additional four sets of data were selected for analysis only to determine the effects of a fifth variable, distortion due to prior processes (see Table 7).

TABLE 7. PARAMETER COMBINATIONS FOR THE  
STATISTICALLY-DESIGNED EXPERIMENTAL STUDY

Test	Carburization Temperature (°C)	Quenchant Oil Temperature (°C)	Austenitization Temperature (°C)	Oil Agitation?
D6.	927	78	900	Yes
D7.	927	24	830	No
D8.	927	78	830	No
D9.	927	24	900	Yes
D11.	944	78	830	Yes
D12.	944	24	900	No
D13.	944	78	900	No
D14.	944	24	830	Yes

## EXPERIMENTAL RESULTS

### Preliminary Experiments

Measured distortion after carburization and quench for one of the two uncarburized disks (D5) and one of the three carburized disks (D1) are shown in Figures 30 and 31. Distortion patterns for the other disks were similar. As the figures illustrate, the non-carburized specimens (D4 and D5) distorted relatively little (less than 0.005 inches) during both the carburization and quench steps. The carburized specimens, however, distorted a great deal more — up to approximately 0.080 inches, due to the gradient in carbon through the thickness of the disk.

The average distortion at the edge of the disk for each of the three carburized tests is summarized in Table 8. As indicated in this table, the distortion following carburization was quite uniform, both around the disk and from disk-to-disk. In marked contrast, the distortion following quench was much more varied. Each of the carburized disks had a tendency to 'potato chip', indicating the presence of a significant amount of variation around the disk.

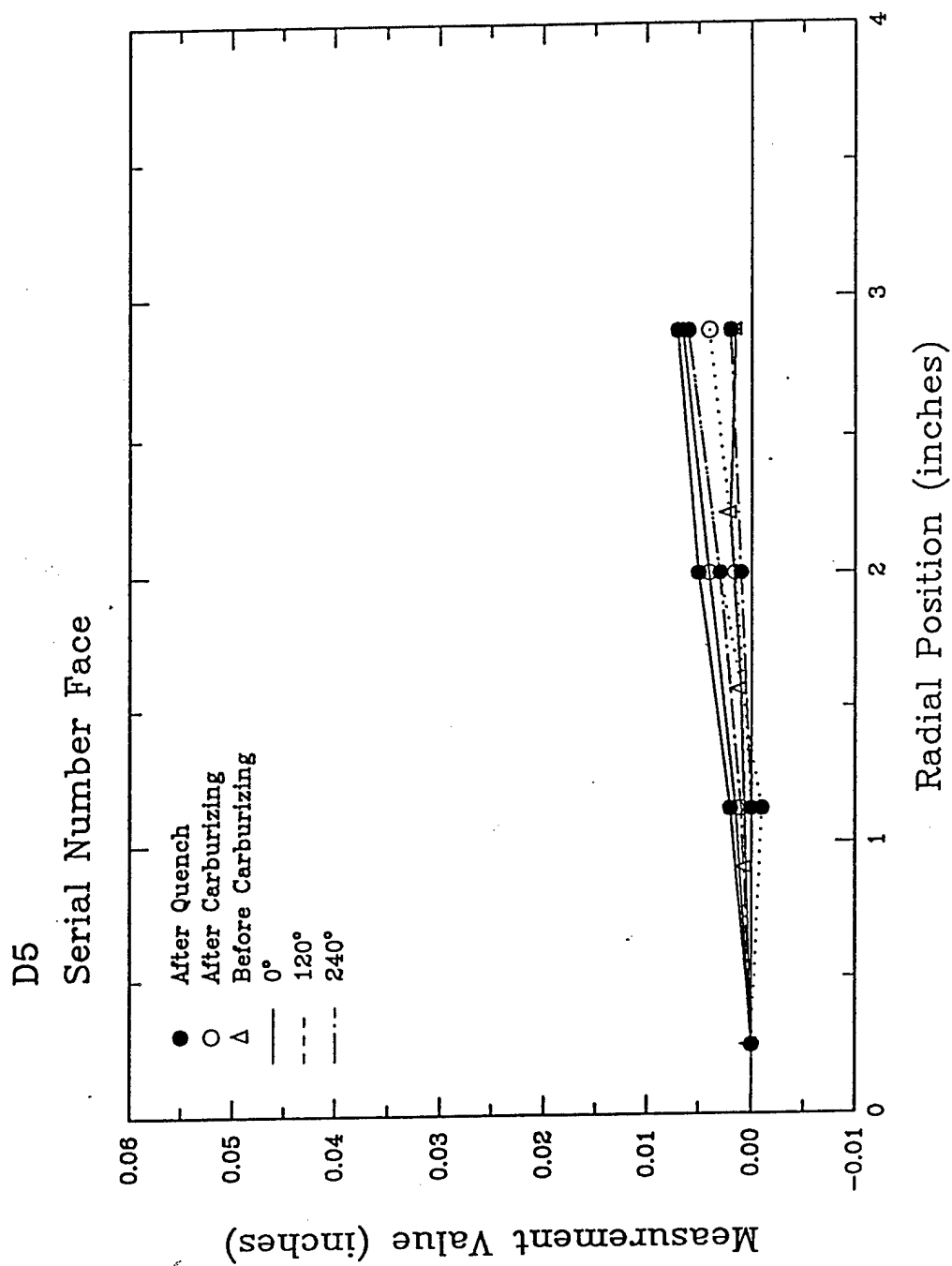


Figure 30. Measured distortion prior to carburizing, following carburizing, and following quench for one of the two uncarburized disk specimens (D5).

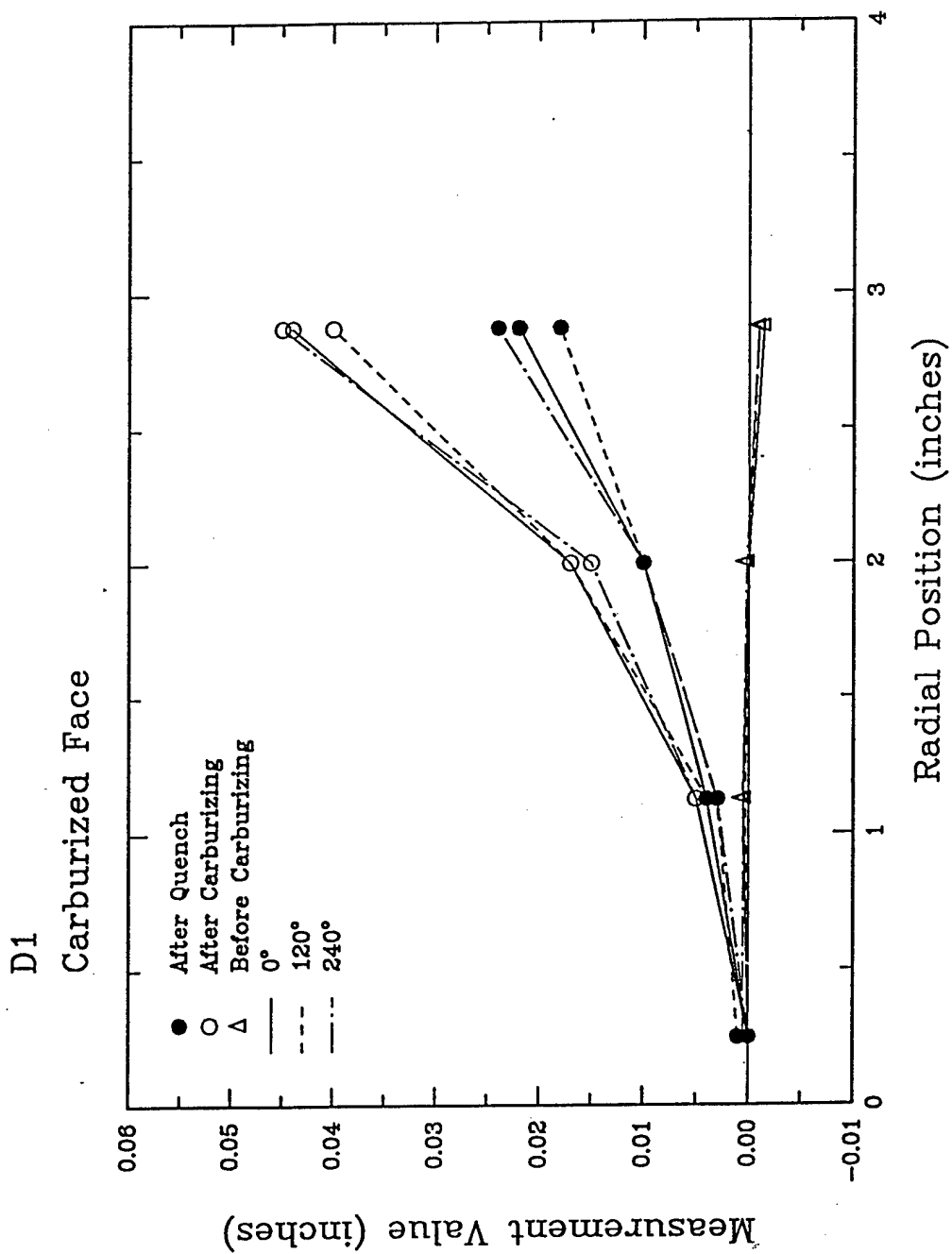


Figure 31. Measured distortion prior to carburization, following carburization, and following quench for one of the three carburized disk specimens (D1).

TABLE 8. MEASUREMENTS OF DISTORTION AFTER CARBURIZATION AND QUENCH FOR EACH OF THE THREE CARBURIZED DISKS

Stage	Specimen	Average Edge Displacement ( $10^{-3}$ in)				
		0°	120°	240°	Average	Std. dev.
after carb.	D1	44.0	40.0	45.0	43.0	2.6
	D2	47.0	48.0	40.0	45.0	4.4
	D3	50.0	48.0	42.0	46.7	4.2
	all meas.				44.9	3.6
after quench	D1	22.0	18.0	24.0	21.3	3.1
	D2	78.0	63.0	59.0	66.7	10.0
	D3	55.0	55.0	40.0	46.7	4.2
	all meas.				46.0	21.0

### Parameter Study

The results of the distortion measurements for the parameter study are summarized in Table 9 below and depicted graphically in Figure 32. (In order to more clearly show the data, this figure contains four graphs, each displaying the results from one test in which  $T_{\text{aust}}=830$  C and one test in which  $T_{\text{aust}}=900$  C.)

TABLE 9. MEASUREMENTS OF DISTORTION FOR EACH OF THE EIGHT EXPERIMENTS OF THE PARAMETER STUDY

Test	Test Conditions				Average Edge Displacement ( $10^{-3}$ in)				
	$T_{\text{carb}}$	$T_{\text{oil}}$	$T_{\text{aust}}$	Agit?	Before Carb	After Carb	After Quench	After Freeze	After Temper
D6	927	24	900	No	-0.3	39.2	-19.8	-25.5	-18.7
D7	927	24	830	Yes	-3.2	37.2	34.0	31.3	41.0
D8	927	78	830	No	-1.0	37.7	36.6	23.5	35.2
D9	927	78	900	Yes	1.0	42.0	-37.6	-42.6	-35.2
D10	944	24	830	No	3.0	39.3	28.7	14.0	31.7
D11	944	24	900	Yes	3.5	43.7	-30.7	-32.8	-21.8
D12	944	78	900	No	1.0	43.7	-39.8	-50.6	-41.4
D13	944	78	830	Yes	0.0	46.0	9.8	0.9	13.3



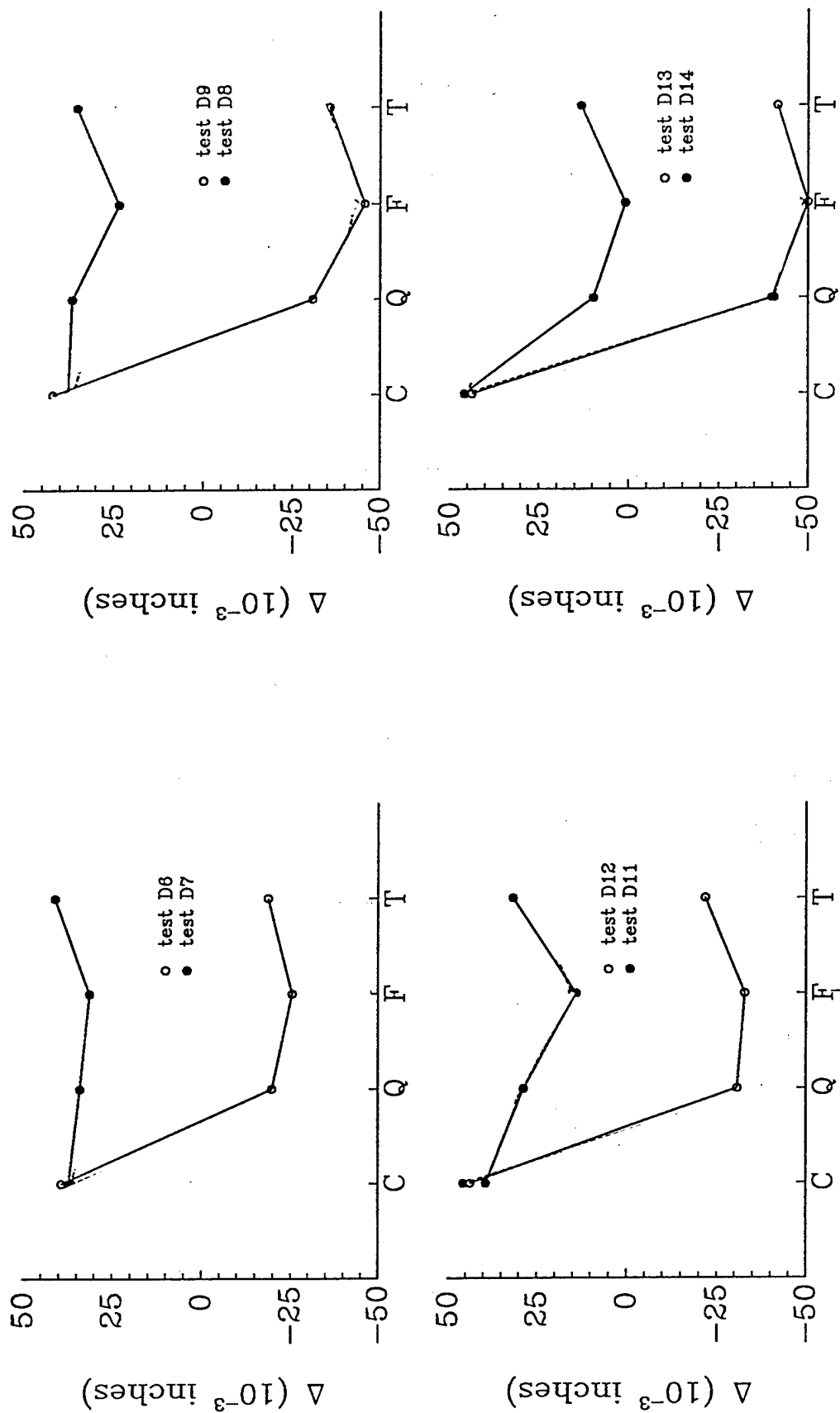


Figure 32. Averaged edge distortion following carburization, quench, deep-freeze and temper operations for each of the eight disks processed in the parameter study.

The results given in Table 9 and pictured in Figure 32 are consistent in that, in each test, the edge of the disk:

- moved toward the carburized side of the disk after carburization;
- moved away from the carburized side of the disk after quench;
- moved away from the carburized side of the disk after deep-freeze;
- moved back toward the carburized side of the disk after temper.

One surprising result was that increasing the austenitization temperature from 830 C to 900 C altered post-quench distortion dramatically, as is evident in both Table 9 and Figure 32. In fact, increasing the austenitization temperature completely reversed the direction of post-quench distortion.

A statistical analysis of the data was performed at Arthur D. Little and reveals that:

- Carburization distortion is significantly dependent upon the carburization temperature;
- Quench distortion is strongly dependent upon the austenitization temperature.

Unfortunately, the strong dependence of quench distortion on austenitization temperature makes it difficult to assess the significance of the other parameters. Nevertheless, statistical analysis revealed that quench distortion is weakly dependent upon carburization and oil temperatures, but not significantly dependent upon agitation.

### FINITE ELEMENT MODEL

The finite element model used for simulation of the disk carburization and quench experiments is shown in Figure 33. The axisymmetric model used 402 elements. Element spacing was biased in order to concentrate more elements near the upper and lower surfaces of the disk in order to capture the temperature and carbon gradients

As noted in section describing our surface heat transfer measurements, prior to running the model, additional surface heat transfer measurements were made using the same oil agitation conditions that were used for the experiments. A smooth curve was fit through these data (Figure 34) and input into the FILM subroutine of the model.

A simulation of carbon diffusion was performed first. The carbon profile generated by the model was compared with direct measurements of the carbon profile made using the Liko method at Dirats laboratories and also compared with a second set of data for percent carbon inferred from hardness measurements. Initial calculations did not produce good agreement with the experimental data. The carbon diffusivity constants taken from the literature (see equation 28) were then modified until the agreement was satisfactory. Figure 35 shows a comparison of the final model prediction for the baseline carbon level compared with the directly- and indirectly-measured carbon profiles. This agreement was made using a carbon diffusivity constant  $D_c = 2.8 \times 10^{-7} \text{ cm}^2/\text{s}$ .

It is clear from Figure 35 that indirectly measured carbon gradients are not accurate very near the surface. This is due to the fact that there is considerable retained austenite at the surface, which lowers hardness.



Figure 33. Finite element mesh used to model the heat treatment of the rim/web gear blank.

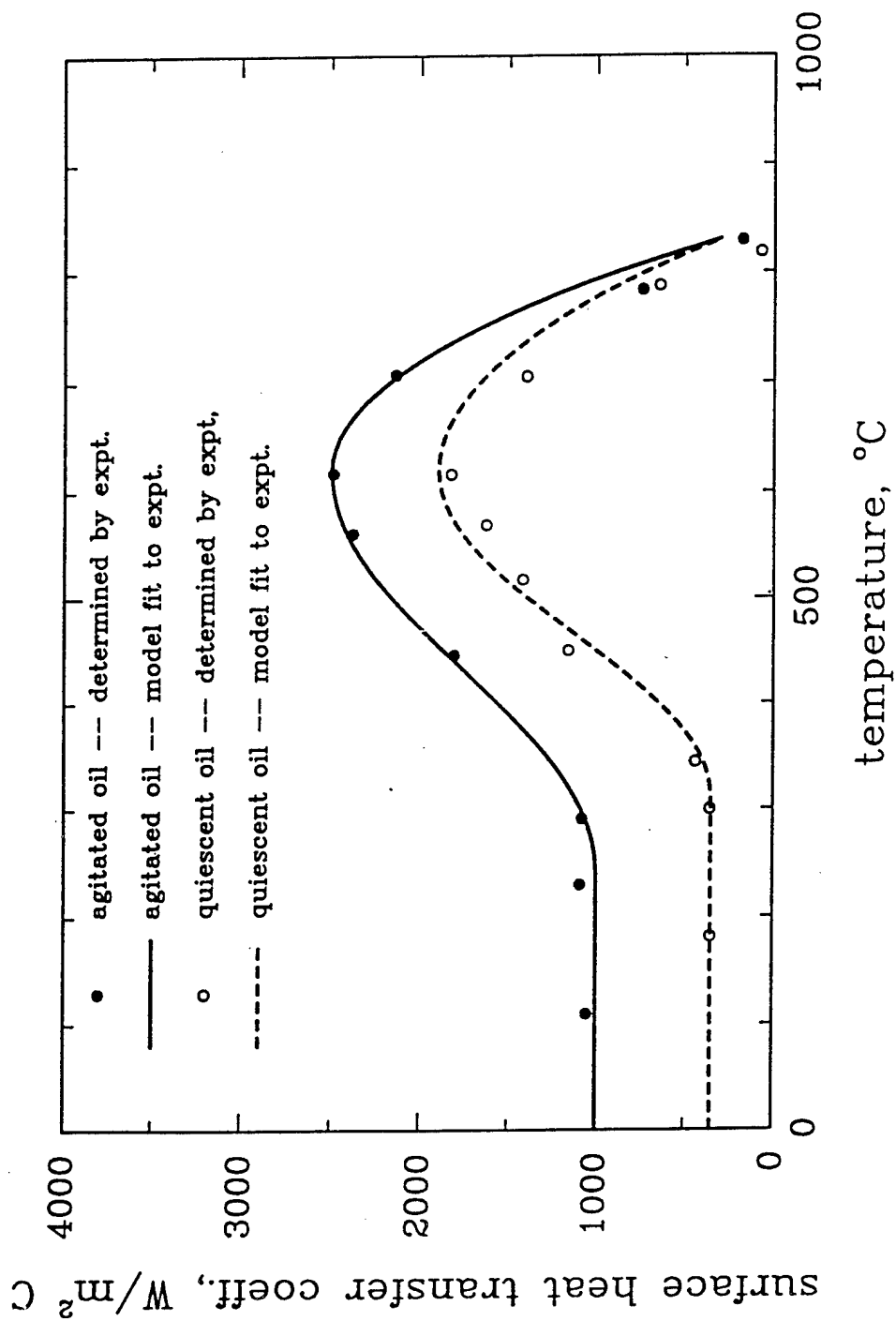


Figure 34. Model fit to experiments performed on 9310 steel specimen to quantify difference between surface heat transfer coefficients for quiescent and agitated oil.

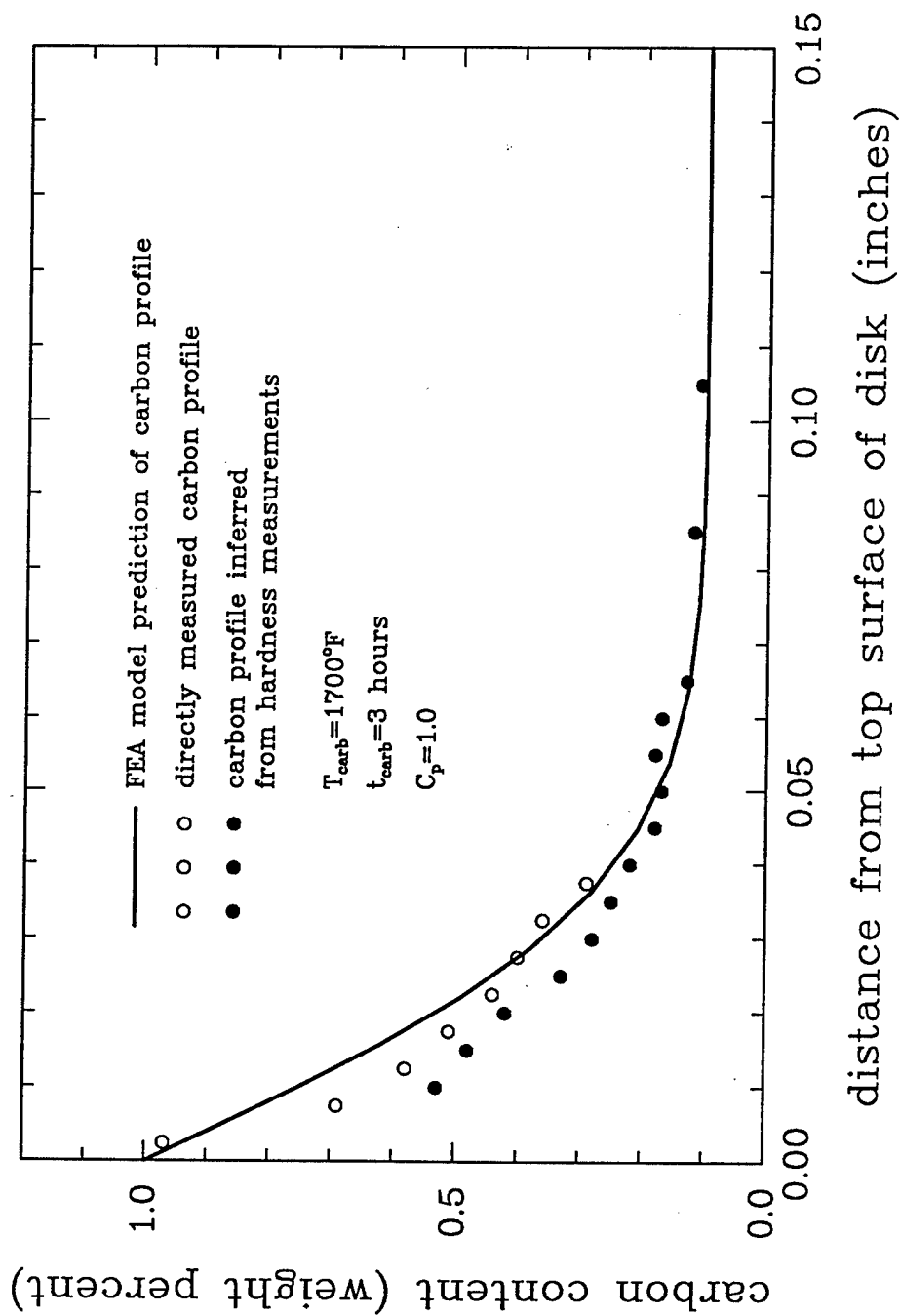


Figure 35. Comparison of model prediction of carbon profile at top surface of disk versus directly and indirectly measured values.

The heat treat processes were modelled in several steps by imposing an initial temperature and several intermediate temperature environments representing each process cycle. A schematic showing the temperature history imposed for each process step is shown in Figure 36.

In order to illustrate a few features of the simulation of the carburization and quench processes, diagrams showing deformation and contours of temperature, phase fraction, and plastic strain are pictured in Figures 37 through 44 at several stages of each process.

When first heated to the carburization temperature (Figure 37), the disk expands uniformly due to thermal expansion. When cooled below the bainite transformation start temperature (Figure 38), the uncarburized, lower portion of the disk expands, bending the disk upward. Further cooling (Figure 39) bends the disk further upward, as the bainite transformation of the lower, uncarburized region nears completion. At still lower temperatures (Figure 40), the carburized layer begins to transform, causing the disk to straighten out. At room temperature (Figure 41), there is still distortion upward, due to the untransformed upper surface layer, and plasticity that occurred at higher temperatures.

When reheated to the austenitization temperature (Figure 42), much of the distortion due to carburization remains. When the temperature drops below the martensite start temperature of the uncarburized region (Figure 43), the disk again bends upward. When the disk cools to room temperature (Figure 44), there again is residual distortion due to the untransformed upper surface layer and plasticity. In the subsequent deep-freeze operation (not shown), the disk bends further downward due to transformation of the thin, high carbon content layer at the top of the disk. Finally, during the temper operation, the disk bends slightly upward due to the negative volume change that occurs in the carburized region.

Simulation of the carburization, quench, deep-freeze and temper steps were made for each of the eight parameter set combinations. For those cases for which the austenitization temperatures were raised to 900 C, initial calculations accounted for only the increased austenitization temperature, but not the effect that this temperature difference would have on material properties. These calculations did not capture the dramatic effect that the high austenitization temperature had on distortion during quench. It became clear upon further examination of technical literature [11] that an increase of 70 C in the austenitization temperature would have a dramatic effect on material properties. In particular, the parameters governing transformation kinetics are strongly affected by such a change, including a dramatic decrease in the martensite start and finish temperatures.

The effects of an increased austenitization temperature were introduced into the model based upon this literature review. It should be noted that these data were not measured and cannot be considered to be nearly as accurate as those for the baseline austenitization temperature, 830 C.

Using the updated material parameters determined from the literature review, the four simulations for the high (900 C) austenitization temperature were repeated. Model predictions of heat treat distortion for the eight cases are compared with experimental results in Table 10. The data are depicted in graphical form in Figure 45.

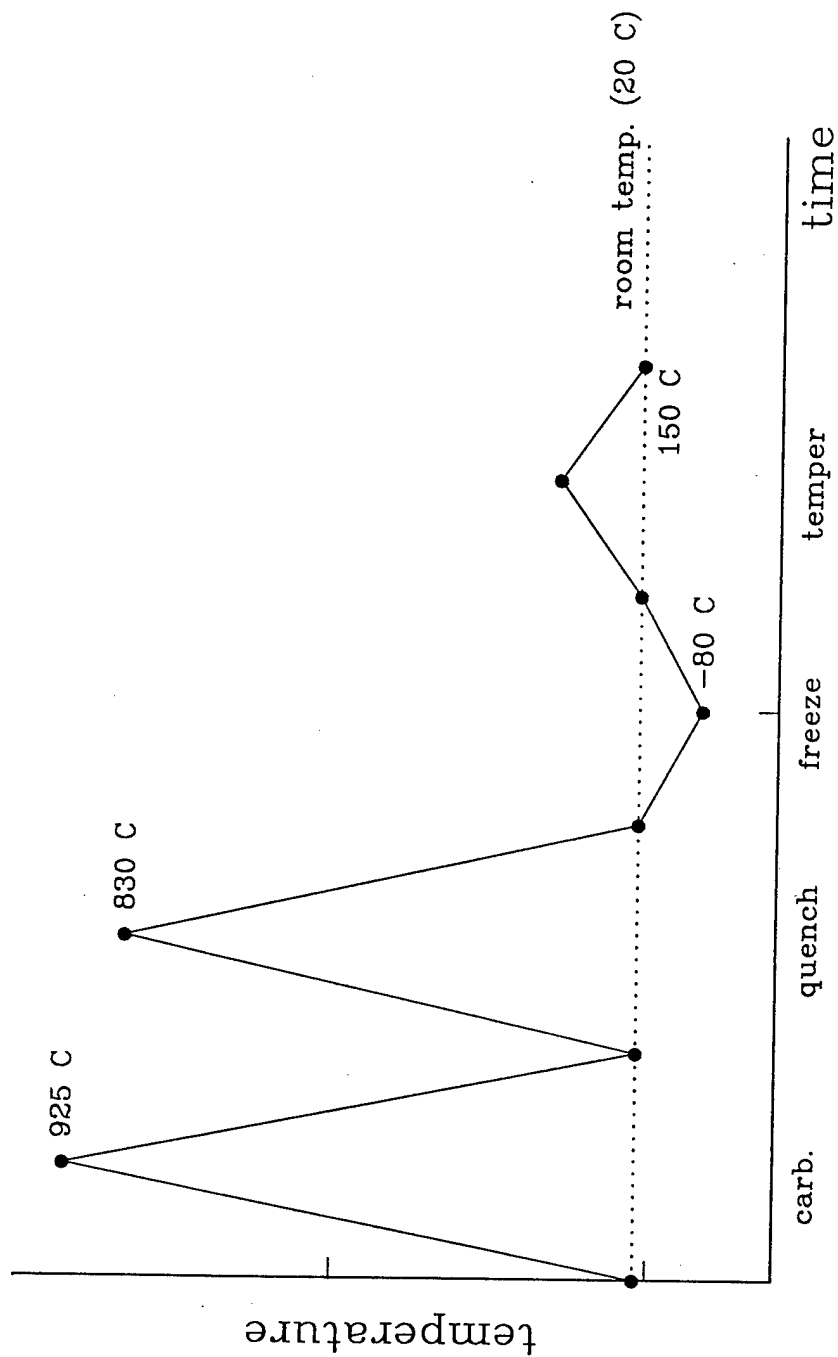


Figure 36. Temperature history of the surrounding media imposed as thermal boundary conditions for each of eight steps used to simulate the carburization, quench, deep-freeze and temper operations.

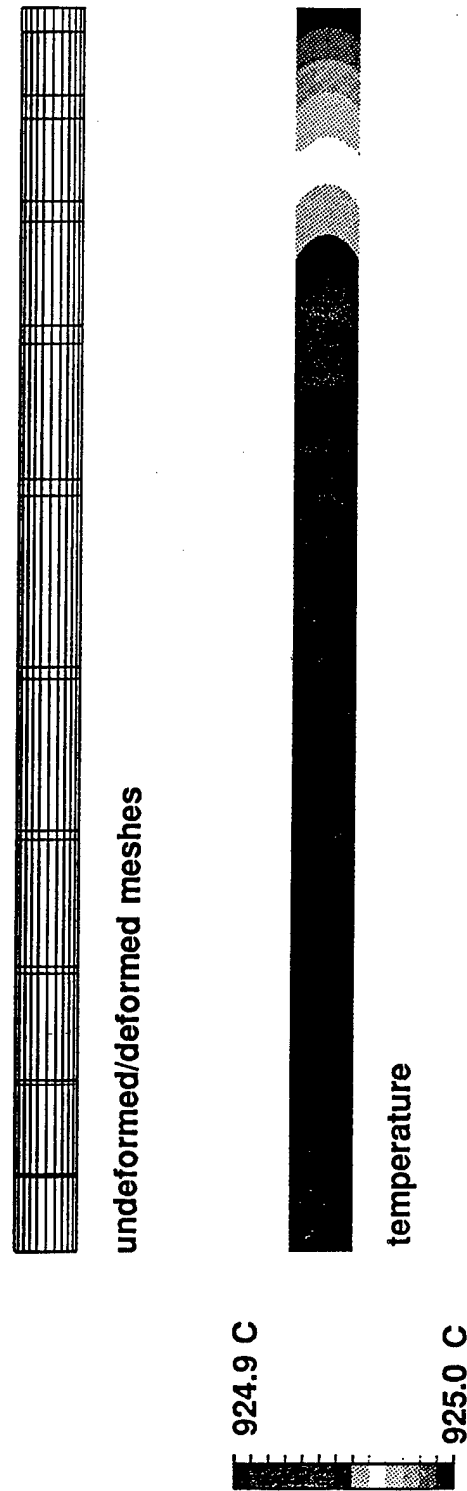


Figure 37. A comparison of undeformed and deformed meshes showing the growth of the disk and a contour diagram showing the nearly uniform temperature distribution following heat-up to the carburization temperature.



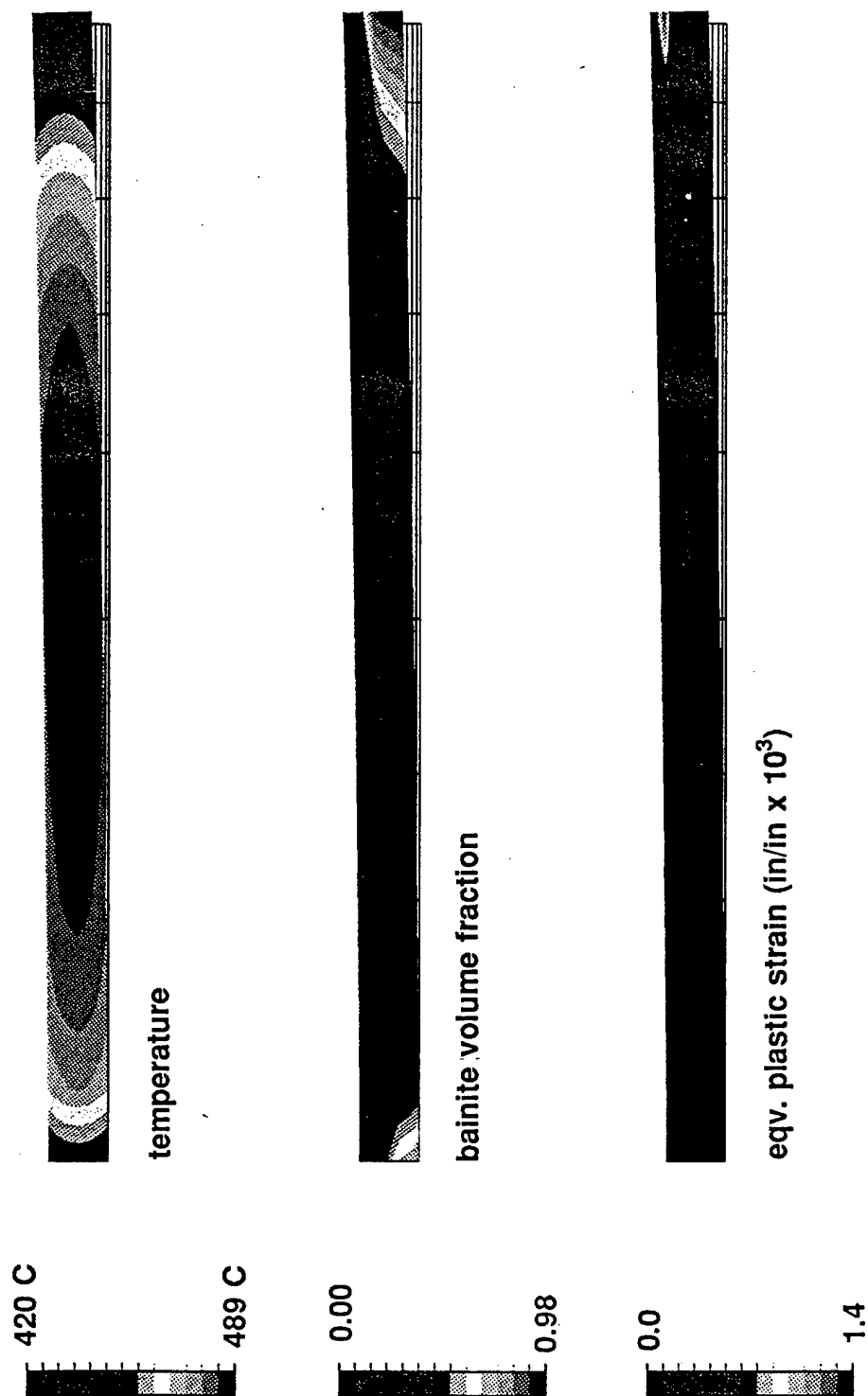


Figure 38. Contours of temperature, bainite volume fraction, and equivalent plastic strain superposed on the deformed mesh for a time just after the temperature has decreased below that for start of the bainite transformation for the uncarburized material, causing the disk to bend upward.

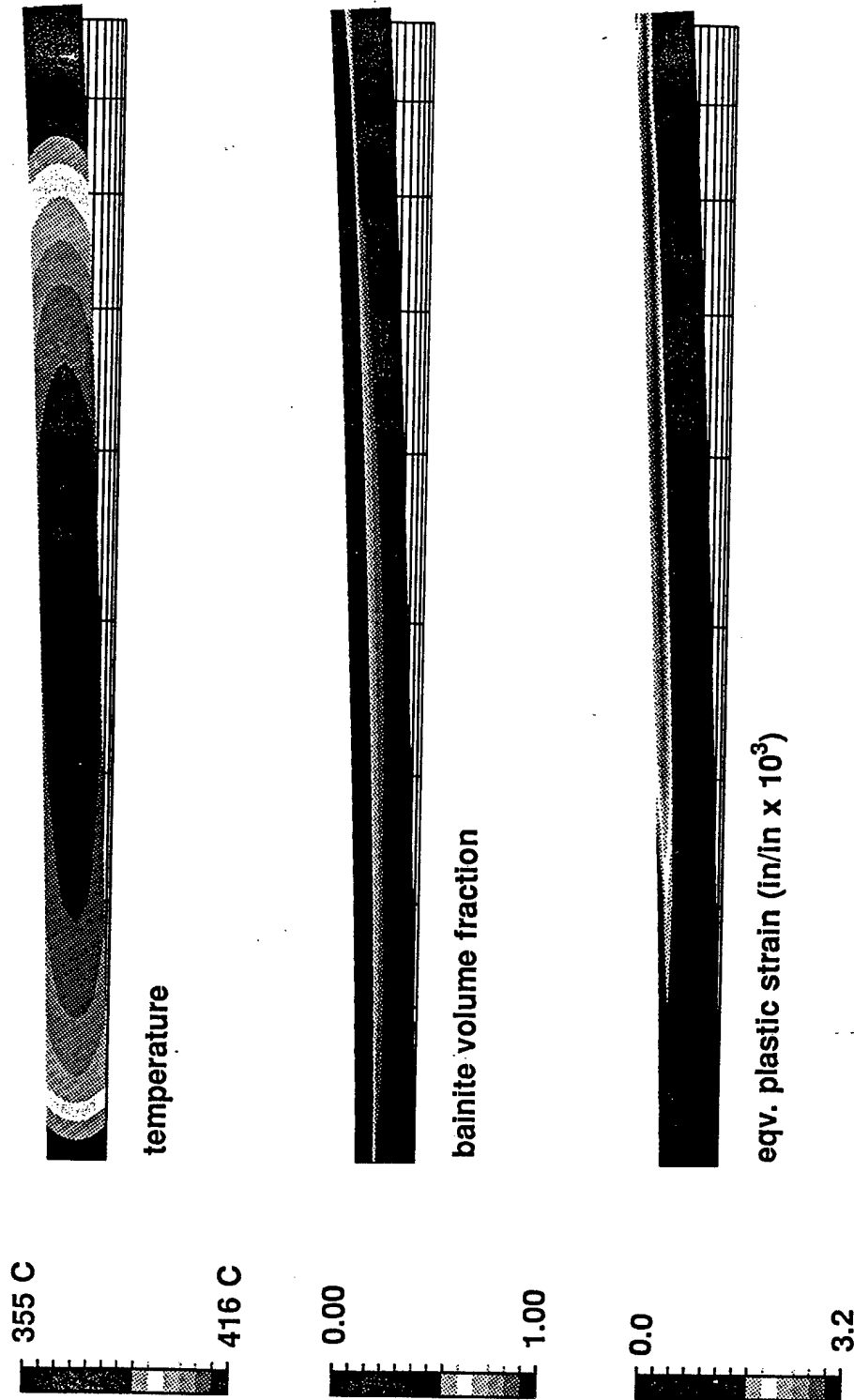


Figure 39. Contours of temperature, bainite volume fraction, and equivalent plastic strain superposed on the deformed mesh for a later time at which the bainite transformation of the uncarburized region is nearing completion, and the disk is bending further upward.

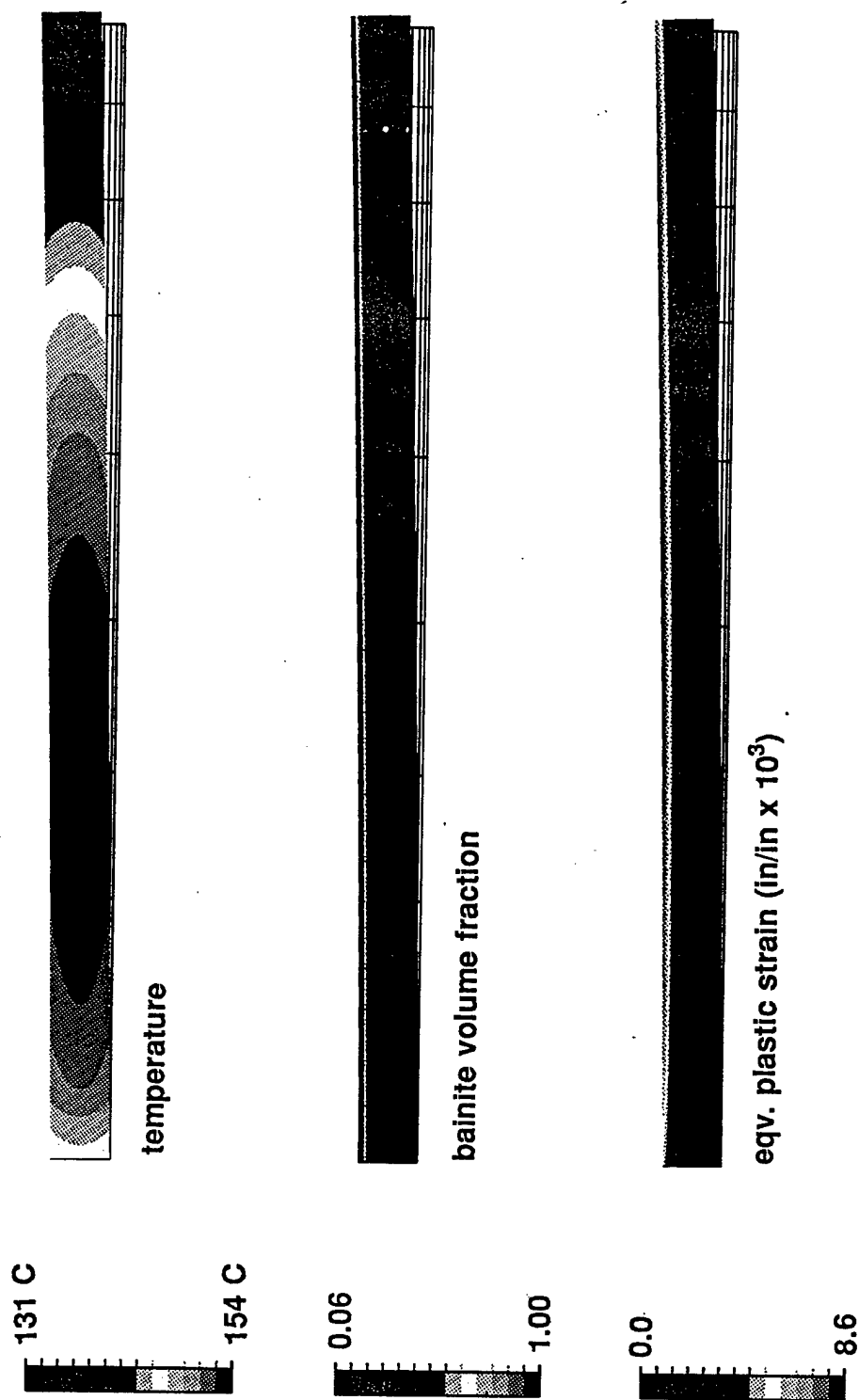


Figure 40. Contours of temperature, bainite volume fraction, and equivalent plastic strain superposed on the deformed mesh for a time at which the carburized layer has begun to transform, straightening the disk out.

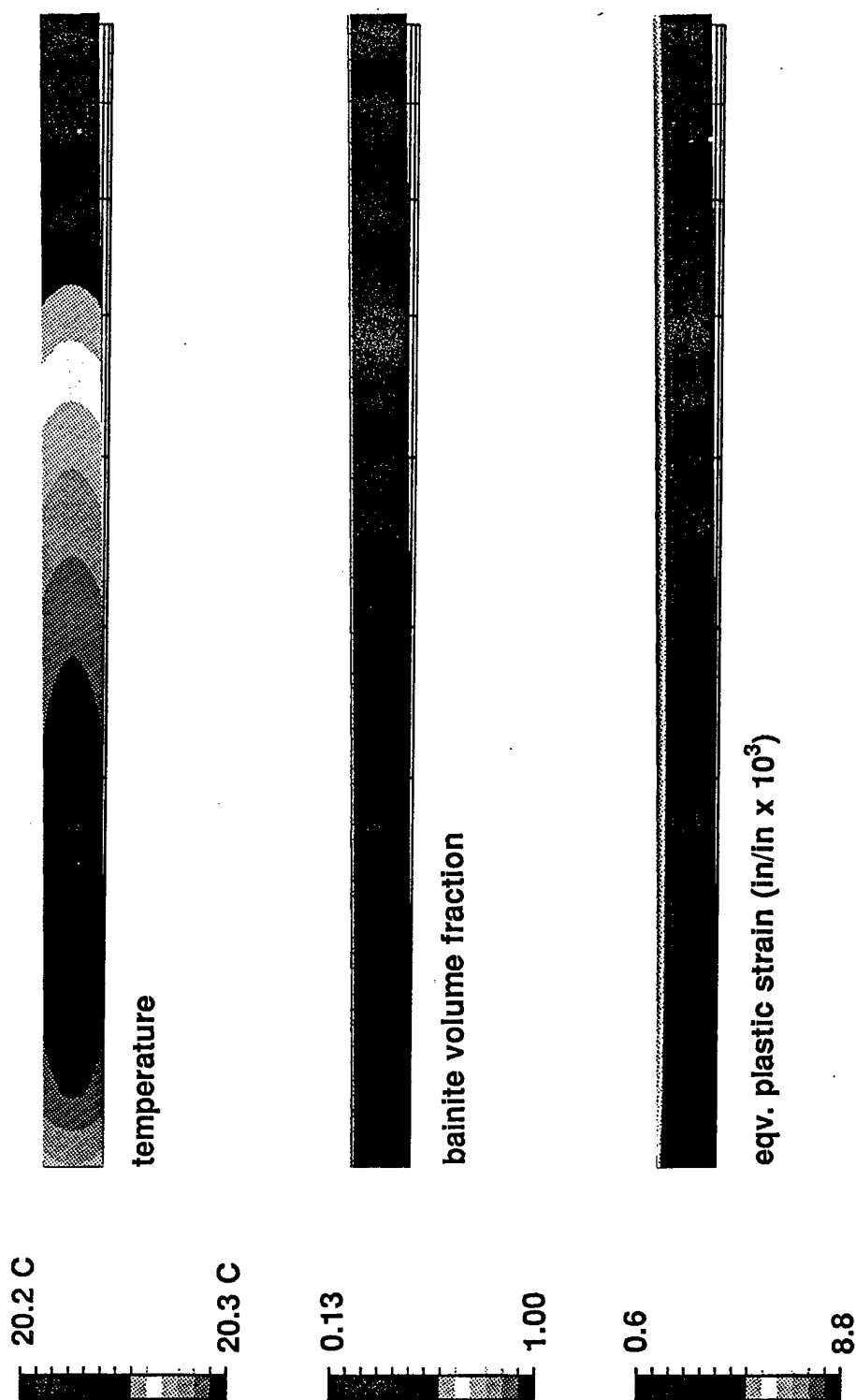


Figure 41. Contours of temperature, bainite volume fraction, and equivalent plastic strain superposed on the deformed mesh after the disk has cooled down, showing the resulting deformation, the untransformed layer, and the residual plastic strain.

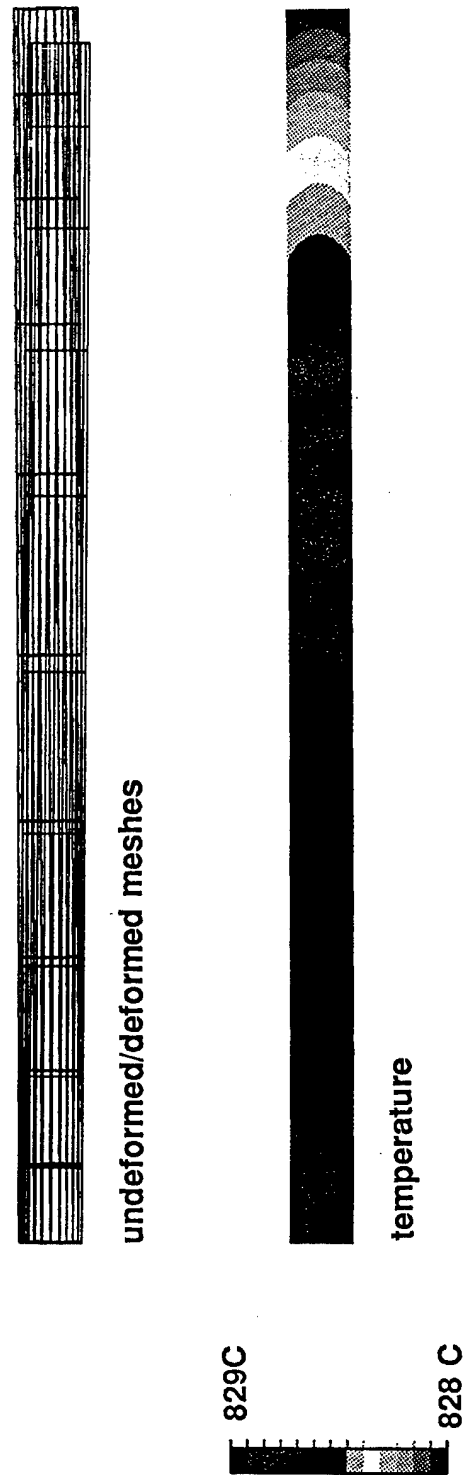


Figure 42. A comparison of undeformed and deformed meshes showing the growth and residual bending due to carburization, and a contour diagram showing the nearly uniform temperature distribution following heat-up to the austenitization temperature.

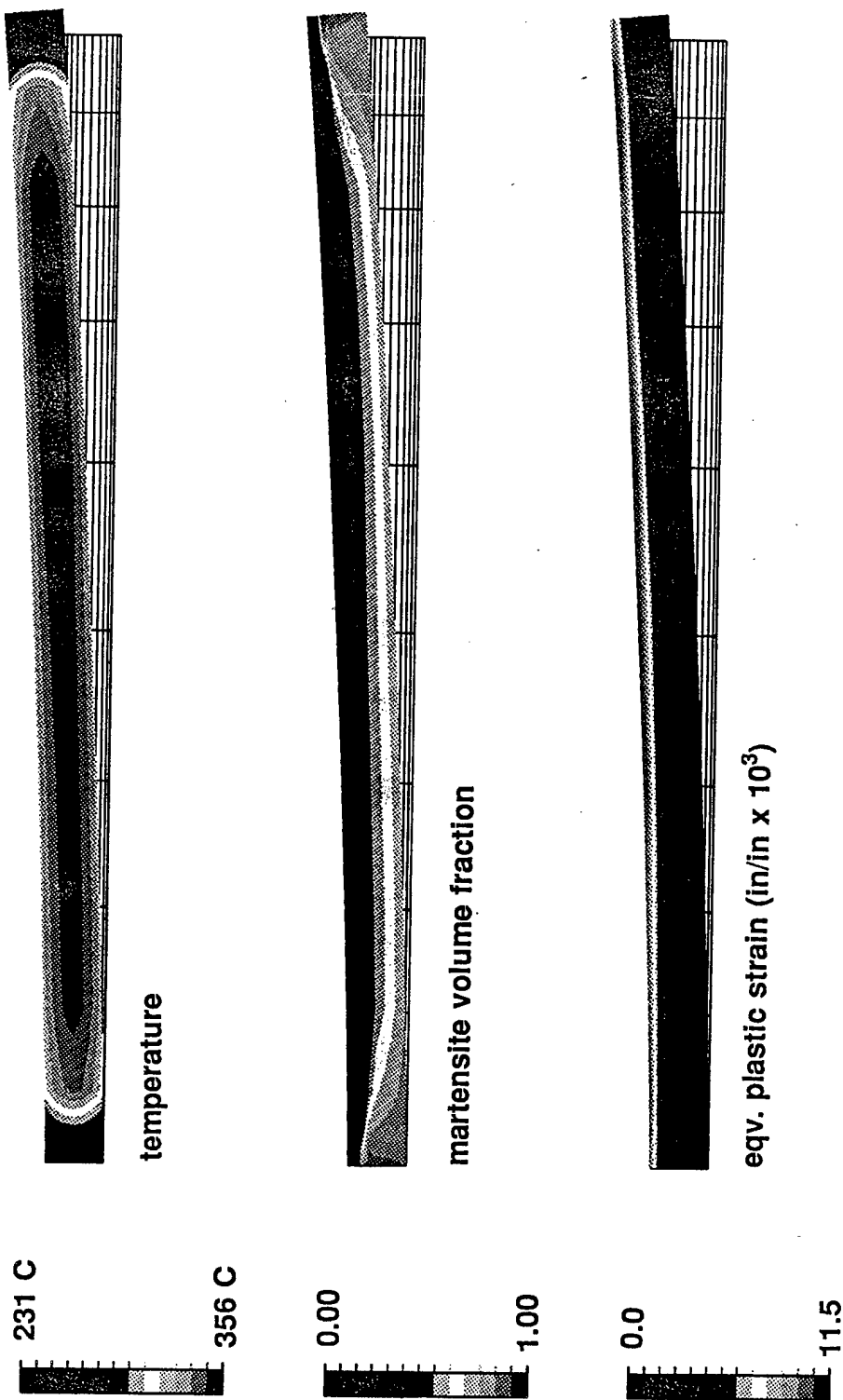


Figure 43. Contours of temperature, martensite volume fraction, and equivalent plastic strain superposed on the deformed mesh for a time just after the temperature has decreased below that for start of the martensite transformation for the uncarburized material, causing the disk to again bend upward.

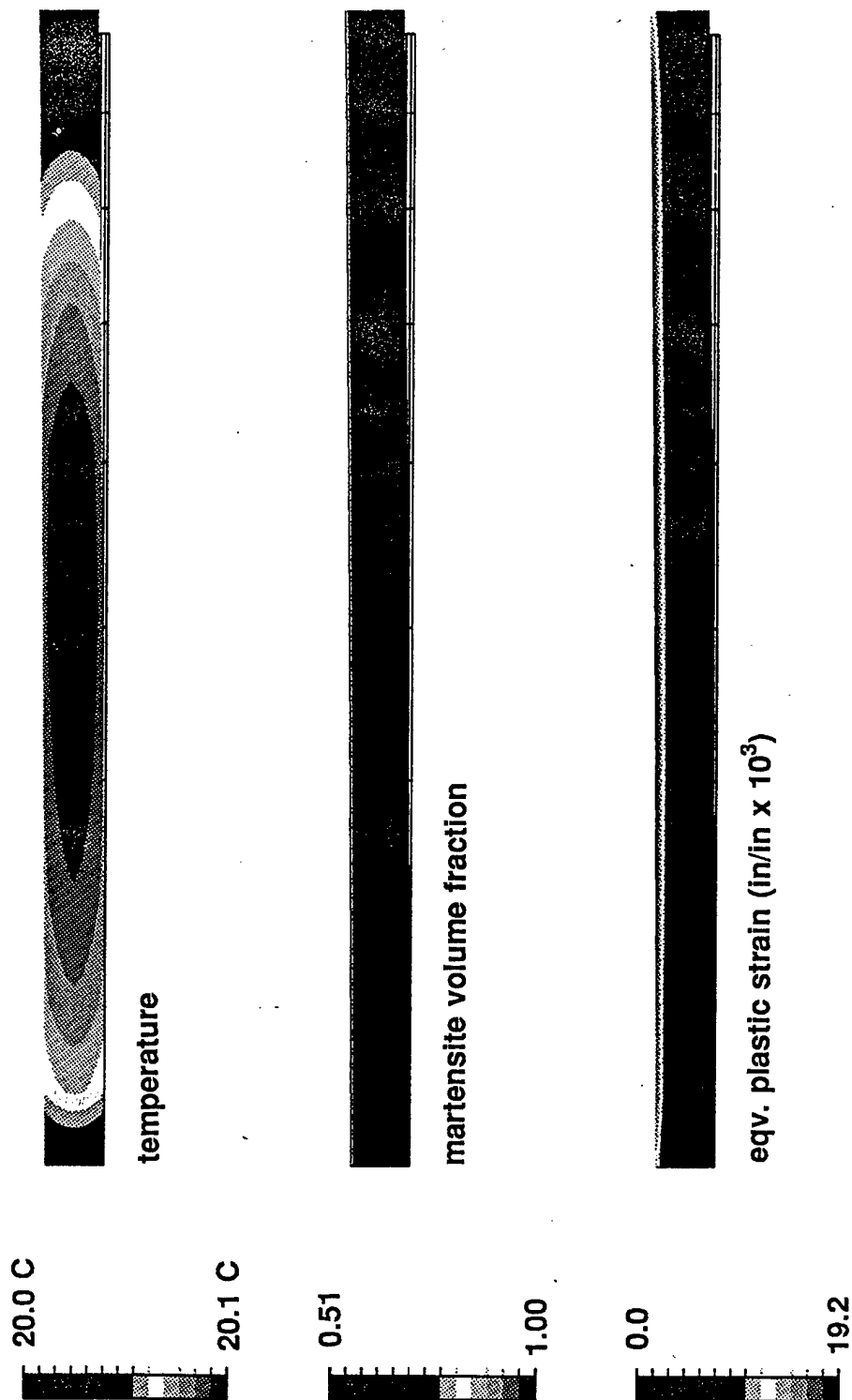


Figure 44. Contours of temperature, martensite volume fraction, and equivalent plastic strain superposed on the deformed mesh after the disk has cooled down, showing the resulting deformation, the untransformed upper layer, and the residual plastic strain.

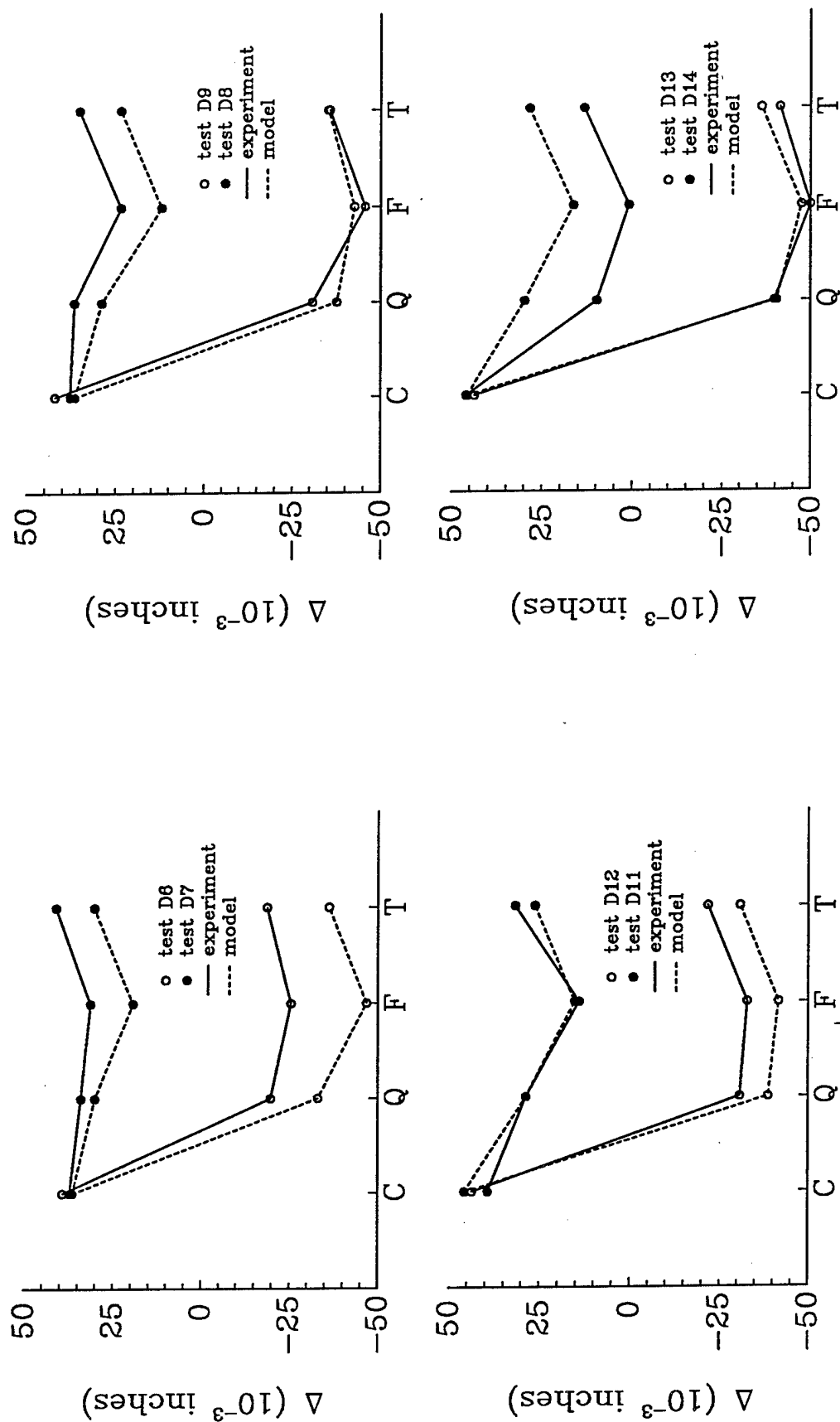


Figure 45. Comparison of model predictions for of edge distortion with averaged measured values following carburization, quench, deep-freeze and temper operations for each of the eight disks processed in the parameter study.



TABLE 10. COMPARISON BETWEEN MODEL AND EXPERIMENTAL PREDICTIONS  
FOR DISTORTION FOLLOWING CARBURIZATION, QUENCH, DEEP-FREEZE AND  
TEMPER OF THE CARBURIZED DISK SPECIMEN

	Test Conditions		Average Edge Displacement (10 <sup>-3</sup> in)									
Test	T <sub>carb</sub> T <sub>oil</sub>	T <sub>aust</sub> Agit?	Before Carb	After Carb		After Quench		After Freeze		After Temper		
				Expt.	Model	Expt.	Model	Expt.	Model	Expt.	Model	
D6	927 24	900 No	-0.3	39.2	36.4	-19.8	-33.1	-25.5	-46.8	-18.7	-36.2	
D7	927 24	830 Yes	-3.2	37.2	36.4	34.0	30.1	31.3	19.3	41.0	30.2	
D8	927 78	830 No	-1.0	37.7	36.4	36.6	28.9	23.5	12.0	35.2	23.5	
D9	927 78	900 Yes	1.0	42.0	36.4	-37.6	-30.0	-42.6	-45.6	-35.2	-35.6	
D10	944 24	830 No	3.0	39.3	45.7	28.7	28.7	14.0	15.2	31.7	26.2	
D11	944 24	900 Yes	3.5	43.7	45.7	-30.7	-38.7	-32.8	-41.6	-21.8	-30.8	
D12	944 78	900 No	1.0	43.7	45.7	-39.8	-40.4	-50.6	-47.5	-41.4	-36.2	
D13	944 78	830 Yes	0.0	46.0	45.7	9.8	29.8	0.9	16.3	13.3	28.4	

As is summarized in Table 11 below, from a statistical viewpoint, model and experiments are not in agreement in revealing significant parameters.

TABLE 11. A COMPARISON BETWEEN MODEL AND EXPERIMENTALLY DETERMINED SIGNIFICANCE OF PROCESSING PARAMETERS ON DISTORTION AFTER QUENCH AND DEEP-FREEZE

	Significant?			
	Experiments		Model	
Parameter	After Quench	After Deep Freeze	After Quench	After Deep Freeze
Carb. Temp.	Y	Y	Y	N
Aust. Temp.	Y	Y	Y	Y
Oil Temp.	Y(?)	Y	N	Y
Agitation	N	N	N	Y

In particular, the model does not predict the statistical significance of the effect of carburization temperature on distortion after deep freeze and the influence of oil temperature on distortion after quench. At the same time, the model predicts a significant effect of agitation on distortion after deep-freeze that is not observed experimentally. This lack of agreement may be due to experimental set-up, rather than a deficiency in the model. Because of the large, unforeseen effect that the change in austenitization temperatures had on distortion during quench, the significance of the other parameters was overshadowed; this made it impossible to accurately assess their significance. A much better test design would have called for only a 10 C change in the austenitization temperature.

This deficiency in the experimental design notwithstanding, model predictions of:

- carburization deformation generally agree well with experiments and showed the significant effect of the carburization temperature;
- distortion during quench, deep freeze and temper were also consistent in that the direction of distortion was predicted correctly for each test.

As one might expect, model results are more consistent with averaged experimental data than with raw experimental data. Also, it is again noted that the strong effect of austenitization temperature could not be predicted without making some assumptions regarding its effect on material properties.

Overall, model predictions of distortion from carburization and quenching showed good agreement with experimental results:

- the direction of distortion is predicted correctly;
- the magnitude of carburization distortion is predicted accurately;
- the average of quench distortion values is also predicted well.

There are some outstanding issues with respect to the flat carburized disk experiment that require further exploration, including: the effect of higher austenitizing temperatures on material properties; and an explanation for the differences between model and experimental determination of significant parameters (i.e., carburization and oil temperatures).

As noted above, the experiments would likely have been more successful if: (1) a smaller change in the austenitization temperature had been used; and (2) a few more experiments to determine the effect of such a change on key material properties, namely tensile and transformation properties, were performed. In addition, because the deformation due to carburizing the disk on one side are so large (up to 80 thousandths versus a few thousandths observed for typical gear quenches), even after carburization, more data for tensile and transformation properties associated with the carburization process would have been helpful.

## APPLICATION OF THE MODEL TO A PRESS-QUENCHED GEAR BLANK

In phase II, we applied the model to the heat treatment of a gear blank with a geometry based upon a Boeing CH-46 Hydraulic Pump Drive accessory gear, which was selected primarily because it satisfied two criteria: (1) it has a rim/web type configuration that met the guidelines that were determined early in the program for selection of a gear; and (2) the press-quench tooling for this gear was made available to the program.

Gear blanks were heat treated at the Instrumented Factory (INFAC) for Gears Heat Treatment Center, in Chicago, IL, which is operated by the Illinois Institute of Technology Research Institute (IITRI). A number of gear blanks were processed through the carburization, press-quench, deep-freeze and temper steps at INFAC. Measurements of surface temperature histories, distortion, hardness profiles, and residual stresses were performed. The model was then used to simulate each of these process steps. In this section, the experimental procedure and results are described, and the modelling results are presented and compared with measured data.

### EXPERIMENTAL PROCEDURE

#### The Rim/Web gear.

The rim/web gear blank is pictured schematically in Figure 46. In order to keep the geometry simple, gear teeth were not machined into the blank prior to heat treating. A simple geometry has several advantages: model calculations are less computationally intensive; model predictions are easier to interpret; variation in surface heat transfer coefficients are less severe. The thickness of the web, 0.15 inches (3.81 mm), was chosen to be representative of a near net-shape dimension, i.e., one that requires minimum stock removal following heat treatment. Current trends in helicopter gear manufacturing appears to be favoring such a near net-shape dimension approach, which is advantageous in that it eliminates much of the post-heat treat machining time and cost, but which is also one that is more dimensionally unstable and therefore more difficult to control.

#### Processing Specifications

The gear blanks were carburized in three locations, as indicated in Figure 46 — at the outside edge of the rim, where there would normally be teeth, and along journal bearing surfaces of the shaft, just above and below the rim.

A total of four gear blanks were heat treated in this study. Each of these gear blanks (RW1, RW2, RW3 and RW4) was carburized. Three of these (RW2, RW3 and RW4) were subsequently quenched and deep-frozen. Finally, two of the three hardened gears (RW3 and RW4) were tempered. An additional gear blank was instrumented and heat treated through quench in order to generate surface temperature data for calibration of the simulation model.

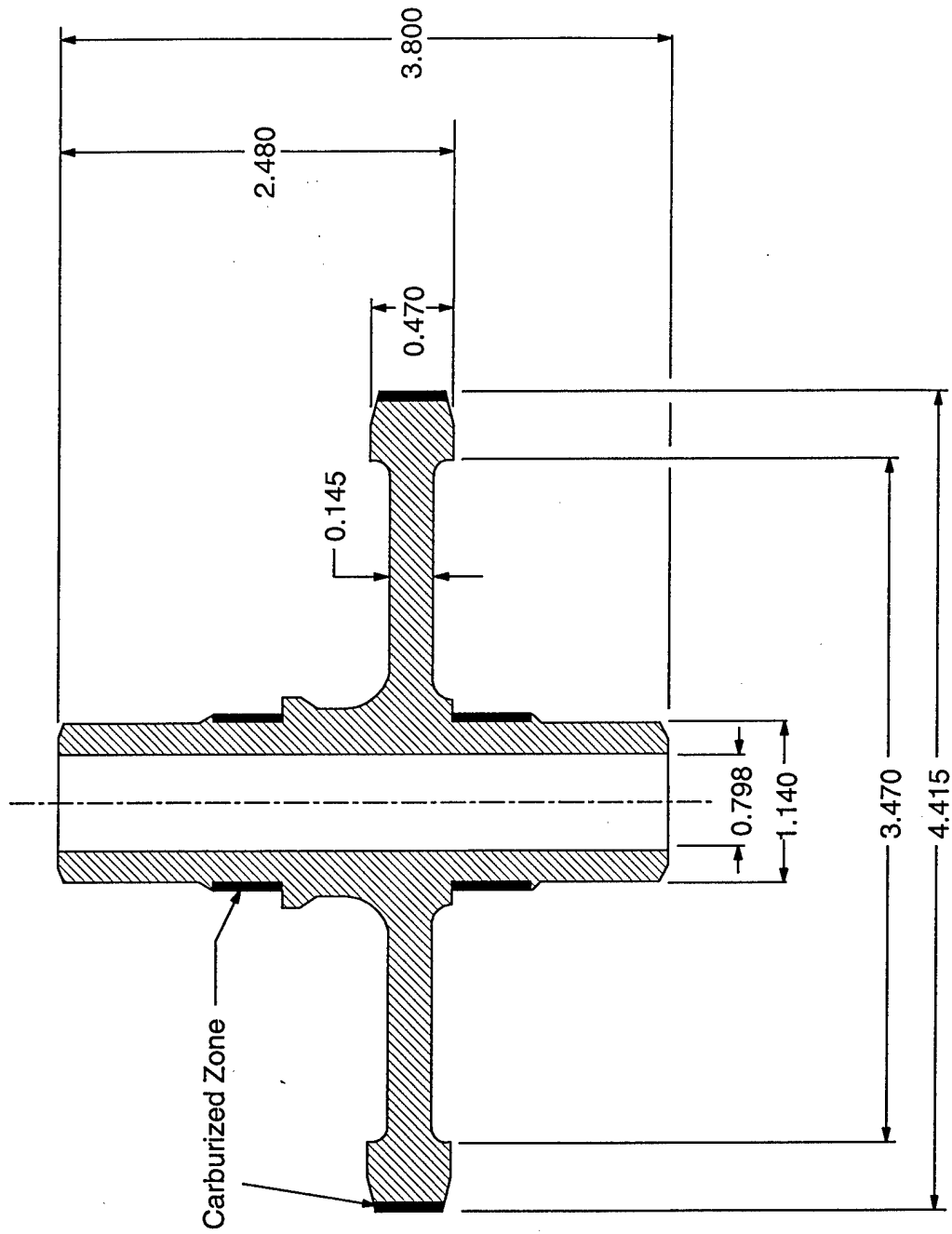


Figure 46. A schematic of the rim/web gear blank with carburized regions indicated (units are in inches).

The gear blanks were generally processed according to Sikorsky gear heat treatment specifications. The processing steps spelled out in this specification include the following operations:

- copper plating of all surfaces;
- carburization at 1700 F (927 C) in a 0.95 to 1.00 percent carbon endothermic gas for a time sufficient to produce the desired case depth (in this case 3 hours and 15 minutes for a case depth of 0.032 to 0.036 inches);
- stripping of copper plating;
- re-copper plating of entire gear blank;
- austenitization at 1525 F (829 C) for 1 hour per inch of cross-section;
- quench in a Gleason 537 press with flowing oil at 80 F (26 C).
- deep-freeze at -110 F (-79 C) for a minimum of one hour;
- tempering at 300 F (149 C) for 2 hours.

### The Quench Press

A Gleason model 537 press was used to constrain the gears during quench. A schematic illustrating the tooling configuration is shown in Figure 47. Prior to quench, the gear blank is placed onto a cylindrical die, with an outside diameter of about 6 inches (15.2 cm) and an inside diameter of about 1.5 inches (3.8 cm) (Figure 48). The underside of the rim is supported on the top surface of this die component, while the shoulder of the lower part of the shaft is supported on a ledge which protrudes from the inside surface of the cylinder. Each of these die surfaces has a number of channels cut into them to allow oil flow. The die has a number of radial holes which allow oil to flow from the outer reservoir into this central section and onto the surface of the lower part of the shaft and the underside of the web. The top surface of the rim is constrained by another cylindrical piece which fits over it (see Figures 47 and 48). This piece is connected at its top to a ram which applies downward pressure during quench. Similarly, the top of the shaft is constrained with a small cylinder (expander) that is connected to a second, independently controlled ram.

The lower die rests on a table that is free to slide in and out of the press. Following austenitization, the gear blank is first placed onto the lower die. The table then slides back into the press, whereupon the upper die and expander are brought into contact with the part and the hydraulic pressure is applied. The hydraulic pressures are adjusted so that the outer die applies a 6000 lb. force (26,400 N) to the outer die and a 500 lb force (2200 N) to the expander. For the contact area of these dies, this represents an applied constraining pressure of 18.3 MPa acting on the rim and 13.3 MPa acting on the shaft. The capability exists for pulsing these pressures, which reduces friction caused by constant pressure and clamping of the component as it contracts during cooling. A pulsing technique was not, however, used in these experiments.

Once the gear blank has been placed into the die, and the table has slid back into the press, oil flow is turned on. An initial oil flow rate of 620 gallons per minute is used for the first 10 seconds in order to rapidly fill the reservoir and bring the temperature of the gear down through the transformation range as quickly as possible. A much lower rate of 130 gallons per minute is used for the next minute in order to allow the temperature of the outer surface of the gear and of the core to equalize, with a minimum build-up of residual stresses.

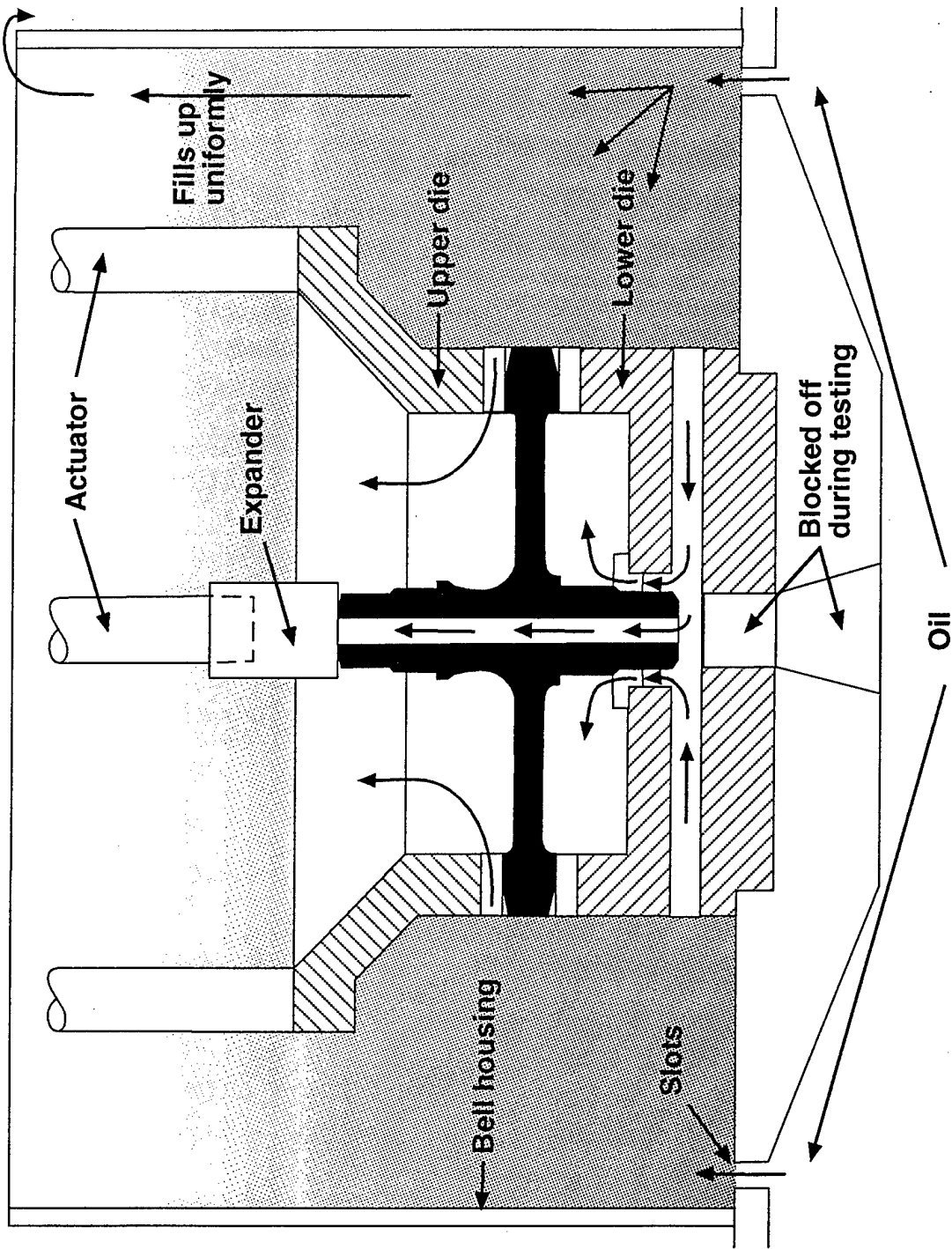


Figure 47. Tooling configuration for the press quench operation.



Figure 48. The lower die.



Finally, when the transformation is nearly complete, a faster rate of 370 gallons per minute is used for the next three minutes to rapidly bring the gear blank down to a temperature at which the operator can handle it.

### Measurements

Surface Temperature Measurements A single gear was instrumented with eight thermocouples (TC1 — TC8) for evaluation of surface temperature histories during quench. A schematic indicating thermocouple placement is shown in Figure 49. Six of the eight thermocouples were placed at the top and bottom surfaces of the web (three at the top surface and three near the bottom surface, each of the three placed 120 degrees apart). The remaining two thermocouples were placed near the outer surface of the shaft—one near the top of the gear blank and one near the bottom. In each case the thermocouple was spot welded to the surface. The instrumented gear is pictured in Figure 50. It was first austenitized, and upon its removal from the furnace, the eight thermocouple leads were quickly connected to the data acquisition device. A trigger for recording temperature was set so that measurement commenced when one of the thermocouples first reached 1500°F. Temperatures were then recorded at a rate of 10 Hz during the quench process for a period of about 40 seconds.

Dimensional Measurements Dimensional measurements were made at several locations on the surface of the gear blank using a coordinate measuring machine (CMM). Dimensional measurements were performed at the following stages of the heat treat process:

- prior to carburization;
- following carburization;
- following deep-freeze;
- following temper.

A schematic indicating the measurement locations is shown in Figure 51. Measurements were made at a total of 54 locations on the gear blank. In addition, the thickness of the web and the length of the shaft were measured at six locations each using calipers. Five measurements of radial position were taken along the outer edge of the shaft and the rim (points 1, 2, 3, 8 and 9 in Figure 51). Four measurements of axial position were made along the underside of the web and the rim (points 4, 5, 6 and 7 in Figure 51). Each of the measurements were made with respect to a reference position indicated by a scribe mark placed on the top end of the shaft.

Hardness Measurements Following the final processing step, the three gears that underwent hardening were subjected to hardness profile measurements at Arthur D. Little using a microhardness indenter. These measurements were obtained in order to help determine the variation of carbon content under the surface of the rim. These data were generated using a microhardness tester, with a 500 g indentation load; measurements of Knoop hardness were recorded and later converted to Rockwell C hardness. A radial profile of data was obtained near the surface of the rim, with data collected every 0.005 inches to a depth of 0.040 inches. Hardness measurements were not made near the journal bearing surfaces.

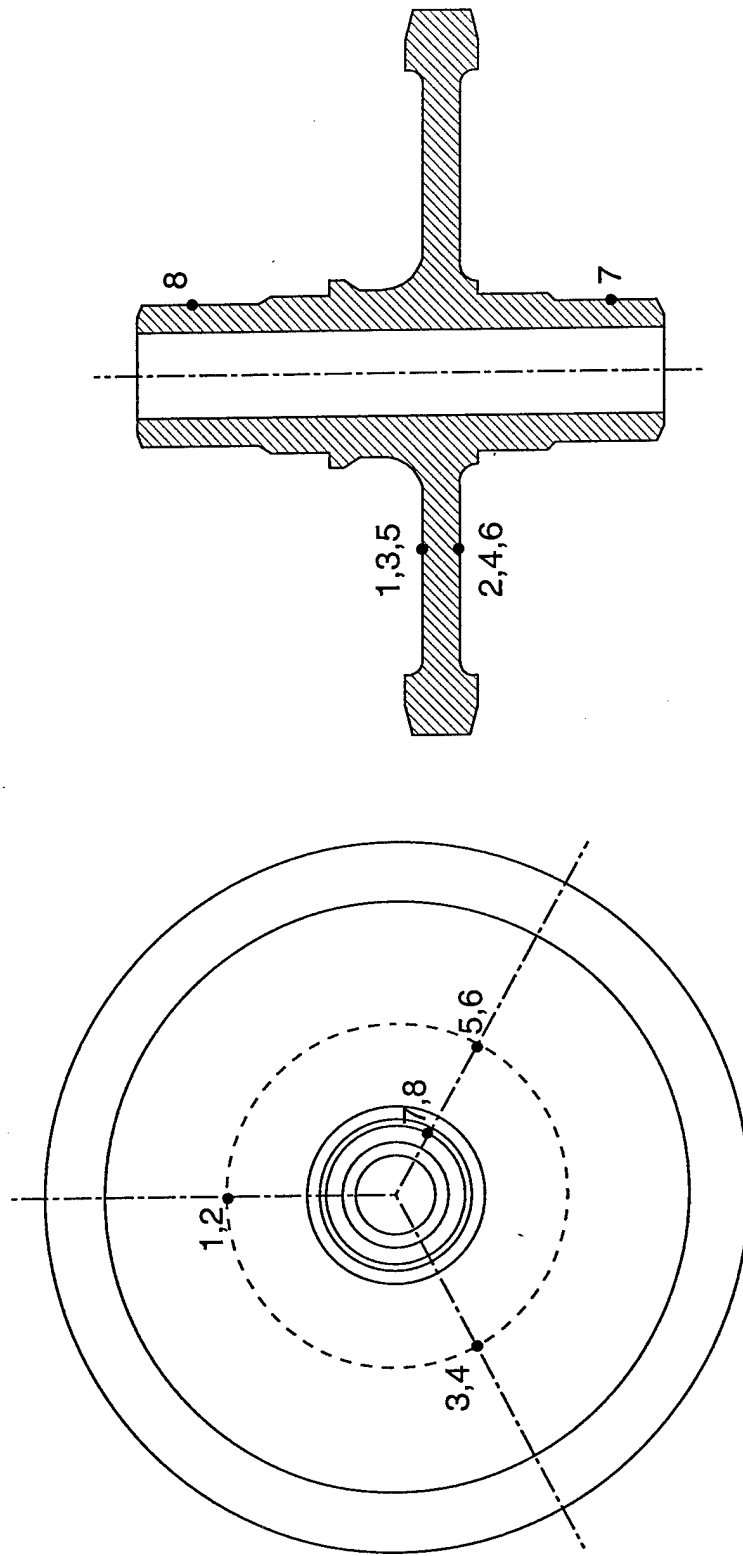


Figure 49. Thermocouple placement for measurement of surface temperature histories.

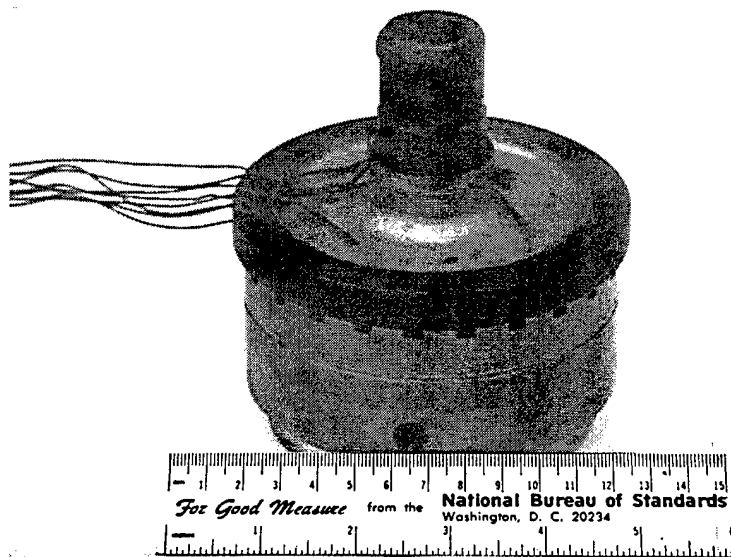


Figure 50. The instrumented gear.

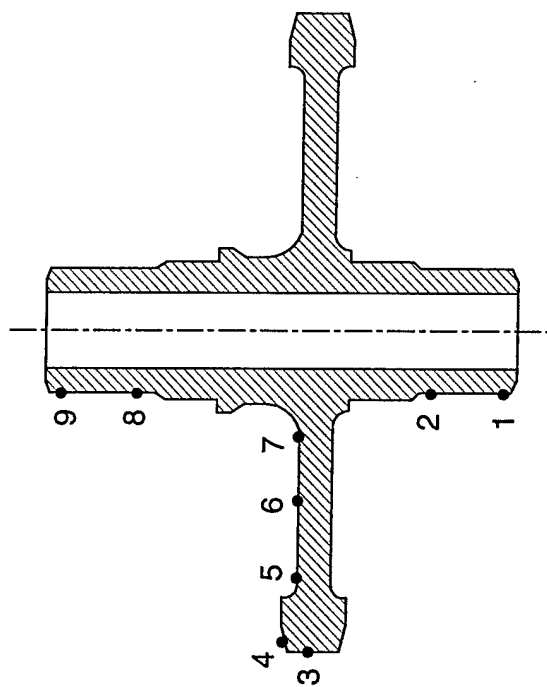
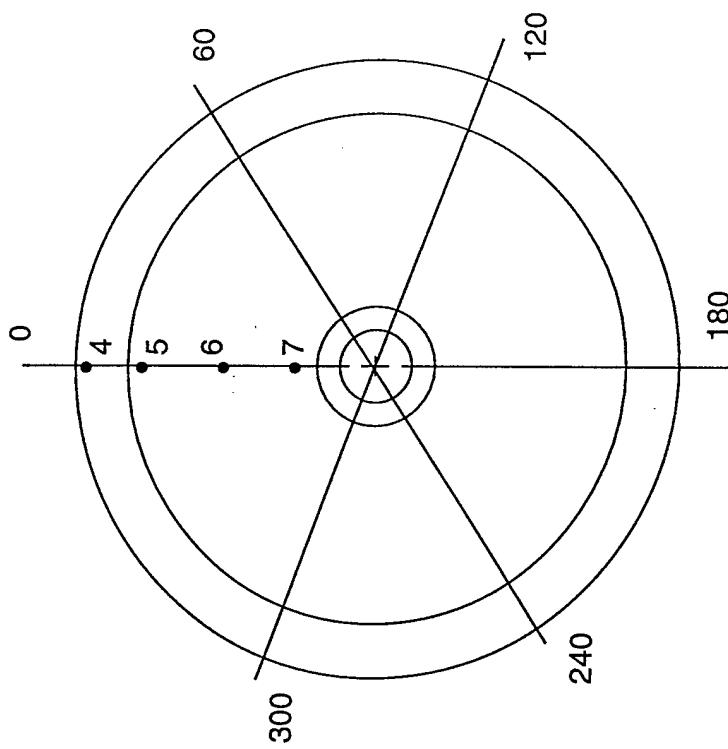


Figure 51. Dimensional measurement locations.

Residual Stress Measurements Residual stress measurements were made using an x-ray diffraction technique for one of the gear blanks processed through the quench operation (RW2) and one of the gear blanks processed through temper operation (RW3). For each of these two gear blanks, measurements of residual hoop stress were made at the center of the outside edge of the rim at three circumferential locations (0, 120 and 240 degrees). For the gear processed through deep-freeze, an additional four measurements of radial residual stress were made along one of the gear diameters—two of which were made about 0.1 inches out from the shaft and two of which were made about 0.1 inches in from the rim.

## EXPERIMENTAL RESULTS

### Surface Temperature Histories

Surface temperature data, averaged for each thermocouple over up to six experiments, are plotted in Figure 52. Not all thermocouples recorded data properly for each experiment. The number of valid data sets for each of the thermocouples is indicated on the figure. As is evident from Figure 52, the temperature varies considerably from point-to-point on the gear blank. In particular, it appears that the temperature at the two locations on the shaft (TC 7 and TC 8) cool-down faster than those on the web. The fact that TC 8, which is located near the bottom of the shaft, cools down more quickly than the others is consistent with the fact that the oil level is rising from the bottom at a rate of approximately two inches (5 cm) per second. The early drop in temperature at TC 7, which is near the top of the shaft, is more puzzling since the oil does not reach this point until about one second after it contacts the thermocouples on the web. This rapid drop in temperature may, however, be due to a level of heat transfer from the top of the shaft to the expander that is more extensive than our experiments would lead us to believe. It should be noted that TC 8 did not function properly for all of the tests — it produced usable data in only the first two of the six experiments.

In order to more clearly distinguish differences between temperature histories on the top and bottom of the web, data from TC 1, TC 3, and TC 5 (bottom surface of the web) and data from TC 2, TC 4, and TC 6 (top surface of the web) were averaged over the first two runs (the only two in which all six thermocouples functioned properly). These data are plotted in Figure 53. Although the two curves in this figure are close together, they indicate that the top surface of the disk is cooling faster than the bottom surface. The maximum temperature difference between the two surfaces appears to be about 100 °C. This difference in temperature is consistent with the fact that oil is able to rise freely away from the top surface of the web, but can get trapped on the underside of the web.

Temperature recordings for each of the eight thermocouples are given in Appendix C. Inspection of data from the controlling thermocouple (TC 2) in Figure 54, reveals that the temperature can vary a few hundred °C from test-to-test.

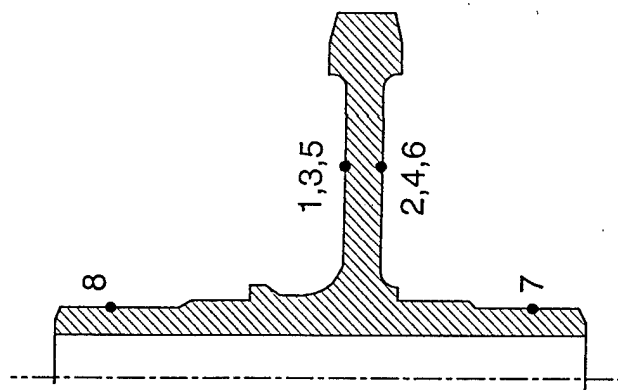
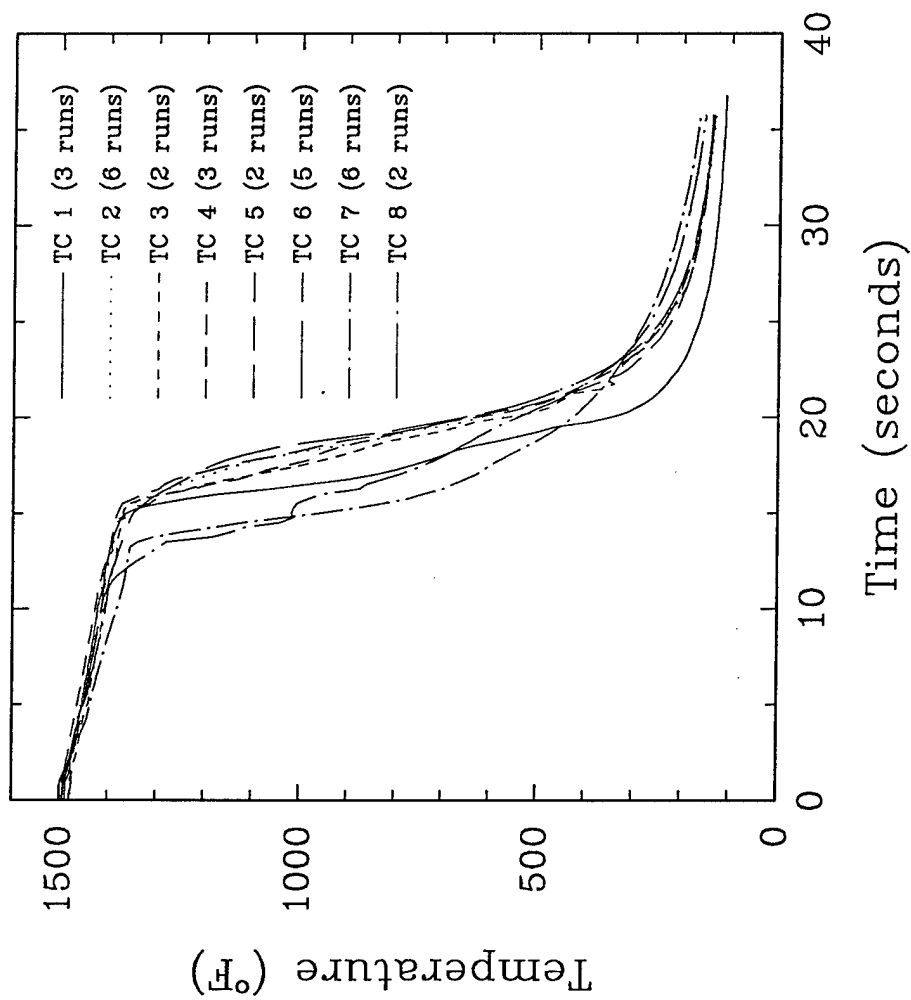


Figure 52. Averaged measured temperature histories. The number of valid data sets for each thermocouple are indicated in parentheses. Oil flow commenced at about 15 sec.

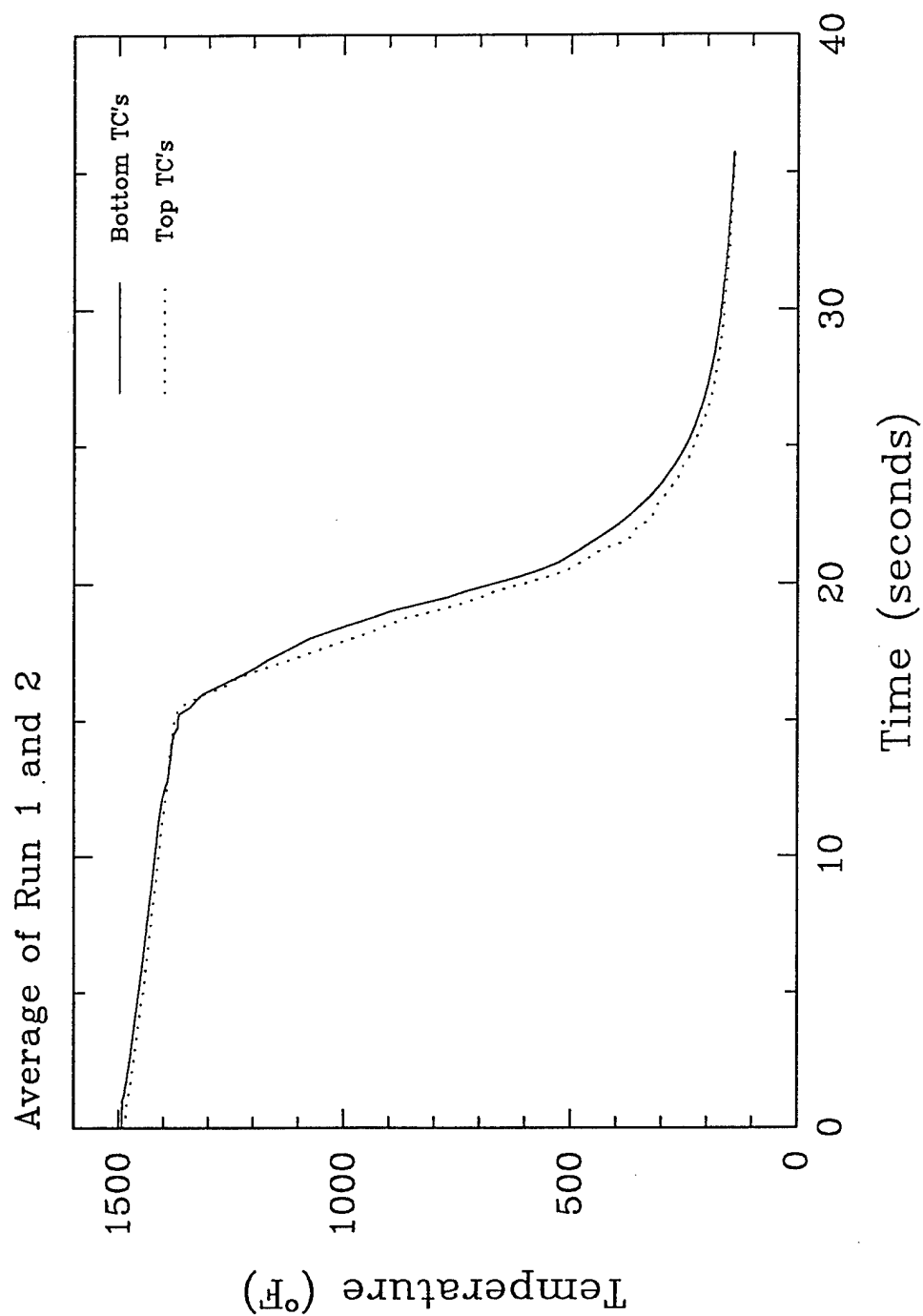


Figure 53. Comparison of averaged measured temperature histories between top and the bottom of the web.

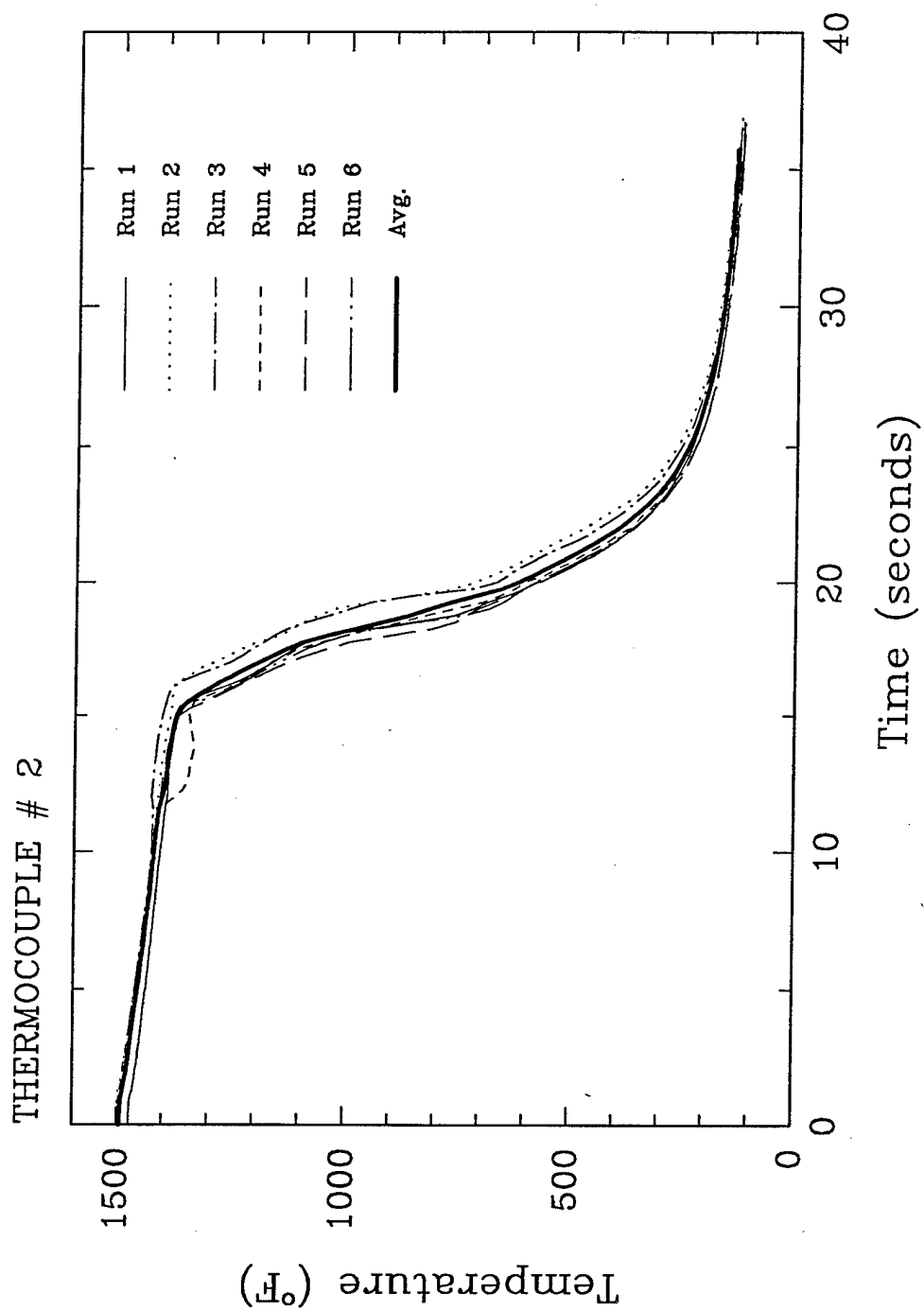


Figure 54. Measured temperature history at thermocouple TC2 for each of the six tests.



## Distortion

Distortion measured after carburization, quench/deep-freeze and temper are summarized below. The complete set of measured distortion data is given in Appendix D along with calculated averages and standard deviations.

Carburization distortion Average distortion following carburization for the four carburized gear blanks is given in Table 12 below and pictured in Figure 55. As evidenced from this data, carburization was minimal (typically less than 0.001 inches). The large magnitude of the standard deviations relative to the averages suggests that this data contains little deterministic information and instead reflects mostly stochastic variation. Only the change in length of the gear blank appears to be statistically significant.

TABLE 12. AVERAGE DISTORTION FOLLOWING CARBURIZATION

measurement location	average distortion ( $10^{-3}$ in)	standard deviation ( $10^{-3}$ in)
1.	0.6	0.3
2.	0.3	0.4
3.	0.8	0.6
4.	0.3	0.5
5.	0.3	0.5
6.	0.2	0.4
7.	0.1	0.3
8.	0.3	0.4
9.	0.4	0.4
shaft length	1.7	0.3
web thickness	0.2	0.3

Quench/deep-freeze/temper distortion For gear blanks RW2, RW3 and RW4, distortion was measured again after the final processing step (deep-freeze for RW2, temper for RW3 and RW4). For each of these gears, it is highly likely that most, if not all, of the distortion occurred during the quench operation, because the temperatures associated with deep-freeze and temper are too low to produce significant plastic deformation, and because the volume changes associated with further martensitic transformation (deep-freeze) and formation of carbides (temper) are limited to a very small region (the carburized zone). Average distortion measured after deep-freeze/temper is given in Table 13 and is depicted

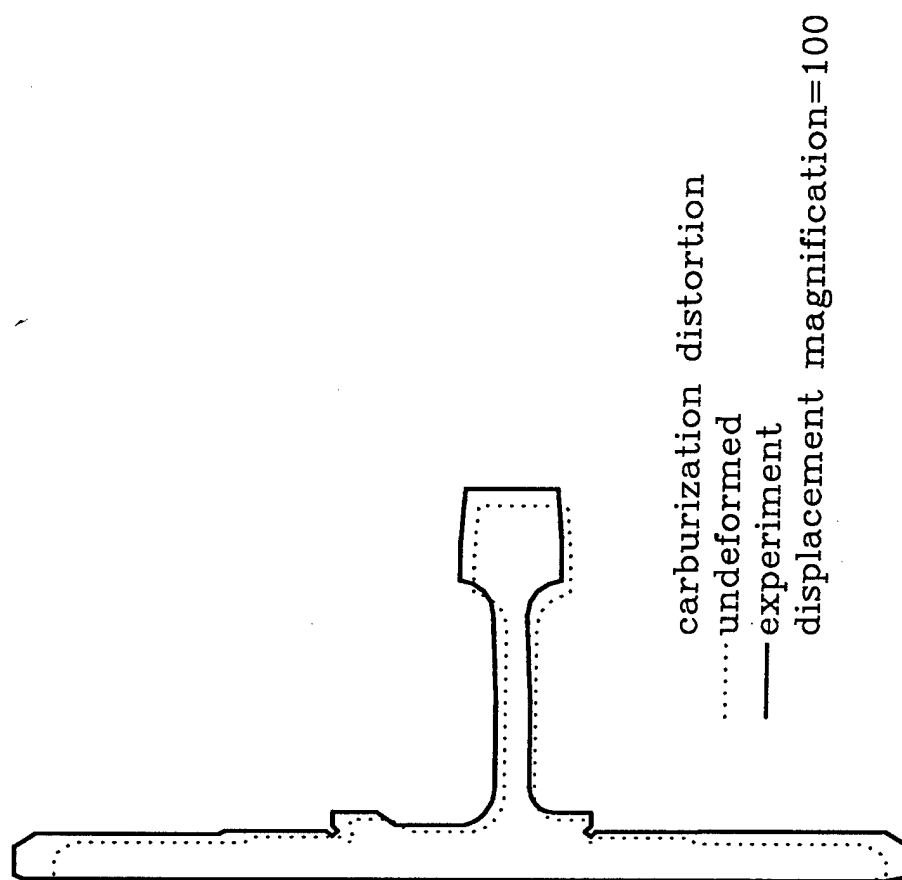


Figure 55. Average measured distortion following carburization.

graphically in Figure 56. Distortion measured following these process steps was more substantial than that measured following carburization. The standard deviations for these distortion measurements were also quite large. This can be attributed to the large circumferential variation in the distortion pattern. Figure 57 shows distortion following deep-freeze at each of the six measurements angles for gear blank RW2. As this figure shows, for some angles the web is bent upward following deep-freeze, and for other angles the web is bent downward.

TABLE 13. AVERAGE DISTORTION FOLLOWING DEEP-FREEZE

measurement location	average distortion ( $10^{-3}$ inches)	standard deviation ( $10^{-3}$ inches)
1.	0.2	0.2
2.	0.6	0.4
3.	3.9	1.1
4.	4.3	5.6
5.	-1.3	6.0
6.	-1.0	3.4
7.	-0.3	1.0
8.	0.1	0.7
9.	0.0	0.9
shaft length	0.4	0.7
web thickness	0.9	0.9

An explanation for this unusually large variation in axial displacement was gained by means of examining the heat treated gear blank. As is shown in Figure 58, there is a clear pattern of indentations on the shoulder on which the shaft was supported during quench. These indentations were most pronounced at one angle of orientation, and became progressively smaller moving from this angle around the disk; they were not visible at all on the opposite side of the disk. Such a pattern is clearly indicative of an irregularity in the support of the gear blank during quench. Subsequent discussions with IITRI indicate that there were problems with the pressure control of the inner ram that led to axial load magnitudes that were much greater than the desired values; these high axial loads were almost certainly the source of the indentation problem.

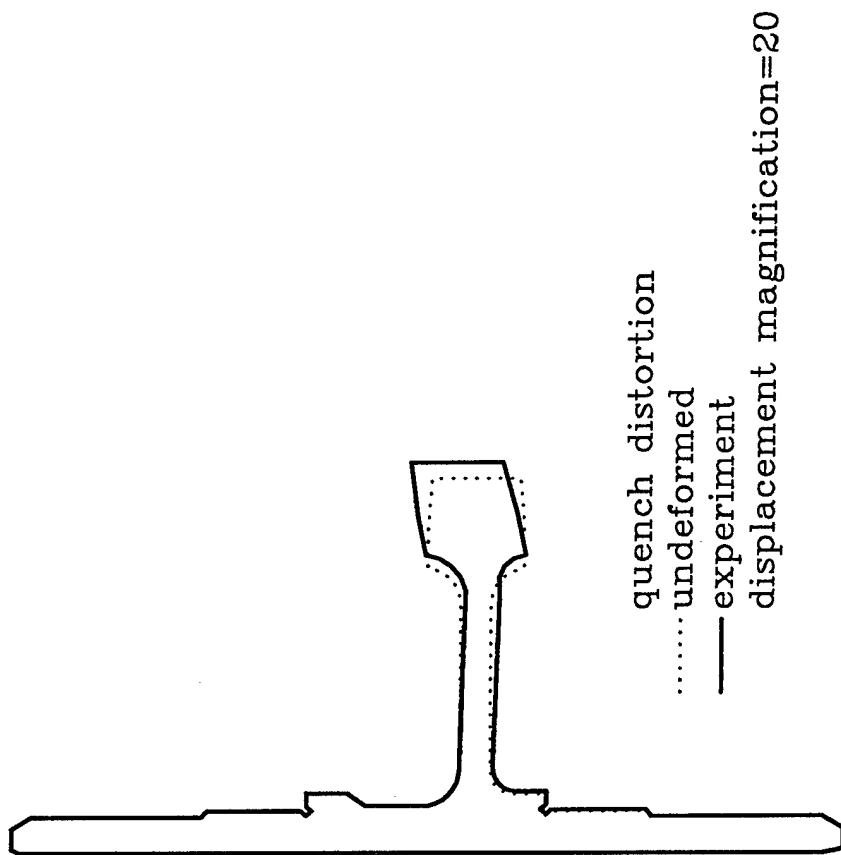


Figure 56. Average measured distortion following deep-freeze/temper.

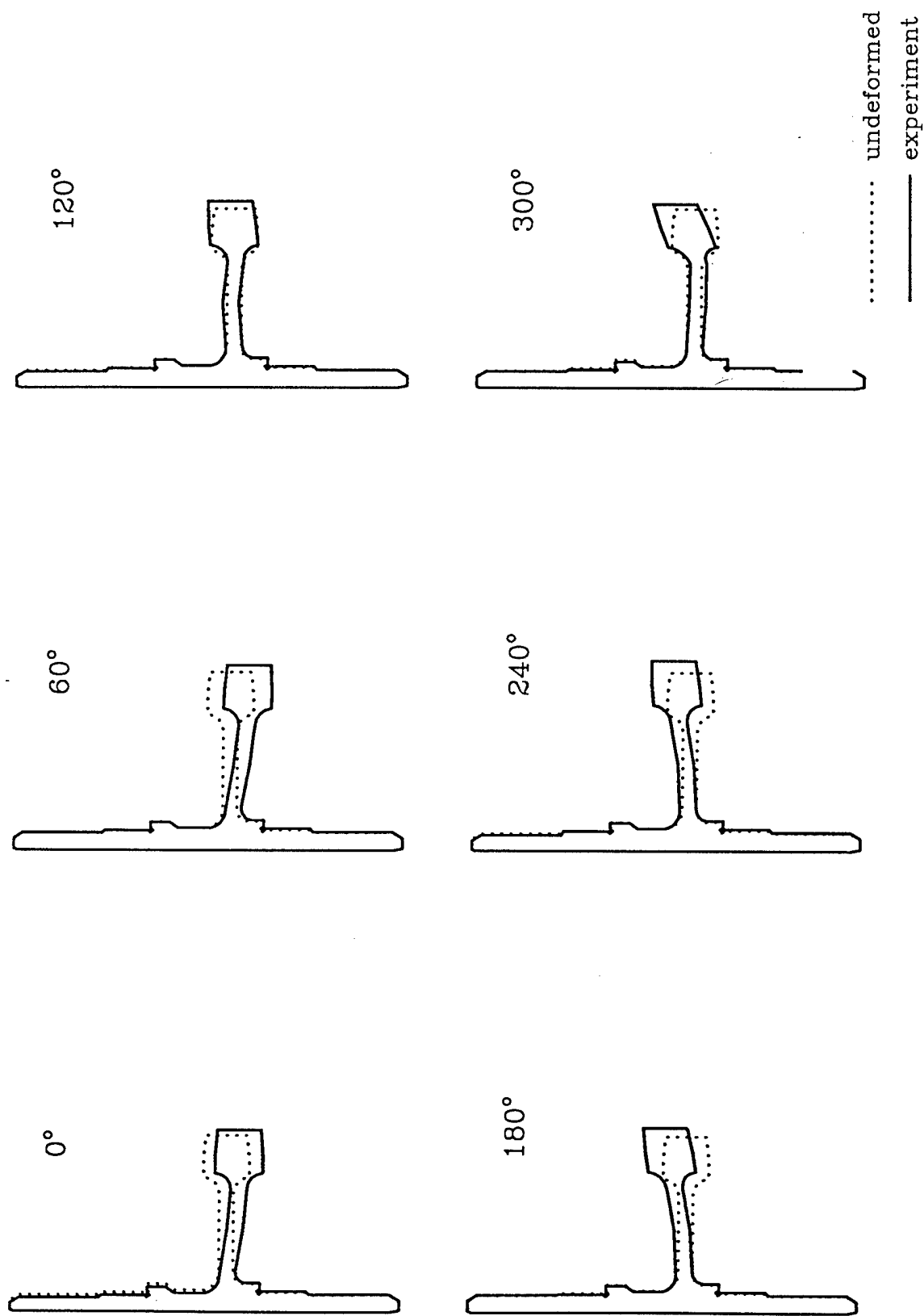


Figure 57. Variation of measured distortion around the circumference following deep-freeze for gear blank RW2.

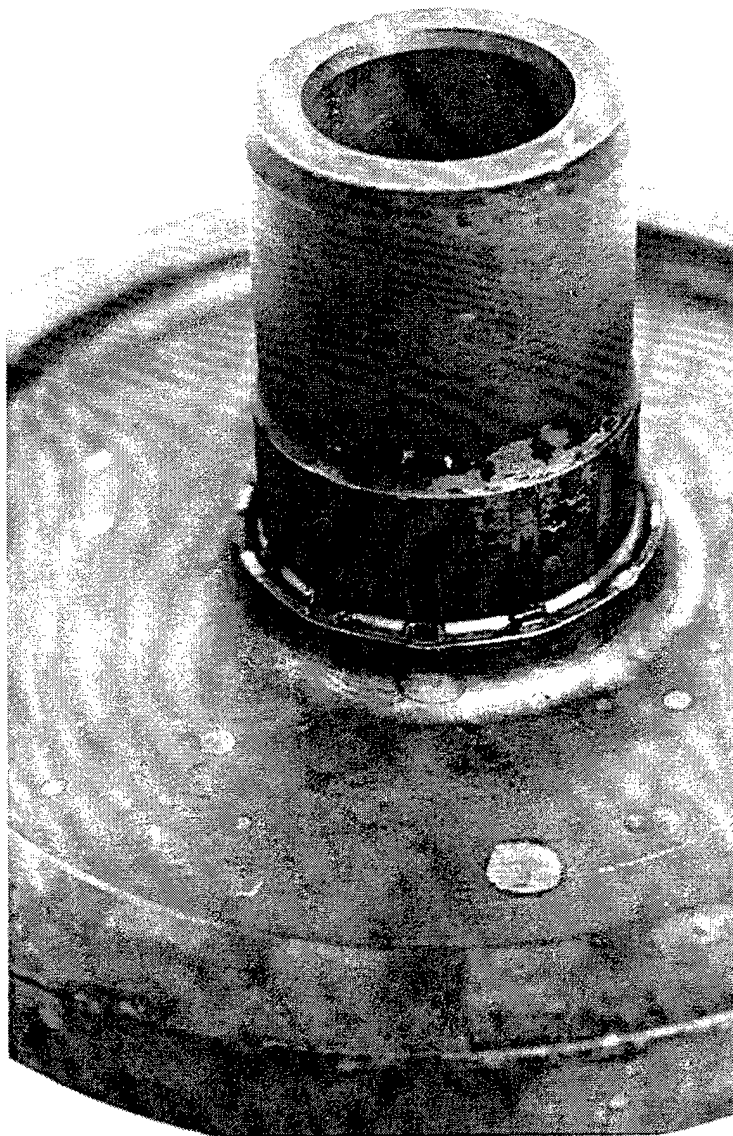


Figure 58. Indentation pattern along support shoulder of lower part of shaft following quench.

It should be noted that, for each gear blank, the angle with the most indentation corresponds to the angle with the greatest positive web distortion. These positive web distortion values are consistent with the tendency for the tilting of the shaft to force the web to move closer to the top of the shaft.

Hardness Measurements Hardness measurements, shown in Figure 59, demonstrate consistent carbon diffusion patterns. They indicate that a case depth of approximately 0.038 inches was achieved (versus a target of 0.032 to 0.036 inches). These data also show that the hardness did not change appreciably during the tempering operation. This is consistent with the use of a relatively low tempering temperature of 150 C.

Residual Stress Measurements Residual stress data are summarized in Table 14. Circumferential residual stress measured after deep-freeze for RW2 is about -36 ksi (-250 MPa) and varies little around the disk. The fact that these data are compressive is consistent with the high level of carbon at the surface of the disk. Circumferential residual stress measured after temper vary a little more — from -24.6 ksi (-170 MPa) at 120° to -29.3 ksi (-200 MPa) at 0°. The lower magnitude of the residual stresses after temper are consistent with the negative volume change associated with carbon coming out of solution to form carbides.

Radial residual stress along a diameter across the web vary from +17.5 ksi (120 MPa) to +30.9 ksi (210 MPa). These stresses arise from the thermal strains associated with the steep gradients in temperature that occur during the early stages of quench; they are likely made more severe by the difference in heat transfer coefficients between the top and bottom of the web. It is not clear at this juncture whether the variation in the magnitude of these stresses is significant.

A complete report regarding residual stress measurements provided by Lambda Research is given as Appendix E.

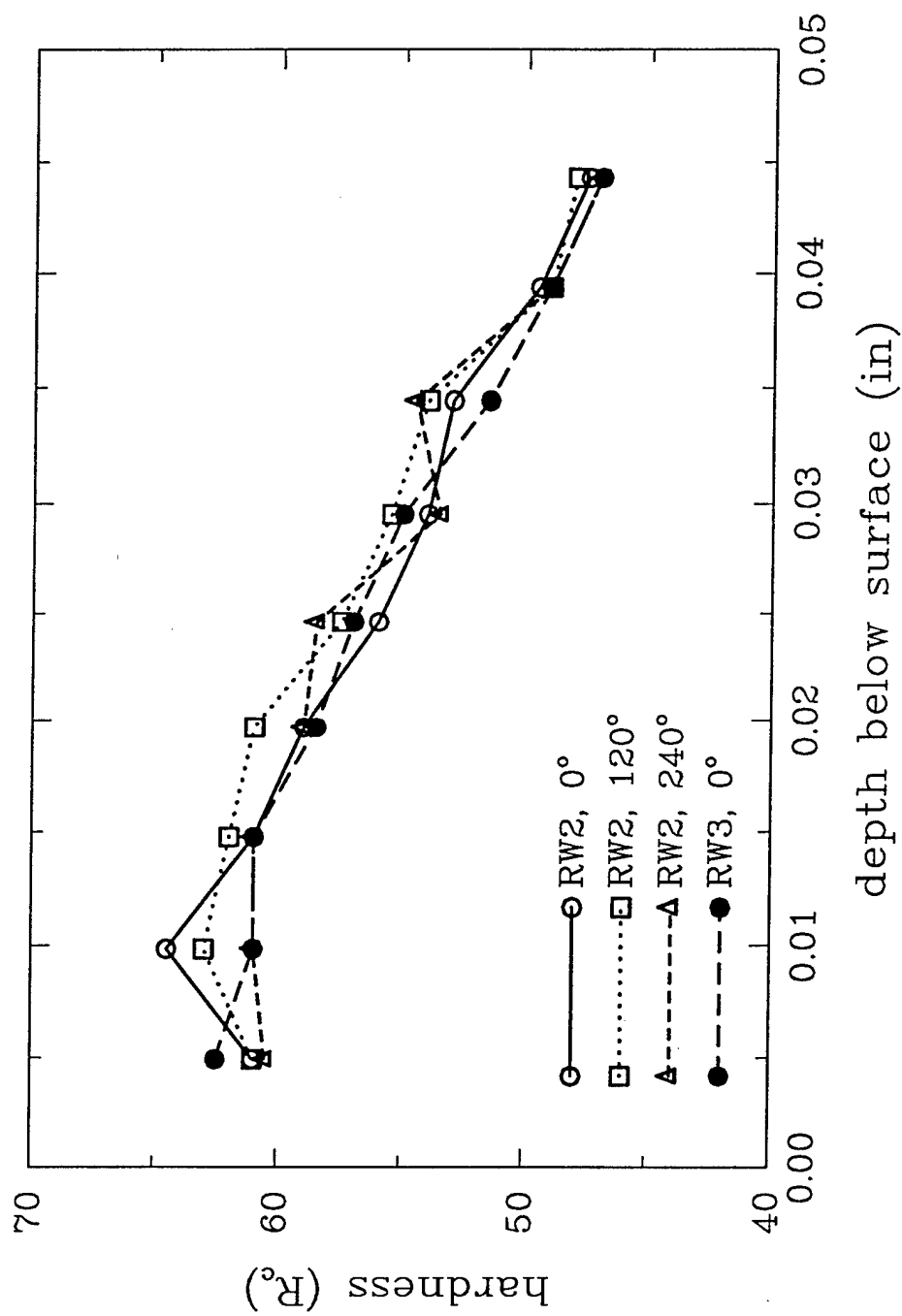


Figure 59. Measured variation of hardness underneath surface of rim following quench and temper.



TABLE 14. DATA FROM RESIDUAL STRESS MEASUREMENTS

Specimen	Direction	Location	Residual Stress — ksi (MPa)
RW2	Circ.	Rim, 0°	-36.0 (-248)
	Circ.	Rim, 120°	-36.6 (-252)
	Circ.	Rim, 240°	-35.0 (-245)
	Radial	Web, 0° (rim edge)	30.9 (216)
	Radial	Web, 0° (hub edge)	23.5 (165)
	Radial	Web, 180° (hub edge)	17.5 (1203)
	Radial	Web, 180° (rim edge)	22.8 (160)
RW3	Circ.	Rim, 0°	-29.3 (-205)
	Circ.	Rim, 120°	-24.6 (-172)
	Circ.	Rim, 240°	-25.4 (-180)

## MODEL DESCRIPTION

### Finite element model

The finite element discretization of the gear blank is illustrated in Figure 60. The model is axisymmetric, and utilizes 402, 4-noded type CAX4T elements. Mesh spacing is biased so that more elements are concentrated near the carburized surfaces.

### Modelling procedure

The procedure used to simulate the heat treat operations is illustrated in the flow chart shown in Figure 61. The carbon diffusion model was first used to determine the carbon distribution following carburization. The carbon profiles from the diffusion model were then fed into the thermomechanical model as a predefined variable. The carburization process was simulated by imposing a temperature of 927 C to the environment surrounding the part (the bath temperature) and surface heat transfer coefficients associated with air. At temperature, the carbon profile was incorporated into the model and the gear blank was cooled-down by imposing a bath temperature of 20 C.

The carbon profile and deformed geometry were then passed into a second thermomechanical model for simulation of quench, deep-freeze and temper. Residual stresses which developed during carburization were not saved, as it was assumed that these were relieved during the austenitization process. The quench process was simulated by first slowly heating up to the austenitization temperature, 830 C, and then applying the constraining pressures from the two rams. Quench was then simulated by imposing surface heat transfer characteristics of first

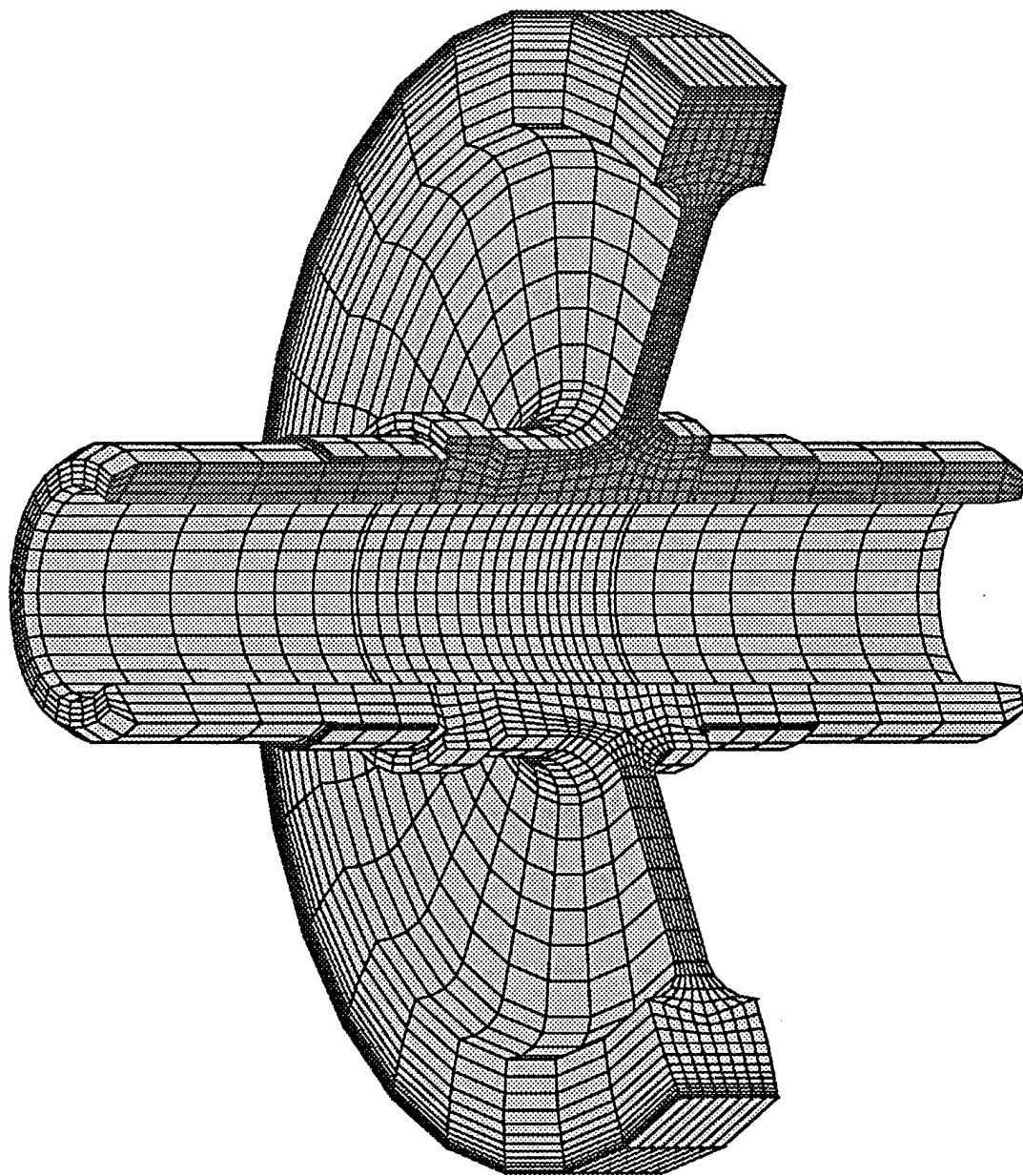


Figure 60. Finite element mesh for the rim/web gear blank.

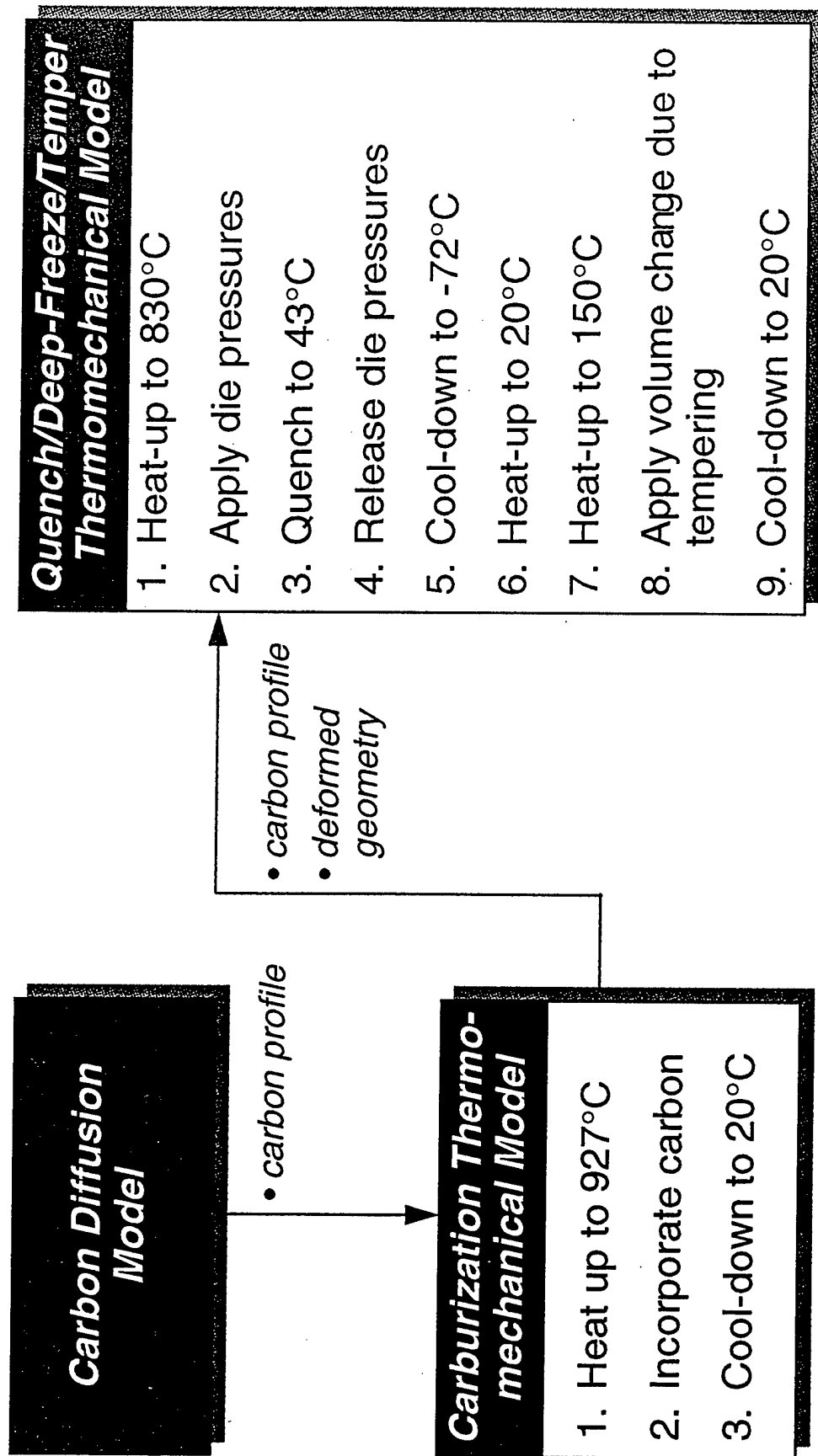


Figure 61. Flow chart illustrating procedure used to model gear blank heat treatment.

Next the gear was cooled down to -72 C and then heated back up to room temperature. Finally, the gear was heated up to the tempering temperature of 150 C, at which point the negative volume change associated with formation of carbides was simulated. The gear blank was then cooled back down to 20 C.

The surface heat transfer boundary conditions used for all of the heat-up and cool-down steps except quench were those determined for air (see Figure 28). For the quench step, the heat transfer conditions are more complex. As noted earlier, oil fills up the quench press reservoir at an initial rate of 620 gallons per second. Based upon the area of the reservoir, this rate translates to an upward linear velocity of 4.6 cm/sec. The gear blank is assumed to be initially surrounded by air for a period of at least 15 seconds, a time that was chosen, based upon measured temperature data, to represent that needed for transfer of the part from the furnace to the press. Then, each point on the gear blank experiences an additional time delay before contacting the oil based upon its axial position and this calculated oil velocity. The applied surface heat transfer coefficients are calculated accordingly. In this manner, the bottom part of the shaft begins to cool first, then the web and rim, and finally the upper part of the shaft.

To add to the complexity of the surface heat transfer conditions, locations on the gear die directly in contact with the die do not see the heat transfer coefficients associated with contact with oil. Since the model is axisymmetric, it is not able to differentiate between the different heat transfer conditions for each of these two distinct regions. Instead, a rule of mixtures approach is used to calculate an effective heat transfer coefficient for these locations, which is based upon the relative area of the contact pads to the flow channels. The ratio of contact area to flow channel area for this die configuration were calculated to be:

- 0.75 for the lower shaft shoulder/lower die contact region (axial);
- 0.68 for the lower shaft journal bearing/lower die contact region (radial);
- 0.53 for the rim/lower die contact region (axial);
- 0.51 for the rim/upper die contact region (axial).

Finally, as demonstrated earlier, the measured temperature histories show that the upper side of the web cools faster than the underside of the web, presumably because the oil flow stagnates under the web. This was accounted for by reducing the heat transfer coefficient along the underside of the web by a factor that produced a temperature history difference between the two sides that matched experimental data.

For all of the analyses, the gear was constrained axially along the shoulder on the lower part of the shaft (the same shoulder, shown in Figure 58, that experienced excessive deformation due to irregular die pressure). For the quench analysis, the inner ram pressure was applied to the top of the shaft and reacted at this shoulder. The pressure from the outer ram was applied to the upper part of the rim and equilibrated with an equal and opposite pressure applied to the bottom part of the rim. The rim was not constrained radially — early analysis efforts with the rim constrained radially predicted far too much radial growth of the rim. It is likely the conditions in the actual press quench are somewhere in between no constraint and complete radial constraint of the rim, i.e., some sort of frictional contact. It was felt that such contact conditions would be too difficult to determine and to model at this time.

## MODELING RESULTS

### Carbon Diffusion Model

Several iterations of the carbon diffusion model were first carried out. As before, the diffusion coefficient was adjusted so that the model prediction of the carbon gradient in the carburized zones was as accurate as possible. For this analysis, the choice of  $D_c = 3.8 \times 10^{-7} \text{ cm}^2/\text{sec}$  yielded the best fit to data. Contours of calculated carbon content are plotted in Figure 62 and illustrate the steep gradients of carbon for the three carburized zones. Figure 63 shows a comparison between the calculated carbon content and that inferred from hardness measurements. It should be noted that the correspondence between these data is valid only up to carbon levels of about 0.4%. Above this level, the inferred carbon levels lose accuracy because of retained austenite. The fit at the lower carbon levels was used to determine the optimal diffusion coefficient.

### Carburization Model

The thermomechanical model for carburization predicts little distortion, just as was seen in the experiments. A comparison of predicted carburization deformation with average measured distortion is depicted in Figure 64 and listed in Table 15. Model predictions are generally consistent with measurements for radial growth of the rim and change in length of the shaft, especially considering the small magnitude of these distortions. The model predicts, however, that the web bends down by 0.0001 inches, whereas the measurements show the web bending up by 0.0005 inches. This discrepancy is not alarming, again considering the large variation in measured distortion. In fact, as is evident in Table 15, the model prediction of axial web distortion is well within the bounds defined by  $\pm$  one standard deviation.

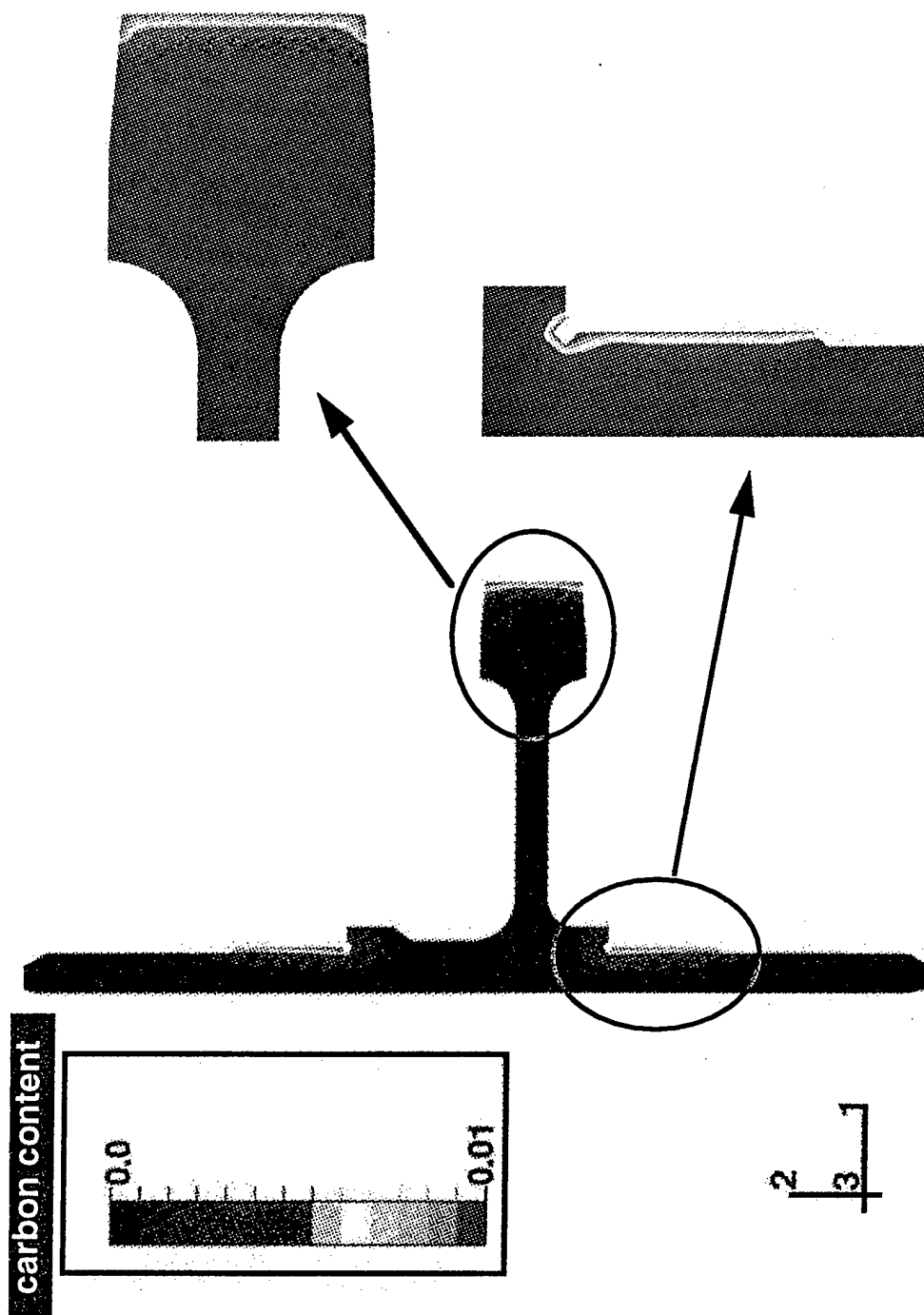


Figure 62. Calculated contours of carbon content showing steep carbon gradient near surface of each carburized region.

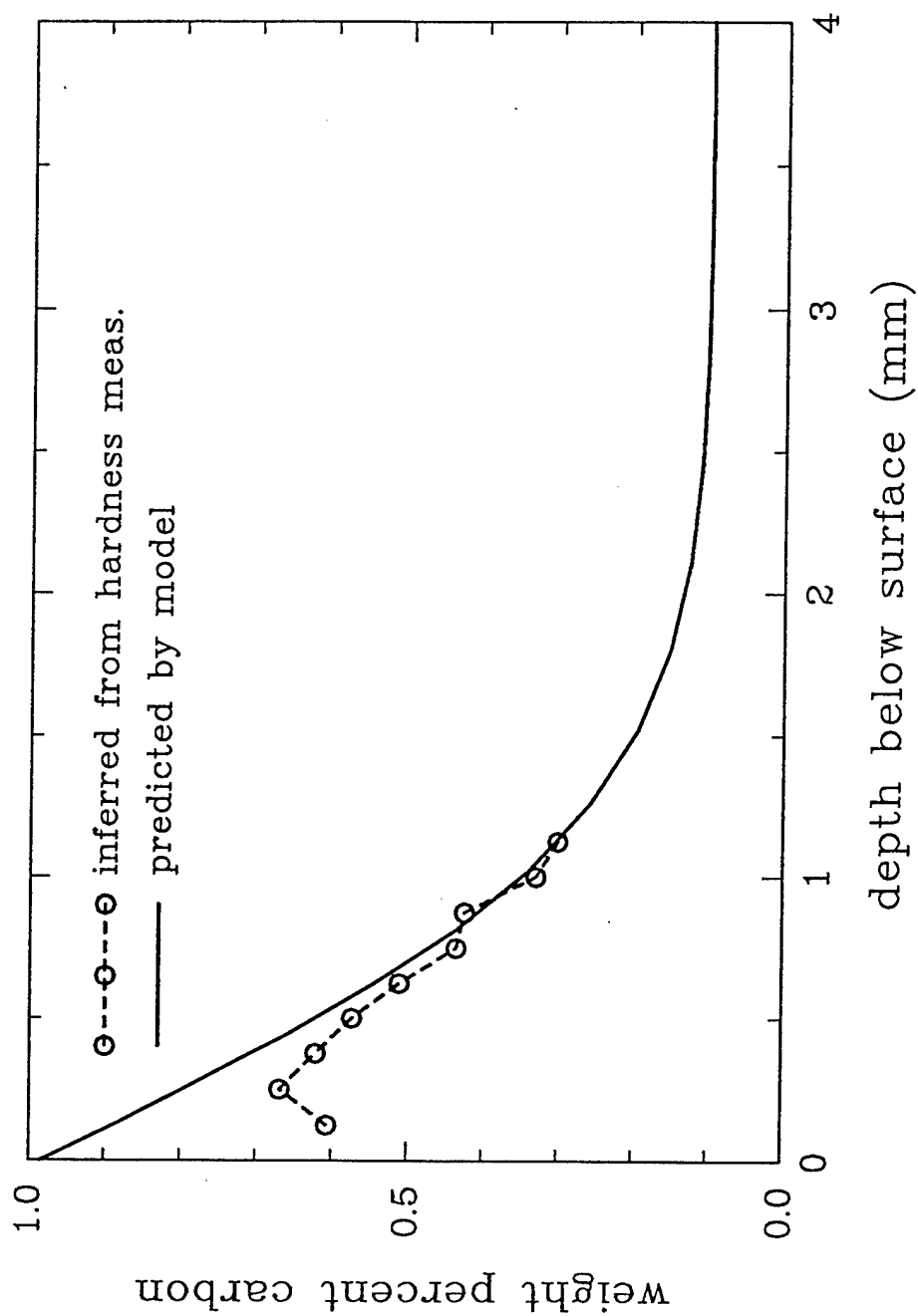


Figure 63. Comparison between calculated carbon content and values inferred from hardness measurements.

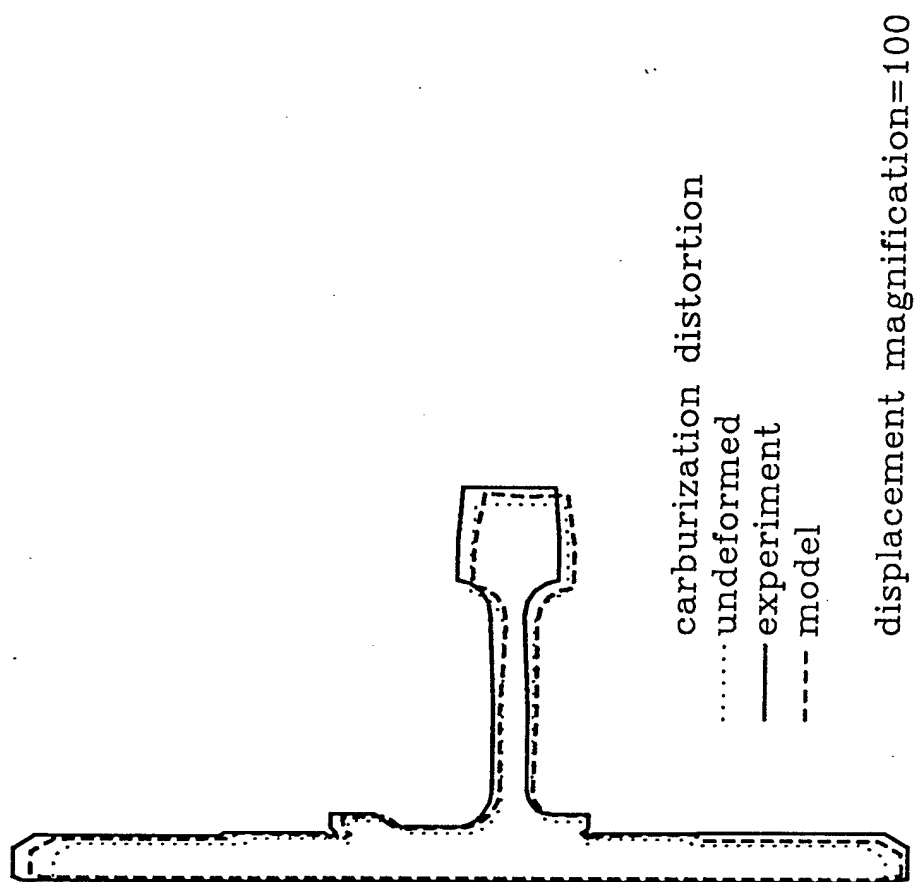


Figure 64. Comparison between model predictions of distortion following carburization and measured values.



TABLE 15. COMPARISON OF MODEL CALCULATED DISTORTION FOLLOWING CARBURIZATION WITH AVERAGED MEASURED VALUES

measurement location	average measured distortion — $10^{-3}$ inches (standard deviation)	calculated distortion ( $10^{-3}$ inches)
1.	0.6 (0.3)	0.2
2.	0.3 (0.4)	0.3
3.	0.8 (0.6)	0.4
4.	0.3 (0.5)	-0.4
5.	0.3 (0.5)	-0.1
6.	0.2 (0.4)	0.1
7.	0.1 (0.3)	0.1
8.	0.3 (0.4)	0.1
9.	0.4 (0.4)	0.2
shaft length	1.7 (0.3)	1.8
web thickness	0.2 (0.3)	0.3

#### Quench model

The quench model is the one that has received the most attention in the research project. In order to illustrate how the simulation provides insight into the thermomechanics of the quench process, a series of contour plots are plotted in Figures 65 through 72. These figures show how the key variables temperature (T) and martensite volume fraction (f) evolve throughout the course of the quench simulation.

- In Figure 65, contours of T and f are shown at  $t=7.2$  seconds. At this time, the gear blank has not been completely transferred to the quench press; the heat transfer medium is air and, as such, the surface heat transfer coefficient is low. The gear blank shows a temperature profile indicative of slow cooling — the thicker parts of the gear blank (the rim and the intersection of the web with the shaft) are about 40 C hotter than the ends of the shaft and the center of the web. Since the lowest temperature is still above the martensite start temperature, none of the austenite has transformed.

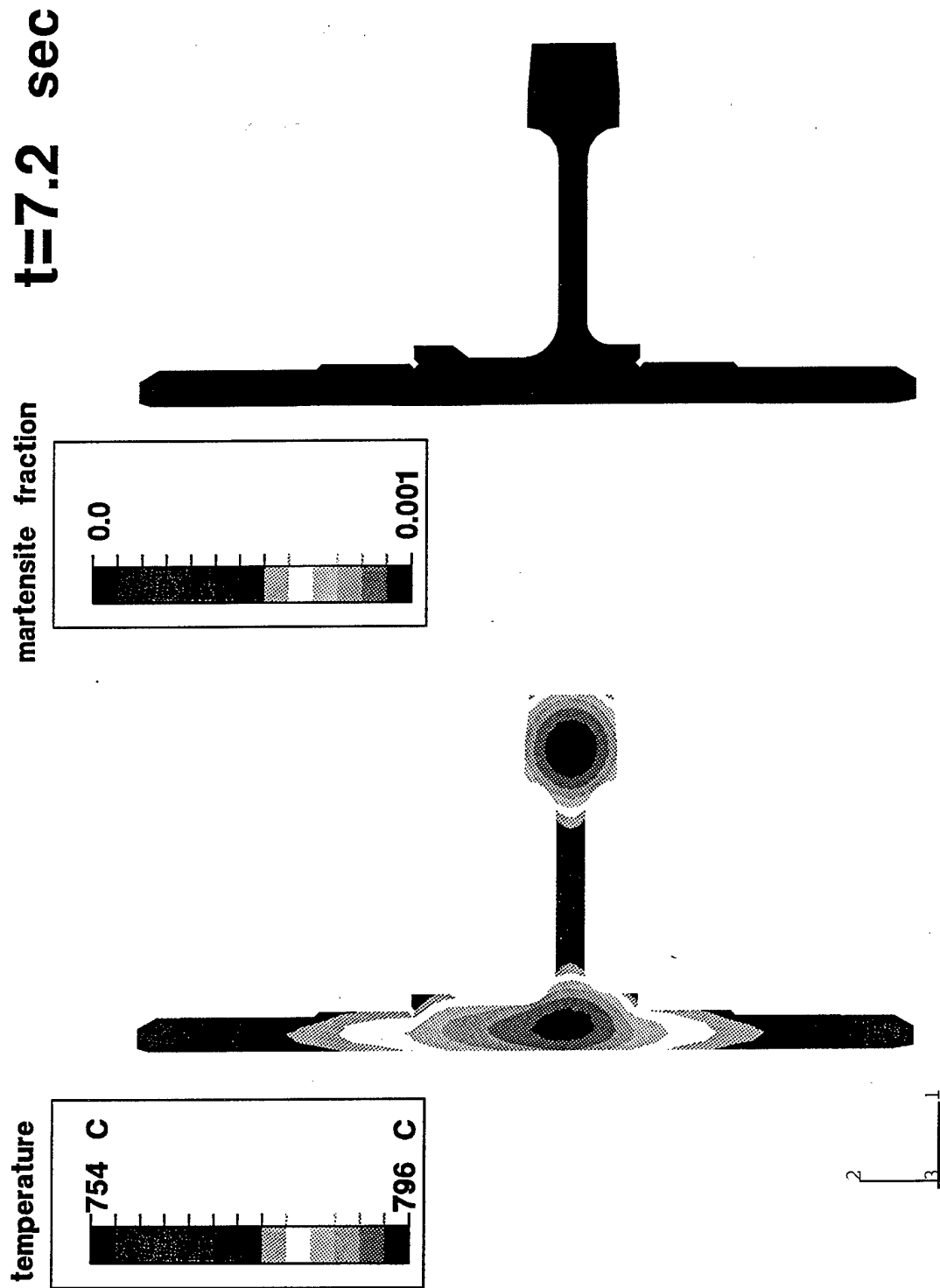


Figure 65. Contours of temperature and martensite volume fraction during quench.  
t = 7.2 seconds.

- Figure 66 shows these same variables at a later time,  $t=15.6$  seconds. At this time the oil has just begun to contact the lower part of the gear blank. The temperature in this region has quickly dropped to 505 C while the temperature of center of the rim and the web/shaft intersection is still at about 750 C. No martensite has yet formed.
- At  $t=17.1$  seconds (Figure 67), the temperature of the lower end of the shaft has dropped to 340 C, while the temperature at the center of the rim is still 727 C. The  $M_s$  temperature is 440 C for the baseline 9310 material, so martensite has begun to form rapidly (80 percent in 1.6 seconds!) at the lower tip of the shaft.
- At  $t=19.2$  seconds (Figure 68), the oil has completely covered the gear blank. The temperature of a much greater portion of the lower end of the shaft has decreased below the martensite start temperature, as has the web and the upper tip of the shaft. Much more martensite has formed in these regions. Note that more martensite has formed near the top surface of the web than near the bottom surface. This is because the heat transfer coefficient is higher here. (Recall that the heat transfer coefficient along the lower end of the web was reduced to account for the stagnation of oil flow.)
- At  $t=20.9$  seconds (Figure 69), the temperature has dropped below the martensite start temperature everywhere except at the center of the thicker parts of the gear blank. Martensite has formed in most of these regions. In the carburized regions, however, very little martensite has formed, due to the suppression of the transformation temperatures that is associated with high carbon content.
- At  $t=23.7$  seconds (Figure 70), as the temperature continues to cool down in a manner consistent with the thickness of various regions of the gear blank, the transformation continues to encompass more and more of the gear blank except in those regions where high carbon levels are present.
- At  $t=28.2$  seconds (Figure 71),  $T$  is everywhere below the martensite finish temperature for the baseline 9310 material, and the transformation to martensite is complete except in the carburized zone, where the transformation propagates through progressively higher carbon levels, reducing the size of the untransformed zone.
- Finally, at  $t=38.0$  seconds (Figure 72), the temperature is approaching the oil temperature of 43 C everywhere except in the rim, where is still up to 70 C hotter. At this point, the transformation is complete everywhere except for a thin band near the surface of the carburized zone, in which the martensite finish temperature is below 45 C.

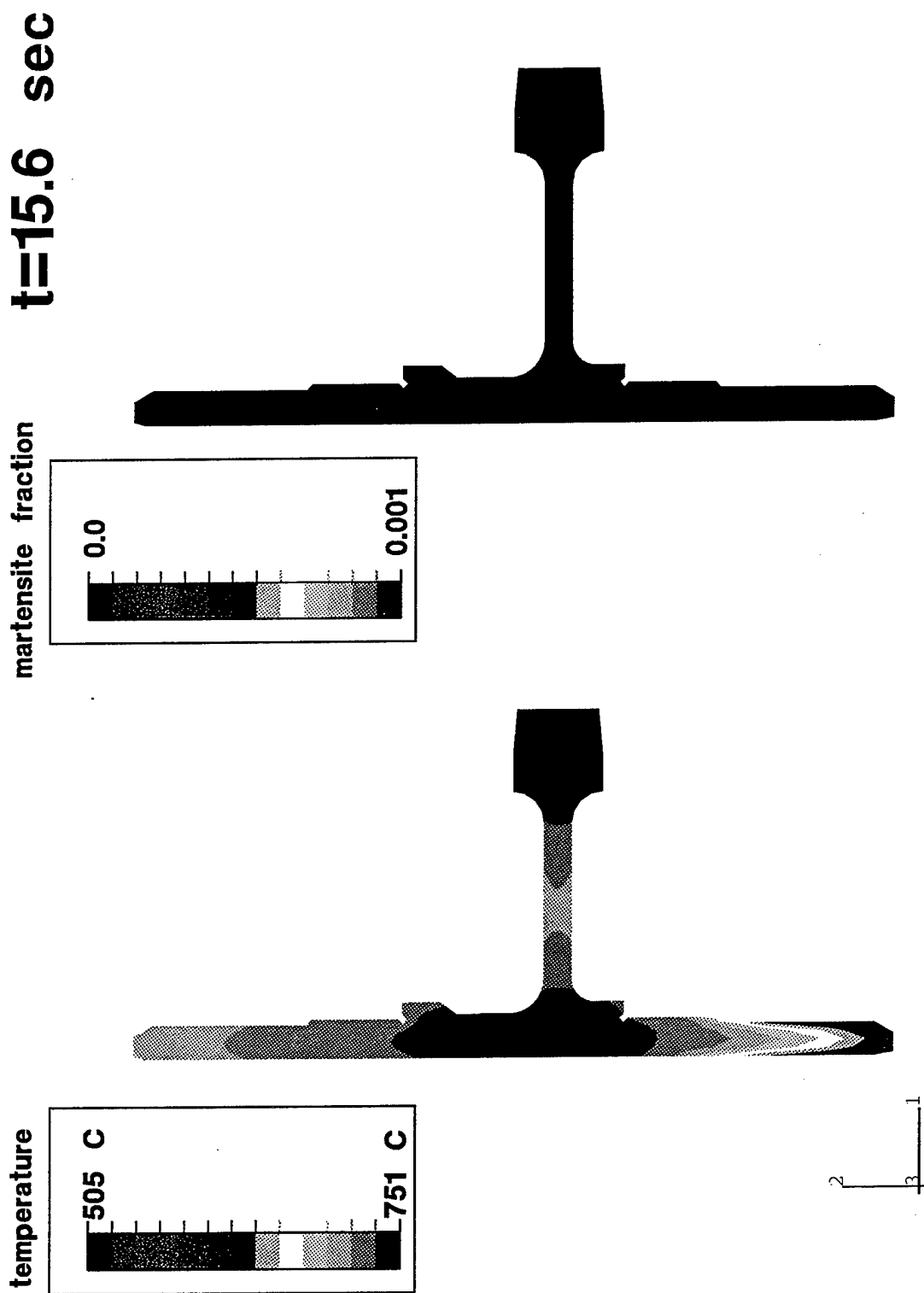


Figure 66. Contours of temperature and martensite volume fraction during quench.  
t = 15.6 seconds.

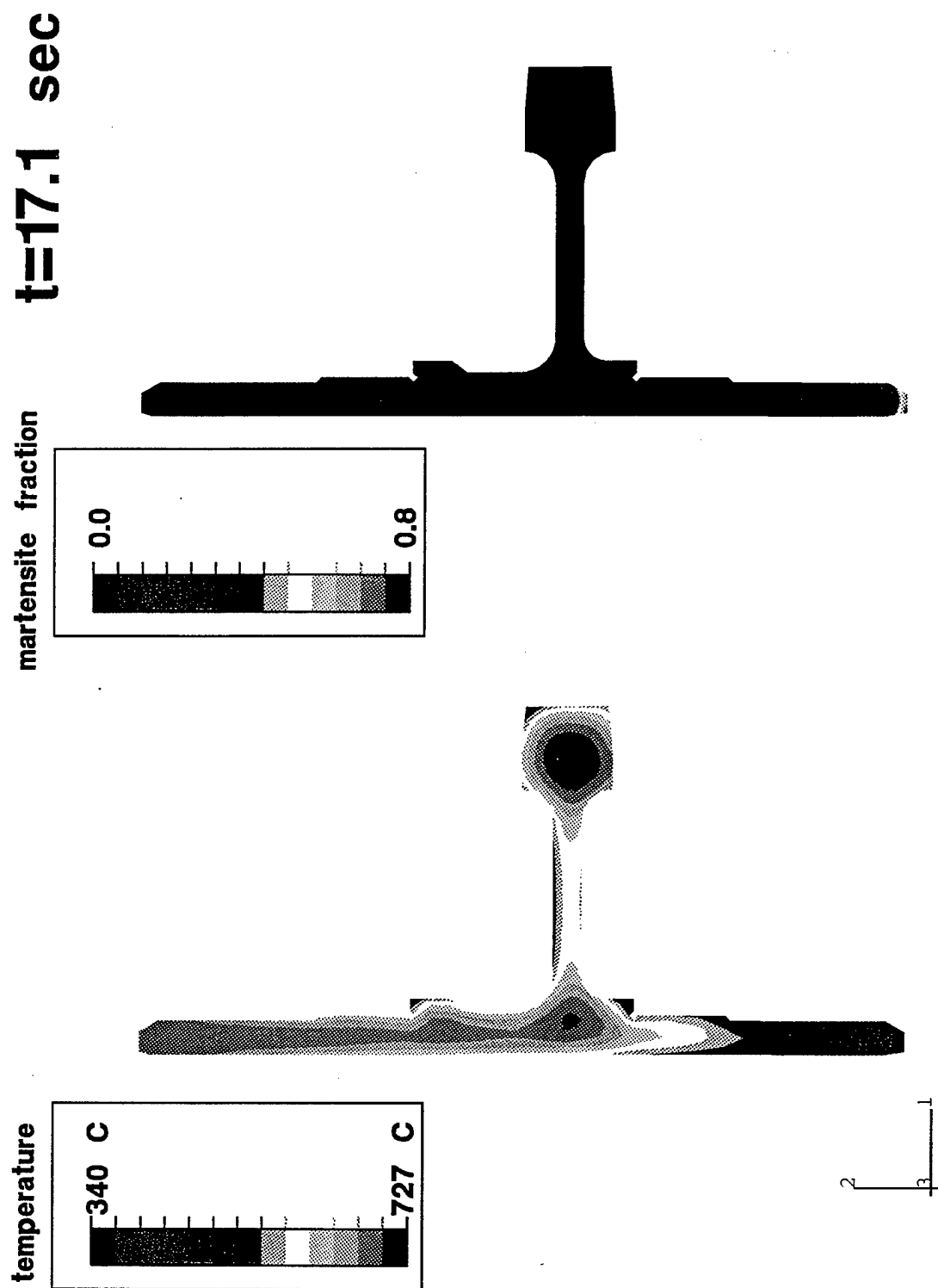


Figure 67. Contours of temperature and martensite volume fraction during quench.  
t = 17.1 seconds.

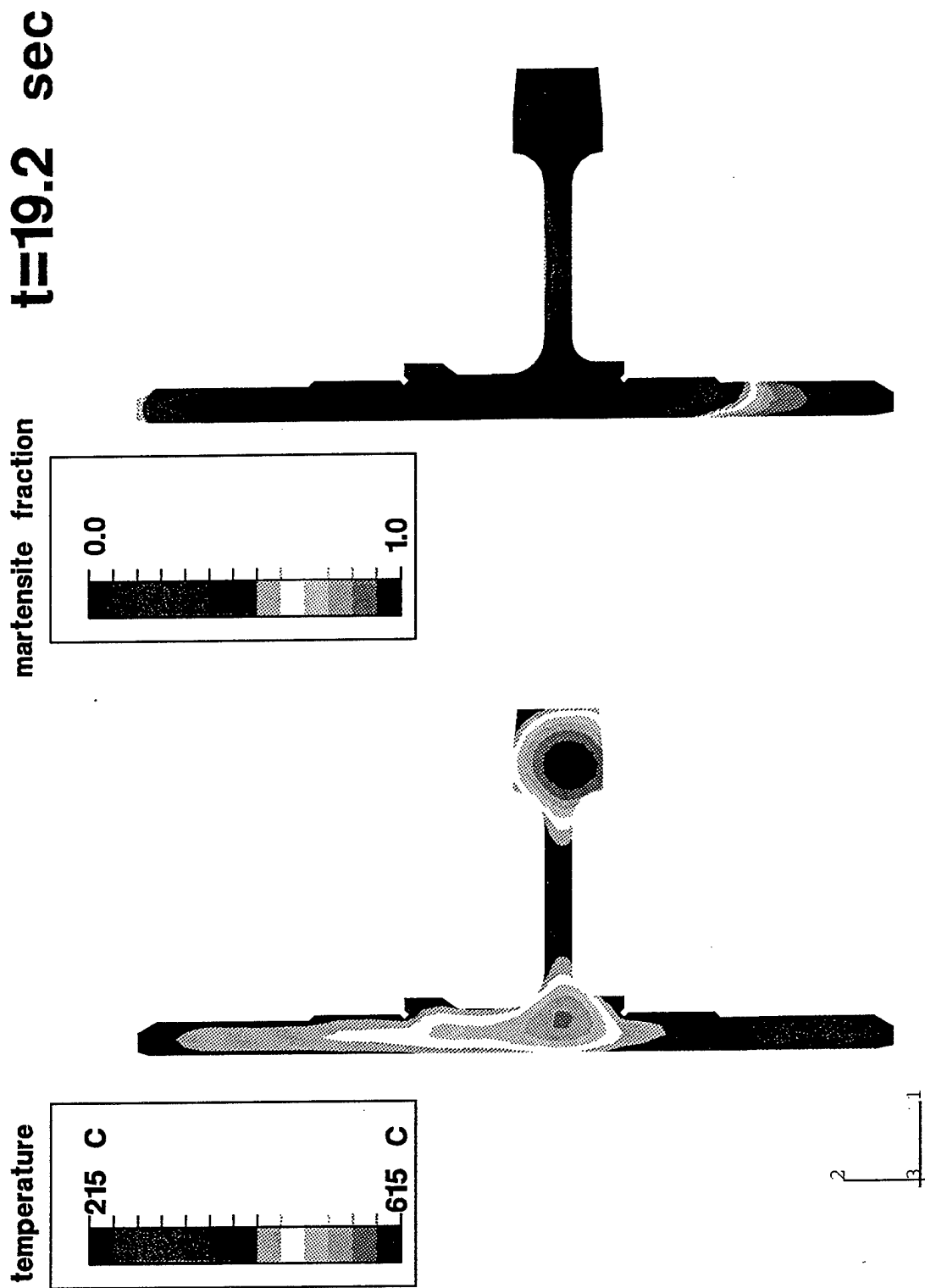


Figure 68. Contours of temperature and martensite volume fraction during quench.  
 $t = 19.2$  seconds.

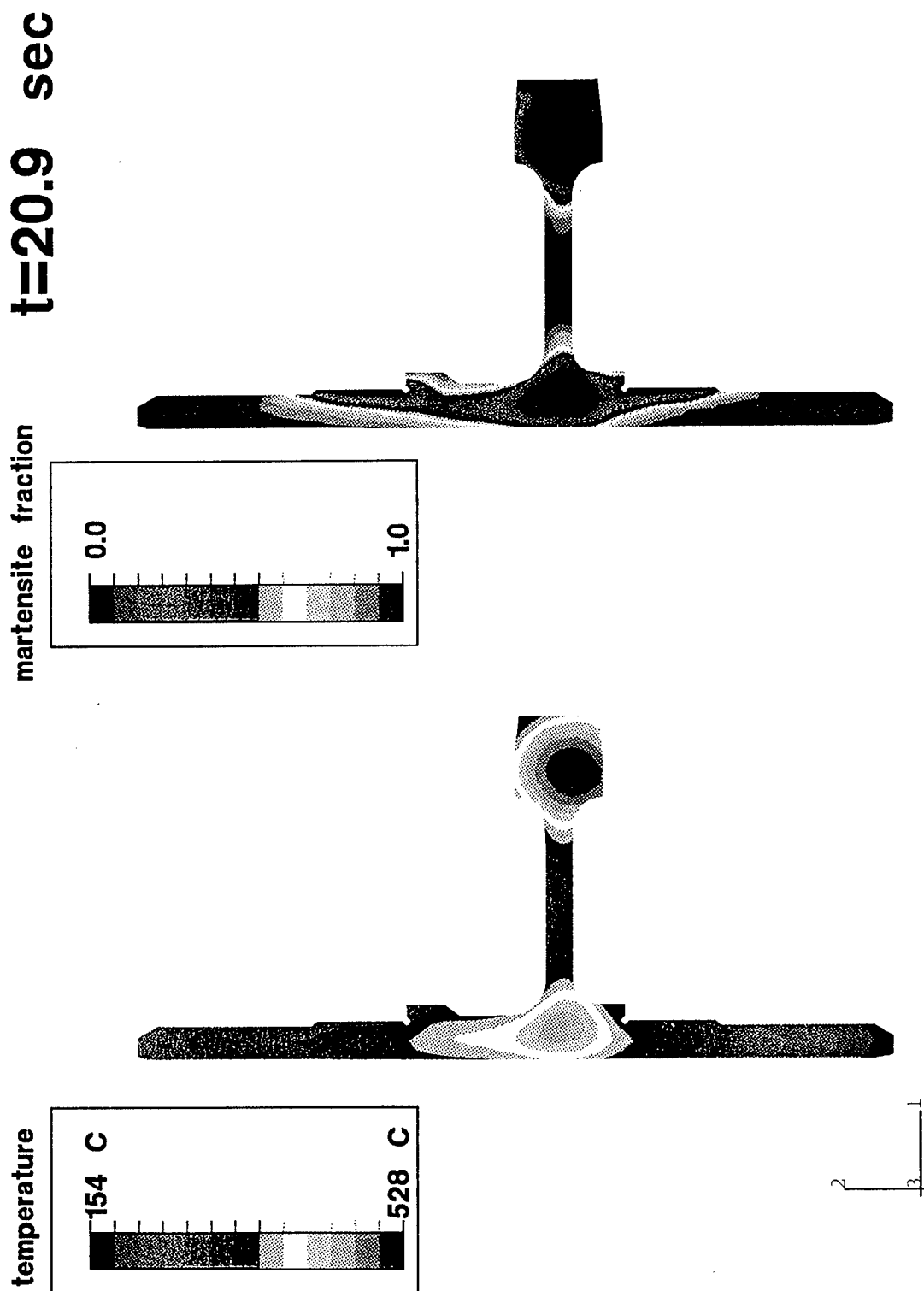


Figure 69. Contours of temperature and martensite volume fraction during quench.  
 $t = 20.9$  seconds.

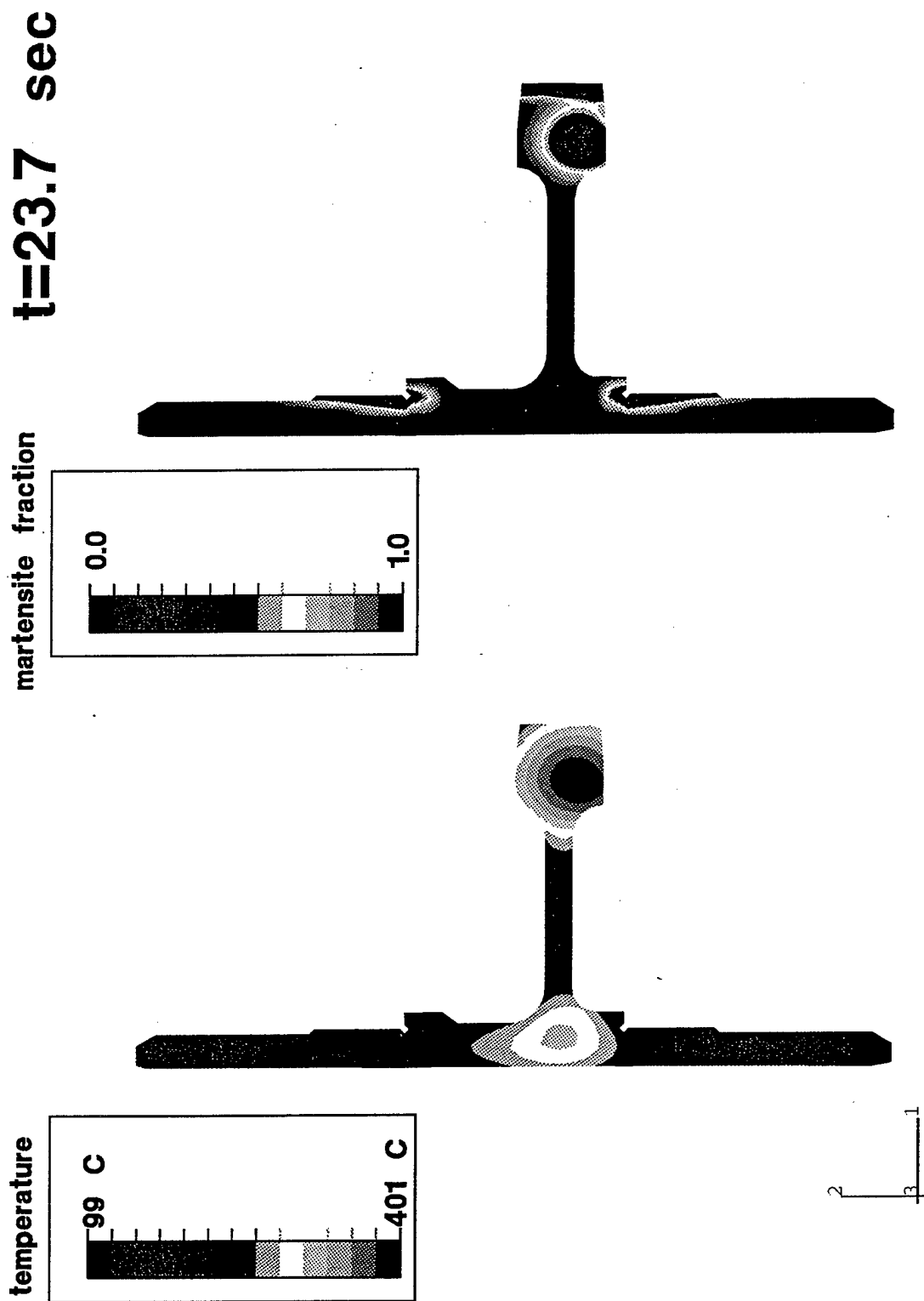


Figure 70. Contours of temperature and martensite volume fraction during quench.  
 $t = 23.7$  seconds.



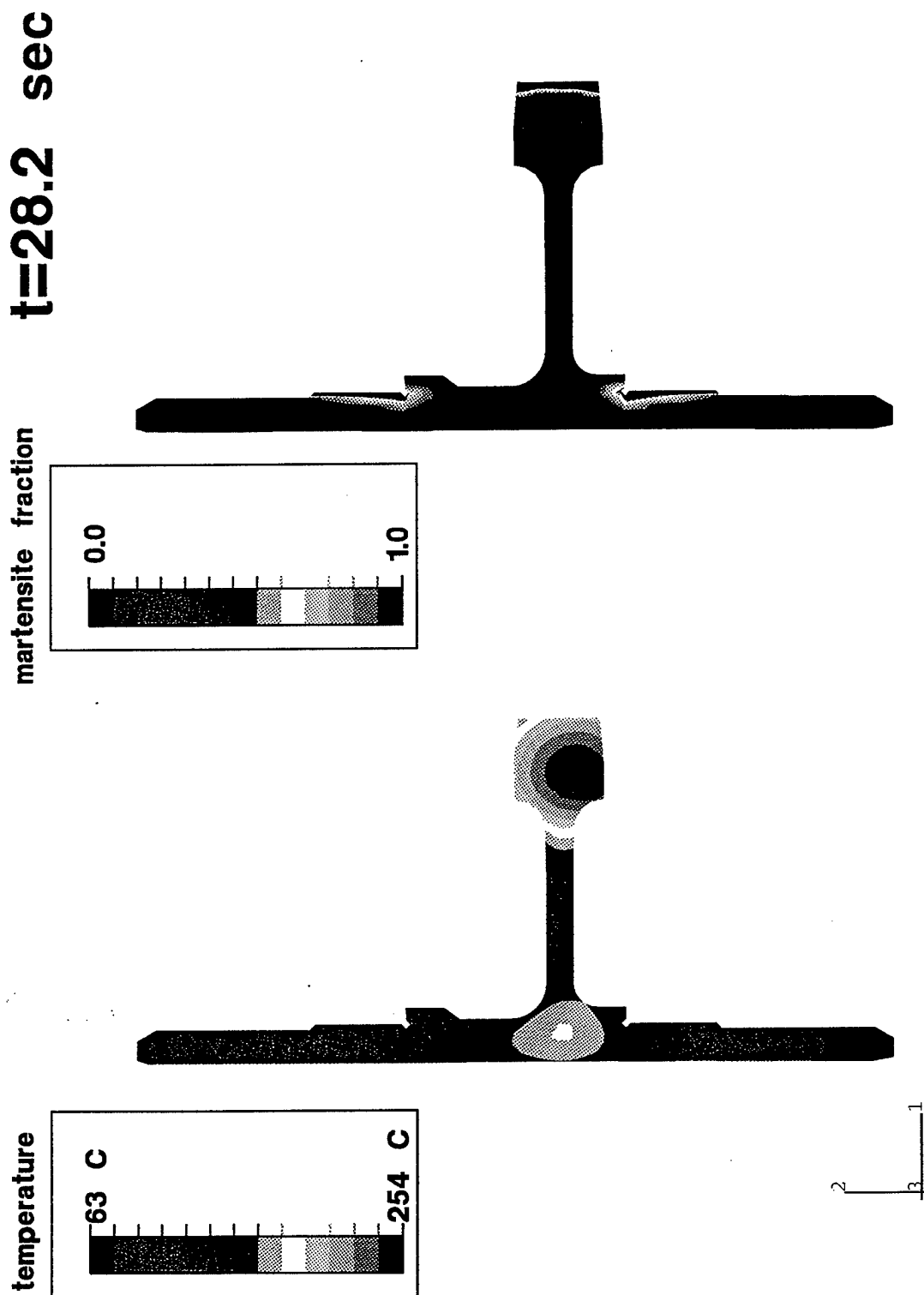


Figure 71. Contours of temperature and martensite volume fraction during quench.  
t = 28.2 seconds.

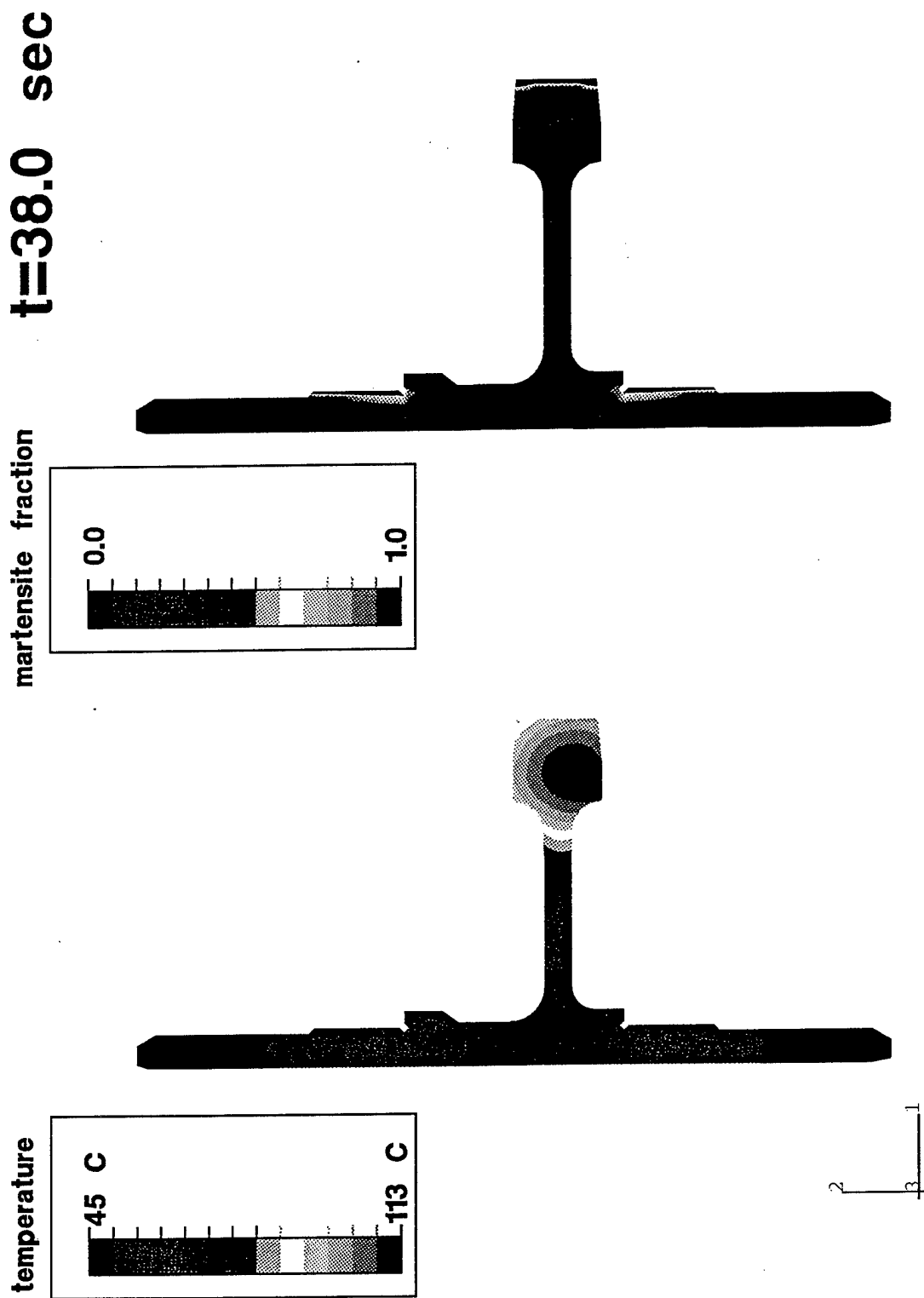


Figure 72. Contours of temperature and martensite volume fraction during quench.  
 $t = 38.0$  seconds.

Model predictions of distortion following quench and deep-freeze are shown together with averaged measurements of distortion following deep-freeze in Table 16 below; a comparison of model predictions of distortion with measured averages is pictured in Figure 73. Although it is not evident in Table 16, model calculations show that most of the distortion occurs during quench, as one might expect, since the effect of the deep-freeze operation is primarily limited to the carburized zone, which is not large enough to affect gear blank distortion appreciably.

TABLE 16. COMPARISON OF MODEL CALCULATED DISTORTION FOLLOWING DEEP-FREEZE WITH AVERAGED MEASURED VALUES

measurement location	average measured distortion — $10^{-3}$ in (standard deviation)	model calculated distortion ( $10^{-3}$ in)
1.	0.2 (0.2)	0.8
2.	0.6 (0.4)	0.1
3.	3.9 (1.1)	3.0
4.	4.3 (5.6)	3.6
5.	-1.3 (6.1)	2.4
6.	-1.0 (3.4)	1.0
7.	-0.3 (1.0)	0.4
8.	0.1 (0.7)	0.1
9.	0.0 (0.9)	0.9
shaft length	0.4 (0.7)	5.9
web thickness	0.9 (0.9)	0.2

Most of the predicted distortion values given in Table 16 are quite consistent with averaged measured values. In particular, model predictions of the radial growth of the rim (3.0 mils) and the axial distortion of the rim (3.6 mils), which one might expect to be the distortions with the highest magnitudes, compare favorably with their respective measured averages (4.3 and 3.9 mils). Predictions for the radial growth of the shaft (points 1, 2, 8 and 9) are all small (less than one mil) and generally in the range of measured values. The only data that are not consistent with the experiment averages are the axial distortion at interior points of the web (5,6, and 7) and the change in length of the shaft.

An explanation for these differences would seem to lie in the aforementioned problems with pressure control of the inner ram. The small average measured change in length of the shaft (0.4 mils) and the fact that in some cases the shaft actually shortened do not appear to be consistent with the change in volume accompanying the transformation. It seems very likely that the length of the shaft was adversely affected by the irregular die pressure. Moreover,

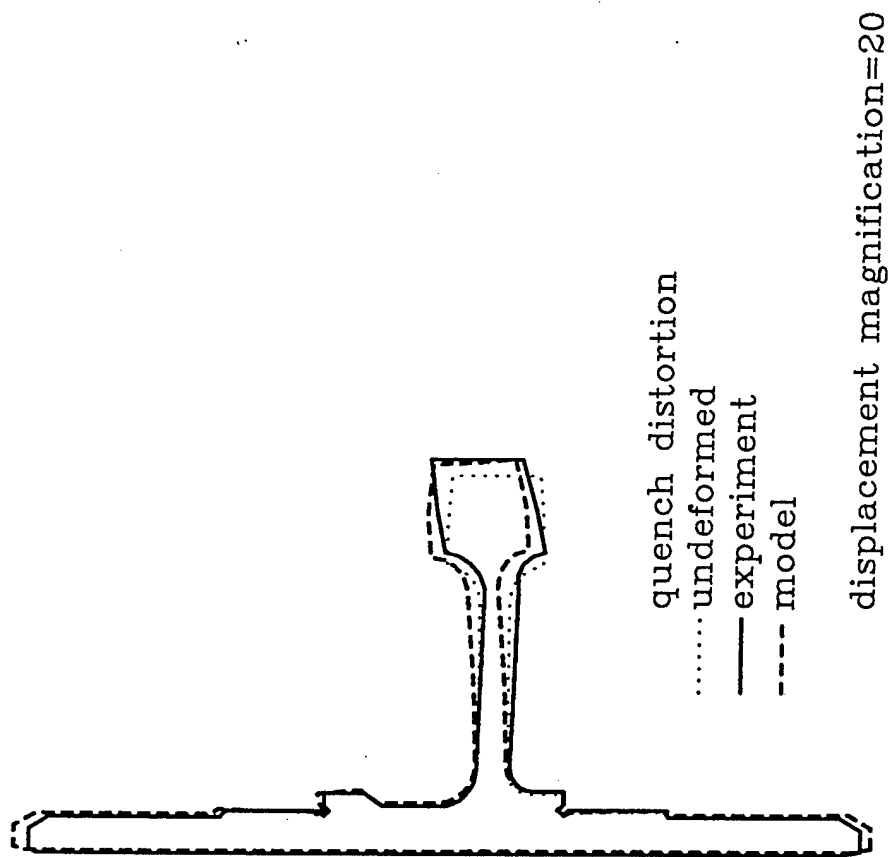


Figure 73. Comparison between model predictions of distortion following carburization and measured values.

the very large standard deviations associated with measurements along the web clearly show that the averaged values have little statistical significance. Of course, one could argue that the good agreement demonstrated at point 4 is of questionable significance, as well. In fact, of all the data presented in Table 16, only data for location 3 is statistically robust. The good agreement between model predictions and measurements for this location are encouraging. For the other locations, model predictions are generally well within one standard deviation of the average measured value; however, the large magnitude of the standard deviation precludes a more quantitative assessment of model accuracy.

### Residual Stresses

Contours of residual radial stress and circumferential stress are plotted in Figure 74. Circumferential residual stresses are highest in the carburized regions; this is clearly due to the effect that carbon has on transformation kinetics and transformation volume change. Compressive stresses arise because, as the carburized region transforms, the material in this region tries to expand, but it is constrained from expanding fully because the surrounding material, which is at a lower carbon level, does not expand as much. Figure 75 shows profiles of circumferential stress near the edge of the rim following deep/freeze and temper. Compressive residual stresses peak about 0.5 mm below the surface due to the enhanced volume change associated with high carbon levels, and then become less severe at the surface due to the presence of retained austenite. (Although not considered in this model, decarburization at the surface during austenitization can also cause the compressive stresses at the surface to lessen; however, at the relatively low austenitization temperature, 830 C, this effect should be small.) During the temper operation, the profile of residual stress changes, with the surface values decreasing in magnitude due to the negative volume change associated with formation of carbides.

Included in this figure are the measured residual stress values. They are consistent with model predictions both in magnitude and the trend toward decreasing magnitude after temper. It should be noted, however, that model predictions of these stress profiles are sensitive to the values of key parameters which are not accurately known. In particular, the residual stresses following deep-freeze are quite sensitive to the effect of carbon content on the transformation volume change and the transformation temperature. At high carbon levels the transformation is not complete at room temperature (see Figure 15), and thus the complete measurement of transformation parameters could not be made with the experimental set-up that was used. Instead, the values at higher temperatures/lower carbon levels were extrapolated. In addition, the change in residual hoop stress following temper is quite sensitive to the choice of the volume change coefficient. This coefficient was taken from available literature data for another alloy. Based upon the fact that the model predicts a decrease in stress magnitude that is much greater than that measured, it is likely that the coefficient that was used (0.002), is much too high.

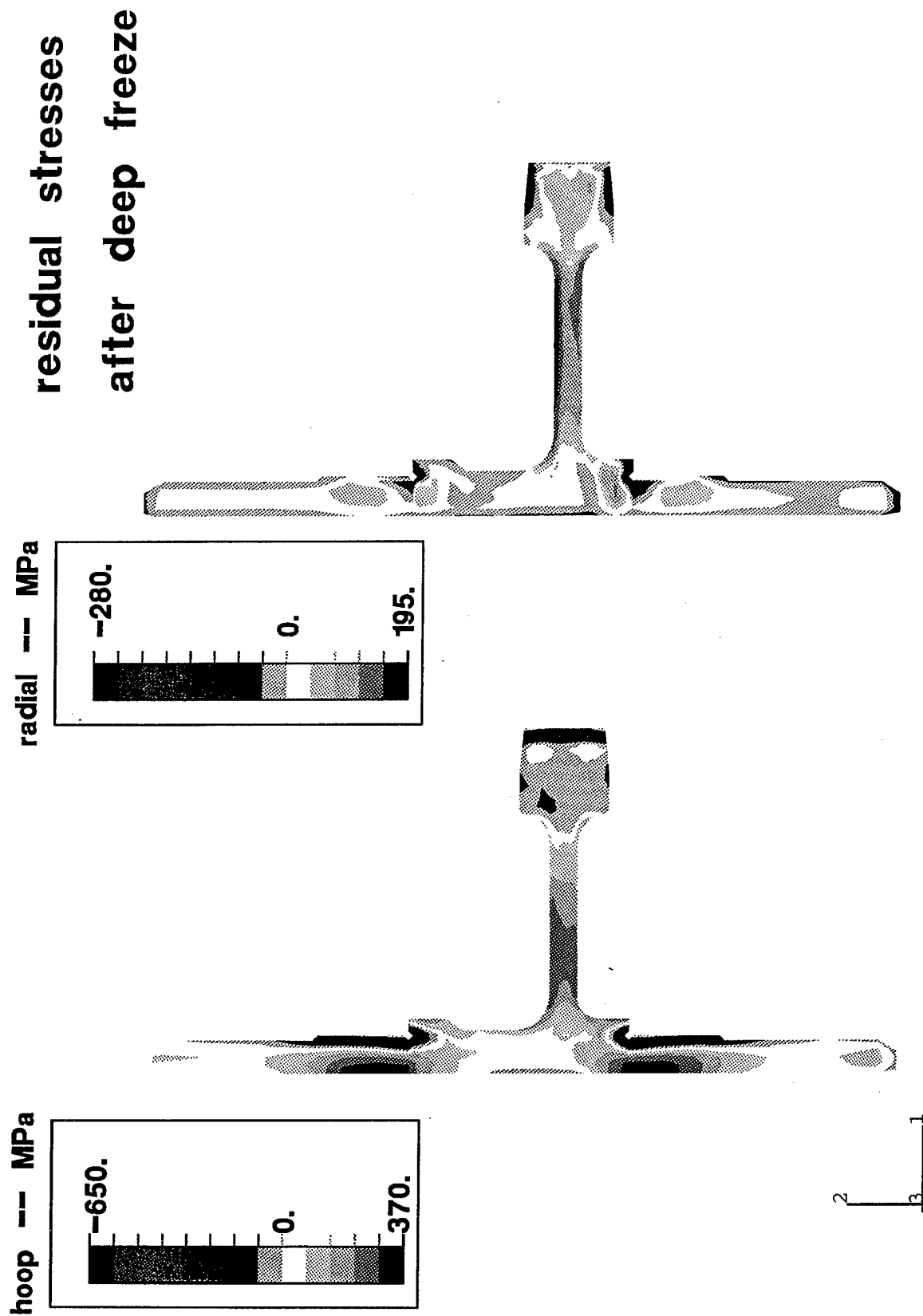


Figure 74. Contours of calculated residual circumferential stress (left) and radial stress (right), in MPa, following quench.

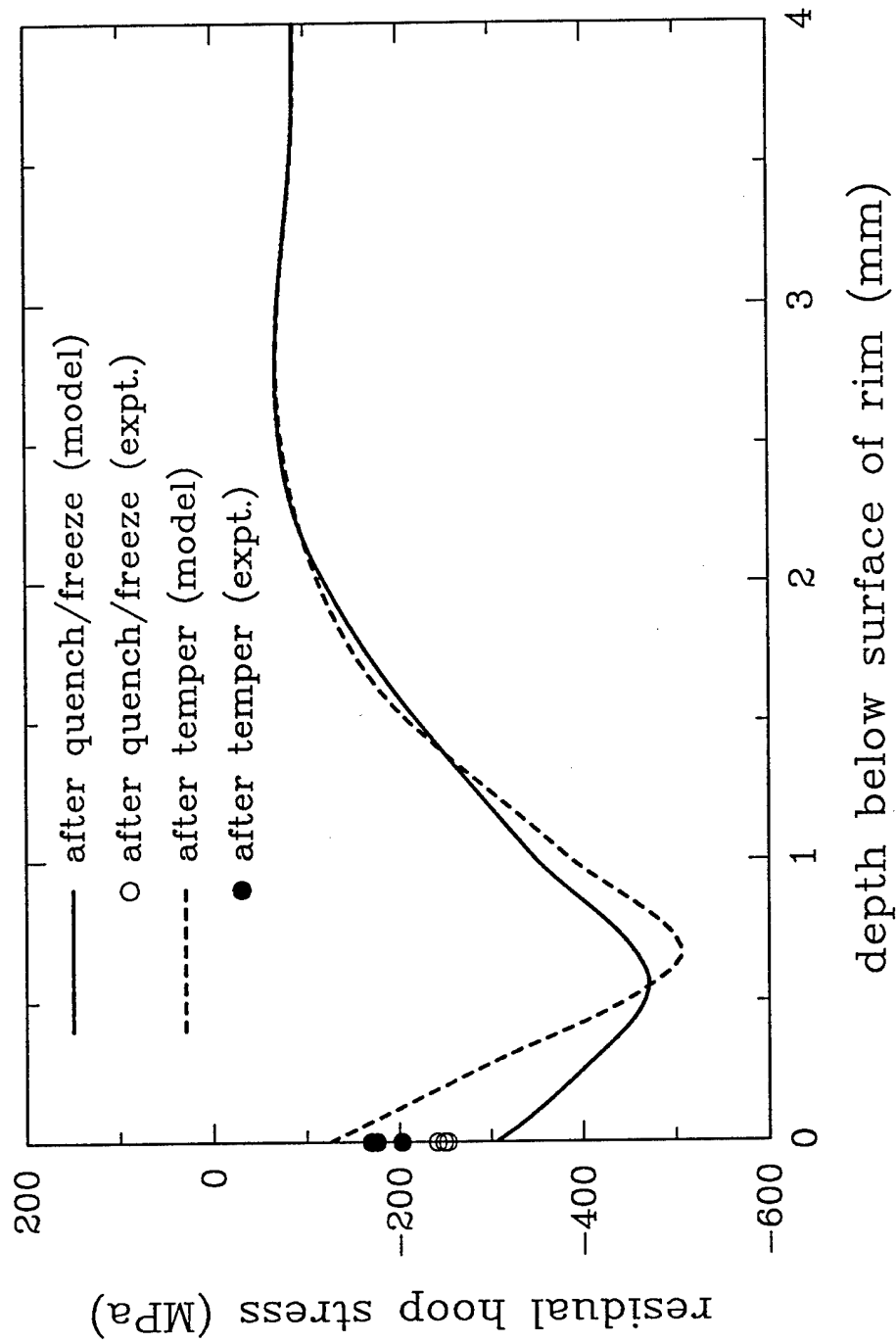


Figure 75. Profiles of calculated circumferential stress near the edge of the rim following deep-freeze and temper. Measured values are indicated.

Profiles of residual radial stress along the top of the web are plotted in Figure 76. These profiles are quite consistent with the indicated measured values; their magnitude is likely a strong function of the magnitude of the surface heat transfer coefficients and the differences in surface heat transfer coefficients between the top of the web and the bottom. (Note the difference in residual stress between the top and the bottom of the web in Figure 74.) It is not clear whether these stresses were affected by the irregular inner die pressure.

## SUMMARY

Overall, development and application of the model to a gear-type configuration has provided good predictions of distortion patterns and magnitudes and other parameters important in the heat treating process.

As summarized in Table 17, model predictions are consistent with measured data for:

- radial growth of the rim;
- residual hoop stress at the edge of the rim;
- residual radial stress along the top surface of the web.

Although there is tremendous variability in the measurements of the axial distortion of the web, model predictions of axial distortion also lie in the middle of the experimentally-observed range.

TABLE 17. COMPARISON OF KEY MODEL PREDICTIONS WITH MEASUREMENTS

Parameter	Observed Range	Predicted Value
Distortion		
– peak axial distortion of web	-0.0013 to 0.0099 inches (-0.03 to 0.25 mm)	0.0036 inches (0.09 mm)
– radial growth of rim	0.0028 to 0.0050 inches (0.07 to 0.13 mm)	0.0039 inches (0.10 mm)
Residual stress		
– Rim (hoop)	-252 to -241 MPa	-306 MPa
– Web (radial)	162 to 213 MPa	180 MPa

In regard to the data presented in Table 17, the good agreement between the radial growth of the rim and the residual radial stress along the web provides a first level of confidence in the model's predictive capabilities. The reasonable agreement between the predicted and measured values for residual hoop stresses are also encouraging, but less quantitatively significant because of the lack of measured transformation data below room temperature. Unfortunately, due the variability in web distortion patterns caused by irregular die pressures,



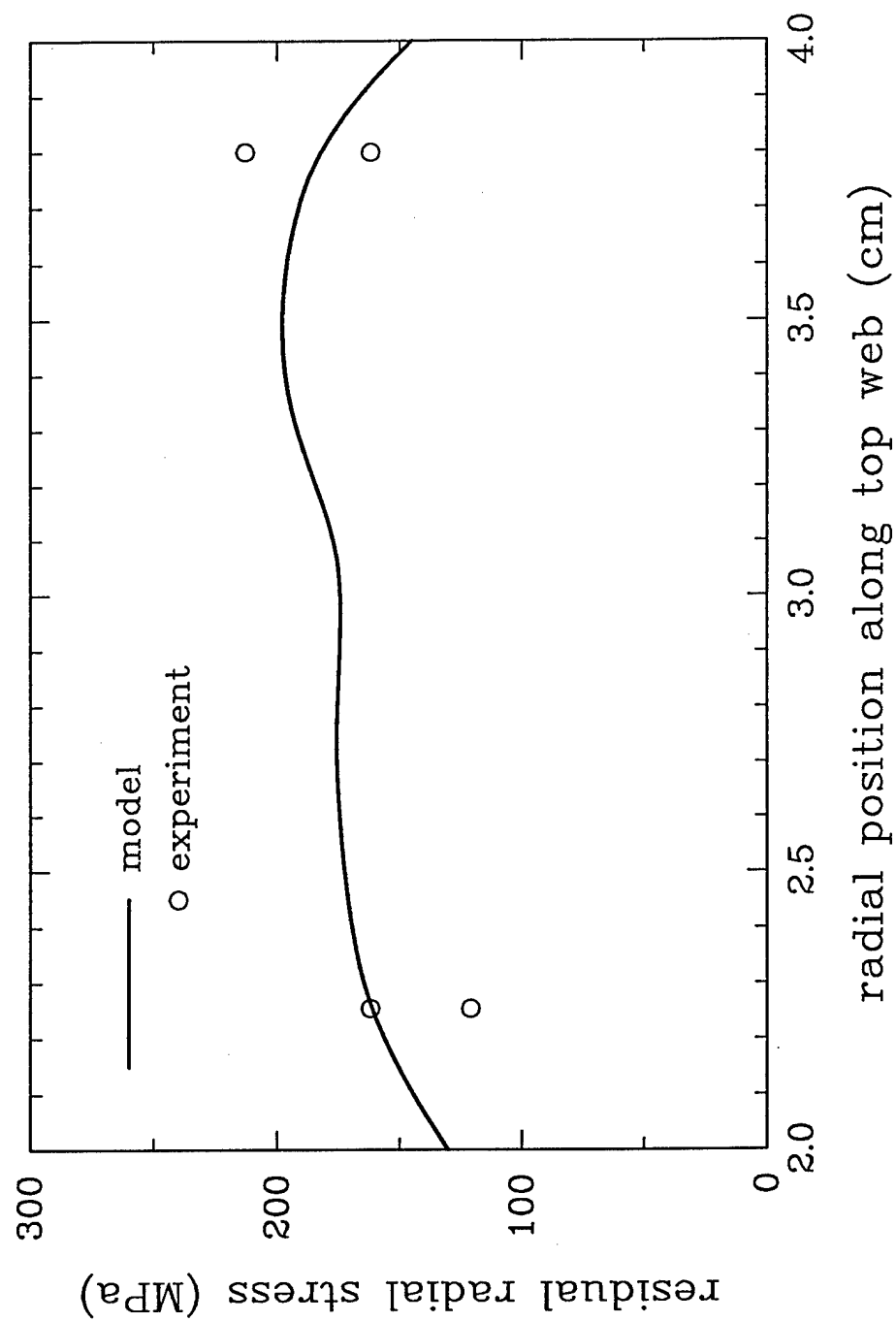


Figure 76. Profiles of calculated radial stress along the top of the web following deep-freeze.

the good agreement between the model predictions of peak axial web distortion and the average of measured values is less significant and prevents a more quantitative assessment of model accuracy.

Simulation of the heat treatment of the gear blank has been a valuable experience; some of the lessons learned from this case study include the following:

- carburization distortion is small; prior residual stresses likely have little effect on distortion;
- change in part size is a strong function of the relative magnitudes of thermal and transformation volume change;
- although, in the experiments, web distortion and web residual radial stresses were most strongly influenced by control of the quench press die, model calculations suggest that differences in heat transfer above and below the web are also an important factor;
- rim hoop residual stresses are a strong function of the carbon gradient, its influence on transformation parameters, and the deep-freeze temperature;
- Overall, the most important parameters for this study appear to be surface heat transfer coefficients and volume change parameters;

## CONCLUSIONS

In this investigation, a model for simulation of heat treatment processes for helicopter gears, namely carburization, quench, deep-freeze and temper, has been developed and has been incorporated into the commercially available finite element code ABAQUS. The extensive list of material properties and boundary conditions, both thermal and mechanical, have been determined through measurement or literature review. Finally, the modelling approach has been tested and improved through application to two simple problems.

While there are clearly many issues that still must be explored regarding the physics of the model, the level of accuracy of the material properties that are required, and the methods by which surface conditions are accounted for, it is the belief of the authors that the approach taken in this study has provided a methodology which can be successfully applied to improve heat treatment processes for helicopter gears and other precision components.

The thermomechanical modelling framework that has been developed provides a relatively straightforward means to probe the interrelationships between the material properties of the steel, the geometry of the gear, the heat treatment processing parameters and the performance requirements of the finished product. The structure of the model has been developed to a state at which, as more data are gathered, it can easily be extended to account for features that are deemed to be important, and it can also be easily simplified so that calculation time is not wasted in accounting for unimportant features.

The material property set that has been determined for 9310 steel, although by no means complete, is arguably one of the most comprehensive sets in existence for modelling of this sort and provides a firm basis from which to continue to build a comprehensive material database.

The investigation of the flat disk provided an initial means to validate the model. The results of this study also clearly showed the importance of having material property data that are accurate for the processing conditions that are being simulated. Further material property tests must be designed to account for process parameter variation.

The application of the model to the rim/web gear blank provided an invaluable first look at how the model will be applied as a tool. There are several conclusions that can be drawn from this experience:

- While experimental difficulties and a lack of some material property data prevented a more quantitative assessment of the model's capabilities, the general agreement between average predicted and measured distortion and residual stresses is encouraging and provides an initial degree of confidence that the finite element modelling methodology that has been developed can provide reasonable predictions of distortion and residual stress.
- the boundary conditions associated with the press quench are quite complex and need to be better understood, both from the point of view of making more accurate models and for improving die design. For example, some questions that must be answered

include: how much frictional constraint do the dies impose? Would more or less of a constraint provide for more distortion control? How much pressure should be applied to various parts of the gear? Can optimal pressure levels be determined through modelling? Finally, it is clear that heat transfer coefficients play a key role in distortion during quench. How can modelling help determine better oil flow rates and flow paths?

- In the absence of die pressure irregularities, it appears that distortion during quench is most dramatically affected by the interaction of the following parameters:
  - variations in surface heat transfer coefficients;
  - thermal expansion coefficients;
  - martensite transformation parameters, i.e. transformation temperatures and transformation volume change;
  - strength levels.

It is the chain of interaction during quench that is governed by the values of these parameters that produce distortion: (1) gradients in temperature are caused by rapid heat transfer through the surface of the part, which become more severe when the heat transfer conditions vary; (2) these gradients in temperature produce gradients in volume change due to thermal expansion and martensitic transformation; (3) the accommodation of gradients in volume change produce internal stresses; (4) finally, distortion results from the plastic deformation that occurs when the internal stresses exceed the strength level of the alloy.

This chain of interaction implies is that the accuracy of computer simulations models will be greatest when these fundamental parameters are accurately modelled. Thermal expansion coefficients are relatively easy to determine, but all of the other parameters on this list are harder to pin down. Martensite transformation parameters are easily measured above room temperature, but are more difficult to determine below room temperature. Strength levels are difficult to determine because of the transient nature of the parameters on which they depend, namely temperature and volume fraction. Finally, heat transfer conditions, which are perhaps the most critical, unfortunately seem to be the most difficult to quantify. Unlike the other parameters, which are material properties and are therefore not gear-specific, heat transfer conditions depend strongly on the geometry of the gear and the die, and the flow characteristics of the oil. More effort needs to be put into the development of methods to quantify heat transfer coefficients without relying on the extensive use of data obtained from instrumented gears.

One question that still remains is whether the models can provide predictions of the very small distortions associated press-quenching with sufficient accuracy, given the large variability of observed distortions. The model is certainly capable of predicting very small distortions, but the merit of these predictions is diminished if the magnitude of the predicted distortions are swamped by the magnitude of the observed variability. It may turn out that the model will be best used as a tool that predicts distortion patterns, and how these patterns change with variations in processing parameters, as opposed to one that will be used to predict absolute magnitudes of distortion for a particular set of processing conditions.

## RECOMMENDATIONS

The work presented here represents a first step toward development of practical heat treat simulation tool that can provide great benefit to the designer of heat treat processes for helicopter gears. Given the complex nature of the problem, however, further development of the model is required to bring it to such a practical level. Continued work on this topic should include:

- Refining the model and using it to explore the relative importance of process parameters. The scope of work in this program did not call for such exploration, but at this juncture, it is necessary to determine which of the many parameters which affect distortion are the most significant. The structure of the model that has been developed is flexible and can easily be extended to account for material behaviors, such as transformation-induced plasticity, that have not yet been considered. Of course, many of the parameters that describe such behavior have not yet been measured, so some estimation of their magnitude, based upon sound engineering judgment, will be required. It should be noted that it is not only the magnitude of the various parameters that is important — the extent and nature of the variation of these parameters must be explored as part of this effort.
- Depending upon the results of these sensitivity studies, gaps in the 9310 material property database should be filled. It is already clear from the simulations that have been performed in this study that better information is needed regarding material expansion behavior during heat-up and that regarding cooling behavior at high carbon levels. Also, better data is needed to feed the carbon diffusion model. Finally, a more accurate value for the volume change accompanying temper is required.
- While it was certainly beneficial to explore the use of the model for simulation of distortion during press-quench, it is probably prudent to now take a step back and study the free-quench of a part with a geometry of intermediate complexity. In this manner, the complications inherent with the press-quench itself can be separated from those associated with exposure of the part to a flowing quench medium.
- Once the model's ability to simulate heat treatment of structures of intermediate complexity has been confirmed, the application of the model to actual gears, with teeth, must be explored. Including the teeth complicates matters in two ways: (1) it increases computation time extensively, and thus it is important to optimize the program to minimize computation requirements; (2) oil flow nonuniformities become much more significant, and therefore the variation in surface heat transfer coefficients become more difficult to predict. Included in such an effort must be a study of the variation in heat transfer coefficients around the gear and, in particular, at different locations on the teeth.
- More extensive study of quench-press boundary conditions is also clearly needed. If the ultimate utility of the model is to lie in modelling the press quench operation, then the parameters of the press-quench that affect the gear most need to be better understood. Such a study will have the added benefit of providing a means to

improve die designs and optimize flow controls.

- Finally, how to best integrate the software into manufacturer's CAD systems must be investigated. Several questions must be answered: What, if any, specialized front-end programs must be connected to the ABAQUS-based analysis tool? To what extent should the user of the program be familiar with the details of the code? Will the code need to be transferred to other analysis platforms? System integration is a logical step that should follow-up refinement of the model and confirmation of its utility as a tool.

### ACKNOWLEDGMENTS

This investigation was funded by the U.S. Army Aviation and Troop Command (ATCOM) through the Advanced Concepts and Technology Program (ACT) under contract DAAJ02-92-0030. The author wishes to thank the following individuals for their contributions to this effort: Philip LaFerriere of the Aviation Applied Technology Directorate of ATCOM in Fort Eustis, Virginia; Oscar Gomez and Nirmal Singh from ATCOM in St. Louis; Joyce Illinger of the ACT program; Bruce Hansen and John Walsh of Sikorsky Aircraft; Gerry Koller, Maurice Howes, Michael Skrzypchak, and Terry Phillipi of IITRI; George Eldis of Climax Research Laboratories, Lorenzo Majno of MANLABS; Ron Mayville and Shaun Berry of Arthur D. Little; and Peter Hilton and Jack O'Brien, formerly of Arthur D. Little.

## REFERENCES

- [1.] G.A. Stickels, "Gas Carburizing," in ASM Handbook on Heat Treating, Vol. 4, ASM International, 1991, p. 312.
- [2.] ABAQUS, version 5.4, Hibbitt, Karlsson and Sorensen, Inc., Pawtucket, RI.
- [3.] R.D. Krieg and D.B. Krieg, J. Press Vessel Tech., Vol. 99, 1977, p. 510.
- [4.] G.L. Tibbetts, J. Appl. Phys., Vol. 51, 1980, p. 4813.
- [5.] R.E. Reed-Hill, "Physical Metallurgy Principles," D. Van Nostrand Company, 1973, p. 723.
- [6.] R.F. Price and A.J. Fletcher, "Determination of Surface Heat Transfer Coefficients During Quenching of Steel Plates," Metals Technology, May 1980, p. 203.
- [7.] F.G. Rammerstorfer, D.F. Fischer, W. Mitter, K.J. Bathe and M.D. Snyder, "On Thermo-elastic-plastic Analysis of Heat-treatment Processes Including Creep and Phase Changes," Computers and Structures, Vol. 13, 1981, p 771.
- [8.] L. Kaufman, "Thermodynamics of Martensitic Transformations," in Martensite, edited by G.B. Olson and W.S. Owen, ASM, Metals Park, OH, 1992, p. 41.
- [9.] H.-J. Solter, "Changes in Thermal Diffusivity of the 32 NiCrMoV 12 3 steel associated with phase transformations.
- [10.] M. Henriksen, D.B. Larson, and C.J Van Tyne, "Modeling Distortion and Residual Stress in Carburized Steels," in Quenching and Distortion Control, Edited by G.E. Totten, ASM, Metals Park, OH 1992.
- [11.] G. Krauss, "Steels, Heat Treatment and Processing Principals," ASM, Metals Park, OH, 1989.



Appendix A. Carbon Content and Hardness Measurements Performed by Dirats Laboratories.

Richard G. Stringfellow, Ph.D.  
 Arthur D. Little, Inc.  
 20 Acorn Park  
 Cambridge, MA 02140-2390

Report Number 177991  
 Report Date 2-FEB-93  
 Page 1 of 1  
 Client Number 504475  
 Client Order 202973-00

RECEIVED 1 Test Sample approx. .126" dia. x 1"  
 IDENT AS \*  
 MATERIAL 9310 Steel  
 CONDITION Through Carburized  
 TEST TO \*  
 TEST PER Client Instructions  
 PURPOSE \*  
 SPEC INST Fax report 617-864-4912

PHONE 617-864-5770

PROPERTIES AS SUPPLIED

**QUANTITATIVE ANALYSIS BY COMBUSTION**

%  
 C 0.34

For Info

**MICROHARDNESS TEST**

Depth	Hardness	Equiv
0.00625" Surface	HV(500G) 544	HRC 52
0.01250"	HV(500G) 546	HRC 52
0.01875"	HV(500G) 552	HRC 52.5
0.02500"	HV(500G) 514	HRC 52
0.03125"	HV(500G) 472	HRC 47
0.03750"	HV(500G) 526	HRC 51
0.04375"	HV(500G) 479	HRC 47.5
0.05000"	HV(500G) 521	HRC 50.5
0.05625"	HV(500G) 509	HRC 50
0.06250" Core	HV(500G) 516	HRC 50

Disp  
 For Info

WE CERTIFY THIS IS A TRUE COPY OF OUR RECORDS

Signed for J. Dirats and Co. by Eric Dirats, Audit Manager

NOTE: The recording of false, fictitious or fraudulent statements or entries on this document may be punished as a felony under federal law.



Richard G. Stringfellow, Ph.D.  
 Arthur D. Little, Inc.  
 20 Acorn Park  
 Cambridge, MA 02140-2390

Report Number 177262  
 Report Date 14-JAN-93  
 Page 1 of 1  
 Client Number 504475  
 Client Order 202973-00

RECEIVED 1 Test Sample approx. .126" dia. x 1"  
 IDENT AS \*  
 MATERIAL 9310 Steel  
 CONDITION Through Carburized  
 TEST TO \*  
 TEST PER Client Instructions  
 PURPOSE \*  
 SPEC INST Fax report 617-864-4912  
 PHONE 617-864-5770

PROPERTIES AS SUPPLIED

QUANTITATIVE ANALYSIS BY COMBUSTION

EL	%	
C	0.58	Disp For Info

MICROHARDNESS TEST

Depth	Scale	Reading	Equivalent	Disp For Info
0.00625" Surface	HV(500G)	689	HRC 60	
0.01250"	HV(500G)	692	HRC 60	
0.01875"	HV(500G)	689	HRC 60	
0.02500"	HV(500G)	704	HRC 60	
0.03125"	HV(500G)	692	HRC 60	
0.03750"	HV(500G)	678	HRC 59	
0.04375"	HV(500G)	681	HRC 59	
0.05000"	HV(500G)	678	HRC 59	
0.05625"	HV(500G)	678	HRC 59	
0.0625" Core	HV(500G)	678	HRC 59	

WE CERTIFY THIS IS A TRUE COPY OF OUR RECORDS

Signed for J. Dirats and Co. by Eric Dirats, Audit Manager

NOTE: The recording of false, fictitious or fraudulent statements or entries on this document may be punished as a felony under federal law.

Arthur D. Little, Inc.  
20 Acorn Park  
Cambridge, MA 02140-2390

Report Number 176599  
Report Date 30-DEC-92  
Page 1 of 1  
Client Number 504475  
Client Order 202973-00

RECEIVED 1 Test Sample approx. .122" dia. x 1"  
IDENT AS \*  
MATERIAL 9310 Steel  
CONDITION Through-Carburized  
TEST TO \*  
TEST PER Client Instructions  
PURPOSE \*

PHONE 617-864-5770

PROPERTIES AS SUPPLIED

QUANTITATIVE ANALYSIS BY COMBUSTION

EL %  
C 0.83

Disp  
For Info

MICROHARDNESS TEST

Depth	Scale	Reading	Equivalent
0.00000" Surface	HV(500G)	601	HRC 55
0.00625"	HV(500G)	619	HRC 56
0.01250"	HV(500G)	619	HRC 56
0.01875"	HV(500G)	623	HRC 56.5
0.02500"	HV(500G)	636	HRC 57
0.03125"	HV(500G)	653	HRC 58
0.03750"	HV(500G)	642	HRC 57.5
0.04375"	HV(500G)	653	HRC 58
0.05000"	HV(500G)	629	HRC 57
0.05625" Core	HV(500G)	626	HRC 57

For Info

WE CERTIFY THIS IS A TRUE COPY OF OUR RECORDS

Signed for J. Dirats and Co. by Eric Dirats, Audit Manager

NOTE: The recording of false, fictitious or fraudulent statements or entries on this document may be punished as a felony under federal law.

Appendix B. CCT Diagram Development Performed by Climax Research Services.



# CLIMAX RESEARCH SERVICES

39205 COUNTRY CLUB DRIVE • FARMINGTON HILLS, MI 48331 • (313) 489-0720 • FACSIMILE 489-8997

---

Report S-1895

CONTINUOUS COOLING TRANSFORMATION BEHAVIOR OF SAE 9310 STEEL

Prepared for Arthur D. Little Co.

18 September 1992

## Continuous Cooling Transformation Behavior of SAE 9310 Steel

Background Information

SAE 9310 is a "premium" grade of carburizing steel containing nominally 0.1% C, 0.55% Mn, 0.25% Si, 3.25% Ni, 1.2% Cr and 0.1% Mo. Climax Research Services (CRS) was provided a sample of this steel by Arthur D. Little Company (ADL) for dilatometric studies. CRS was requested to determine the continuous cooling transformation (CCT) behavior of the material after austenitizing at 1525F (829C). Because of the quenching procedures and section sizes relevant to the application of current interest to ADL, very good definition of the transformation behavior at relatively rapid cooling rates (cooling times of 10 minutes and less) was requested, with less precise definition of the CCT diagram at slower cooling rates.

Procedures

The material was received as a single piece of hot-rolled bar stock, nominally 0.5 inch diameter by 12 inches length. Cylindrical dilatometer specimens were machined from this stock, 3 mm diameter by 10 mm length, with a 2 mm diameter hole drilled axially into one end to a depth of approximately 5 mm.

A quenching dilatometer was used for all thermal processing. This instrument employs induction heating of the test specimens *in vacuo*. Temperature measurement and control is accomplished via a Pt/Pt-13%Rh thermocouple spot welded to the specimen in the axial hole. The desired thermal cycles are achieved with a programmable controller, balancing the induction power input to the specimen against thermal losses due to radiation; at lower temperatures where radiation losses are small, and/or when fast cooling rates are required, He gas is admitted to the specimen chamber to provide additional, convective cooling. Specimen temperature and length are continuously monitored and recorded during thermal processing. The temperature ranges over which phase transformation occurs are established from the specimen length vs. temperature data, as described in the literature.<sup>1</sup>

The lower and upper critical temperatures,  $Ac_1$  and  $Ac_3$ , of the steel were determined on a single dilatometer specimen. This was heated rapidly to 600C and stabilized at temperature, then heated further to 960C at a controlled rate of 2 C/min.

Usually, CCT behavior is determined by examining individual samples at nine to ten different cooling rates more-or-less equally spaced on a logarithmic scale and covering cooling times ranging from several seconds to 24 hours. In the present study, however, given the special needs of ADL, the ten cooling programs were chosen so that the maximum cooling time was 270 minutes, with

-----

1. G.T. Eldis, "A Critical Review of Data Sources for Isothermal Transformation and Continuous Cooling Transformation Diagrams," Hardenability Concepts with Application to Steels, D.V. Doane & J.S. Kirkaldy, eds., AIME, Warrendale PA, 1978, p. 126.

six of the ten programs equally and logarithmically spaced over 10 seconds to 10 minutes cooling time. Linear programs were used on all ten specimens, and linear cooling was generally well maintained except as disturbed by transformation recalescence. Prior to cooling, each sample was held for 20 minutes at the austenitizing temperature of 1525F (829C). Table 1 summarizes the programmed cooling times and actual average cooling rates (800-500C) for all ten specimens.

After dilatometer processing, the ten program cooled specimens were mounted in room-temperature curing epoxy resin and prepared for metallographic examination by normal mechanical methods. The specimens were etched in 2% Nital and examined optically at magnifications to 1000X to identify the transformation products present. Following metallographic examination, the hardness of each specimen was measured using a diamond pyramid indenter and 10 kg load.

### Results and Discussion

The CCT diagram established from the dilatometric records, microstructural examinations and hardness tests combined, is presented in Figure 1. On the diagram, horizontal lines indicate the austenitizing temperature,  $T_A$ , and the critical temperatures,  $Ac_{1,3}$ . The number written at the end of each cooling curve is the dilatometer specimen hardness (HV10) after cooling as indicated. Transformation "phase boundaries," indicating the temperature ranges over which dilatometrically detectable transformation to various microconstituents occurs on cooling, are defined by the solid lines intersecting the cooling curves. The dashed lines within these transformation regions are iso-transformation contours and indicate, approximately, the volume fraction of austenite that has transformed on reaching the indicated temperature. This approximation, deduced from the specimen length vs. temperature data as described elsewhere,<sup>1</sup> is reasonably accurate when austenite transformation is essentially completed upon reaching room temperature; the accuracy of the estimate decreases as the amount of retained austenite remaining in the specimen increases.

Under the processing conditions investigated here, substantial quantities of bainite form in the material at intermediate cooling times. The bainite that forms is of the "granular" or "carbide-free" type (see Figure 2a), consisting of small islands of carbon-enriched austenite in a dislocated / acicular ferrite matrix as opposed to the conventional acicular ferrite + carbide structure. This retained austenite partially transforms to martensite at lower temperatures; close examination of the specimen length vs. temperature records suggests the  $M_s$  of the carbon-enriched austenite islands is on the order of 150C (302F).

At the two fastest cooling rates examined, the dilatometer records indicated a fully martensitic structure is obtained, and this was generally confirmed by microstructural examination (Figure 2b). The  $M_s$  is approximately 435C (815F). However, prolonged scanning of the metallographic sample suggested to this writer the presence of trace amounts of bainite in the microstructure of the two most rapidly cooled samples, and this is indicated in the CCT diagram by the "Traces Bainite" legend written just above the  $M_s$ .

The microstructure obtained at the two slowest cooling rates examined consists of polygonal ferrite, some relatively large islands of retained



austenite + martensite (M-A constituent), and granular bainite (Figures 2d and 2e). Pearlite, presumably requiring much slower cooling rates to form, was not observed. The larger islands of M-A constituent apparently result from localized carbon enrichment of the austenite during the growth of polygonal ferrite. These carbon-enriched regions remain stable during cooling through the bainite transformation range, partially transforming to martensite at temperatures below 150C (302F). The granular bainite formed in these more slowly cooled samples apparently nucleates and grows in regions that have not been significantly enriched in carbon as a result of the polygonal ferrite formation.

#### Summary

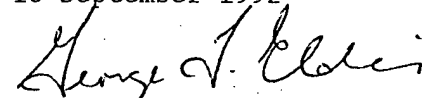
The lower and upper critical temperatures of the hot rolled SAE 9310 examined are 670C and 760C, respectively (1238 and 1400F).

At cooling rates faster than about 30 C/s (54 F/s), a predominately martensitic structure is obtained, with traces of bainite detectable by careful metallographic examination but not by dilatometry. The Ms is approximately 435C (815F).

Under the processing conditions examined, the bainite that forms in this material is of the granular or carbide-free type, consisting of islands of M-A constituent in acicular ferrite. The Ms of the carbon-enriched austenite islands initially in the bainite is on the order of 150C (302F).

High temperature transformation products, e.g. polygonal ferrite, form at cooling rates slower than about 0.3 C/s (0.5 F/s).

CLIMAX RESEARCH SERVICES  
18 September 1992



Dr. George T. Eldis  
Metallurgical Engineer

Table 1. Summary of Cooling Rates Investigated

Cooling <sup>(a)</sup> Curve	Programmed Linear Cooling Time	Actual <sup>(b)</sup> Cooling Rate, C/s
1	10s	81
2	20s	41
3	40s	19.4
4	1m 20s	9.9
5	2m 40s	4.0
6	5m	2.7
7	10m	1.4
8	30m	0.45
9	1h 30m	0.15
10	4h 30m	0.05

Notes: (a) Reading left to right on the CCT diagram, Figure 1.

(b) Average cooling rate over the temperature range 800 to 500C (1470 to 930F).

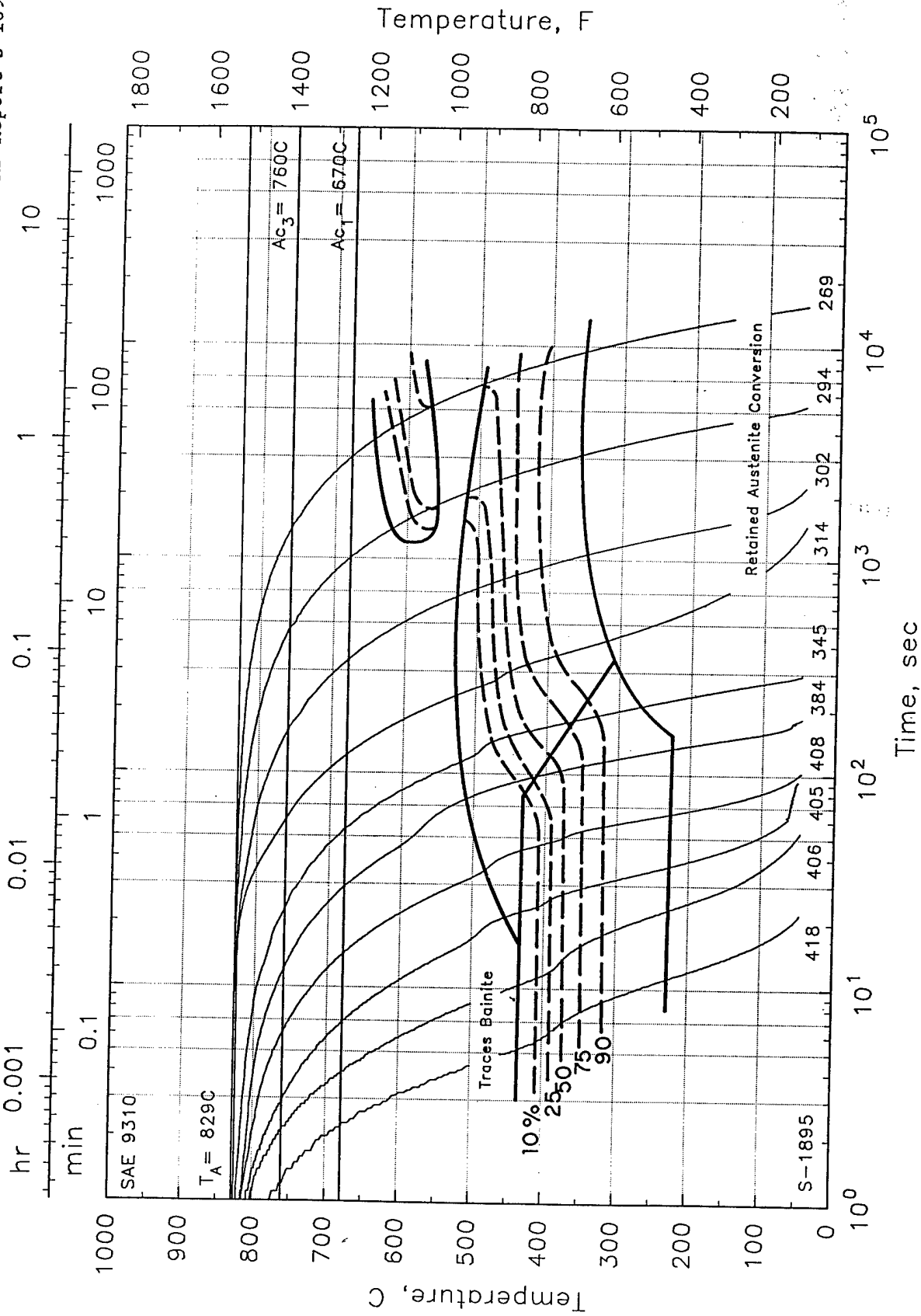
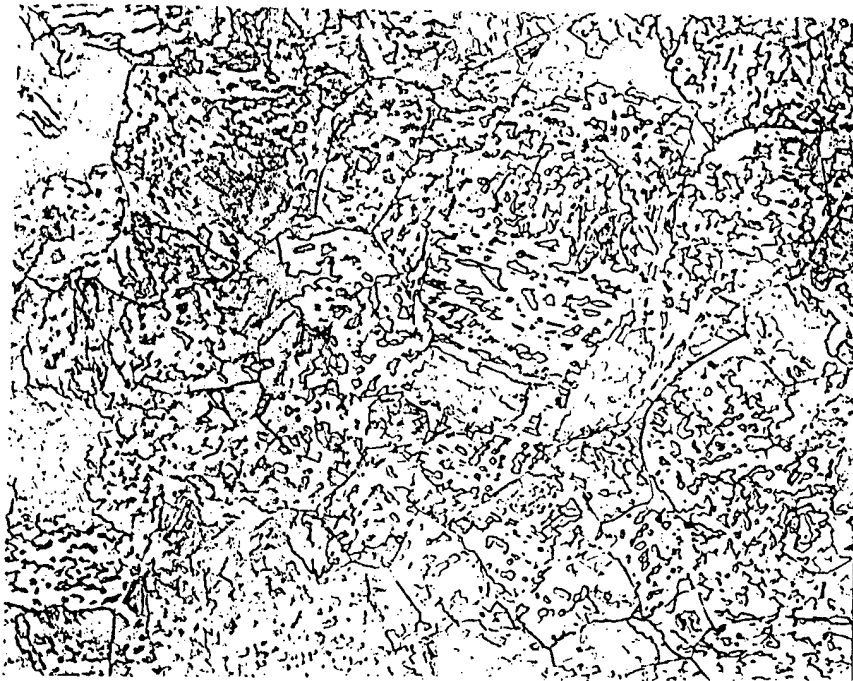


Figure 1. CCT diagram for SAE 9310, austenitized 20 minutes at 829C (1525F).



(a) Granular bainite structure. Sample cooled at 1.4 C/s, final hardness 314 HV10. 1200X.



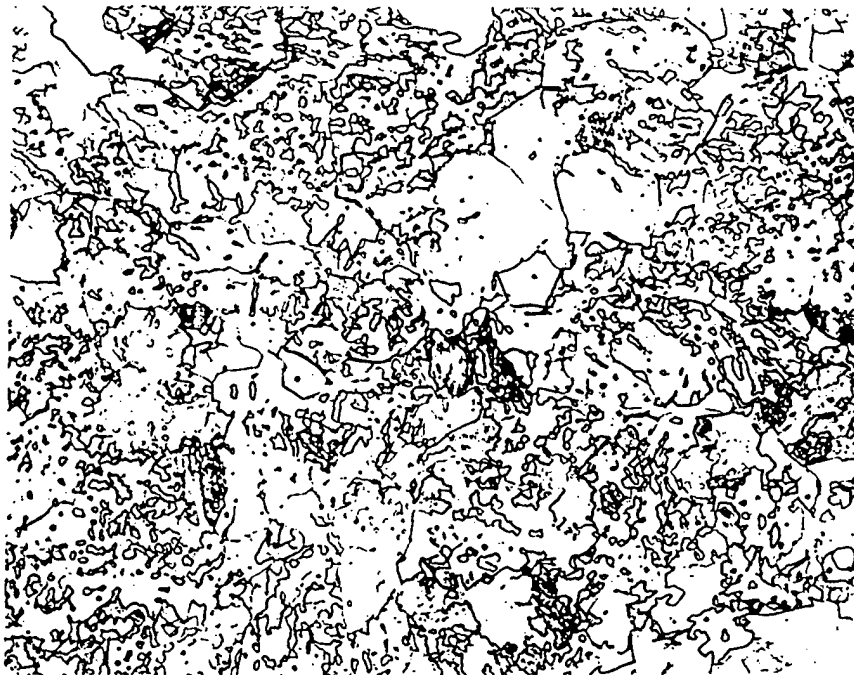
(b) Predominately martensitic structure. Sample cooled at 41 C/s, final hardness 406 HV10. 1200X.

Figure 2. Microstructures of the transformed dilatometer specimens.  
2% Nital etch.

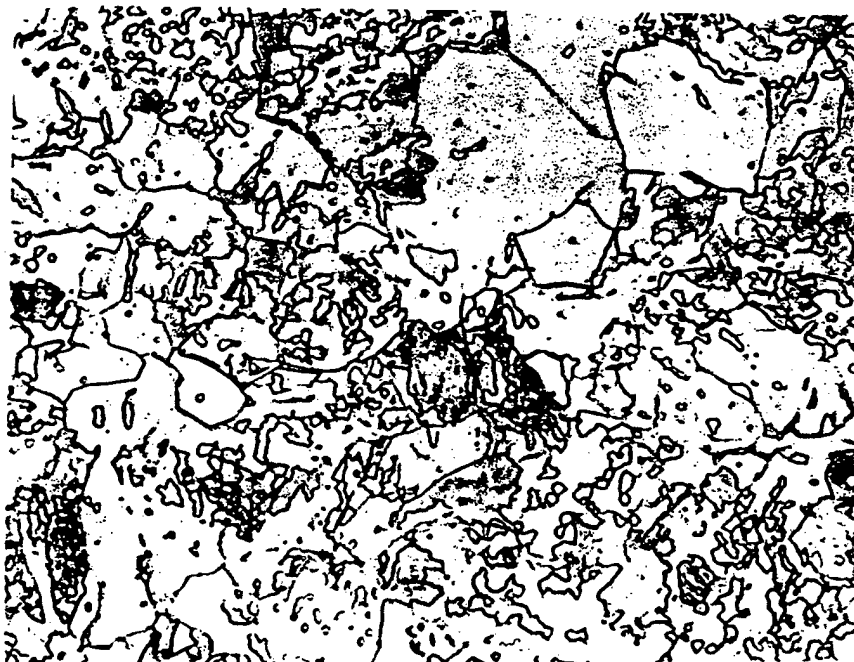


(c) Mixed microstructure of martensite + granular bainite. Sample cooled at 19.4 C/s, final hardness 405 HV10. 1200X.

Figure 2 (continued).



(d) Mixed microstructure of polygonal ferrite, granular bainite and M-A constituent. Sample cooled at 0.05 C/s, final hardness 269 HV10. 1200X.



(e) Same area as (d) above. 2000X.

Figure 2 (concluded).



# CLIMAX RESEARCH SERVICES

39205 COUNTRY CLUB DRIVE • FARMINGTON HILLS, MI 48331 • (313) 489-0720 • FACSIMILE 489-8997

---

Report S-1895-2

CONTINUOUS COOLING TRANSFORMATION BEHAVIOR OF SAE 9310 STEEL  
THROUGH-CARBURIZED TO FOUR DIFFERENT CARBON CONTENTS

Prepared for Arthur D. Little Co.

3 March 1993

## Continuous Cooling Transformation Behavior of SAE 9310 Steel Through-Carburized to Four Different Carbon Contents

### Background

In a previous study,<sup>1</sup> Climax Research Services (CRS) determined the continuous cooling transformation (CCT) behavior of SAE 9310 steel. Subsequent to that investigation, Arthur D. Little Co. (ADL) provided CRS with an additional piece of 9310 for further study. CRS was requested to prepare dilatometer samples from the material provided which were then to be through-carburized to four different carbon contents. The CCT behavior would then be determined, for relatively rapid cooling rates, at all four carbon levels. The goal was to establish the transformation behavior at various locations in the case of a carburized component.

### Procedure

The material was received as a single piece of bar stock, nominally 17 mm diameter by 275 mm length. Twenty dilatometer samples were machined from the bar, each 10 mm length by 3 mm diameter with a 2 mm diameter hole drilled axially into one end to a depth of 5 mm. At the request of ADL, these samples were shipped to Klock Company in Manchester, Connecticut, where four groups of five samples each were through carburized to four different carbon contents.

Quenching dilatometry was used to determine the CCT behavior of the carburized samples. The test apparatus, test procedures and general methods of interpreting the data have been described elsewhere.<sup>1,2</sup>

In the present study, the lower and upper critical temperatures,  $Ac_1$  and  $Ac_3$  or  $Ac_{cm}$ , were determined by heating a single sample of each carbon content at 2C/min (3.6F/min) between the temperatures of 600 and 960C (1112 and 1760F). Transformation behavior on cooling was determined by austenitizing individual samples at 829C (1525F) for 20 minutes and then quenching at controlled rates of nominally 80, 40, 20 or 10 C/s (144, 72, 36 or 18 F/s).

After processing in the dilatometer, the controlled-cooled samples were mounted in room temperature curing epoxy resin and prepared for metallographic observation by normal mechanical methods. The final plane of observation was transverse to the specimen axis and 1-2 mm below the solid end of the sample. After polishing to a 1 $\mu$  finish, the hardness of each sample was measured with a diamond pyramid indenter and 10 kg load. The samples were then finish polished, etched in 2% Nital and examined optically at magnifications to 1250X to identify the microconstituents that had formed during cooling.

### Results and Discussion

#### Condition of the As-Carburized Samples

The small amount of material available for study precluded examination of the starting microstructure of the as-carburized specimens. The matte, dark gray external appearance of the samples reportedly carburized to carbon contents of 0.34, 0.58 and 0.83% suggests to this writer that those treatments were performed in an endothermic type of atmosphere. The substantial amount



of intergranular/surface oxidation (IGO) visible on the metallographic sections of these samples after dilatometer processing (see Figure 1) supports this view. In contrast, the bright, shiny appearance of the samples reportedly containing 0.1% carbon indicates that these were mock or blank carburized in either a vacuum or in a quite clean inert or slightly reducing atmosphere. No IGO was detected after dilatometer processing of these lower carbon specimens. The depth of IGO on the higher carbon samples is on the order of 0.02 mm (0.001 in). However, at the four cooling rates investigated, the IGO was not accompanied by any significant amount of high temperature transformation products. Thus, its presence in these samples is not expected to have had a measurable effect on the CCT behavior.

The reader is cautioned that, as of this writing, it is not known if the material provided for this investigation is from the same heat of steel used in the previous study; whether or not this is the case will influence the comparison of the partial CCT diagrams produced here with the more complete diagram produced previously.

### Transformation Behavior

The partial CCT diagrams determined for the SAE 9310 at the four different carbon contents are presented in Figures 2 and 3. These constructions represent the final results of analysis of the dilatometric, metallographic and hardness data combined. The figures are constructed to the same scale as the CCT diagram produced in the previous study, to facilitate comparison by overlay if desired.

Table 1 presents the actual cooling rates imposed on each individual test specimen. The deviation of the actual cooling rates from the aim nominal cooling rates of 80, 40, 20 and 10 C/s is a result of the inability of the apparatus to provide complete and reproducible control over the separate, competing processes of He gas quenching and induction heating which are superimposed on the specimen to achieve the desired linear quenching rates. This lack of precision in control increases with increasing quenching rate.

Table 2 shows, for each of the four carbon contents in question, the lower and upper critical temperatures, the average  $M_s$ , and a dilatometric and metallographic estimate of the amount of retained austenite remaining in the material at room temperature. The decrease in  $M_s$  with increasing carbon content is on the order of 420 C/wt.-%, in reasonable agreement with data in the literature.<sup>2</sup> Within experimental error, the lower critical temperature is independent of carbon content, as is to be expected. For the hypoeutectoid carbon contents (0.10 and 0.34%), the upper critical temperature decreases with increasing carbon content, again as expected. Increasing the carbon content further to 0.58% results in an increase in the upper critical temperature, suggesting the steel is hypereutectoid at this carbon content. On this basis alone, the author has designated the upper critical temperature as  $Ac_{cm}$  rather than  $Ac_3$  on the partial CCT diagram for this carbon level (Figure 3, left). At 0.83%C, the material is unquestionably hypereutectoid, as demonstrated by the transformation products formed on cooling (see discussion below). The fact that the apparent  $Ac_{cm}$  is lower for the 0.83%C material compared with the 0.58%C material is not too surprising in this writer's experience: The apparent  $Ac_{cm}$  is influenced by the rate of carbide dissolution at the heating rates employed, which in turn is strongly influenced by

the starting carbide morphology and distribution. As noted above, the starting condition of the as-carburized dilatometer specimens was not determined here.

The retained austenite estimates in Table 2 refer to those regions of the FCC constituent which might transform to additional martensite on sub-zero cooling. For the two lower carbon contents, the dilatometric length vs. temperature records indicated resumption of linear thermal contraction behavior (i.e., an  $M_f$ ) at sufficiently high temperatures that this writer feels quite confident of the estimates of 0% transformable austenite at room temperature in these materials. For the two higher carbon contents, the  $M_f$  was unquestionably below room temperature and could only be roughly estimated by extrapolation of the non-linear "tails" on the length-temperature curves. The estimates of transformable retained austenite for these two materials are thus rough approximations that may easily be too low by 5 to 10 vol.-%.

#### Base Alloy (0.1%C)

This is "the same" material previously studied, and comparison of the current partial CCT diagram (Figure 2, left) with that determined earlier reveals generally minor differences between the two. Traces of bainite can be observed in the microstructure after cooling at even the fastest rates, even though the amount of transformation was insufficient to be detected by the dilatometer. The slightly lower  $M_s$  and greater delay in the onset of significant (i.e., dilatometrically detectable) bainite transformation in the present study might be considered within the realm of experimental error. There is, however, one significant difference between the two sets of samples in question, namely in the as-quenched hardness of the dilatometer specimens, indicated at the lower end of the respective cooling curves. In the present study, the hardness is consistently 20-30 HV10 lower (2-3 HRC equivalent). This major difference, combined with the other differences noted above, suggests to this writer that the material used in the present study is indeed from a different heat of steel than previously used, a heat with somewhat lower carbon content and greater total alloy content.

Figure 4 presents optical micrographs of the most rapidly and the most slowly cooled of the base alloy specimens.

#### Material Carburized to 0.34 and 0.58%C

The CCT diagrams of these two intermediate carbon materials, Figure 2 (right) and Figure 3 (left), indicate only martensite formation at the four cooling rates examined. With increasing carbon content, the transformation temperature range decreases, and the transformed hardness increases, as expected.

Optical micrographs of the most slowly cooled sample of each carbon content are presented in Figures 5 and 6. Increasing carbon content from 0.1 to 0.34% results in a very pronounced change in martensite morphology, from a predominately lath structure (Figure 4a) to more randomly oriented platelets (Figure 5). The morphological change on going from 0.34 to 0.58%C is less pronounced (compare Figures 5 and 6) and appears to involve a decrease in definition of the inter-platelet boundaries more than any other change. This may be simply the result of a lower etching response in the higher carbon

material due to a decrease in the amount of autotempering possible with decreasing transformation temperature.

#### Material Carburized to 0.83%C

The CCT diagram for the highest carbon material (Figure 3, right) indicates, in addition to martensite formation at still lower temperatures, the precipitation of carbides in the austenite prior to martensite formation. Note that the transformed hardness has decreased somewhat relative to the 0.58%C material, apparently because of the higher retained austenite content of the higher carbon samples.

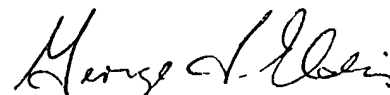
The carbide precipitation is not detectable dilatometrically, but is readily evident when the microstructure is examined. At the fastest cooling rate, there is no evidence of carbide; the micrograph (Figure 7a) shows only small white patches of retained austenite in a martensitic matrix that is very unresponsive to the etchant. At a nominal cooling rate of 40 C/s, a small amount of carbide precipitate is seen decorating prior austenite grain boundaries (Figure 7b). At the slowest cooling rate, nominally 10 C/s, grain boundary precipitation is very pronounced, and some carbide precipitation within the prior austenite grains is evident as well (Figure 7c). Throughout, the martensitic matrix remains very unresponsive to etching, apparently due to the nearly complete absence of any autotempering at the low transformation temperatures involved.

#### Summary

Raising the carbon content of the SAE 9310 base composition to 0.34% and higher eliminates the formation of bainitic microconstituent at cooling rates of 10 C/s or faster. With increasing carbon content, the martensite transformation temperatures decrease, and the martensite morphology changes from generally parallel laths to more randomly oriented platelets. Transformed hardness increases with carbon content from 0.1 to 0.58%C. At 0.83%C, the transformed hardness is significantly lower than at 0.58%C, apparently due to the increased amount of retained austenite present.

The dilatometric and metallographic data indicate that the 9310 base composition is most probably hypereutectoid at 0.58%C, and definitely hypereutectoid at 0.83%C. In the 0.83%C material, at cooling rates of 40 C/s or slower, formation of martensite is preceded by precipitation of carbides in the austenite, first at austenite grain boundaries and then within the grains themselves.

CLIMAX RESEARCH SERVICES  
3 March 1993



Dr. George T. Eldis  
Metallurgical Engineer

References

1. G.T. Eldis, "Continuous Cooling Transformation Behavior of SAE 9310 Steel," CRS Report S-1895, 18 September 1992.
2. G.T. Eldis, "A Critical Review of Data Sources for Isothermal Transformation and Continuous Cooling Transformation Diagrams," Hardenability Concepts with Application to Steels, D.V. Doane & J.S. Kirkaldy, eds., AIME, Warrendale PA, 1978, p. 126.

Table 1. Cooling Rate Data for the Individual Test Specimens

<u>Steel Carbon Content, Wt.-%</u>	<u>Cooling<sup>(a)</sup> Curve</u>	<u>Aim. Nominal Cooling Rate, C/s</u>	<u>Actual<sup>(b)</sup> Cooling Rate, C/s</u>
0.10	1	80	82
	2	40	37
	3	20	21
	4	10	10
0.34	1	80	76
	2	40	39
	3	20	21
	4	10	10
0.58	1	80	91
	2	40	40
	3	20	20
	4	10	9
0.83	1	80	87
	2	40	38
	3	20	20
	4	10	10

Notes: (a) Reading from left to right on the diagram.

(b) Average cooling rate from 800 to 500C.

Table 2. Critical Temperatures,  $M_s$  and Retained Austenite After Quenching

<u>Carbon, Wt.-%</u>	<u>Critical Temperatures, C (F)</u>		<u><math>M_s</math>, C (F)</u>	<u>Approx. Retained<sup>(a)</sup> Austenite, Vol.-%</u>
	<u>Lower</u>	<u>Upper</u>		
0.10	665 (1229)	760 (1400)	427 (801)	0
0.34	668 (1234)	730 (1346)	288 (550)	0
0.58	670 (1238)	760 (1400)	201 (394)	5
0.83	668 (1234)	740 (1364)	119 (246)	12

Notes: (a) Estimated from dilatometry and metallographic examination.

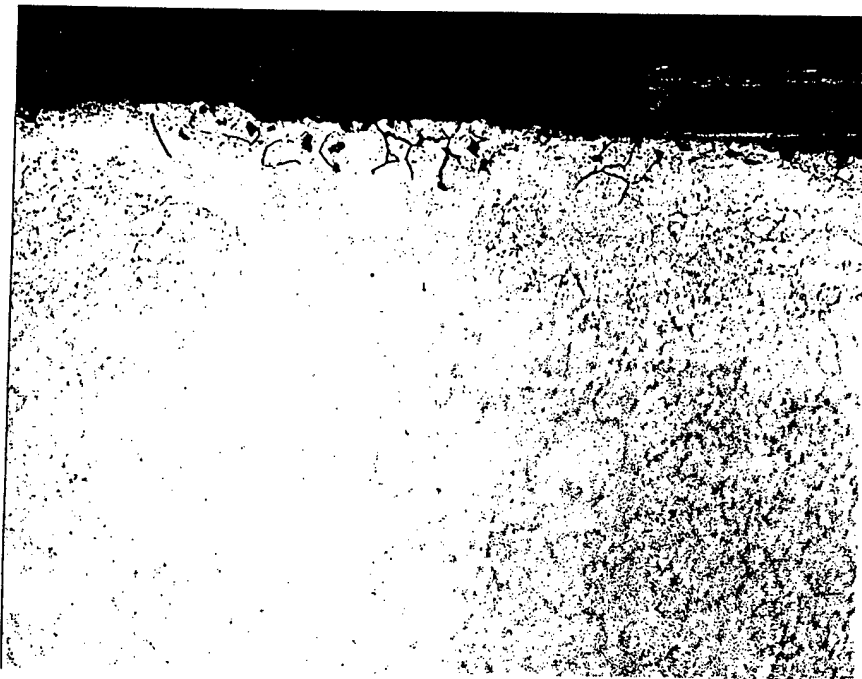


Figure 1. Typical appearance of IGO on dilatometer specimens carburized to 0.34%C or greater. 0.83%C specimen quenched at 10 C/s. 2% Nital etch, 500X.

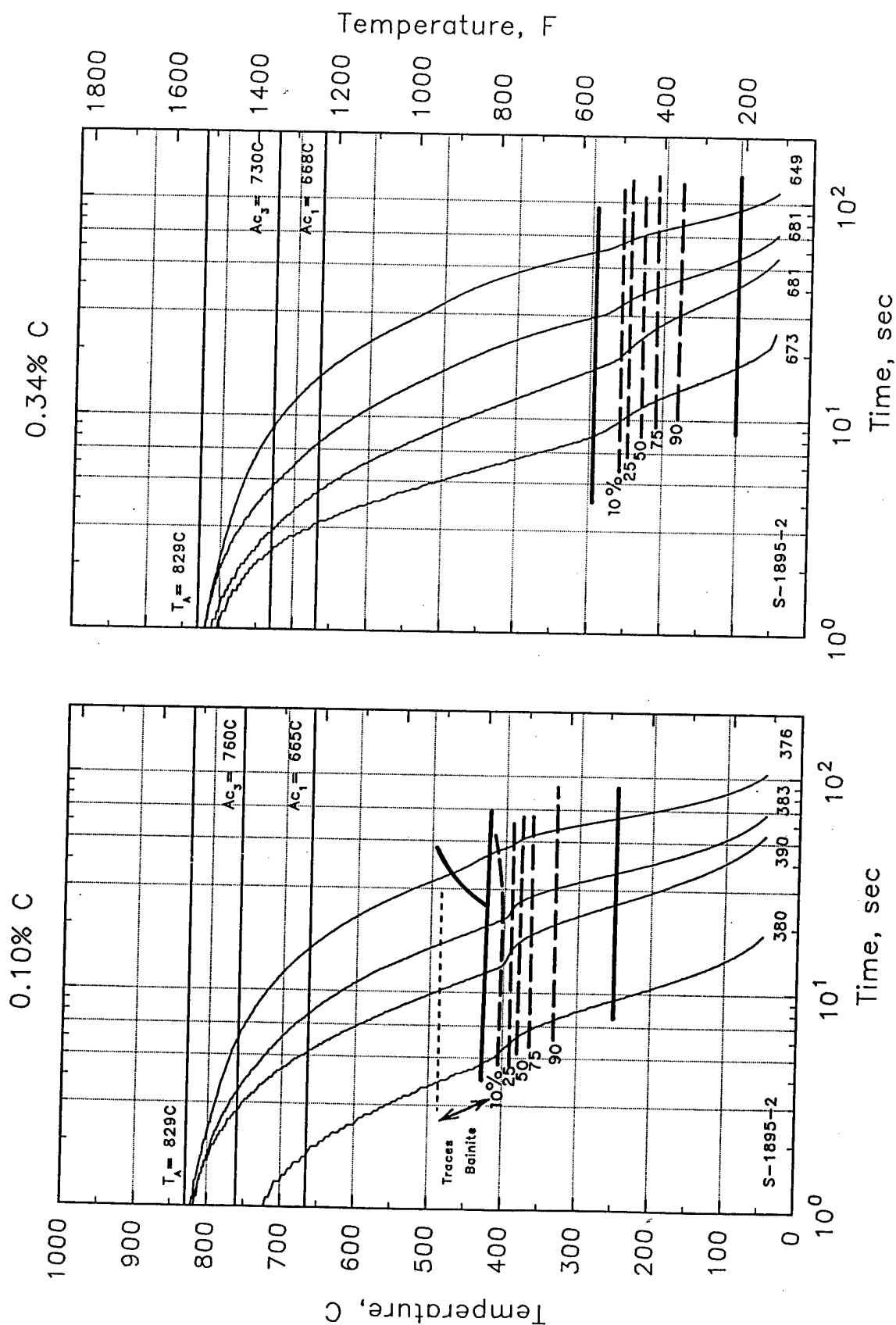


Figure 2. CCT diagram for SAE 9310 at two different carbon contents. Left: blank carburized base alloy at 0.1% C. Right: Base alloy through carburized to 0.34% C.

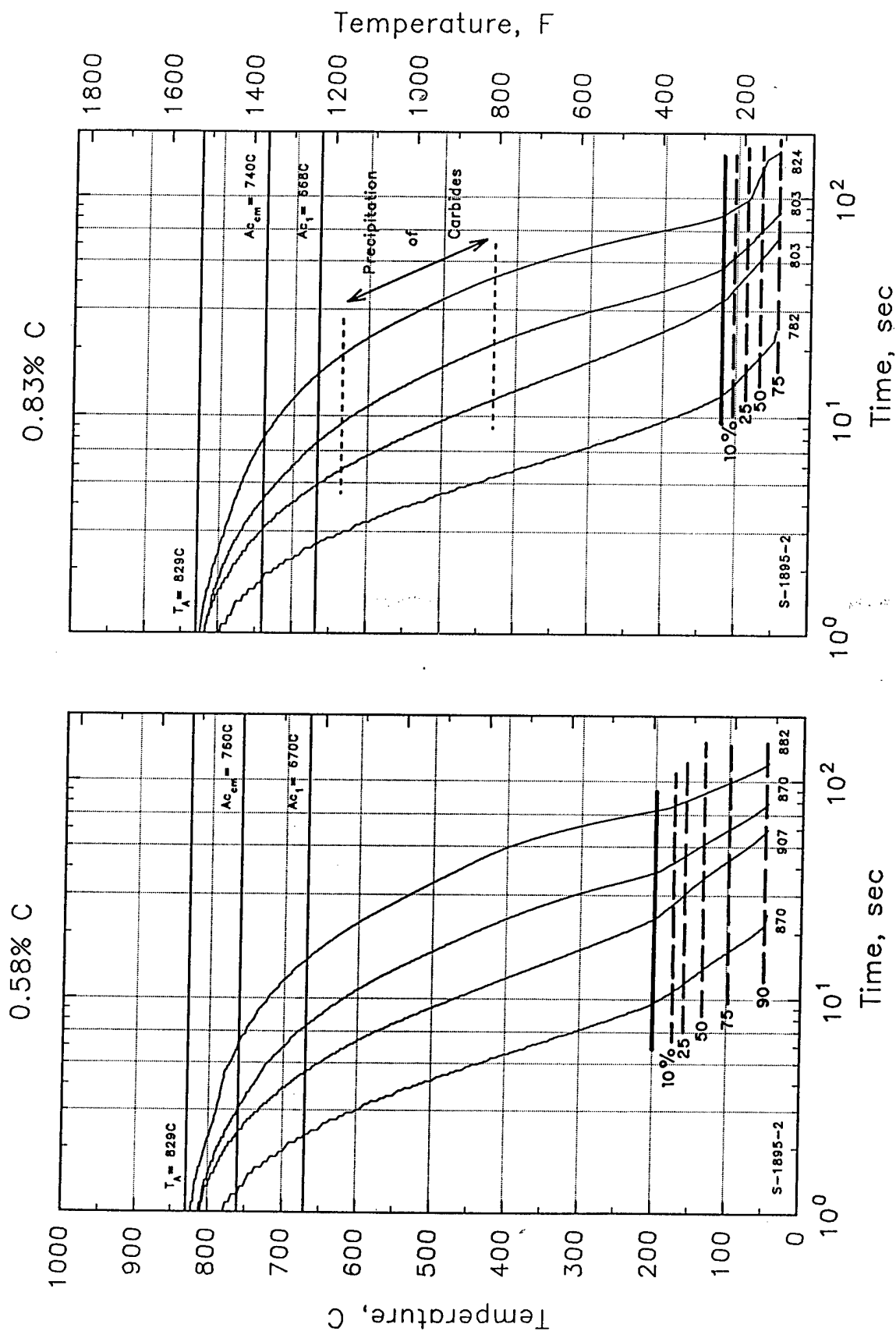


Figure 3. CCT diagram for SAE 9310 at two different carbon contents. Left: Base alloy through carburized to 0.58% C. Right: Base alloy through carburized to 0.83% C.





(a) Quenched at nominally 80 C/s. Predominately martensite, 380 HV10.



(b) Quenched at nominally 10 C/s. Martensite + Bainite, 376 HV10.

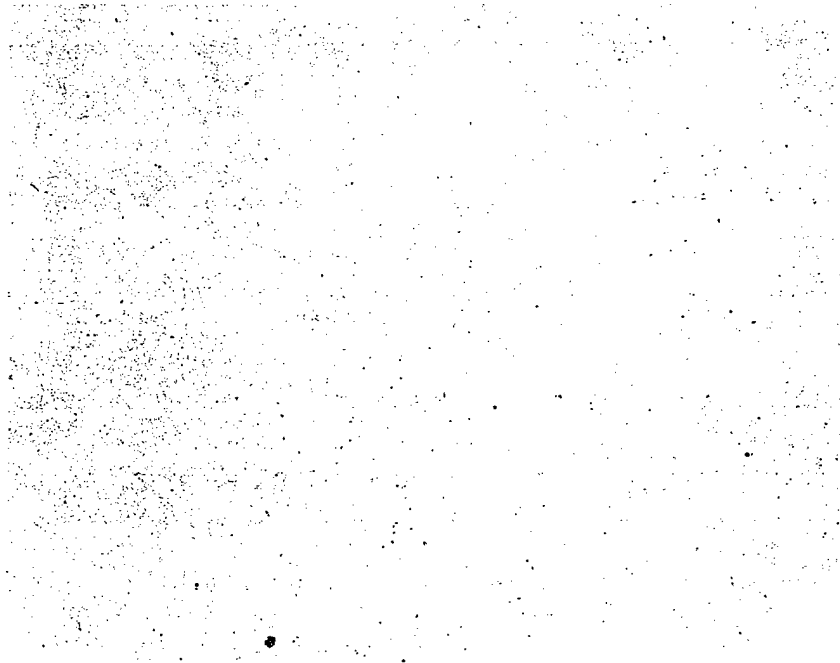
Figure 4. Microstructure of the base alloy (0.1% C) after quenching as indicated. 2% Nital etch, 1250X.



Figure 5. Microstructure of 0.34% C material quenched at nominally 10 C/s.  
2% Nital, 1250X.

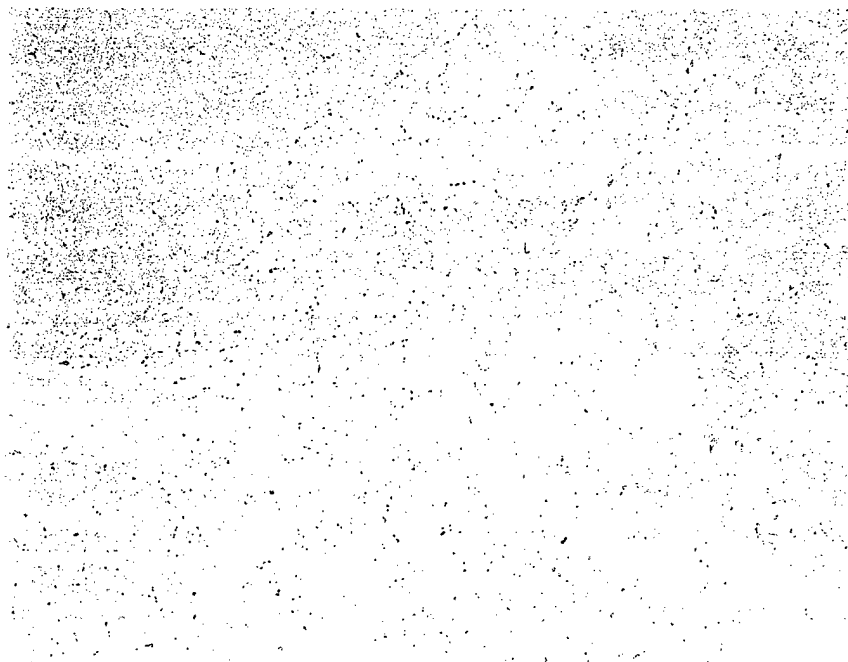


Figure 6. Microstructure of 0.58% C material quenched at nominally 10 C/s.  
2% Nital etch, 1250X.

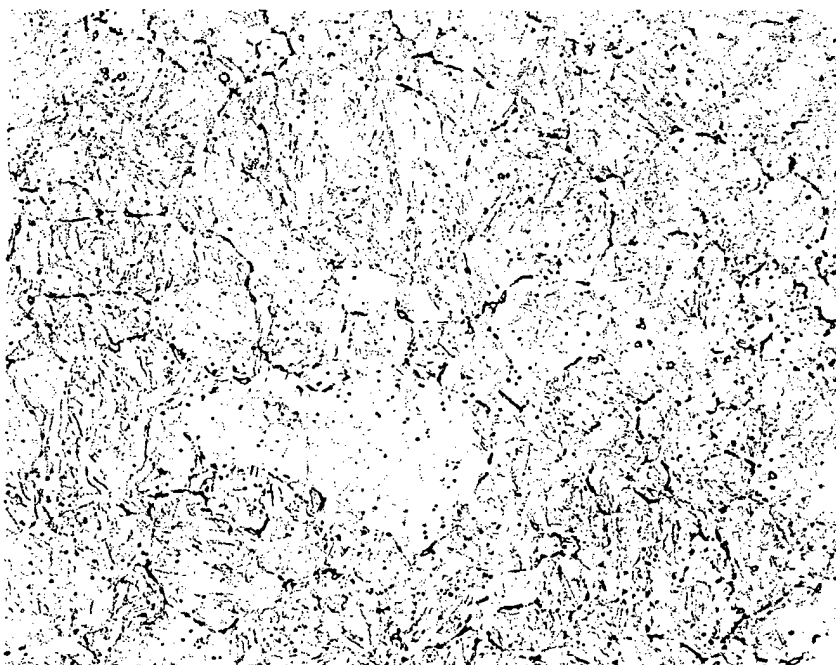


(a) Quenched at nominally 80 C/s.

Figure 7. Microstructure of 0.83% C material after quenching at indicated rates. 2% Nital etch, 1250X.



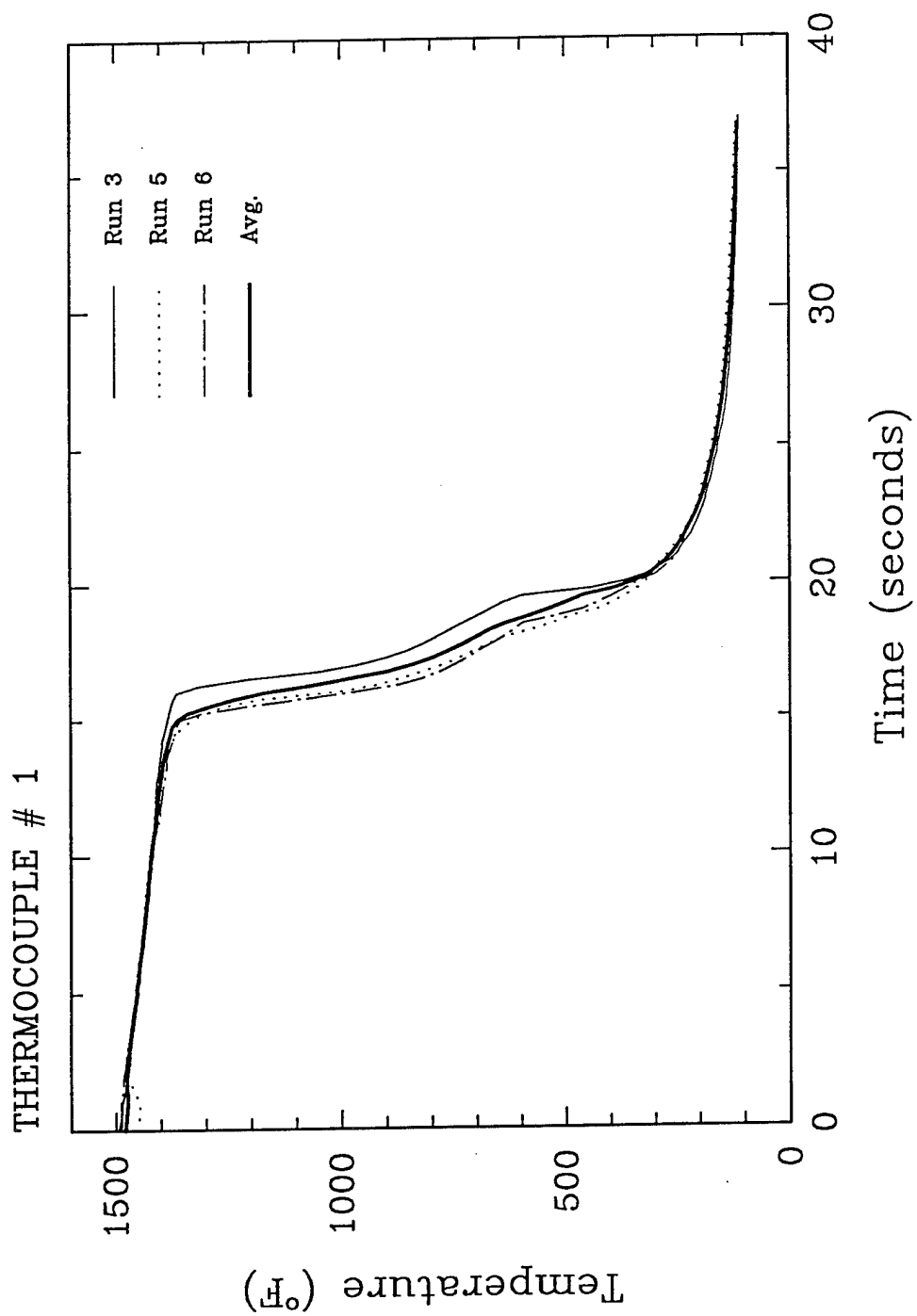
(b) Quenched at nominally 40 C/s.

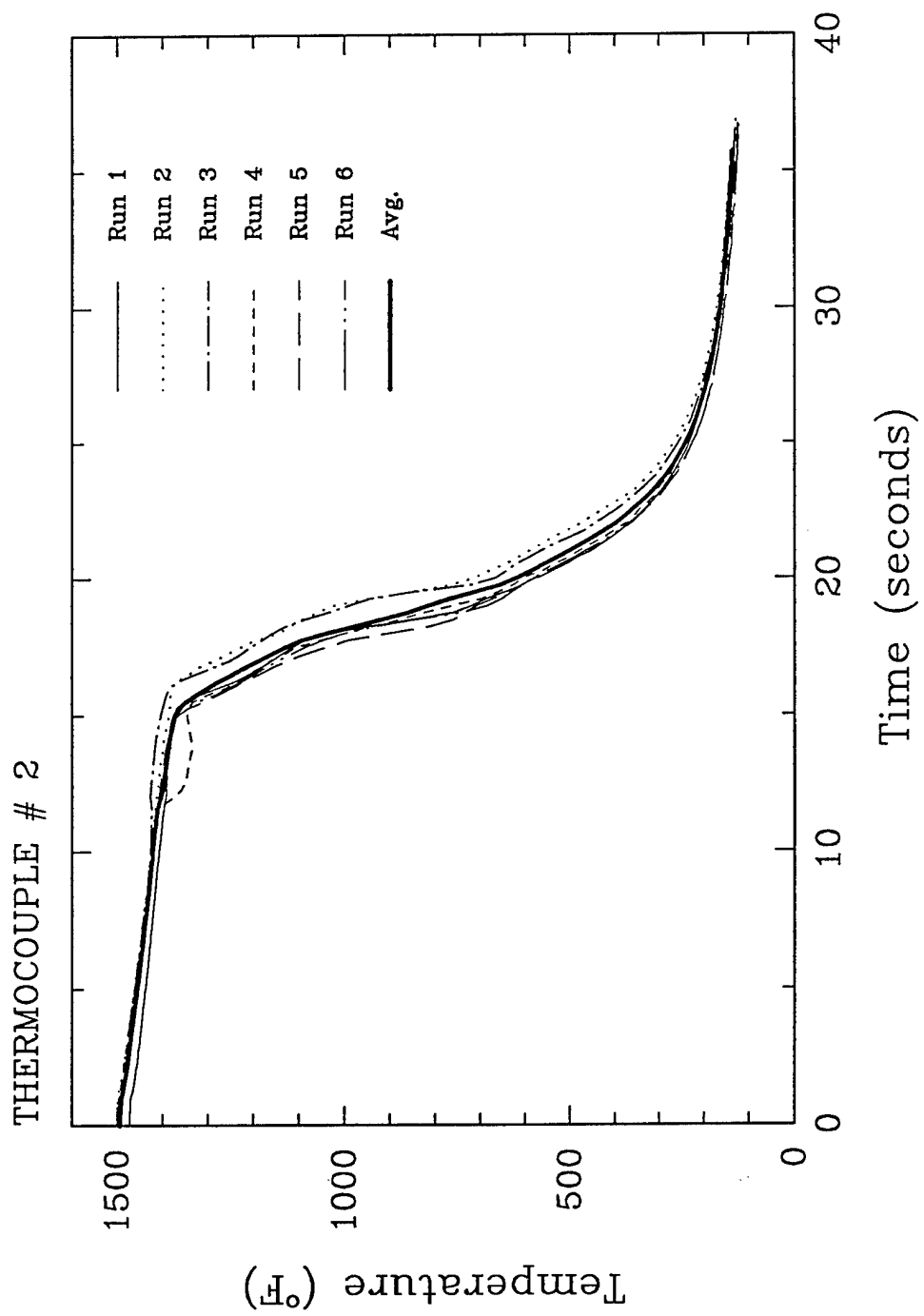


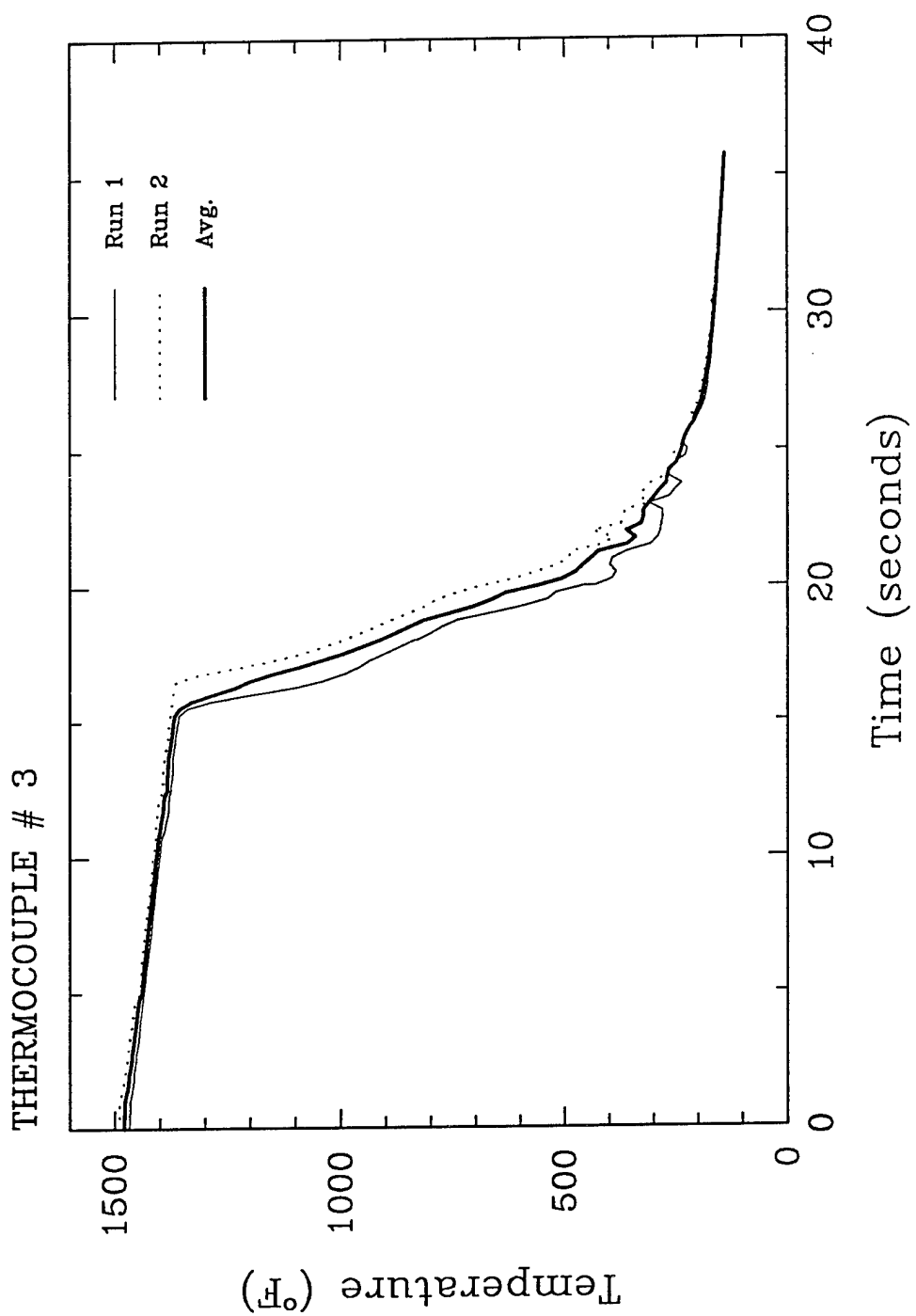
(c) Quenched at nominally 10 C/s.

Figure 7 (concluded).

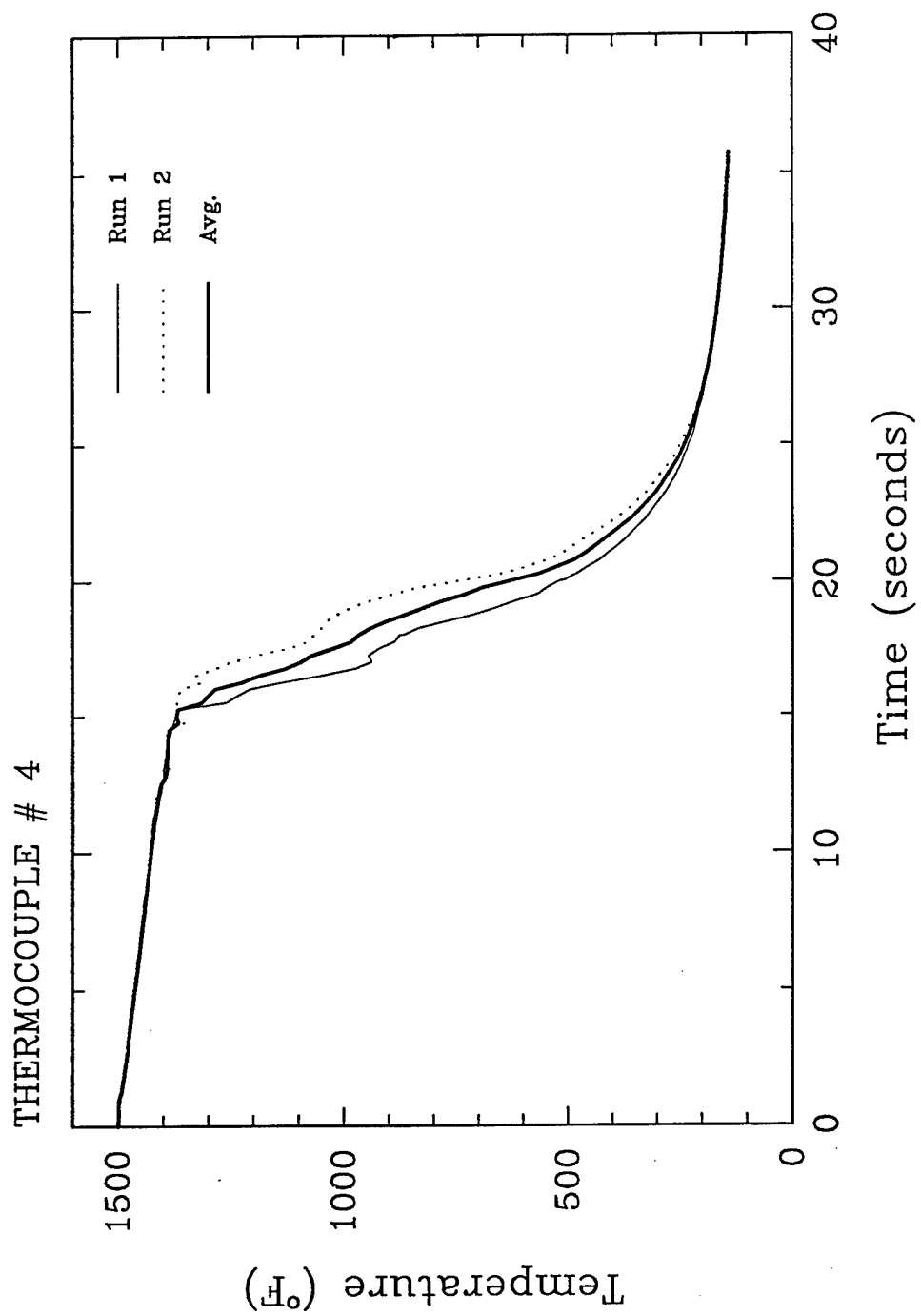
Appendix C. Rim/Web Gear Experiment — Surface Temperature History Measurements.

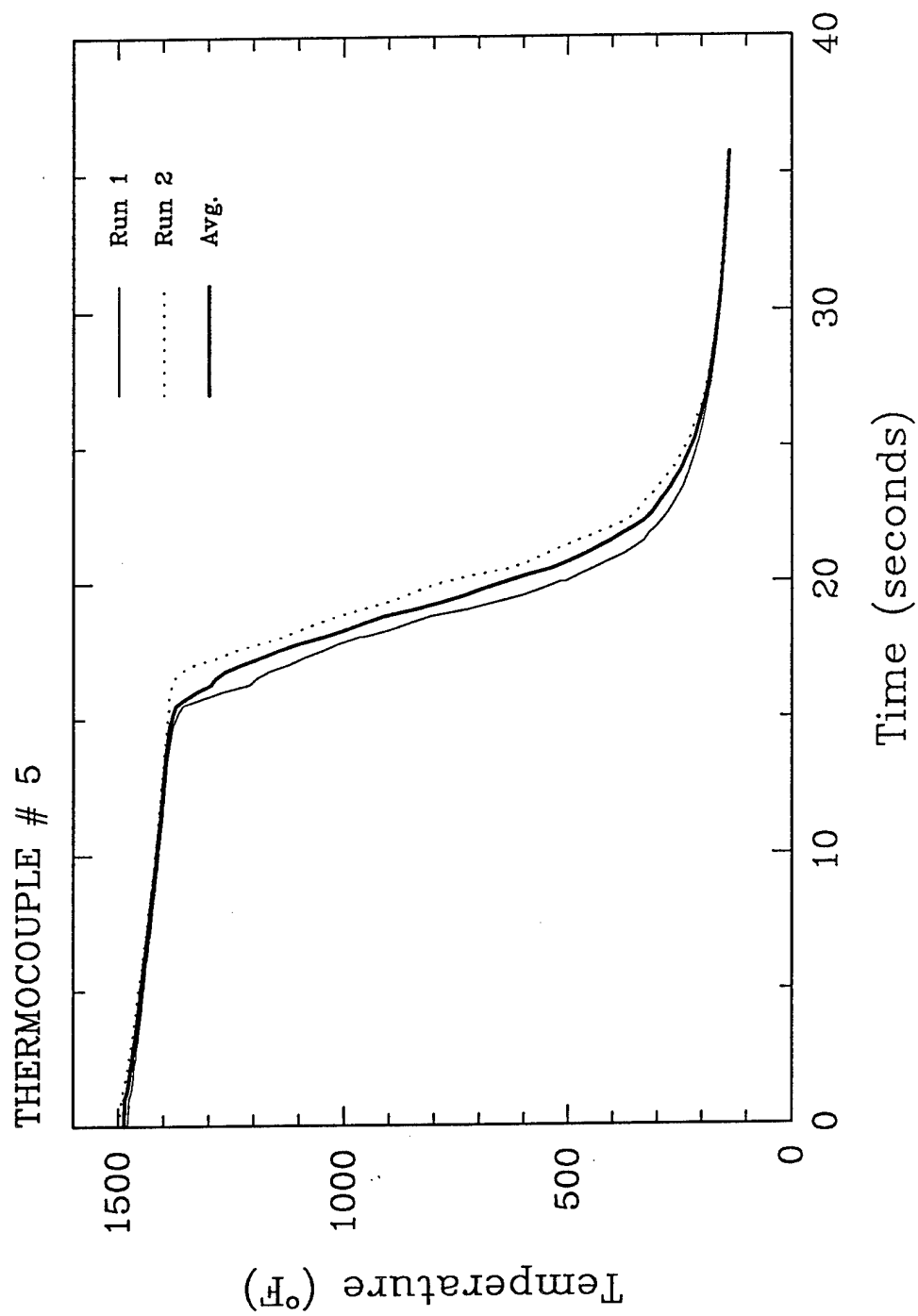


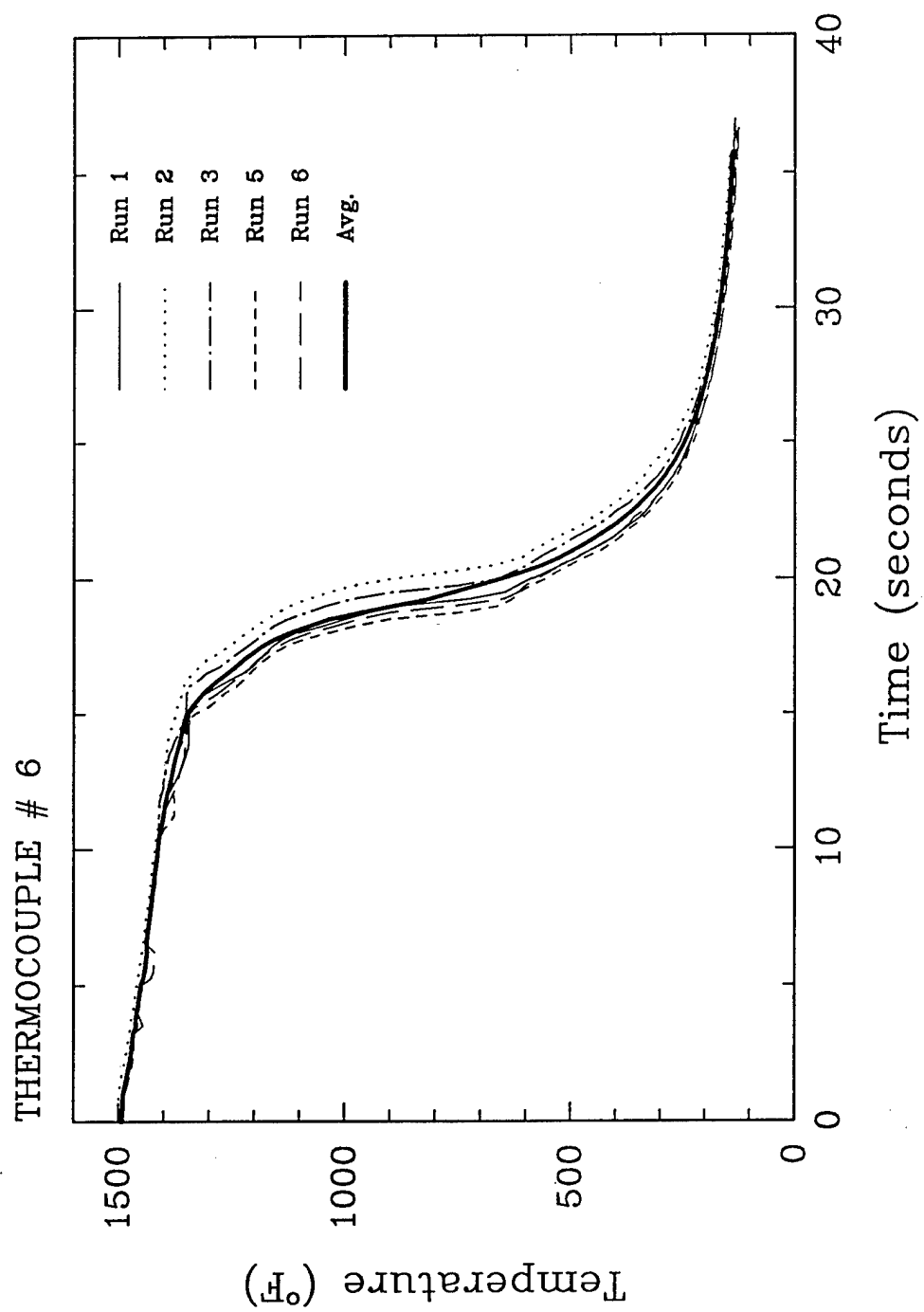


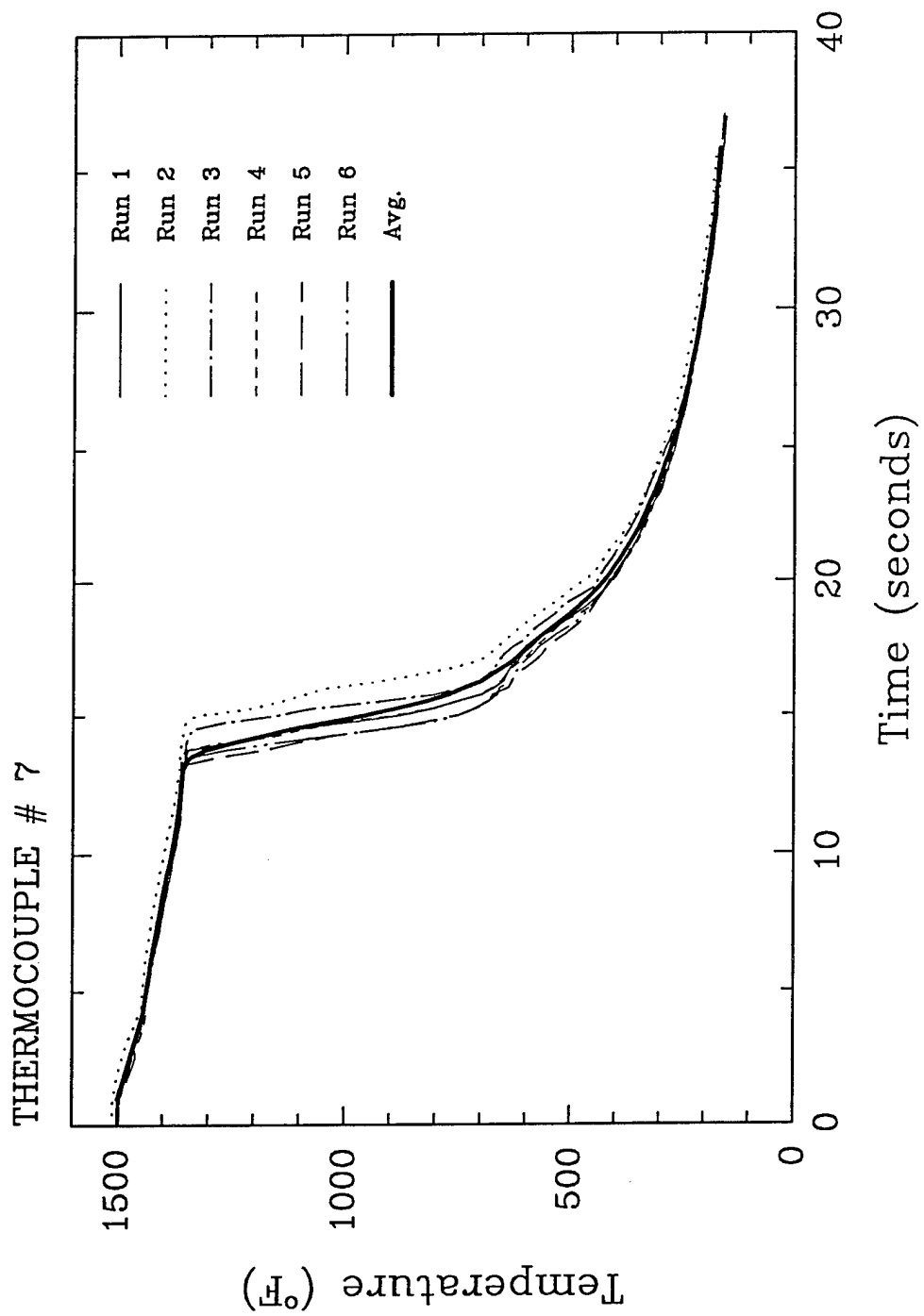


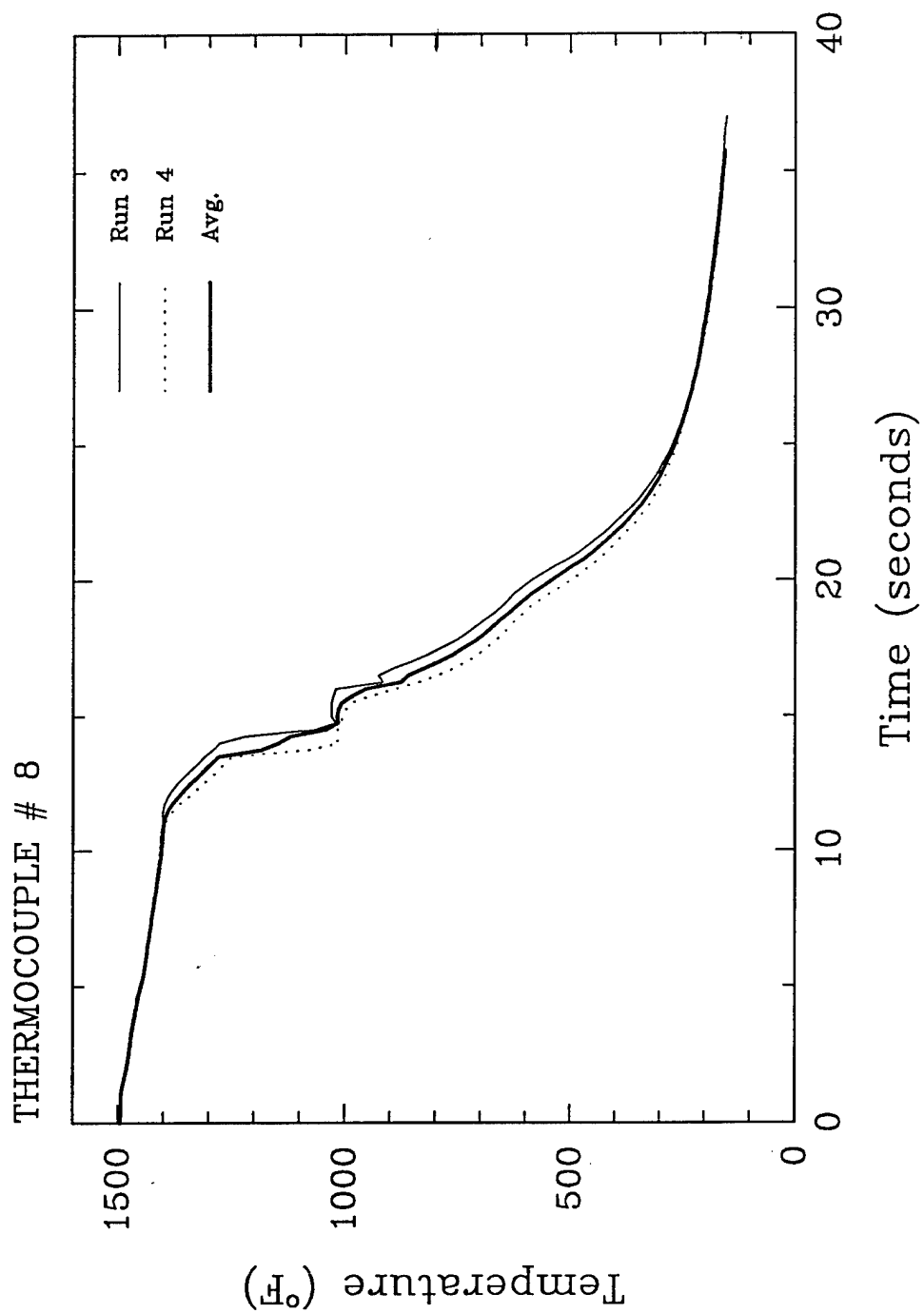












Appendix D. Rim/Web Gear Experiment — Dimensional Measurement Data

Average of the Average of Each Measurement Point for Each Gear

Measurement Point	Before Carburation	After Carburation	After Quench	Delta Carburation	Delta Quench	Standard Deviation Carburation	Standard Deviation Quench
1	0.5719	0.5725	0.5720	0.0006	0.0002	0.0003	0.0002
2	0.5713	0.5717	0.5719	0.0003	0.0006	0.0004	0.0004
3	2.2065	2.2072	2.2104	0.0008	0.0039	0.0006	0.0011
4	1.9400	1.9402	1.9438	0.0003	0.0043	0.0005	0.0056
5	1.7943	1.7947	1.7924	0.0003	-0.0013	0.0005	0.0060
6	1.7940	1.7942	1.7913	0.0001	-0.0022	0.0004	0.0034
7	1.7938	1.7939	1.7930	0.0001	-0.0003	0.0003	0.0010
8	0.5717	0.5721	0.5719	0.0003	0.0001	0.0004	0.0007
9	0.5719	0.5723	0.5719	0.0004	0.0000	0.0004	0.0009

# Web Thickness and Overall Length Measurements

## Overall Length

RW2

Location	Before Carburizing	After Carburizing	After Quench	Delta Carb	Delta Quench
0"	3.9657	3.9674	3.9665	0.0017	0.0008
120"	3.9658	3.9688	3.9666	0.0030	0.0008
240"	3.966	3.9677	3.9671	0.0017	0.0011
AVG	3.9658	3.9680	3.9667	0.0021	0.0009

RW3

Location	Before Carburizing	After Carburizing	After Quench	Delta Carb	Delta Quench
0"	3.9679	3.9686	3.9678	0.0007	-0.0001
120"	3.9682	3.9697	3.9687	0.0015	0.0005
240"	3.9678	3.9688	3.9673	0.0010	-0.0005
AVG	3.9680	3.9690	3.9679	0.0011	0.0000

RW4

Location	Before Carburizing	After Carburizing	After Quench	Delta Carb	Delta Quench
0"	3.9652	3.9675	3.9671	0.0023	0.0019
120"	3.9658	3.9678	3.9657	0.0020	-0.0001
240"	3.9664	3.968	3.9659	0.0016	-0.0005
AVG	3.9658	3.9678	3.9662	0.0020	0.0004

Average of all measurements for all gears

	Before Carburizing	After Carburizing	After Quench	Delta Carb	Delta Quench
Length	3.9665	3.9683	3.9670	0.0017	0.0004
Web Thick	0.1514	0.1516	0.1523	0.0002	0.0009

## Web Thickness

	Before Carburizing	After Carburizing	After Quench	Delta Carb	Delta Quench
	0.1515	0.1513	0.1520	-0.0002	0.0005
	0.1511	0.1516	0.1523	0.0005	0.0012
	0.1516	0.1517	0.1519	0.0001	0.0003
	0.1514	0.1515	0.1521	0.0001	0.0007

	Before Carburizing	After Carburizing	After Quench	Delta Carb	Delta Quench
	0.1532	0.1535	0.1542	0.0003	0.0010
	0.1536	0.1538	0.1547	0.0002	0.0011
	0.1531	0.1538	0.1542	0.0007	0.0011
	0.1533	0.1537	0.1544	0.0004	0.0011

	Before Carburizing	After Carburizing	After Quench	Delta Carb	Delta Quench
	0.1507	0.1502	0.1523	-0.0005	0.0016
	0.1484	0.1487	0.1490	0.0003	0.0006
	0.1498	0.1500	0.1502	0.0002	0.0004
	0.1496	0.1496	0.1505	0.0000	0.0009



## RW1

## Web Distortion

0° "z" measurement from reference  
(point 1 side)

Point	Radial Position	Before Carburizing	After Carburizing	Delta
7	0.9	1.7957	1.7959	0.0002
6	1.22	1.7957	1.7964	0.0007
5	1.65	1.7965	1.7973	0.0008
4	2.17	1.9411	1.9421	0.0010

60°

Point	Radial Position	Before Carburizing	After Carburizing	Delta
7	0.9	1.7956	1.796	0.0004
6	1.22	1.7959	1.7963	0.0004
5	1.65	1.7962	1.7971	0.0009
4	2.17	1.941	1.9422	0.0012

120°

Point	Radial Position	Before Carburizing	After Carburizing	Delta
7	0.9	1.7954	1.7954	0.0000
6	1.22	1.7956	1.7957	0.0001
5	1.65	1.7961	1.7963	0.0002
4	2.17	1.941	1.9413	0.0003

180°

Point	Radial Position	Before Carburizing	After Carburizing	Delta
7	0.9	1.7952	1.7954	0.0002
6	1.22	1.7952	1.7954	0.0002
5	1.65	1.7958	1.7958	0.0000
4	2.17	1.9414	1.9404	-0.0010

240°

Point	Radial Position	Before Carburizing	After Carburizing	Delta
7	0.9	1.7955	1.7952	-0.0003
6	1.22	1.7959	1.7953	-0.0006
5	1.65	1.7961	1.7958	-0.0003
4	2.17	1.9412	1.9406	-0.0006

300°

Point	Radial Position	Before Carburizing	After Carburizing	Delta
7	0.9	1.7958	1.7959	0.0001
6	1.22	1.7961	1.7963	0.0002
5	1.65	1.7965	1.7972	0.0007
4	2.17	1.941	1.9418	0.0008

Average

point	Before Carb.	After Carb.	Delta	Standard Deviation
7	1.7955	1.7956	0.0001	0.0002
6	1.7957	1.7959	0.0002	0.0004
5	1.7962	1.7968	0.0004	0.0004
4	1.9411	1.9414	0.0003	0.0008

## Radial Distortion

0° "x" measurement from reference

Point	z	Position	Before Carburizing	After Carburizing	Delta
1	0.122	0.5724	0.5724	0.5724	0.0000
2	0.85	0.5716	0.5723	0.5723	0.0007
3	1.725	2.2046	2.2064	2.2064	0.0018
8	3.125	0.5717	0.5723	0.5723	0.0006
9	3.85	0.5726	0.5723	0.5723	-0.0003

60°

Point	z	Position	Before Carburizing	After Carburizing	Delta
1	0.122	0.5722	0.5722	0.5726	0.0004
2	0.85	0.5716	0.5723	0.5723	0.0007
3	1.725	2.207	2.2089	2.2089	0.0019
8	3.125	0.5718	0.5723	0.5723	0.0005
9	3.85	0.5727	0.5728	0.5728	0.0001

120°

Point	z	Position	Before Carburizing	After Carburizing	Delta
1	0.122	0.5722	0.5722	0.5727	0.0005
2	0.85	0.5714	0.572	0.572	0.0006
3	1.725	2.2072	2.2079	2.2079	0.0007
8	3.125	0.572	0.572	0.572	0.0000
9	3.85	0.5724	0.5722	0.5722	-0.0002

180°

Point	z	Position	Before Carburizing	After Carburizing	Delta
1	0.122	0.5722	0.5727	0.5727	0.0005
2	0.85	0.5713	0.5716	0.5716	0.0003
3	1.725	2.2071	2.2075	2.2075	0.0004
8	3.125	0.5721	0.5718	0.5718	-0.0003
9	3.85	0.5723	0.5726	0.5726	0.0003

240°

Point	z	Position	Before Carburizing	After Carburizing	Delta
1	0.122	0.5723	0.5727	0.5727	0.0004
2	0.85	0.5716	0.5711	0.5711	-0.0005
3	1.725	2.207	2.2059	2.2059	-0.0011
8	3.125	0.572	0.5707	0.5707	-0.0013
9	3.85	0.5724	0.5721	0.5721	-0.0003

300°

Point	z	Position	Before Carburizing	After Carburizing	Delta
1	0.122	0.5723	0.5724	0.5724	0.0001
2	0.85	0.5715	0.5709	0.5709	-0.0006
3	1.725	2.2065	2.2061	2.2061	-0.0004
8	3.125	0.5719	0.5703	0.5703	-0.0016
9	3.85	0.5725	0.5713	0.5713	-0.0012

Average

point	Before Carb.	After Carb.	Delta	Standard Deviation
1	0.5723	0.5726	0.0003	0.0002
2	0.5715	0.5717	0.0002	0.0005
3	2.2066	2.2071	0.0006	0.0011
8	0.5719	0.5716	-0.0003	0.0008
9	0.5725	0.5722	-0.0003	0.0005

## Web Distortion

"z" measurement from reference

0°

Point	Radial Position	Before Carburizing	After Carburizing	After Quench	Delta Carb	Delta Quench
7	0.9	1.7933	1.7935	1.7920	0.0002	-0.0013
6	1.22	1.7937	1.7941	1.7892	0.0004	-0.0045
5	1.65	1.7942	1.7954	1.7892	0.0012	-0.0050
4	2.17	1.9391	1.9394	1.9334	0.0003	-0.0057

60°

Point	Radial Position	Before Carburizing	After Carburizing	After Quench	Delta Carb	Delta Quench
7	0.9	1.7933	1.7939	1.7935	0.0006	0.0002
6	1.22	1.7932	1.7943	1.7935	0.0011	0.0003
5	1.65	1.7938	1.7952	1.7962	0.0014	0.0024
4	2.17	1.939	1.9394	1.9469	0.0004	0.0079

120°

Point	Radial Position	Before Carburizing	After Carburizing	After Quench	Delta Carb	Delta Quench
7	0.9	1.7934	1.7935	1.7939	0.0001	0.0005
6	1.22	1.7935	1.7934	1.7954	-0.0001	0.0019
5	1.65	1.794	1.7934	1.7993	-0.0006	0.0053
4	2.17	1.9395	1.9393	1.9370	-0.0002	-0.0025

180°

Point	Radial Position	Before Carburizing	After Carburizing	After Quench	Delta Carb	Delta Quench
7	0.9	1.7932	1.7933	1.7933	0.0001	0.0001
6	1.22	1.7934	1.7934	1.7925	0.0000	-0.0009
5	1.65	1.7939	1.7938	1.7959	-0.0001	0.0020
4	2.17	1.9394	1.9395	1.9452	0.0001	0.0058

240°

Point	Radial Position	Before Carburizing	After Carburizing	After Quench	Delta Carb	Delta Quench
7	0.9	1.7936	1.7936	1.7930	0.0000	-0.0006
6	1.22	1.7937	1.7937	1.7915	0.0000	-0.0022
5	1.65	1.7944	1.7943	1.7915	-0.0001	-0.0029
4	2.17	1.9385	1.9388	1.9380	0.0003	-0.0005

300°

Point	Radial Position	Before Carburizing	After Carburizing	After Quench	Delta Carb	Delta Quench
7	0.9	1.7931	1.7934	1.7926	0.0003	-0.0005
6	1.22	1.7937	1.7937	1.7892	0.0000	-0.0045
5	1.65	1.794	1.7944	1.7871	0.0004	-0.0069
4	2.17	1.939	1.9382	1.9312	-0.0008	-0.0078

## Average

point	Before Carb.	After Carb.	After Quench	Delta Carb	Delta Quench	Standard Deviation (Carb)	Standard Deviation (Quench)
7	1.7933	1.7935	1.7931	0.0002	-0.0003	0.0002	0.0006
6	1.7935	1.7938	1.7919	0.0002	-0.0017	0.0004	-0.0024
5	1.7941	1.7944	1.7932	0.0004	-0.0009	0.0007	0.0044
4	1.9391	1.9391	1.9386	0.0000	-0.0005	0.0004	0.0057

## Radial Distortion

"r" measurement from reference

0°

Point	z Position	Before Carburizing	After Carburizing	After Quench	Delta Carb	Delta Quench
1	0.122	0.5717	0.5725	0.5718	0.0008	0.0001
2	0.85	0.5712	0.5715	0.5713	0.0003	0.0001
3	1.725	2.2065	2.2069	2.2101	0.0004	0.0036
8	3.125	0.571	0.5711	0.5706	0.0001	-0.0004
9	3.85	0.5715	0.5723	0.5717	0.0008	0.0002

60°

Point	z Position	Before Carburizing	After Carburizing	After Quench	Delta Carb	Delta Quench
1	0.122	0.5717	0.5727	0.5718	0.0010	0.0001
2	0.85	0.5711	0.5717	0.5711	0.0000	0.0000
3	1.725	2.2067	2.2073	2.2090	0.0006	0.0023
8	3.125	0.5711	0.5713	0.5692	0.0002	-0.0019
9	3.85	0.5717	0.5720	0.5692	0.0003	-0.0025

120°

Point	z Position	Before Carburizing	After Carburizing	After Quench	Delta Carb	Delta Quench
1	0.122	0.5718	0.5722	0.5720	0.0004	0.0002
2	0.85	0.5713	0.5714	0.5720	0.0001	0.0007
3	1.725	2.2069	2.2075	2.2103	0.0006	0.0034
8	3.125	0.5712	0.5715	0.5719	0.0003	0.0007
9	3.85	0.5716	0.5716	0.5719	0.0001	0.0004

180°

Point	z Position	Before Carburizing	After Carburizing	After Quench	Delta Carb	Delta Quench
1	0.122	0.5717	0.5723	0.5716	0.0006	-0.0001
2	0.85	0.5713	0.5717	0.5721	0.0004	0.0008
3	1.725	2.2065	2.2076	2.2102	0.0011	0.0037
8	3.125	0.5713	0.5715	0.5725	0.0002	0.0012
9	3.85	0.5716	0.5718	0.5724	0.0002	0.0008

240°

Point	z Position	Before Carburizing	After Carburizing	After Quench	Delta Carb	Delta Quench
1	0.122	0.5716	0.5729	0.5712	0.0013	-0.0004
2	0.85	0.5713	0.572	0.572	0.0007	0.0006
3	1.725	2.2064	2.2081	2.2091	0.0017	0.0027
8	3.125	0.5711	0.5717	0.5722	0.0006	0.0011
9	3.85	0.5716	0.5724	0.5732	0.0008	0.0016

300°

Point	z Position	Before Carburizing	After Carburizing	After Quench	Delta Carb	Delta Quench
1	0.122	0.5716	0.5724	0.5723	0.0008	0.0007
2	0.85	0.5712	0.5713	0.5728	0.0001	0.0014
3	1.725	2.2067	2.2084	2.2093	0.0003	0.0026
8	3.125	0.5714	0.5719	0.5721	0.0005	0.0007
9	3.85	0.5713	0.5723	0.5725	0.0010	0.0012

## Average

point	Before Carb.	After Carb.	After Quench	Delta Carb	Delta Quench	Standard Deviation (Carb)	Standard Deviation (Quench)
1	0.5717	0.5725	0.5718	0.0008	0.0001	0.0003	0.0003
2	0.5712	0.5716	0.5718	0.0004	0.0006	0.0002	0.0005
3	2.2066	2.2073	2.2097	0.0007	0.0030	0.0006	0.0005
8	0.5712	0.5715	0.5715	0.0003	0.0002	0.0002	0.0011
9	0.5715	0.5721	0.5718	0.0005	0.0003	0.0003	0.0013

## RW3

## Web Distortion

"z" measurement from reference

0°

Point	Radial Position	Before Carburizing	After Carburizing	After Quench	Delta Carb	Delta Quench
7	0.9	1.7951	1.7951	1.7944	-0.0001	-0.0007
6	1.22	1.7952	1.7952	1.7907	0.0000	-0.0045
5	1.65	1.7953	1.796	1.7889	0.0007	-0.0064
4	2.17	1.9409	1.9411	1.9344	0.0002	-0.0065

60°

Point	Radial Position	Before Carburizing	After Carburizing	After Quench	Delta Carb	Delta Quench
7	0.9	1.7947	1.7954	1.7947	0.0003	0.0000
6	1.22	1.7951	1.7951	1.7933	0.0000	-0.0018
5	1.65	1.795	1.7955	1.7954	0.0005	0.0004
4	2.17	1.9412	1.9417	1.9434	0.0005	0.0022

120°

Point	Radial Position	Before Carburizing	After Carburizing	After Quench	Delta Carb	Delta Quench
7	0.9	1.7952	1.7954	1.7959	0.0002	0.0007
6	1.22	1.7956	1.7956	1.7975	0.0000	0.0019
5	1.65	1.7951	1.7959	1.8012	0.0008	0.0061
4	2.17	1.9408	1.9413	1.9513	0.0005	0.0105

180°

Point	Radial Position	Before Carburizing	After Carburizing	After Quench	Delta Carb	Delta Quench
7	0.9	1.7953	1.7957	1.7961	0.0004	0.0008
6	1.22	1.7954	1.7962	1.7975	0.0008	0.0021
5	1.65	1.7952	1.7962	1.8013	0.0010	0.0061
4	2.17	1.9411	1.9419	1.9497	0.0008	0.0086

240°

Point	Radial Position	Before Carburizing	After Carburizing	After Quench	Delta Carb	Delta Quench
7	0.9	1.7952	1.7948	1.7949	-0.0004	-0.0003
6	1.22	1.7953	1.7954	1.7937	0.0001	-0.0016
5	1.65	1.7955	1.7961	1.7943	0.0006	-0.0012
4	2.17	1.9409	1.9405	1.9504	-0.0004	0.0095

300°

Point	Radial Position	Before Carburizing	After Carburizing	After Quench	Delta Carb	Delta Quench
7	0.9	1.7954	1.7944	1.7935	-0.0010	-0.0019
6	1.22	1.7952	1.7948	1.7894	-0.0004	-0.0058
5	1.65	1.7955	1.7957	1.7871	0.0002	-0.0084
4	2.17	1.9407	1.9402	1.9314	-0.0005	-0.0093

Average

point	Before Carb.	After Carb.	After Quench	Delta Carb	Delta Quench	Standard Deviation (Quench)
7	1.7952	1.7951	1.7949	-0.0001	-0.0002	0.0005
6	1.7953	1.7954	1.7937	0.0001	-0.0016	0.0004
5	1.7953	1.7959	1.7947	0.0006	-0.0006	0.0029
4	1.9409	1.9411	1.9434	0.0002	0.0025	0.0056

## Radial Distortion

"r" measurement from reference

0°

Point	z Position	Before Carburizing	After Carburizing	After Quench	Delta Carb	Delta Quench
1	0.122	0.5719	0.5727	0.5722	0.0008	0.0003
2	0.85	0.5712	0.5715	0.5717	0.0003	0.0005
3	1.725	2.2061	2.2068	2.2088	0.0007	0.0027
8	3.125	0.5717	0.5717	0.5701	0.0000	-0.0016
9	3.83	0.5722	0.5726	0.5706	0.0004	-0.0016

60°

Point	z Position	Before Carburizing	After Carburizing	After Quench	Delta Carb	Delta Quench
1	0.122	0.5721	0.5726	0.5722	0.0005	0.0001
2	0.85	0.5716	0.5716	0.5722	0.0000	0.0006
3	1.725	2.2064	2.2067	2.2102	0.0003	0.0038
8	3.125	0.5719	0.5719	0.5716	-0.0001	-0.0004
9	3.85	0.5722	0.5725	0.5717	0.0003	-0.0005

120°

Point	z Position	Before Carburizing	After Carburizing	After Quench	Delta Carb	Delta Quench
1	0.122	0.5723	0.5723	0.5723	0.0010	0.0003
2	0.85	0.5717	0.5724	0.5723	0.0007	0.0006
3	1.725	2.2068	2.2068	2.2111	-0.0002	0.0043
8	3.125	0.5721	0.5728	0.5726	0.0007	0.0005
9	3.85	0.5724	0.5729	0.5721	0.0005	-0.0003

180°

Point	z Position	Before Carburizing	After Carburizing	After Quench	Delta Carb	Delta Quench
1	0.122	0.5718	0.5727	0.5724	0.0009	0.0006
2	0.85	0.5714	0.5723	0.5721	0.0009	0.0007
3	1.725	2.2067	2.2062	2.2128	-0.0005	0.0061
8	3.125	0.5721	0.5725	0.5718	0.0004	-0.0003
9	3.85	0.5723	0.5729	0.5714	0.0008	-0.0009

240°

Point	z Position	Before Carburizing	After Carburizing	After Quench	Delta Carb	Delta Quench
1	0.122	0.5717	0.5726	0.5721	0.0009	0.0004
2	0.85	0.5716	0.5718	0.5719	0.0002	0.0003
3	1.725	2.2065	2.2073	2.2091	0.0008	0.0028
8	3.125	0.5722	0.5718	0.5714	-0.0004	-0.0008
9	3.85	0.5722	0.5726	0.5719	0.0004	-0.0003

300°

Point	z Position	Before Carburizing	After Carburizing	After Quench	Delta Carb	Delta Quench
1	0.122	0.5721	0.5727	0.5724	0.0006	0.0003
2	0.85	0.5713	0.5716	0.5720	0.0003	0.0007
3	1.725	2.2063	2.2059	2.2059	-0.0004	0.0036
8	3.125	0.5718	0.5719	0.5716	0.0001	-0.0002
9	3.85	0.5721	0.5727	0.5721	0.0006	0.0000

Average

point	Before Carb.	After Carb.	After Quench	Delta Carb	Delta Quench	Standard Deviation (Quench)
1	0.5719	0.5727	0.5723	0.0008	0.0003	0.0002
2	0.5715	0.5719	0.5720	0.0004	0.0006	0.0003
3	2.2065	2.2066	2.2103	0.0001	0.0038	0.0005
8	0.5720	0.5715	0.0001	-0.0005	-0.0004	0.0006
9	0.5722	0.5727	0.5716	0.0005	-0.0006	0.0001

## Web Distortion

"z" measurement from reference

0°

Point	Radial Position	Before Carburizing	After Carburizing	After Quench	Delta Carb	Delta Quench
7	0.9	1.7914	1.7915	1.7927	0.0001	0.0013
6	1.22	1.7916	1.792	1.7952	0.0004	0.0036
5	1.65	1.7919	1.7925	1.7996	0.0006	0.0077
4	2.17	1.9381	1.9389	1.9509	0.0008	0.0128

60°

Point	Radial Position	Before Carburizing	After Carburizing	After Quench	Delta Carb	Delta Quench
7	0.9	1.7914	1.7915	1.7910	0.0001	-0.0004
6	1.22	1.7918	1.7915	1.7886	0.0000	-0.0032
5	1.65	1.7921	1.7925	1.7882	0.0004	-0.0039
4	2.17	1.9384	1.9393	1.9544	0.0009	0.0160

120°

Point	Radial Position	Before Carburizing	After Carburizing	After Quench	Delta Carb	Delta Quench
7	0.9	1.7912	1.7915	1.7887	0.0003	-0.0025
6	1.22	1.7915	1.7915	1.7838	0.0000	-0.0077
5	1.65	1.7917	1.7913	1.7891	-0.0004	-0.0026
4	2.17	1.9387	1.9385	1.9477	-0.0002	0.0090

180°

Point	Radial Position	Before Carburizing	After Carburizing	After Quench	Delta Carb	Delta Quench
7	0.9	1.7916	1.7914	1.7900	-0.0002	-0.0016
6	1.22	1.7916	1.7912	1.7842	-0.0004	-0.0074
5	1.65	1.7919	1.7911	1.7796	-0.0008	-0.0123
4	2.17	1.9391	1.9395	1.9460	0.0004	0.0069

240°

Point	Radial Position	Before Carburizing	After Carburizing	After Quench	Delta Carb	Delta Quench
7	0.9	1.7913	1.7917	1.7902	0.0004	-0.0011
6	1.22	1.7916	1.7916	1.7845	0.0000	-0.0071
5	1.65	1.7915	1.7915	1.7800	0.0000	-0.0115
4	2.17	1.9389	1.9401	1.9463	0.0012	0.0074

300°

Point	Radial Position	Before Carburizing	After Carburizing	After Quench	Delta Carb	Delta Quench
7	0.9	1.7914	1.7915	1.7926	0.0001	0.0012
6	1.22	1.7914	1.7918	1.7943	0.0004	0.0029
5	1.65	1.7918	1.792	1.7952	0.0002	0.0074
4	2.17	1.939	1.9397	1.9516	0.0007	0.0126

Average

point	Before Carb.	After Carb.	After Quench	Delta Carb	Delta Quench	Standard Deviation (Carb)	Standard Deviation (Quench)
7	1.7914	1.7915	1.7909	0.0001	-0.0005	0.0002	0.0014
6	1.7916	1.7917	1.7884	0.0001	-0.0032	0.0003	0.0048
5	1.7918	1.7918	1.7893	0.0000	-0.0025	0.0005	0.0080
4	1.9387	1.9393	1.9495	0.0006	0.0108	0.0004	0.0033

## Radial Distortion

"z" measurement from reference

0°

Point	z	Position	Before Carburizing	After Carburizing	After Quench	Delta Carb	Delta Quench
1	0.122	0.5712	0.5713	0.5722	0.5718	0.0009	0.0005
2	0.85	0.5708	0.5717	0.5712	0.5717	0.0009	0.0004
3	1.725	2.2074	2.2078	2.2074	2.2088	0.0014	0.0028
8	3.125	0.5717	0.5727	0.5726	0.5727	0.0010	0.0009
9	3.85	0.5718	0.5733	0.5723	0.5733	0.0015	0.0005

60°

Point	z	Position	Before Carburizing	After Carburizing	After Quench	Delta Carb	Delta Quench
1	0.122	0.5712	0.5712	0.5722	0.5719	0.0010	0.0007
2	0.85	0.5705	0.5715	0.5714	0.5714	0.0010	0.0009
3	1.725	2.2059	2.2078	2.2107	2.2107	0.0019	0.0048
8	3.125	0.572	0.5726	0.5722	0.5726	0.0006	0.0002
9	3.85	0.5722	0.5731	0.5734	0.5734	0.0009	0.0012

120°

Point	z	Position	Before Carburizing	After Carburizing	After Quench	Delta Carb	Delta Quench
1	0.122	0.5716	0.572	0.5718	0.572	0.0004	0.0002
2	0.85	0.5709	0.5714	0.5723	0.5714	0.0005	0.0014
3	1.725	2.2063	2.2146	0.0020	0.0083	0.0020	0.0083
8	3.125	0.5719	0.5725	0.5730	0.5730	0.0006	0.0011
9	3.85	0.5720	0.5730	0.5708	0.5708	0.0010	-0.0012

180°

Point	z	Position	Before Carburizing	After Carburizing	After Quench	Delta Carb	Delta Quench
1	0.122	0.5716	0.5722	0.5715	0.5720	0.0006	-0.0001
2	0.85	0.5714	0.5718	0.5720	0.5720	0.0004	0.0006
3	1.725	2.2057	2.2085	2.2115	0.0018	0.0048	0.0048
8	3.125	0.5721	0.5728	0.5728	0.5728	0.0002	0.0007
9	3.85	0.5720	0.5730	0.5718	0.5718	0.0010	-0.0002

240°

Point	z	Position	Before Carburizing	After Carburizing	After Quench	Delta Carb	Delta Quench
1	0.122	0.5719	0.5717	0.5718	-0.0002	-0.0001	-0.0001
2	0.85	0.5716	0.5722	0.5711	-0.0005	0.0006	0.0006
3	1.725	2.2065	2.2079	2.2117	0.0014	0.0052	0.0052
8	3.125	0.5720	0.5723	0.5723	0.0003	0.0012	0.0012
9	3.85	0.5722	0.5726	0.5722	0.0004	0.0000	0.0000

300°

Point	z	Position	Before Carburizing	After Carburizing	After Quench	Delta Carb	Delta Quench
1	0.122	0.5717	0.5721	0.5719	0.5719	0.0004	0.0002
2	0.85	0.5715	0.5713	0.5714	-0.0002	-0.0001	-0.0001
3	1.725	2.2063	2.2080	2.2100	0.0017	0.0037	0.0037
8	3.125	0.5718	0.5724	0.5721	0.0006	0.0006	0.0006
9	3.85	0.5718	0.5724	0.5724	0.0014	0.0006	0.0006

Average

point	Before Carb.	After Carb.	After Quench	Delta Carb	Delta Quench	Standard Deviation (Carb)	Standard Deviation (Quench)
1	0.5716	0.5721	0.5718	0.0005	0.0002	0.0004	0.0003
2	0.5711	0.5715	0.5718	0.0004	0.0006	0.0005	0.0005
3	2.2063	2.2080	2.2112	0.0017	0.0049	0.0002	0.0017
8	0.5719	0.5725	0.5727	0.0006	0.0007	0.0003	0.0004
9	0.5720	0.5730	0.5722	0.0010	0.0002	0.0004	0.0008

Appendix E. Residual Stress Measurements Performed by Lambda Research



# LAMBDA RESEARCH

5521 FAIR LANE

CINCINNATI, OHIO 45227

PHONE: 513/561-0883

FAX: 513/561-0886

Arthur D. Little, Inc.  
25 Acorn Park  
Cambridge, MA 02140-2390

## X-RAY DIFFRACTION DETERMINATION OF THE SURFACE RESIDUAL STRESSES ON TWO 9310 STEEL GEAR BLANKS

REPORT: 401-5649  
DATE: February 16, 1995

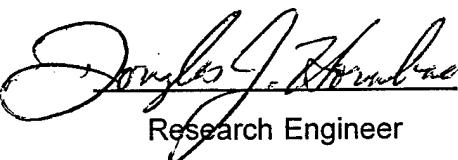
ATTN:  
AUTHORIZATION:

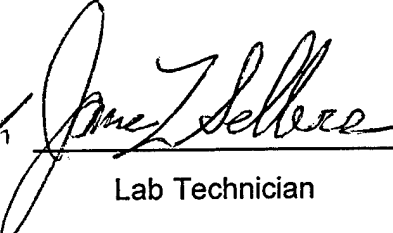
Mr. Shaun Berry  
207023-00S

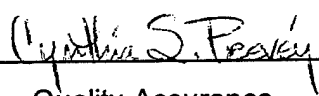
### INTRODUCTION

Two gear blanks were received from Arthur D. Little Inc. for the purpose of determining the circumferential and radial surface residual stresses. The gear blanks, identified as RW2 and RW3, were reportedly manufactured from 9310 steel, and were nominally 4 in. long with a 0.4 in. thick by 4.5 in. diameter disk mid length on the axis.

The purpose of this study was to determine the residual stresses in each specimen due to carburizing the rim.

  
Research Engineer

  
Lab Technician

  
Quality Assurance



This report shall not be reproduced, except in full, without the approval of Lambda Research, Inc. The results reported apply only to the specific sample/s submitted for analysis. Lambda Research is accredited by the American Association for Laboratory Accreditation (Certificate Number 0138-01) and operates a quality system in accordance with ISO/IEC Guide 25. Lambda Research is a member of the American Council of Independent Laboratories.



## TECHNIQUE

X-ray diffraction residual stress measurements were made at the surface only on two gear blanks. Measurements were made on specimens RW3 and RW2 in a circumferential direction at three rim locations 120 deg. apart. The rim locations were identified as #1, #2, and #3. Residual stress measurements were also made on specimen RW2 in the radial direction at two 0 deg. web locations and at two 180 deg. web locations. The web locations, measured on the long shaft side, were identified as #4, #5, #6, and #7. There was a 0 deg. reference mark on each gear blank. All of the measurement locations are shown in Figure 1.

X-ray diffraction residual stress measurements were performed using a two-angle sine-squared-psi technique, in accordance with GE specification 4013195-991 and SAE J784a, employing the diffraction of chromium K-alpha radiation from the (211) planes of the BCC structure of the 9310 steel. The diffraction peak angular positions at each of the psi tilts employed for measurement were determined from the position of the K-alpha 1 diffraction peak separated from the superimposed K-alpha doublet assuming a Pearson VII function diffraction peak profile in the high back-reflection region.<sup>(1)</sup> The diffracted intensity, peak breadth, and position of the K-alpha 1 diffraction peak were determined by fitting the Pearson VII function peak profile by least squares regression after correction for the Lorentz polarization and absorption effects and for a linearly sloping background intensity.

Details of the diffractometer fixturing are outlined below:

Incident Beam Divergence:	0.5 deg.
Detector:	Scintillation set for 90% acceptance of the chromium K-alpha energy
Psi Rotation:	10 and 50 deg.
Irradiated Area:	0.1 by 0.1 in.

The value of the x-ray elastic constant,  $E/(1 + \nu)$ , required to calculate the macroscopic residual stress from the strain measured normal to the (211) planes of 9310 steel was previously determined empirically <sup>(2)</sup> employing a simple rectangular beam manufactured from 9310 steel loaded in four-point bending on the diffractometer to known stress levels and measuring the resulting change in the spacing of the (211) planes in accordance with ASTM E1426-91.

Because only surface measurements were performed for this investigation, it was not possible to correct the results for the effects of penetration of the radiation employed for residual stress measurement into the subsurface stress gradient. The magnitude of this correction can be quite significant, particularly on machined or ground surfaces, and can even change the sign of surface results. It is recommended that subsurface residual stress profiles be obtained in the future to ascertain the magnitude of this correction and to define the subsurface residual stress profile.

## RESULTS AND DISCUSSION

The circumferential and radial surface residual stresses are presented in Table I. Compressive stresses are shown as negative values, tensile as positive, in units of ksi ( $10^3$  psi).

The (211) diffraction peak width was calculated simultaneously with the macroscopic residual stress from the peak width in the  $\psi=10^\circ$  orientation. The (211) diffraction peak width is a sensitive function of the chemistry, hardness, and the degree to which the material has been cold worked. In martensitic steels, it is commonly observed that plastic deformation produced by processes such as shot peening or grinding will cause work softening, and a reduction in the peak width. In work hardening materials, the diffraction peak width increases significantly as a result of an increase in the average microstrain and the reduced crystallite size produced by cold working. The (211) diffraction peak width can be indicative of how the material may have been processed, and the depth to which it has been plastically deformed.

The error shown for each residual stress measurement is one standard deviation resulting from random error in the determination of the diffraction peak angular positions and in the empirically determined value of  $E/(1 + \nu)$  in the  $\langle 211 \rangle$  direction. An additional semi-systematic error on the order of  $\pm 2$  ksi ( $\pm 14$  MPa) may result from sample positioning and instrument alignment errors. The magnitude of this systematic error was monitored using a powdered metal zero-stress standard in accordance with ASTM specification E915, and found to be +0.9 ksi during the course of this investigation.

## CONCLUSIONS

The residual stress results, listed in Table I, indicate compression ranging from -24 ksi to -30 ksi for the measurements made at the rim of the RW3 specimen. The RW2 rim data indicate compressive stresses ranging from -35 ksi to -37 ksi. The web locations for specimen RW2 are in tension ranging from +17 ksi to +31 ksi.

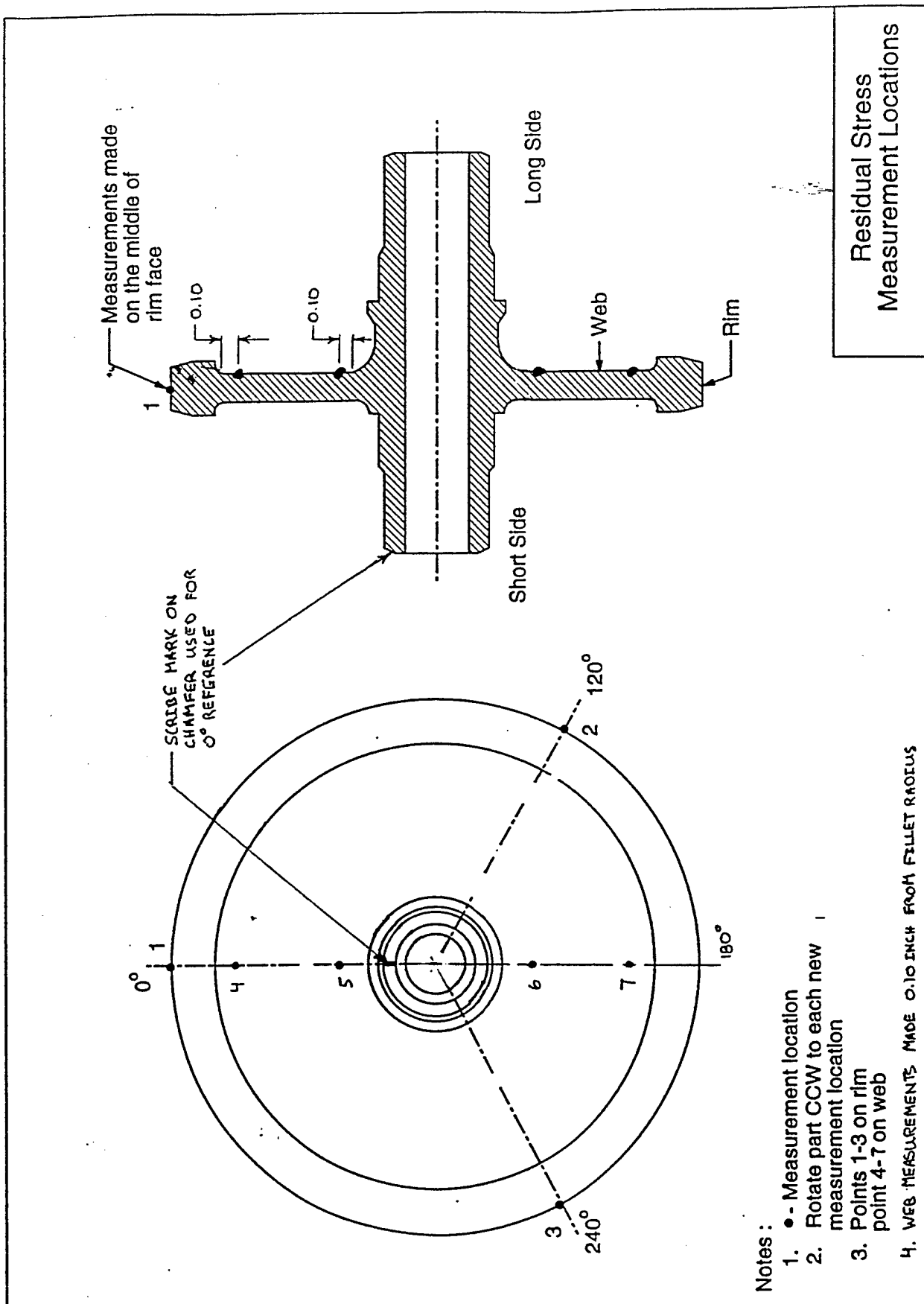
The (211) peak width data indicate hardened rim material. The RW2 specimen shows slightly harder material at the rim location compared to RW3. The web location data show relatively softer material compared to the rim location.

## REFERENCES:

[sf.fm.0893]

- (1) P.S. Prevey, ADV. IN X-RAY ANAL., Vol. 29, 1986, pp. 103-112.
- (2) P.S. Prevey, ADV. IN X-RAY ANAL., Vol. 20, 1977, pp. 345-354.





SURFACE RESIDUAL STRESSES  
9310 STEEL GEAR BLANKS  
RIM AND WEB LOCATION

	<u>Specimen</u>	<u>Direction</u>	<u>Location</u>	<u>Residual Stress (ksi)</u>	<u>Peak Width (deg.)</u>
1	RW3	Circ.	Rim #1 (0 deg.)	-29.3 $\pm$ 3.4	6.29
		Circ.	Rim #2 (120 deg.)	-24.6 $\pm$ 3.2	6.18
		Circ.	Rim #3 (240 deg.)	-25.4 $\pm$ 3.3	6.33
2	RW2	Circ.	Rim #1 (0 deg.)	-36.0 $\pm$ 4.1	7.39
		Circ.	Rim #2 (120 deg.)	-36.6 $\pm$ 4.1	7.19
		Circ.	Rim #3 (240 deg.)	-35.0 $\pm$ 4.0	7.23
		Radial	Web #4 (Rim Edge)	+30.9 $\pm$ 2.9	3.58
		Radial	Web #5 (Hub Edge)	+23.5 $\pm$ 2.1	3.67
		Radial	Web #6 (Hub Edge)	+17.5 $\pm$ 2.0	3.69
		Radial	Web #7 (Rim Edge)	+22.8 $\pm$ 2.8	3.51